



**Numerical hydrodynamic analysis of wave energy
converter arrays with inter-body mooring
connections with the spar-buoy OWC
as a case study**

Charikleia Oikonomou

MSc in Physical Oceanography, Bangor University, Wales

Undergraduate degree in Marine Sciences, University of the Aegean, Greece

A thesis submitted in partial fulfillment
for the degree of Doctor of Philosophy

Supervisor: Professor George A. Aggidis

**Engineering Department,
Faculty of Science and Technology
Lancaster University, UK**

2018

Declaration

The author declares that this thesis has not been previously submitted for award for a higher degree to this or any university, and that the contents, except where otherwise stated, are the author's own work.

Charikleia Oikonomou

Date:.....

Signature:.....

Declaration by Charikleia Oikonomou

This thesis was submitted to Lancaster University for the Degree of Doctor of Philosophy on the 4th of October 2018. Chapter 4 of the thesis includes material that was presented in a conference proceeding [1], and output that is currently under review in a scientific journal [2]:

[1] Oikonomou, C., Gomes, R. P. F., Gato, L. M. C. and Falcão, A. F. O. (2017), Analysis of a triangular array of floating oscillating water column devices with inter-body mooring connections in regular waves, *in*: '12th European Wave and Tidal Energy Conference', Cork, Ireland.

[2] Oikonomou, C. L. G., Gomes, R. P. F., Gato, L. M. C. and Falcão, A. F. O. (2018), 'On the dynamics of an array of spar-buoy oscillating water column devices with inter-body mooring connections', *Ren. Energy*, under review. Ms. Ref. No.: RENE-D-18-02101R1

I hereby declare that all material in this chapter is my own work except for where otherwise stated. The research was conducted by myself under the supervision of Professor Luís Gato, Dr. Rui Gomes and Professor António Falcão. Dr. Rui Gomes provided training on the Boundary Integral Element Method and provided the viscous damping data from small-scale experiments. The numerical model was developed by myself with advice by Dr. Rui Gomes. Professor Luís Gato and Professor António Falcão provided advice and comments. The spar-buoy OWC with a non-uniform cross-section tube is a patented wave energy technology by Instituto Superior Técnico (IST).

Charikleia Oikonomou



Professor Luís M. C. Gato



Abstract

Numerical hydrodynamic analysis of wave energy converter arrays with inter-body mooring connections with the spar-buoy OWC as a case study

Charikleia Oikonomou, MSc

Submitted for the degree of Doctor of Philosophy

This PhD thesis explores the hydrodynamics and the performance of a moored array of Wave Energy Converters (WECs). A comparison is made between the performance of an array with bottom mooring lines and the performance of an array that uses shared mooring lines (i.e. inter-body mooring connections). The fundamental equations for arrays with shared moorings are developed in the frequency-domain where simple spherical devices moving in the three translational modes are considered. The numerical model uses linear hydrodynamic and hydrostatic forces, while the mooring connections are linearised using perturbation theory. This is further elaborated upon by considering cylindrical devices, so that the three rotational modes may be considered, as well as their hydrodynamic coupling with the three translational modes. This moored array of cylindrical devices moving in all six Degrees-of-Freedom (DoF) is used as a foundation to explore the hydrodynamics and the performance of an array of floating Oscillating Water Column (OWC) devices known as spar-buoy OWC. Real fluid viscous effects are accounted for by using a linear approximation. The frequency-domain numerical model of the moored array of spar-buoy OWCs is used as a basis for a stochastic model, where the array's performance for a Portuguese wave climate is assessed. The performance of arrays with shared mooring connections VS arrays with bottom mooring connections is explored in both the frequency and stochastic domain models for the spar-buoy OWC array. Both models have confirmed that there is minimal difference in performance between the two mooring systems, which is desirable because the one has been suggested as a more economically viable solution than the other due to drastic reductions in the amount of mooring cables and anchors.

Keywords

Renewable energy, Wave energy conversion, Wave energy converter arrays, Inter-body mooring connections, Shared moorings, Floating oscillating water column, Spar-buoy OWC, Irregular waves, Stochastic modelling, Park effect, Two-body wave energy conversion systems, Point absorbers

Dedication

I would like to dedicate this effort to my mother Vicky and my boyfriend Marty.

«Ήτον πνοή, ἴνδαλμα ἀφάνταστον, ὄνειρον ἐπιπλέον εἰς τό
κῦμα· ἦτο νηρηίς, νύμφη, σειρήν, πλέουσα, ὡς πλέει ναῦς
μαγική, ἡ ναῦς τῶν ὀνείρων...»

Απόσπασμα από το «Όνειρο στο κύμα» του Αλ. Παπαδιαμάντη

Acknowledgements

First I would like to thank my supervisor Professor George Aggidis, Professor of Energy Engineering and director of the Lancaster University Renewable Energy Group (LUREG) for his encouragement and support throughout these four years of this academic process, and for giving me the opportunity to enroll in the PhD program at Lancaster University and the freedom to shape this PhD towards the direction it finally took. I would like to thank the Engineering department at Lancaster University, and especially Miss Laura Gracie. I also acknowledge my examiners Professor Jianqiao Ye from Lancaster University and Professor Lars Johanning from the University of Exeter for their constructive feedback.

I would like to thank Professor António Falcão and Professor Luís Gato from Instituto Superior Técnico (IST), for welcoming me to their research group in Mecânica IV, and facilitating a friendly environment for me for a semester, but also for sharing with me their knowledge in the scientific field. A great word of thank you to Dr. Rui Gomes, postdoctoral researcher at IST with whom I collaborated on the array of spar-buoys, and he introduced me to the Boundary Integral Element Method used in this thesis. It has been great luck to work together. Also, I would like to thank Dr. Pedro Vicente from WavEC Offshore Renewables, for always answering to my questions on his initial work, which inspired the content of this thesis.

A special thanks to Marty Gradowski from Bombora Wave Power for the endless discussions on hydrodynamics, and for proofreading this thesis. I would also like to thank Dr. Suzi Illic and Dr. Dan Potter from Lancaster University who discussed with me ideas, Ross Robertson for providing feedback on scientific writing, and Dr. John Miritzis from the University of the Aegean for always being available to discuss with me on mathematical aspects. For non-scientific support I would like to thank Dr. Dan Potter, Dr. Suzi Illic, Dr. Bella Chatterjee, Maria Karamanou, Meriem Baccouche, Ilias Kotronis, Andrés Sánchez, Xinha Jardine, Sue Tyson, Joop Brouwer, and Márcia Tavares. A word of thank you to my good friends from Greece, Katerina Tavri, Marilia Avgerinou, Effie Konstantinidou, Eva Manoutsoglou, and Elena Akritopoulou for all these years of friendship and for always seeing the best in me.

Finally, I would like to thank my parents Giorgos and Vicky and my brother Alex, for their love and support - financial and moral. I also would like to thank my boyfriend Marty for his love and patience.

Published Work

1. **Oikonomou, C.**, Gomes, R. P. F., Gato, L. M. C. and Falcão, A. F. O. (2018), ‘On the dynamics of an array of spar-buoy oscillating water column devices with inter-body mooring connections’, *Ren. Energy*, under review.
2. **Oikonomou, C.**, Gomes, R. P. F., Gato, L. M. C. and Falcão, A. F. O. (2017), Analysis of a triangular array of floating oscillating water column devices with inter-body mooring connections in regular waves, *in*: ‘12th European Wave and Tidal Energy Conference’, Cork, Ireland.
3. **Oikonomou, C.** and Aggidis, G. A. (2015). Wave Energy Resource Assessment and Device Selection. SuperGen UKCMER Annual Assembly 2015. Friday 27th November, 2015, Edinburgh, Scotland. (Poster presentation).
4. **Oikonomou, C.** and Aggidis, G. A. (2015). Wave energy resource assessment in the seas around Greece: estimation and prospects, *in* ‘SCACR2015 - International Short Course/Conference on Applied Coastal Research’, Florence, Italy.

Talks

1. **Oikonomou, C.** and Aggidis, G. A. (2018), ‘Hydrodynamic Analysis of moored axially symmetric arrays’, LUREG Seminar Series, Lancaster University, 24.05.2018.
2. **Oikonomou, C.** (2018), ‘Numerical modelling for wave energy converter arrays’, Institute for Marine and Atmospheric research, Utrecht University, the Netherlands, 24.01.2018.
3. **Oikonomou, C.** (2017), ‘Hydrodynamic Analysis of a Triangular Array of Arbitrary Geometry Wave Energy Converters Devices with Inter-body Mooring Connections in Regular Waves’, LUREG Seminar Series, Lancaster University, 20.11.2017.
4. **Oikonomou, C.** and Aggidis, G. A. (2017), ‘Climate analysis and numerical modelling of wave energy conversion’, Postgraduate Review Conference, Engineering Department, Lancaster University, 06.07.2017.
5. **Oikonomou, C.** and Aggidis, G. A. (2016), ‘Wave energy conversion modelling: a frequency domain analysis’, Postgraduate Review conference, Engineering department, Lancaster University, 29.06.2016.
6. **Oikonomou, C.** and Aggidis, G. A. (2015), ‘Wave energy resource in the seas around Greece: Estimation and prospects’, SCACR 2015 - 7th International short course/conference on applied coastal research, Florence, Italy, 29.09.2015.
7. **Oikonomou, C.** and Aggidis, G. A. (2015), ‘Wave energy modelling and application in the Mediterranean Sea’, Postgraduate Review Conference, Engineering Department, Lancaster University, 01.07.2015.

-
8. **Oikonomou, C.** (2015), ‘Wave energy modelling’, LUREG Seminar Series, Lancaster University, 21.01.2015.

Academic Achievements & Courses

17.02.2016 – 29.07.2016, Advanced Formation Diploma in Marine Renewable Energies (30 ECTS), Instituto Superior Técnico, Universidade de Lisboa, Portugal: During my PhD and in parallel with my research activity I completed an advanced postgraduate diploma supervised by Professor Luís Gato. The course included the modules: Ocean Energy Resources, Modelling and Control of Ocean Energy Systems, Ocean Energy Systems technologies, Economics Policy and Environment.

14.09.2015 – 16.09.2015, DHI course, Queen’s University, Belfast, Ireland:

I attended the course “Understanding the coastal ocean: a foundation course in the modelling of waves and tides”, by the Queen’s University Belfast, and DHI Water Environments.

Nominee, Dean’s Award: I was a nominee for the Lancaster University Faculty of Science and Technology Dean’s Award for Excellence in PhD Studies in first year (2014 - 2015).

19.05.2015 – 17.06.2015, Department of Physics, University of Athens, Greece:

I was a visiting researcher at the Atmospheric Modelling and Weather Forecasting Group, under the supervision of Professor George Kallos, to learn numerical tools for wave forecasting and resource analysis.

Michaelmas Term 2014 - 2015, Student Physics of Fluids (PHYS323), Department of Physics, Lancaster University: I attended the course Physics of Fluids, by Dr. Jonathan Gratus. The course covered the topics: Introduction to continuum mechanics, Static fluids, Ideal Fluids, Newtonian fluids, Waves, Fluid mechanics of plasmas.

Outreach activities

School liaison activities, Lancaster Girls Grammar School (LGGS), Lancaster, UK - Winter 2015: I organised the activity “Engineering challenge: designing a wave energy conversion plant for Morecambe Bay, UK”. LGGS students received first and second prize, competing with students from other Lancaster high schools.

Contents

Nomenclature	xiv
Abbreviations	xiv
Latin symbols	xiv
Subscripts	xvi
Superscripts	xvii
Greek symbols	xvii
List of Figures	xxv
List of Tables	xxvi
1 Introduction	1
1.1 State of the art	2
1.1.1 Wave energy resource	2
1.1.2 Arrays of WECs	3
1.1.3 Moorings for WECs	4
1.2 Aim and objectives	6
1.3 Research methodology and approaches	6
1.4 Contribution to knowledge and practice	7
1.5 Thesis layout	7
2 Background theory and motivation	9
2.1 Wave generation theories	9
2.2 Classifying WECs based on the deployment location	10
2.2.1 Onshore zone	10
2.2.2 Nearshore zone	11
2.2.3 Offshore zone	11
2.3 WEC technologies	12
2.3.1 Attenuators	12
2.3.2 Point absorbers	12
2.3.3 Oscillating wave surge converters	13
2.3.4 Submerged Pressure Differential devices	13
2.3.5 Bulge wave devices	13
2.3.6 Rotating mass devices	14
2.3.7 OWCs	14

2.3.8	Overtopping/ terminator devices	14
2.4	Power take-off mechanisms	14
2.4.1	Air turbine energy transfer	15
2.4.2	Hydropower turbine energy transfer	15
2.4.3	Hydraulic oil circuit energy transfer	16
2.4.4	Linear generator energy transfer	16
2.5	Fixed structure WECs	17
2.5.1	Fixed structure oscillating body converters	17
2.5.2	Fixed structure overtopping converters	17
2.5.3	Fixed structure oscillating water column converters	18
2.6	Floating structure WECs	18
2.6.1	Floating oscillating water column converters	18
2.6.2	Floating oscillating body converters	20
2.6.3	Floating over-topping converters	22
2.7	Submerged structure WECs	23
2.8	Moorings for WECs	25
2.8.1	Anchors	27
2.9	Mooring systems	27
2.9.1	Catenary system	28
2.9.2	Taut mooring system	28
2.10	Fundamentals of ocean waves	29
2.10.1	The momentum equation	29
2.10.2	The continuity equation	30
2.10.3	Wave theories in brief	30
2.10.4	Modelling of ocean waves using linear wave theory	30
2.10.5	The wave climate	35
2.11	Wave force theories	36
2.11.1	Morison's equation	37
2.11.2	Froude-Krylov theory	37
2.11.3	Diffraction theory	38
2.12	Oscillating body type wave energy converters	39
2.12.1	Single body system in the frequency-domain	40
2.12.2	Single body system in the time-domain	43
2.12.3	Two-body system in the frequency-domain	44
2.12.4	Two-body system in the time-domain	45
2.13	Numerical modelling of mooring connections	47
2.13.1	Experimentally obtained mooring properties	48
2.13.2	Quasi-static modelling	49
2.13.3	Dynamic analysis modelling	50
3	Moored array of point absorbers	53
3.1	Introduction	53
3.2	Numerical model: spherical WECs	55

3.2.1	Equation of motion for the array	55
3.2.2	Hydrodynamic radiation and excitation coefficients	57
3.2.3	Hydrostatic coefficients	57
3.2.4	Linear PTO	59
3.2.5	Clump weight and inter-body mooring connections	59
3.2.6	Bottom mooring line forces	62
3.3	Numerical model: cylindrical WECs	63
3.3.1	Equation of motion for the array	63
3.3.2	Hydrostatic coefficients	64
3.3.3	Cylindrical point absorbers: viscous damping	65
3.4	Results: array of spherical point absorbers	68
3.4.1	Resonance frequency	69
3.4.2	Sensitivity analysis	74
3.4.3	Comparison with Vicente et al. (2009a)	76
3.5	Results: array of cylindrical point absorbers	77
3.6	Limitations	80
3.7	Chapter discussion and concluding remarks	83
4	Moored array of spar-buoy OWCs	86
4.1	Introduction	86
4.2	Numerical model: regular wave analysis	87
4.2.1	Equation of motion for the array	87
4.2.2	Hydrodynamic radiation and excitation coefficients	90
4.2.3	Hydrostatic coefficients	91
4.2.4	Power absorption and air compressibility effects	92
4.2.5	Drag force for regular waves	93
4.2.6	Clump weight and inter-body mooring connections	95
4.2.7	Bottom mooring line forces	97
4.2.8	Independently moored array	97
4.2.9	Capture width ratio	99
4.3	Numerical model: irregular wave analysis	100
4.3.1	Wave spectrum	100
4.3.2	Power available to the turbine	101
4.3.3	Viscous damping	101
4.3.4	Gain factor	102
4.4	Results and discussion	102
4.4.1	Regular wave analysis	103
4.4.2	Array of spar-buoy OWCs	107
4.4.3	Effect of wave incidence angle	115
4.4.4	Irregular wave analysis	124
4.5	Preliminary model verification: critical reflection	131
4.6	Chapter summary and concluding remarks	132

5	Conclusions	134
5.1	Limitations of the presented research	135
5.2	Recommendations for future work	136
	References	152
	Appendices	153
A	Mesh sensitivity analysis	154
B	Spherical point absorbers: sensitivity analysis	157
C	Single spar-buoy OWC	171

Nomenclature

Abbreviations

AWS	Archimedes Wave Swing
BBDB	Backward Bent Duct Buoy
BIEM	Boundary Integral Element Method
CALM	Catenary Anchor Leg Mooring
CFD	Computational Fluid Dynamics
CoB	Centre of Buoyancy
CoG	Centre of Gravity
CPA	Cylindrical Point Absorber
CW	Clump Weight
CWR	Capture Width Ratio
DFIGs	Doubly Fed Induction Generators
DNV	Det Norske Veritas
DoF	Degrees-of-Freedom
EMEC	European Marine Energy Centre
EPSRC	Engineering and Physical Sciences Research Council
FEA	Finite Element Analysis
IPS Buoy	Inter Project Service Buoy
IST	Instituto Superior Técnico
JONSWAP	Joint North Sea Wave Observation Project
KC	Keulegan-Carpenter number
LIMPET	Land Installed Marine Power Energy Transmitter
LUREG	Lancaster University Renewable Energy Group
MaRINET	Marine Renewables Infrastructure Network for Emerging Technologies
OPERA	Open Sea Operating Experience to Reduce Wave Energy Costs
PA	Point Absorber
P-M	Pierson-Moskowitz
PMSGs	Permanent Magnet Synchronous Generators
PTO	Power Take-Off

RAO	Response Amplitude Operator
SALM	Single Anchor Leg Mooring
SEAREV	Système Électrique Autonome de Récupération de l'énergie des Vagues
SPA	Spherical Point Absorber
SSG	Sea-wave-Slot-cone-Generator
SW	Solid Works
SWAN	Simulating WAVes Nearshore
TAPCHAN	Tapered Channel Wave Power Device
TLP	Tension Leg Platform
UoA	University of Athens
VLA	Vertical Load Anchors
VW	Virtual Works
WAMIT	WAVes Massachusetts Institute of Technology
WavEC	Wave Energy Centre
WEC	Wave Energy Converter
WETFREET	Wave Energy Transition to Future by Evolution of Engineering and Technology
WRASPA	Wave-driven, Resonant, Arcuate action, Surging Point-Absorber Technology

Latin symbols

a_{cw}	clump weight radius
A_{33}, A_{99}	added mass coefficients in heave (two-body system)
$A_{d,i}$	drag area or drag area moment
$A_{d,m}$	mooring line drag diameter
A_{ij}	added mass coefficient
A_w	wave amplitude
$A_{w,i}$	wave amplitude of the i -th regular wave
B_{33}, B_{99}	radiation damping coefficients in heave (two-body system)
B_{ij}	radiation damping coefficient
B_{PTO}	PTO damping coefficient
c_a	speed of sound in air
$c_{d,i}$	drag coefficient
$c_{d,m}$	mooring line drag coefficient
C	hydrostatic restoring term
C_{bm}	bottom mooring line stiffness

C_m	mooring line stiffness
C_{PTO}	spring coefficient
C_w	capture width
d_1	buoy diameter
d_2	OWC diameter
EA	axial stiffness
ET	effective tension
\bar{f}	bottom mooring line force under calm sea conditions
f	perturbation to bottom mooring line force \bar{f}
$f(t)$	force
\mathbf{F}	force vector (force amplitude)
g	acceleration of gravity
g_r	impulse response function
G	length of the cable between each buoy and the clump weight
\overline{GM}	metacentric height
h	water depth
H_s	significant wave height
i	imaginary unit
i, j	modes of the bodies
I_{ij}	moments of inertia
k	wavenumber
k_i	wavenumber of the i -th regular wave
k_t	turbine coefficient
l_t	draught
L	distance between buoys and centre of the array
L_0	unstretched length of a segment
L_{ins}	instantaneous length of a segment
m_3, m_9	body masses (two-body system)
m_b	buoy mass
m_n	moment of the wave spectrum
M	total number of sea states
M_{ij}	inertia coefficient
n	index of the drag surface
N	total number of bodies
p	pressure difference between the air chamber and the atmosphere
\bar{P}	time-averaged instantaneous power
\bar{P}_t	average power available to the turbine
\bar{P}_w	time-averaged power transported by a wave per unit wave crest length

q	gain factor
\bar{r}	inter-body mooring force under calm sea conditions
r	perturbation to inter-body mooring force \bar{r}
$\Re \{ \}$	real part of a complex number
s	line designation
S_1, S_2	body waterplane areas (two-body system)
S_b	buoy waterplane area
S_o	OWC waterplane area
S_w	wave energy density
t	time
T	period
T_e	energy period
T_p	peak period
\mathbf{u}	velocity
u_{dS}	velocity of the mooring line element
v	phase velocity
v_{cw}	clump weight volume
V	buoy's displaced water volume
V_0	air chamber volume under calm sea conditions
x_i	complex amplitudes of displacement
x, y, z	position coordinates
z_b	z -coordinate of centre of buoyancy
z_g	z -coordinate of centre of gravity
z_{cw}	z -coordinate of clump weight position
Z	heave complex amplitude of displacement

Subscripts

ann	annual
b	buoy
bm	bottom mooring
cw	clump weight
d	drag
exc	excitation
ext	external
hr	horizontal
hst	hydrostatic
im	inter-body mooring

in	internal
irr	irregular
iso	isolated
max	maximum
p	pressure
r	relative
rad	radiation
t	turbine
tb	tube

Superscripts

(e)	estimated value
*	dimensionless value

Greek symbols

α	angle of inter-body mooring force
β	angle of bottom mooring force
Γ	wave excitation coefficient
δ, ε	perturbations to inter-body mooring angles
Δ	interval
η	free-surface elevation
θ	angle of wave incidence
λ	wave length
λ_e	extension factor of a mooring line segment
ν	Poisson ratio
$\xi_i(t)$	body displacement (i -th mode)
ρ_a	air density
ρ_w	water density
σ	standard deviation
φ	phase angle
φ_i	i -th arbitrary phase angle
ϕ_j	bottom mooring line extension
ϕ	velocity potential
ϕ_0	complex amplitude of the velocity potential
ϕ_m	frequency of occurrence of sea state

ω	wave frequency
ω_n	natural frequency

List of Figures

1.1	Wave power in Europe for Autumn (1.1a), Winter (1.1b), Spring (1.1c), and Summer (1.1d), by hindcast wave data from the University of Athens (UoA), source: Kalogeri et al. (2016).	3
2.1	The axisymmetric WEC, denoted as spar-buoy OWC, oscillating in six DoF, source: Malvar Ferreira (2016).	13
2.2	Wells turbine, rotor (left) and guide vanes (right). Source: Falcão et al. (2016)	15
2.3	The bi-radial turbine, source: Falcão et al. (2016).	16
2.4	Bi-radial turbine for the Mutriku breakwater power plant by IST. Photo courtesy of Professor António Falcão.	20
2.5	Illustration of the floating OWC, known as spar-buoy OWC, patented by IST (after Gomes (2013)).	21
2.6	PS Frog (Mk5), illustration adapted from Falcão (2010).	22
2.7	Possible mooring configurations for an axisymmetric device. From left to right, taut moored systems with single, taut moored with multiple lines, basic catenary system, catenary system with auxiliary surface buoy, and lazy wave system with subsea floater and sinker. Source: Karimirad et al. (2016).	29
2.8	Load theories and their various regions of applicability, according to Chakrabarti (1987), where H is water depth, D is the characteristic dimension, and λ is the wavelength. Redrawn from Det Norske Veritas (DNV) (2014).	38
2.9	Single-body system oscillating in heave.	41
2.10	Two-body system oscillating in heave only.	45
2.11	Flow chart for the procedure followed for mooring design. Redrawn from Johanning et al. (2005).	48
3.1	Three dimensional view of the array of SPAs, under calm sea conditions, along with inter-mooring connections and bottom mooring connections. The waves approach the three body array from left to right. Not to be scaled.	54
3.2	Top view of the array of spherical point absorbers, with bottom mooring and inter-body mooring connections.	56

3.3	Mesh (3.3a) and top panel (3.3b) for the SPAs of the array used in the WAMIT calculations, higher-order discretisation method.	58
3.4	Three dimensional view of the array of cylindrical WECs, under calm sea conditions, along with inter-mooring connections and bottom mooring connections. The waves approach the three body array from left to right.	63
3.5	The body in still water force equilibrium (3.5a) and righting moment (3.5b).	66
3.6	Mesh (3.6a) and top panel (3.6b) for the CPAs of the array used in the WAMIT calculations, with higher-order discretisation method.	67
3.7	Heave RAO for an isolated SPA, against the wave frequency ω , for $A_w = 1$ m, and various PTO damping values. The value $1.0 * B_{PTO}$ corresponds to the optimum PTO value. The dotted vertical line corresponds to the body's resonance frequency.	70
3.8	Hydrodynamic coefficients for the three spheres in surge (Figs 3.8a, 3.8c), and heave (3.8b, 3.8d), as a function of the wave frequency ω . Excitation force amplitudes for the three spheres in surge and heave (3.8e, 3.8f) as a function of the wave frequency ω , for $A_w = 1$ m, $\theta = 0$. These values were calculated by the BIEM.	72
3.9	Cross terms of the radiation damping for the three spheres, as a function of the wave frequency ω , for $A_w = 1$ m and $\theta = 0$	73
3.10	Surge RAOs for the three SPAs for the inter-body moored array, as a function of the wave frequency ω , for $A_w = 1$ m, $\theta = 0$, $C_{cw}^* = 0.1$, $\alpha = 30^\circ$, and $\beta = 30^\circ$. The surge RAOs for the unmoored array, and the single body are provided for comparison.	74
3.11	Sway RAOs for the three spheres for the inter-body moored array, as a function of the wave frequency ω , for $A_w = 1$ m, $\theta = 0$, $C_{cw}^* = 0.1$, $\alpha = 30^\circ$, and $\beta = 30^\circ$. The sway RAOs for the unmoored array, and the single SPA are provided for comparison.	75
3.12	Heave RAOs for the three spheres for the inter-body moored array, as a function of the wave frequency ω , for $A_w = 1$ m, $\theta = 0$, $C_{cw}^* = 0.1$, $\alpha = 30^\circ$, and $\beta = 30^\circ$. The heave RAOs for the unmoored array, and the single body are provided for comparison.	76
3.13	RAOs for a single cylinder as a function of the wave frequency ω , in surge (3.13a), heave (3.13b), and pitch (3.13c), with drag in surge and heave. The optimum PTO damping is applied, for $A_w = 1$ m as a function of the wave frequency ω	78
3.14	Surge RAOs for the three CPAs with inter-body mooring connections, as a function of the wave frequency ω , for $A_w = 1$ m, $\theta = 0$, $C_{bm}^* = 0.1$, $\alpha = 30^\circ$, and $\beta = 30^\circ$. The surge RAOs for the unmoored array, and the single CPA are provided for comparison.	79
3.15	Sway RAOs for the three CPAs with inter-body mooring connections, as a function of the wave frequency ω , for $A_w = 1$ m, $\theta = 0$, $C_{bm}^* = 0.1$, $\alpha = 30^\circ$, and $\beta = 30^\circ$. The surge RAOs for the unmoored array, and the single CPA are provided for comparison.	80

3.16	Heave RAOs for the three cylinders with inter-body mooring connections, as a function of the wave frequency ω , for $A_w = 1$ m, $\theta = 0$, $C_{bm}^* = 0.1$, $\alpha = 30^\circ$, and $\beta = 30^\circ$. The surge RAOs for the unmoored array, and the single buoy are provided for comparison.	81
3.17	Pitch RAOs for the three cylinders with inter-body mooring connections, as a function of the wave frequency ω , for $A_w = 1$ m, $\theta = 0$, $C_{bm}^* = 0.1$, $\alpha = 30^\circ$, and $\beta = 30^\circ$. The pitch RAOs for the unmoored array, and the single buoy are provided for comparison.	82
4.1	Top view of the triangular array with inter-body mooring connections. The spar-buoy OWC devices are represented by indices 1-3 and the clump weight is represented by index 4.	88
4.2	Three-dimensional view of the triangular array with inter-body mooring connections.	89
4.3	Grid of an array of three spar-buoy OWC devices, as modelled in WAMIT (higher order discretisation method).	90
4.4	Illustration of the cross section of a spar-buoy OWC, redrawn from Gomes et al. (2016).	91
4.5	Cross-section of the spar-buoy OWC grid, the bottom surface of the piston is highlighted in red, while the free surface grid (in blue) was introduced for irregular frequency removal.	92
4.6	Surfaces experiencing drag. Originally from Gomes et al. (2016).	96
4.7	Three-dimensional view of the triangular array with inter-body mooring connections.	99
4.8	Heave RAO and relative motion RAO for a single spar-buoy OWC, as a function of the wave frequency ω , for a variation of turbine coefficients: $k_t = 0.00023, 0.00150, 0.005, 0.01, 0.02909$ ms.	106
4.9	CWR as a function of the wave frequency ω for a single spar-buoy OWC, for a variation of turbine coefficients: $k_t = 0.00023, 0.00150, 0.005, 0.01, 0.02909$ ms.	107
4.10	Surge RAOs against the wave frequency ω , for $k_t = 0.0015$ ms, $A_w = 1$ m, $C_{bm}^* = 0.1$, $\alpha = 30^\circ$, $\beta = 30^\circ$, and $\theta = 30^\circ$, for the unmoored array (Case I), the individually moored array (Case II), and the array with bottom and inter-body mooring connections (Case III), for the three buoys and the clump weight.	111
4.11	Heave RAOs against the wave frequency ω , for $k_t = 0.0015$ ms, $A_w = 1$ m, $C_{bm}^* = 0.1$, $\alpha = 30^\circ$, $\beta = 30^\circ$, and $\theta = 30^\circ$, for the unmoored array (Case I), the individually moored array (Case II), and the array with bottom and inter-body mooring connections (Case III), for the three buoys and the clump weight.	112

4.12	Pitch RAOs against the wave frequency ω , for $k_t = 0.0015$ ms, $A_w = 1$ m, $C_{bm}^* = 0.1$, $\alpha = 30^\circ$, $\beta = 30^\circ$, and $\theta = 30^\circ$, for the unmoored array (Case I), the individually moored array (Case II), and the array with bottom and inter-body mooring connections (Case III), for the three buoys and the clump weight.	113
4.13	CWRs against the wave frequency ω , for $k_t = 0.0015$ ms, $A_w = 1$ m, $C_{bm}^* = 0.1$, $\alpha = 30^\circ$, $\beta = 30^\circ$, and $\theta = 30^\circ$, for the unmoored array (Case I), the individually moored array (Case II), and the array with bottom and inter-body mooring connections (Case III), for the three buoys and the clump weight.	114
4.14	Surge RAOs against the wave frequency ω , for $k_t = 0.0015$ ms, $A_w = 1$ m, $C_{bm}^* = 0.1$, $\beta = 30^\circ$, for the individually moored array (Case II), for the three buoys, for three angles of wave incidence θ (0° , 30° , 60°). The results for the single buoy without moorings are provided for comparison.	116
4.15	Sway RAOs against the wave frequency ω , for $k_t = 0.0015$ ms, $A_w = 1$ m, $C_{bm}^* = 0.1$, $\beta = 30^\circ$, for the individually moored array (Case II), for the three buoys, for three angles of wave incidence θ (0° , 30° , 60°). The results for the single buoy without moorings are provided for comparison.	117
4.16	Heave RAOs against the wave frequency ω , for $k_t = 0.0015$ ms, $A_w = 1$ m, $C_{bm}^* = 0.1$, $\beta = 30^\circ$, for the individually moored array (Case II), for the three buoys, for three angles of wave incidence θ (0° , 30° , 60°). The results for the single buoy without moorings are provided for comparison.	118
4.17	CWRs against the wave frequency ω , for $k_t = 0.0015$ ms, $A_w = 1$ m, $C_{bm}^* = 0.1$, $\beta = 30^\circ$, for the individually moored array (Case II), for the three buoys, for three angles of wave incidence θ (0° , 30° , 60°). The results for the single buoy without moorings are provided for comparison.	119
4.18	Surge RAOs against the wave frequency ω , for $k_t = 0.0015$ ms, $A_w = 1$ m, $C_{bm}^* = 0.1$, $\beta = 30^\circ$, $\alpha = 30^\circ$ for the array with shared moorings (Case III), for the three buoys and the clump weight, for three angles of wave incidence θ (0° , 30° , 60°). The results for the single buoy without moorings are provided for comparison.	120
4.19	Sway RAOs against the wave frequency ω , for $k_t = 0.0015$ ms, $A_w = 1$ m, $C_{bm}^* = 0.1$, $\beta = 30^\circ$, $\alpha = 30^\circ$ for the array with shared moorings (Case III), for the three buoys and the clump weight, for three angles of wave incidence θ (0° , 30° , 60°). The results for the single buoy without moorings are provided for comparison.	121
4.20	Heave RAOs against the wave frequency ω , for $k_t = 0.0015$ ms, $A_w = 1$ m, $C_{bm}^* = 0.1$, $\beta = 30^\circ$, $\alpha = 30^\circ$ for the array with inter-body and bottom mooring connections (Case III), for the three buoys and the clump weight, for three angles of wave incidence θ (0° , 30° , 60°). The results for the single buoy without moorings are provided for comparison.	122

4.21	Heave RAOs against the wave frequency ω , for $k_t = 0.0015$ ms, $A_w = 1$ m, $C_{bm}^* = 0.1$, $\beta = 30^\circ$, $\alpha = 30^\circ$ for the array with inter-body and bottom mooring connections (Case III), for the three buoys, for three angles of wave incidence θ (0° , 30° , 60°). The results for the single buoy without moorings are provided for comparison.	123
4.22	Standard deviation for surge against the energy period T_e , for an isolated device, for $k_t = 0.0015$ ms, $\theta = 0$, and various values of H_s	125
4.23	Standard deviation for heave against the energy period T_e , for an isolated device, for $k_t = 0.0015$ ms, $\theta = 0$, and various values of H_s	125
4.24	Standard deviation for pitch against the energy period T_e , for an isolated device, for $k_t = 0.0015$ ms, $\theta = 0$, and various values of H_s	126
4.25	Standard deviations for the CWR_{irr} against the energy period T_e , for an isolated device, for $k_t = 0.0015$ ms, $\theta = 0$, and various values of H_s	126
4.26	Standard deviations for surge, against the energy period T_e , for $k_t = 0.0015$ ms, $H_s=1.62$ m, $C_{bm}^* = 0.1$, $\beta = 30^\circ$, $\alpha = 30^\circ$, and $\theta = 0$. For the array cases, the values presented refer to the array-averaged motions.	127
4.27	Standard deviations for heave, against the energy period T_e , for $k_t = 0.0015$ ms, $H_s=1.62$ m, $C_{bm}^* = 0.1$, $\beta = 30^\circ$, $\alpha = 30^\circ$, and $\theta = 0$. For the array cases, the values presented refer to the array-averaged motions.	127
4.28	Standard deviation for pitch, against the energy period T_e , for $k_t = 0.0015$ ms, $H_s=1.62$ m, $C_{bm}^* = 0.1$, $\beta = 30^\circ$, $\alpha = 30^\circ$, and $\theta = 0$. For the array cases, the values presented refer to the array-averaged motions.	128
4.29	Standard deviation for CWR_{irr} , against the energy period T_e , for $k_t = 0.0015$ ms, $H_s=1.62$ m, $C_{bm}^* = 0.1$, $\beta = 30^\circ$, $\alpha = 30^\circ$, and $\theta = 0$. For the array cases, the values presented refer to the array-averaged motions.	128
A.1	Meshes for the SPAs used in the WAMIT calculations with the higher-order discretisation method, for a varying number of panels, $N=2$ (A.1a), $N=4$ (A.1b), $N=6$ (A.1c), $N=8$ (A.1d), $N=10$ (A.1e). The top panel for irregular frequency removal is depicted in A.1f.	155
A.2	Meshes for CPAs used in the WAMIT calculations with the higher order discretisation method, for a varying number of panels, $N=2$ (A.2a), $N=4$ (A.2b), $N=6$ (A.2c), $N=8$ (A.2d), $N=10$ (A.2e). The top panel for irregular frequency removal is depicted in A.2f.	156
B.1	Surge RAOs against the wave frequency ω for the three SPAs with bottom and inter-body mooring connections, and the clump weight for different values of the inter-body mooring force angle $\alpha=(20^\circ, 30^\circ, 40^\circ)$, with $A_w=1$ m, $C_{bm}^*=0.1$, $\theta = 30^\circ$, and $\beta = 30^\circ$	159
B.2	Sway RAOs against the wave frequency ω for the three SPAs with bottom and inter-body mooring connections, and the clump weight for different values of the inter-body mooring force angle $\alpha=(20^\circ, 30^\circ, 40^\circ)$, with $A_w=1$ m, $C_{bm}^*=0.1$, $\theta = 30^\circ$, and $\beta = 30^\circ$	160

B.3	Heave RAOs against the wave frequency ω for the three SPAs with bottom and inter-body mooring connections, and the clump weight for different values of the inter-body mooring force angle $\alpha=(20^\circ, 30^\circ, 40^\circ)$, with $A_w=1$ m, $C_{bm^*}=0.1$, $\theta = 30^\circ$, and $\beta = 30^\circ$. The vertical green lines represent the SPA's resonance frequency.	161
B.4	Surge RAOs against the wave frequency ω for the three SPAs with bottom and inter-body mooring connections, and the clump weight for different values of the angle of the bottom mooring force $\beta=(0^\circ, 30^\circ, 60^\circ)$, with $A_w=1$ m, $\alpha = 30^\circ$, $\theta = 0^\circ$, and $C_{bm^*}^*=0.1$	162
B.5	Sway RAOs against the wave frequency ω for the three SPAs with bottom and inter-body mooring connections, and the clump weight for different values of the angle of the bottom mooring force $\beta=(0^\circ, 30^\circ, 60^\circ)$, with $A_w=1$ m, $\alpha = 30^\circ$, $\theta = 0^\circ$, and $C_{bm^*}^*=0.1$	163
B.6	Heave RAOs against the wave frequency ω for the three SPAs with bottom and inter-body mooring connections, and the clump weight for different values of the angle of the bottom mooring force $\beta=(0^\circ, 30^\circ, 60^\circ)$, with $A_w=1$ m, $\alpha = 30^\circ$, $\theta = 0^\circ$, and $C_{bm^*}^*=0.1$. The green vertical lines corresponds to the SPA resonance frequency.	164
B.7	Surge RAOs against the wave frequency ω for the three SPAs with bottom and inter-body mooring connections, and the clump weight, for different values the bottom mooring line stiffness $C_{bm^*}=(0.05, 0.1, 0.2)$, with $A_w=1$ m, $\alpha = 30^\circ$, $\theta = 0^\circ$, and $\beta = 30^\circ$	165
B.8	Sway RAOs against the wave frequency ω for the three SPAs with bottom and inter-body mooring connections, and the clump weight, for different values the bottom mooring line stiffness $C_{bm^*}=(0.05, 0.1, 0.2)$, with $A_w=1$ m, $\alpha = 30^\circ$, $\theta = 0^\circ$, and $\beta = 30^\circ$	166
B.9	Heave RAOs against the wave frequency ω for the three SPAs with bottom and inter-body mooring connections, and the clump weight, for different values the bottom mooring line stiffness $C_{bm^*}=(0.05, 0.1, 0.2)$, with $A_w=1$ m, $\alpha = 30^\circ$, $\theta = 0^\circ$, and $\beta = 30^\circ$. The green vertical lines correspond to the natural frequency of the SPA.	167
B.10	Surge RAOs against the wave frequency ω for the three SPAs with bottom and inter-body mooring connections, for different values the angle of wave incidence $\theta=(0^\circ, 30^\circ, 60^\circ)$, with $A_w=1$ m, $\alpha = 30^\circ$, $\beta = 30^\circ$, and $C_{bm^*} = 0.1$	168
B.11	Sway RAOs against the wave frequency ω for the three SPAs with bottom and inter-body mooring connections, for different values the angle of wave incidence $\theta=(0^\circ, 30^\circ, 60^\circ)$, with $A_w=1$ m, $\alpha = 30^\circ$, $\beta = 30^\circ$, and $C_{bm^*} = 0.1$	169
B.12	Heave RAOs against the wave frequency ω for the three SPAs with bottom and inter-body mooring connections, for different values the angle of wave incidence $\theta=(0^\circ, 30^\circ, 60^\circ)$, with $A_w=1$ m, $\alpha = 30^\circ$, $\beta = 30^\circ$, and $C_{bm^*} = 0.1$. The green vertical lines correspond to the SPA resonance frequency.	170

C.1	Surge RAO for a single unmoored spar-buoy OWC, as a function of the wave frequency ω , with and without drag, for $A_w = 1$ m, $k_t = 0.0015$ ms.	172
C.2	Heave RAO for a single unmoored spar-buoy OWC, as a function of the wave frequency ω , with and without viscous damping, for $A_w = 1$ m, $k_t = 0.0015$ ms.	172
C.3	Pitch RAO for a single unmoored spar-buoy OWC, as a function of the wave frequency ω , with and without viscous damping, for $A_w = 1$ m, $k_t = 0.0015$ ms.	173
C.4	Heave RAO of the relative motion between the buoy and the OWC, as a function of the wave frequency ω , for a single unmoored spar-buoy OWC, with and without viscous damping, for $A_w = 1$ m, $k_t = 0.0015$ ms.	173

List of Tables

2.1	A summary of several representative fixed structure devices.	19
2.2	A summary of several representative floating devices.	24
2.3	A summary of several representative submerged devices.	26
2.4	A summary of techniques for modelling wave energy conversion systems.	40
3.1	Notation for the complex amplitudes of the displacements of the spherical point absorbers and the clump weight oscillating in three DoF. The rotational modes are not active.	57
3.2	Notation for the complex amplitudes of the displacements of the cylindrical point absorbers oscillating in six DoF, and the clump weight oscillating in three DoF.	64
3.3	Cylindrical point absorber, physical properties.	68
4.1	Notation for the modes of the three buoys and their corresponding OWCs, as well as the weight mode notations.	89
4.2	The 14 sea states and their characteristics, source: Gomes et al. (2010, 2012).	103
4.3	Spar-buoy OWC physical properties. The moments of inertia are measured at the axes of the device reference frame. The table also includes the model default parameters.	104
4.4	Schematic representation of the array cases studied.	108
4.5	Annual-averaged gain factor q for the studied cases, for three angles of wave incidence θ , and varying model parameters.	130

Chapter 1

Introduction

It is likely that in the near future, the supply of fossil fuels in Europe will become highly uncertain, due to the complexity of extraction from ever-increasing depths and the prohibitive costs involved. Were it not for the USA's schistolithic oil resources, this problem of resource security would be even more profound (Saussay, 2018). The increasing concentration of atmospheric CO₂ will play a significant role in the cost calculations and comparisons between fossil fuels and sustainable energy resources, as emissions become more heavily taxed by governmental entities (World Energy Council, 2016). Therefore, investments in green energy and hybrid technologies will likely become less expensive in the near future. A notable example of this is the recent evolution in the cost reduction of solar energy. As in the case of many renewable resources, solar energy has the distinct disadvantage of diurnal and seasonal variability (Mulder, 2014) which is particularly difficult to manage in isolated areas (e.g. islands and places off the grid). Thus, besides improving current renewable technologies, it will be necessary to use a combination of several renewable resources to meet current and future energetic demands.

The most explored marine renewable energy technologies include tidal energy conversion, wave energy conversion, and offshore wind. Significant research efforts have been invested in developing cost-effective wave energy conversion technologies, since the potential global wave energy resource has been estimated to be approximately 2 TW (Cruz, 2008). Nonetheless, the concept of wave energy conversion is not new. As early as in 1799, the idea of wave energy conversion was introduced, when Girard and his son filed the first patent for wave energy extraction technology (Clément et al., 2002). More recently, the attention of the scientific community on wave energy conversion was drawn when Stephen Salter published a paper in *Nature* during the oil crisis in the UK (Salter, 1974). By the early 1980s, the period of high energy prices ended and, as a result, the economic and political climate in which WECs were being developed changed drastically. Nevertheless, research dedicated to WECs continued, but a greater emphasis was placed upon the economic, efficient and physical modelling of WECs, with hundreds of WECs being developed during the last few decades.

Despite the large number of patents, potential investors and government participation,

wave energy technologies have failed to make a real impact due to failed concepts, high risks, and high upfront capital costs compared to other more mature renewables (e.g. solar panels and wind power). Some aspects of the current high costs of wave energy conversion concern the design of mooring lines, the survivability of long term deployments and the operation and maintenance of offshore systems. When wave energy technologies become commercially viable, it is likely that they will be deployed in the form of arrays. This is because the offshore environment serves as a good deployment zone owing to its more energetic wave climate and its reduced visual impact. Although wave energy is a promising renewable resource, research on the basic design strategies of wave energy farms to reduce costs and increase energetic performance is needed to ensure future commercial viability.

A key element of offshore wave energy deployments is the design and implementation of moorings in order to keep the individual devices in place without restricting their motion to the point where they can no longer absorb wave energy (Johanning et al. (2006), Davidson and Ringwood (2017)). Compared to conventional mooring configurations where each converter in the array is attached to the seabed by at least three bottom mooring lines, shared mooring systems significantly decrease the number of bottom mooring lines and anchors required, thereby decreasing the overall costs of the array (Vicente et al. (2009a), WETFEEET D6.1 (2016)). It is of practical importance and academic interest to investigate the influence of the shared mooring configuration on the array hydrodynamics and the energetic performance.

1.1 State of the art

1.1.1 Wave energy resource

The resource of the energy contained in ocean waves is expressed as the wave energy density in kW/m, which is a function of the energy period and the square of the significant wave height. Wave energy is distributed around the world in an irregular way. Areas characterised by high wave energy potential are more likely to be placed on the Western European coast, off the Canadian coasts and the USA and the southern Australian and South American coasts (CRES (2002), Gunn and Stock-Williams (2012)). Immense activity with respect to ocean waves takes place between the latitudes of approximately 30° degrees and 60° on the two hemispheres, caused by subsequent westerly winds. Higher wave energy intensity is reported to be in the Southern hemisphere. Another advantage of the Southern hemisphere is with respect to variability (seasonal, wave to wave, etc.), which is lower than the variability of the Northern hemisphere. However, in the Northern hemisphere, this seasonal variability can be advantageous for the operation and maintenance of WEC arrays during the summer months, due to availability of weather windows. In Europe, the highest wave energy resource has been detected in the NW offshore areas, and in the North Sea (Fig. 1.1). The resource of ocean waves can be easily estimated, since a vast amount of validated hindcast data is available, based

on advanced numerical models that take into consideration various non-linear effects such as white capping, wave-wave interaction and wave-current interaction (Neill and Hashemi, 2013). Nevertheless, when conducting a resource assessment, it is necessary to also account for the analysis and prediction of extreme waves, as this information will be crucial for the determination of the design wave height for the device and the mooring system. Statistical distributions are available to predict the probability of occurrence of extreme events, based on past extreme events for a particular location (Goda (2010), Ferreira and Guedes Soares (1998), Sartini et al. (2015)).

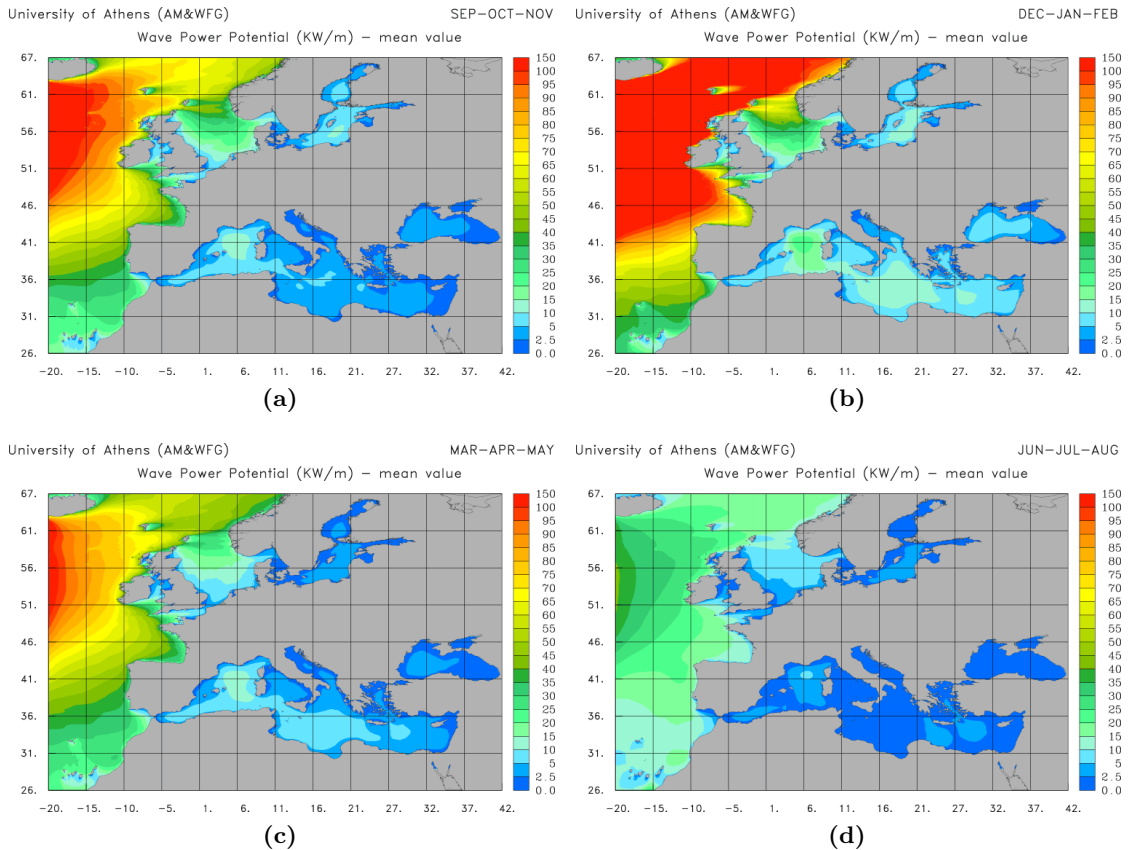


Figure 1.1: Wave power in Europe for Autumn (1.1a), Winter (1.1b), Spring (1.1c), and Summer (1.1d), by hindcast wave data from the University of Athens (UoA), source: Kalogeri et al. (2016).

1.1.2 Arrays of WECs

The need to benefit from high wave energy resource, but also the availability of space and the minimisation of the optical impact has led to organising WECs into arrays. The vast majority of these studies, though, are still at a research and development stage. Only a limited number of sea trials have ever been concluded, possibly because of their very ambitious nature. For example, the Pelamis wave farm in Aguçadora in Portugal was installed as an array but was decommissioned just a few months after installation (Dalton et al., 2010).

Numerical studies on arrays of WECs have been ongoing for four decades. In 1977,

Budal raised awareness on the wave interactions that WECs in array configurations can demonstrate (Budal, 1977). A mathematical theory for power absorption for an array of a certain number of interacting bodies was described by Evans (1976) and later on by Falnes (1980). By using the point absorber approximations for an array of heaving devices, simple analytic expressions were derived based on wave excitation forces, radiation coefficients, and device motions. The initial works by Falnes and Evans concluded that the interaction for arrays of WECs can be constructive for certain frequencies and destructive for others. Notably, constructive interference leads to an increase in the amount of power generated by an array when compared to an equal number of isolated devices. This phenomenon is known as the “park effect” (Babarit, 2013). Hydrodynamic interactions within arrays have been analysed throughout various studies including those of Thomas and Evans (1981), Mavrakos and McIver (1997), Justino and Clément (2003), Borgarino et al. (2012), and Falnes and Hals (2012). Other studies suggest the consideration of an-equal spacing between the devices of the array (McGuinness and Thomas, 2016). Various papers have emphasised the importance of the wave climate directionality on the array performance.

Several methods have been proposed for designing efficient array configurations, including genetic algorithms, examples of which are the parabolic intersection and the multiple scattering method (Mavrakos and McIver, 1997). Most of these methods were applied only to arbitrary geometries (WECs that resemble spheres, cylinders, etc.) and are usually restricted to oscillation in the vertical direction only, which is not the case for the majority of existing technologies.

Although most of the existing studies on the dynamics of arrays of WECs are either numerical or theoretical, few experimental studies have been conducted. Ashton et al. (2009) tested the hydrodynamics of five Oscillating Water Column (OWC) type devices under regular and irregular waves. Stratigaki et al. (2014) performed an experiment of 25 heaving buoys in order to investigate the near-field effects of an array, which they then compared with numerical results of a wave propagation model. Troch et al. (2014) performed more tests following the study carried out by Stratigaki et al. in a 3D shallow water basin. Both these last studies were part of EU funded projects.

1.1.3 Moorings for WECs

The design and implementation of moorings is an essential part for the deployment of WEC arrays. Mooring systems for free floating WECs in offshore deployments must be designed to keep the devices on station even when subjected to extreme drifting forces (waves, currents, winds), while simultaneously avoiding a negative impact on the extracted wave energy (Johanning et al. (2006), Davidson and Ringwood (2017)). Three different materials are typically used: chain, steel wire and synthetic rope. Significant knowledge has been acquired on the operation of moored offshore platforms, although there are several consequences when directly applying this knowledge to WECs (Paredes et al. (2013), Weller et al. (2014)). For example, the effect of the mooring system on the wave energy absorption capability of the WEC should be examined. It has been suggested

by previous work that the mooring lines should be considered in the numerical modelling from the initial stages of the design of wave energy conversion projects (Fitzgerald and Bergdahl, 2008). General guidelines are available for the design of WEC mooring systems (Bergdahl, 2017). There is growing scientific interest in the impacts of structural loading and extreme events on the moorings of floating structures, and more specifically on those of WECs (Liu and Bergdahl (1998), Brown and Mavrakos (1999), Parmeggiani et al. (2013), Harnois et al. (2016)). These advances even include the determination of snap loads on the mooring lines (Palm et al., 2017).

It seems that mooring lines, electric cables and anchors represent a large percentage of the total cost of a WEC project (Astariz and Iglesias, 2015). As the installation of anchors in a mooring system is very costly and depends on the number of anchor points (Huang and Aggidis, 2008), it is preferable to share as many anchors as possible in WECs arrays (shared moorings). Compared to conventional mooring configurations where each converter in the array is attached to the seabed by at least three bottom mooring lines, shared moorings allow a reduction in the number of bottom mooring lines, as shown in a numerical analysis of a triangular array of spherical bodies oscillating in three degrees-of-freedom with bottom and shared mooring connections (Vicente et al., 2009a). There is limited bibliography on mooring configurations for WEC arrays. An analysis of an array of FO3 buoys with mooring was performed by Gao and Moan (2009). Correia da Fonseca et al. (2016) performed experiments on an array of spar-buoy OWCs with mooring connections under moderate and extreme wave conditions.

Experimental data from large-scale experiments collected in the EU-funded MaRINET and WETFEEET projects suggested that shared mooring connections are less expensive than individual mooring systems and do not significantly compromise the performance of WECs (MARINET-TA1-SPAR-BUOY ARRAY (2016), WETFEEET D6.1 (2016)). Nevertheless, although shared mooring configurations for WEC arrays show great potential as an economically viable solution when compared to conventional mooring configurations, detailed estimations of the hydrodynamics and the energetic performance are currently lacking as studies addressing this question present some limitations.

The existing numerical studies relevant to the hydrodynamic analysis of WECs with moorings have certain drawbacks since they either: 1. refer to devices restricted to oscillating in particular Degrees-of-Freedom (DoF) (i.e. the effect of hydrodynamic interference is underestimated), 2. focus on the generic geometry of single-body WECs, 3. incorporate idealised values for device damping from the power extraction system; 4. model the mooring connection forces in an oversimplified way, without considering the physical properties of the mooring system; 5. are not supported by relevant experimental validation.

1.2 Aim and objectives

The aim of this PhD thesis is to contribute to the design phase of a WEC array project. This is achieved by performing a hydrodynamic analysis of WEC arrays with shared mooring connections using a newly developed numerical code and building on the theoretical work of Vicente et al. (2009*a*). As a case study, the model uses a version of floating Oscillating Water Column (OWC) technology that has been patented and developed by Instituto Superior Técnico (IST), known as spar-buoy OWC (Falcão et al. (2012), Gomes et al. (2012)). Experimental modelling of WEC arrays of floating OWCs with shared moorings has been the objective of past and ongoing EU funded projects such as OPERA, MaRINET and WETFEEET. The objectives of the thesis are described as follows,

Objective 1: To understand the effect of mooring lines on the hydrodynamics of an array of spheres with shared moorings, by developing a numerical hydrodynamic model based on the work of Vicente et al. (2009*a*).

Objective 2: To extend the numerical model to apply for axially symmetric floating bodies in order to generate a generic methodology for arrays of WECs with shared moorings.

Objective 3: To evaluate the effect of shared mooring lines on the hydrodynamics and the performance of an array of spar-buoy OWCs, under regular wave conditions.

Objective 4: To evaluate the effect of shared moorings on the hydrodynamics of an array of spar-buoy OWCs, under irregular wave conditions and to estimate the park effect for different model parameters.

1.3 Research methodology and approaches

Objective 1: A numerical model in the frequency domain is developed in a Python environment based on the formulations presented in the research done by Vicente et al. (2009*a*). The hydrodynamic coefficients of the spheres are calculated with the aid of the Boundary Integral Element Method (BIEM), WAMIT, for a range of wave frequencies. The model uses the higher order discretisation method. The hydrodynamic coefficients are introduced in a Python code written by the present author, where the equation of motion is solved for all DoF. The forces of the mooring lines are modelled using a quasi-static approach. The dynamics of the shared mooring system are formulated based on their geometric relations and the principle of virtual works.

Objective 2: A cylindrical floater is considered, where the moments of inertia are calculated with the aid of SW. The hydrodynamic coefficients of the cylinders of the triangular array are introduced in the Python code. Same methodology applies to the mooring system as in the case of the spheres. Viscous damping is introduced in the

model, using an iterative process.

Objective 3: The aforementioned methodology established is applied to an array of spar-buoy OWCs. Each spar-buoy OWC is modelled as a two-body system, using the piston approach as presented in Gomes et al. (2012). Viscous damping is also accounted for, using an iterative process and drag coefficients from small-scale experiments. The PTO is a Wells turbine which allows for numerical analysis in a linearised manner. A damping term is introduced, representing the extraction of energy from the turbine generator. So too is a restoring term, representing the air compressibility effect.

Objective 4: A stochastic model is developed. The model uses the same formulations as the previously established frequency domain model, but modified to account for irregular waves. The model assumes that each sea state of interest is represented by the superposition of elementary regular wave components.

1.4 Contribution to knowledge and practice

The numerical model developed in this PhD thesis provides new insights into the numerical analysis of moored WEC arrays as part of the design phase of wave energy conversion projects. Although arrays with shared moorings have been the objective of many experimental work projects, there is a limited number of numerical studies on the hydrodynamics of arrays with shared moorings. Most previous research is restricted to arbitrary geometry converters and fewer DoF. To the author's knowledge, the dynamics of spar-buoy OWC arrays configured with a shared mooring system have not been investigated numerically. Although, the present research uses the spar-buoy OWC as a case study, the method employed could be used on any type of optimised floating WEC. Future research may build on the model developed in this PhD thesis by means of more sophisticated models for the mooring system and mathematical techniques for predicting the effects of extreme wave conditions on the shared mooring system.

1.5 Thesis layout

The present thesis is organised in the following chapters:

Chapter 2 presents the background information that is important for the content of this thesis. First, WECs are classified according to their deployment zone. The different mechanisms for converting wave energy into electricity (i.e., Power Take-Off mechanisms) are explained. The main types of WECs are presented based on their basic principles, as classified by EMEC, and some characteristic examples are presented. The two main types of mooring systems for WECs are presented, along with their key advantages and disadvantages. The fundamentals of numerical formulations that are used in the context of this thesis are presented. Since all calculations performed in this thesis lie within the limits of linear wave theory, the fundamentals of Airy's theory are presented for waves

propagating at arbitrary depth. Additional information is presented about irregular waves and resource assessment techniques. The fundamental theory for modelling of oscillating body WECs is presented for single body and two-body systems. The formulations are expressed in the frequency-domain, and the time-domain. Numerical methods for the modelling of mooring connections are briefly reviewed.

Chapter 3 presents the case of arrays of three hemispheres following the work of Vicente et al. (2009a), oscillating in three DoF under regular wave conditions. Based on the principal of linear superposition, numerical model is explained in detail and any simplifications and assumptions considered. The formulations for the analysis of the shared mooring system are clarified. Results are presented for an array of hemispheres without mooring connections and with the addition of the shared mooring system. A sensitivity analysis is presented for varying mooring parameters and the angle of wave incidence. The results using the default values are compared with the original results. Subsequently, this chapter extends the model developed to apply to axially symmetric WECs using cylinders, for example. An array of three cylinders consisting of steel is considered, where each body oscillates in all six DoF. Since the pitch mode is introduced, a mass matrix is introduced to the moments of inertia. Results are presented for the array of cylinders with a shared mooring system, including a formulation for viscous effects.

Chapter 4 applies the generic recipe established in Chapter 3 for an array of spar-buoy OWCs with shared moorings under regular wave conditions. Each device is modelled as a two-body system and the compressibility of the air chamber is taken into consideration. Viscous damping is included in the model, based on the output from small-scale experiments. A different mooring configuration is presented and the hydrodynamic response of the array is analysed for both mooring configurations. A sensitivity analysis is also presented for different angles of wave incidence. Later on, the model of the moored array of spar-buoy OWCs is expressed in the stochastic-domain to account for realistic operational sea-states. The model introduces a different formula for viscous damping. The performance of the array against the performance of the same number of devices operating independently is also discussed. The validity of the numerical output is assessed in a preliminary manner with respect to experimental output available in the literature.

Chapter 5 presents the Conclusions of this PhD research. The limitations, along with and suggestions for the future improvement of the numerical model are presented. Experimental validation of this study, as well as the economic viability of arrays with shared moorings, are recommended for future work.

Chapter 2

Background theory and motivation

The classification of Wave Energy Converters (WECs) has been described in a variety of review papers (Falcão (2010), Falnes (2007)). The mathematical formulas for wave energy conversion started being developed in the 1970s, after the petroleum crisis of 1973 (Evans (1976), Falnes and Budal (1978)) and were recently revisited in Falnes and Kurniawan (2015). Prior to looking at the mathematical background of wave energy conversion, it is important to classify existing WEC technologies based on their location of deployment, working principle, and Power Take-Off (PTO) mechanism. WECs may be deployed in an onshore, nearshore, or offshore environment (Thompson and Aggidis, 2007).

2.1 Wave generation theories

This section covers a brief description of oceanographic theories on the formation of ocean surface waves, in order to provide some context about the propagation medium from which we are interested in extracting energy. Other processes such as tides, freak waves, currents, etc. have been omitted from this discussion. The total energy contained in waves is a combination of potential and kinetic energy.

The first theory on the generation of ocean surface waves was proposed by Jeffreys (Jeffreys, 1924). This was a semi-empirical theory, suggesting that wind flowing over a body of water experiences a fluid friction, thereby giving up some of its energy to put the water into motion and generate waves. According to his theory, viscous terms are responsible both for the formation and the dissipation of waves (de Swart, 2014).

A later interpretation was proposed by Phillips, known as "resonance mechanism", in 1957 (Phillips, 1957). He made the assumption that the atmospheric boundary layer consists of turbulent eddies varying in length scales. The mean wind velocity has a logarithmic profile in the atmospheric boundary layer and transfers the eddies. As a consequence, the eddies affect the sea surface, by causing pressure fluctuations. This

theory was considered to be more valid than Jeffrey's theory, since: i) it is not empirical, ii) waves can grow from nothing (i.e. undisturbed surface), iii) a minimum value of wind speed is needed for the waves to grow, and v) wave energy is super-imposed and grows linearly, when waves are at an initial stage in their growth (this agrees with observations) (de Swart, 2014). The shortcoming of this theory is that it ignores the feedback between wind and wave interaction. Thus, Phillips' theory appears to only be valid during the initial stage of wave growth.

A third mechanism, "the shear instability mechanism", was suggested by Miles (1957). Miles put forward the hypothesis that sea waves arise due to a free instability of the coupled sea atmosphere system. In actual fact, the waves grow by extracting energy from the mean wind velocity field. This proves to be an exact solution of the system in the case of a smooth/undisturbed water surface. Although Miles took measures to provide a thorough explanation, it was still very mathematical; it was difficult to understand the physical mechanism behind his equations. To provide a more practical interpretation on Miles' theory, Lighthill later expanded upon the shear instability mechanism in 1962 (Lighthill, 1962).

The present theory is a combination of the two aforementioned theories: Miles' shear instability mechanism and Phillips' resonance mechanism. This is to say, that both the fluctuations of the sea surface due to the direct action of atmospheric pressure variation (Miles) and the coupling between surface waves and atmospheric boundary layer flow (Phillips) are taken into consideration. All theories on wave generation provoke uncertainties, and need to be further refined due to the irregular nature of waves caused by meteorological phenomena. Attempts at more accurately describing the generation of irregular waves - waves of varying period, amplitude, phase, and directionality - are being made, in combination with improved data collection techniques.

2.2 Classifying WECs based on the deployment location

The wave climate is location dependent in the sense that it is affected by the wind action, the water depth, the topography, the wave-current interaction, the tidal action, the angle wave of incidence and other factors. Here the various locations for the deployment of WECs are defined, and some of their advantages and disadvantages are explained.

2.2.1 Onshore zone

WEC structures placed on the shoreline, rarely experience the action of extreme events to the extent offshore structures might experience during the project's lifecycle. These locations are advantageous in the sense that they are close to the utility network, therefore their Operation and Maintenance can be undertaken within reasonable costs. However, the energy levels at these locations appear to be relatively low compared to the offshore

environment. In addition, recent concerns with regards to climate change flooding led to the development of other MRE technologies for coastal protection (Wadey et al., 2013). This zone is very well known for its contribution to the stability of the coast and ecology (i.e. saltmarsh vegetation) (Pringle, 1995). The deployment of WECs is not very often undertaken in this zone, as it is a zone of stake holder interest, and other human activities.

2.2.2 Nearshore zone

In oceanographic terms, the location close to the coast where wave breaking occurs is known as “the surf zone” (Svedsen et al., 1978). As a wave enters shallow water, it begins to feel the bottom and slows down. Consequently, the wavelength and phase velocity decrease whilst the wave period remains constant, causing the wave height and steepness to increase. When a wave’s steepness (a ratio of its height to its length) exceeds 1:7, wave breaking and energy dissipation takes place (Thurman and Trujillo, 2001). The reduction in wave energy in shallow water areas has encouraged WEC developers to pursue offshore technologies. However, the zone just before the occurrence of wave breaking appears to be quite beneficial for wave energy conversion: during storms, the reduction in deep water wave energy due to shoaling effects reduces engineering requirements on survivability design. Several WECs concepts have been designed to operate in the nearshore environment, and a promising approach in recent years has been the integration of WECs into breakwaters (e.g. the Mutriku Breakwater Wave Plant (Torre-Enciso et al., 2009)). Unfortunately, devices deployed in the nearshore in some cases may negatively affect sediment transport, by interfering with circulation patterns (e.g. locations with rip currents, sandbars, etc. (Davis and Fitzgerald, 2003)). Existing morphodynamic patterns are important for the stability of the coast (Masselink et al., 2011). Previous studies have looked at the impact of nearshore WEC farms on the dynamics of the coastal hydrodynamics (Rusu and Guedes Soares (2013), Porter et al. (2014)), making use of well-established numerical models.

2.2.3 Offshore zone

High energy levels available in the offshore environment, along with a limitation in marine usable space in the nearshore environment, has led to an interest in the deployment of WECs at greater depths. Large arrays of WECs could be deployed further offshore minimising visual impact. The deployment of WECs in an offshore environment could also act as protection for the nearshore, by reducing the wave energy incident on the coast. It is likely that the presence of WECs offshore will contribute to a reduction in the nearshore wave height. A disadvantage of offshore WEC deployments is the increased cost and complexity of operation and maintenance (Rémouit et al., 2018); similar procedures from offshore oil and gas and offshore wind need to be thoroughly studied, since no operational experience has been recorded for a WEC array deployment (Rinaldi et al., 2018).

2.3 WEC technologies

WECs can be free to move in three translational modes (1 - surge, 2 - sway and 3 - heave) and in three rotational modes (4 - roll, 5 - pitch and 6 - yaw) (Ibrahim and Grace, 2010). The six Degrees of Freedom (DoF) are depicted in Fig. 2.1 for an axisymmetric WEC. In most cases, energy is extracted from the heaving motion of the WEC. According to the European Marine Energy Centre (EMEC)¹, WEC technologies can be classified into the following main categories:

1. Attenuators
2. Point absorbers
3. Oscillating wave surge converters
4. Submerged pressure differential devices
5. Bulge wave devices
6. Rotating mass devices
7. Oscillating Water Columns (OWCs)
8. Overtopping/ terminators

The following sections briefly describe these WEC technologies.

2.3.1 Attenuators

These are floating structures, placed perpendicular to the incoming wavefront. They consist of several joints and hinges, whose relative motion due to wave action captures the incident energy. A representative example is the well-known Pelamis. This device was deployed in the form of an array in Aguçadoura, Portugal in 2008, but only lasted for two months before needing to be decommissioned (Dalton et al., 2010).

2.3.2 Point absorbers

These are buoy-shaped designs. During initial numerical research on WEC hydrodynamics using linear wave theory, it was discovered that bodies with characteristic dimensions that are small compared to typical incident wavelengths could capture energy contained in a wave crest length, greater than their own diameter (Falnes, 1980). The majority of point absorbers are axisymmetric, and operate in heave. However, some point absorbers have also been designed to operate in pitch (Folley, 1993), surge (Bhinder et al., 2009), yaw, roll or a combination of these. Point absorbers are small and modular, allowing for gradual expansion in array capacity rather than risking significant capital investment with a single large device. One of their main advantages is that they are not affected by the wave direction, due to their small size and axial symmetry. However the directionality of the incident waves will affect the hydrodynamics when studying WEC arrays (Wolgamot

¹www.emec.org.uk/ (Accessed in October 2017)

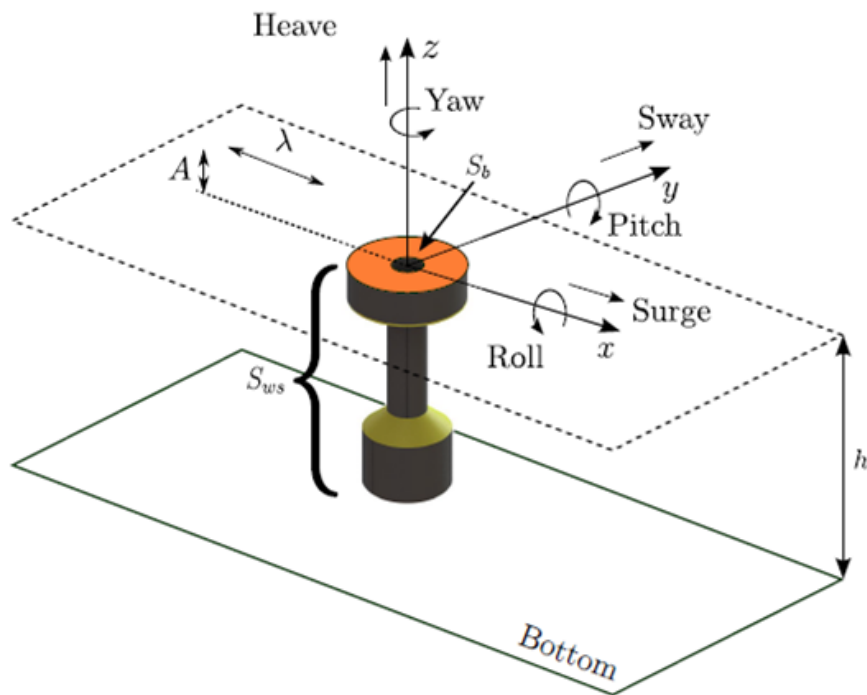


Figure 2.1: The axisymmetric WEC, denoted as spar-buoy OWC, oscillating in six DoF, source: Malvar Ferreira (2016).

et al. (2013), Oikonomou et al. (2017)). This is possibly the most popular device type in terms of the number of concepts under development, with substantial commercial and academic research devoted to devices of this type.

2.3.3 Oscillating wave surge converters

These devices consist of a hinged arm close to the seabed, connected to a near-surface collector. The arm oscillates due to the surging action of waves. Characteristic examples are the Waveroller and Oyster.

2.3.4 Submerged Pressure Differential devices

This is a sea bottom mounted submerged point attenuator, usually located in the nearshore environment. The sea level rises and falls due to the waves' motion, and a pressure differential with respect to hydrostatic equilibrium is formed above the device. An example of this technology is the mWave².

2.3.5 Bulge wave devices

This is a rubber tube filled with water, moored to the seabed. As the water approaches the stern, the passing wave causes pressure variations along the tube (e.g. the Anaconda WEC³). Whilst the bulge travels across the tube, it grows, gathering energy. This energy

²<http://www.bomborawave.com/mwave> (Accessed in June 2018)

³<http://www.energy.soton.ac.uk/anaconda-wave-energy-converter-concept/> (Accessed in January 2018)

is used to drive a low head hydroturbine located at the stern, where the water returns to the sea.

2.3.6 Rotating mass devices

Heaving and swaying motions of a floating device internally drive either an eccentric weight or a gyroscope. This movement is attached to an electric generator inside the device. Not many of the existing devices fall into this category, with the exception of the Penguin, developed by the Finnish company Wello Oy⁴.

2.3.7 OWCs

This is a partially submerged structure with a hollow spar tube. It is open to the sea below the water line, enclosing a column of air on top of a column of water. The waves' action causes the rise and fall of the device relative to the water column, leading to compressions and expansions of the air chamber. The upper part of the structure is in contact with the atmosphere. The enclosed air flows to and from the atmosphere via an air turbine, which is often designed to allow bi-directional air flow by means of self-rectification. This is the most investigated WEC technology to date. The floating version of the OWC is presented in Falcão et al. (2012).

2.3.8 Overtopping/ terminator devices

These structures are placed parallel to the incoming wavefront (perpendicular to the prevailing wave direction), and physically intercept waves. An example of a terminator device is Salter's Duck, developed at the University of Edinburgh (Salter, 2016). Overtopping devices are highly non-linear, and hence difficult to model numerically.

2.4 Power take-off mechanisms

Engineering for low mechanical fatigue has traditionally been geared towards periodic high angular motion with high velocity and low torque. The nature of waves is highly irregular, and WECs whose PTO systems operate at frequencies that are of the same order of magnitude as waves are inherently exposed to low velocities and high forces (Drew et al., 2009). In general, WECs have been designed with a variety of concepts for PTO mechanism. There are several methods in which the captured wave energy may be converted into electricity, but the most common capture medium among point absorber type WEC is the hydraulic PTO (Falcão, 2007). In most PTO systems, captured wave energy is converted into usable electricity by means of high-speed rotary electrical generators. One important aspect of these devices is that they have traditionally been designed to operate at a constant speed, so as to match the frequency of the electrical grid. However, due to the random nature of renewable energy resources, conversion must operate at variable speed. In WECs, several types of rotary generators are used: Doubly Fed Induction Generators (DFIGs), squirrel cage induction generators, and Permanent

⁴<https://wello.eu/> (Accessed in January 2018)

Magnet Synchronous Generators (PMSGs) (Plummer et al., 2018). In some WEC concepts, linear electrical generators have also been employed. The biggest challenge in application of rotary electrical generators in WECs is to make them compatible with conventional rotary electrical devices and gear transmission systems. Three main energy capture systems are described below.

2.4.1 Air turbine energy transfer

This technology is commonly used in OWCs, both land-based and floating concepts (Brito-Melo et al. (2001), Falcão (2010), Falcão et al. (2016)). One very common turbine of this type is the Wells turbine (Fig. 2.2) (Gato and Falcão, 1989). The Wells turbine (axial flow) is historically important, as it was the first air turbine for OWCs, and it is easy to model to its linear pressure head VS flow rate characteristic (Falcão et al., 2014). The disadvantage is that it operates at high efficiency for a very small range of turbine speeds (or flow rates). Another idea is the bi-radial turbine (Fig. 2.4). The bi-radial (radial flow) turbine has been shown to operate close to its peak efficiency for a wider range of flow rates than the Wells turbine. The bi-directional flow air turbines are self-rectifying, but they are of lower efficiency, while the uni-directional flow turbines require rectification via valves, but they are more efficient (Falcão et al., 2013).

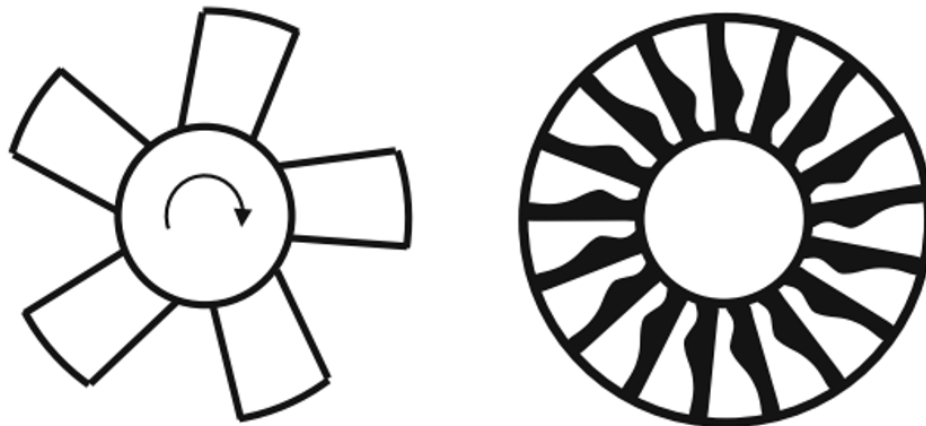


Figure 2.2: Wells turbine, rotor (left) and guide vanes (right). Source: Falcão et al. (2016)

2.4.2 Hydropower turbine energy transfer

In this method for converting the low-speed oscillating motion of the collector body of a WEC, a hydraulic system is used. Hydraulic systems are well suited to absorbing energy in which the waves apply large forces at slow speeds. This technology is commonly applied to over-topping and oscillating body WECs. Its main advantage is that this technology is adopted from mature and well-established hydro power technologies (Aggidis, 2017). Reaction type hydro turbines operating under low-pressure head and high flow-rate conditions are typically employed in over-topping WEC concepts (e.g. Wave Dragon). Impulse type hydroturbines operating under high-pressure head and low-flow conditions

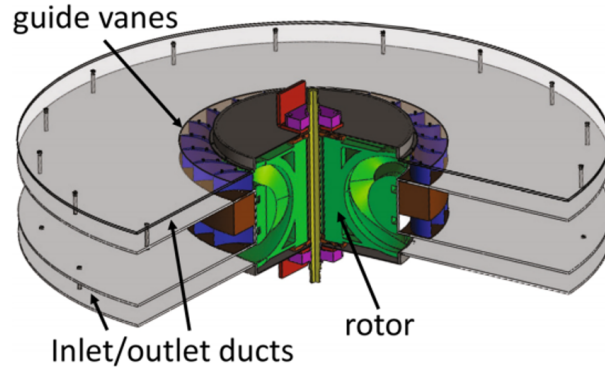


Figure 2.3: The bi-radial turbine, source: Falcão et al. (2016).

are known to have been used in oscillating body WEC concepts (e.g. Oyster and its Pelton wheel PTO system).

2.4.3 Hydraulic oil circuit energy transfer

Hydraulic oil based PTO systems use phase control to tune the WEC velocity to the excitation force of the incoming waves (Gaspar et al., 2016). High and low pressure accumulators are used to provide temporary energy storage, so that a smoother instantaneous power signal can be delivered to the electrical grid (Gaspar et al., 2018). In contrast to energy extraction via air and seawater working fluids, a hydraulic oil circuit PTO has inherent environmental impacts in the event of fluid leakage. Other disadvantages with this type of energy conversion technique involve the relatively high number of components used in the conversion process, and that the instantaneous power of the energy capture mechanism is a product of high force and low speed, which causes increased mechanical fatigue.

2.4.4 Linear generator energy transfer

A changing magnetic field through a coil of wire induces an electrical current, and in this method of energy conversion, a magnet is moved along one of the three translational DoF of the WEC. In early stages of WEC technological readiness, linear generators with electromagnets seem to be a more natural choice over permanent magnets, which are expensive and available only in certain parts of the world. Electromagnets may also be turned off, meaning that electromagnet-based linear generators are easier to handle when performing maintenance. The structure of linear generators must also be built strong enough to withstand the magnetic attraction forces between the shaft and stator (Baker et al., 2004). The latter two disadvantages seem to have been addressed in the design proposed by Mueller and McDonald (2008). Power smoothing of linear generators is inherently more difficult than that of rotary generators: in the case of the former, its motion comes to a complete stop (before switching direction) twice per motion cycle, as opposed to the latter, which continuously rotates.

2.5 Fixed structure WECs

Although the methodology and analysis presented in the forthcoming chapters concerns floating WECs, it is still important to dedicate a short section on fixed structure WECs. This is due to their historical significance, but most importantly, most of the available information comes from fixed plans (similarly to the offshore wind progression).

2.5.1 Fixed structure oscillating body converters

An example of a fixed structure oscillating body WEC is the Eco Wave Power converter⁵, which employs a hydraulic circuit in its PTO system. Likewise, the WaveStar WEC developed in Denmark - also works on the basis of a high pressure oil PTO. In both of these technologies, a floating arm moves with the motion of the waves (Frigaard et al., 2016). The motion moves a piston, compressing and expanding hydraulic fluid. An accumulator then stores compressed fluid. When the compressed fluid is later released, the pneumatic energy is converted into rotational energy via a hydraulic turbine. The shaft of the hydraulic turbine is connected to an electric generator, from a rotating magnetic field. Finally, the hydraulic fluid returns to a low pressure tank, where it is stored until the next wave.

Following the same principle of a fixed oscillating body, the Hyperbaric device was developed in Brazil (Estefen et al., 2008). This technology, also known as the Hyperbaric Coppe UFRJ device, was designed by the Coppe Federal University of Rio de Janeiro. Its modular design allows for plant capacity expansion. Each module consists of 10 m diameter buoy, 22 m long mechanic arm, and a pump connected to a closed circuit of fresh water. The buoy's heaving motion moves the arm about a pivot point fixed to the shore, which activates the hydraulic pump. Through a closed circuit, the hydraulic pump injects fresh water that is kept in a high pressure system formed by a hydro-pneumatic accumulator and hyperbaric chamber. The plan employs a high head hydraulic turbine as a PTO.

2.5.2 Fixed structure overtopping converters

The Tapered Channel Wave Power Device (TAPCHAN) was a shoreline WEC, deployed in the west coast of Norway in 1985. It consisted of a tapered channel needed for collecting the incoming seawater, a reservoir used for storing the collected waves in the form of potential energy, and a hydroelectric power plant for the electricity generation (Fredriksen, 1986).

The Sea-wave-Slot-cone-Generator (SSG) follows the principle of an overtopping device (Margheritini et al., 2009). Several reservoirs are stacked on top of each other, where the energy of incoming waves is stored as potential energy. The captured seawater runs through low-head hydroelectric turbines for electricity generation.

⁵<http://www.ecowavepower.com/> (Accessed in January 2018)

2.5.3 Fixed structure oscillating water column converters

Pico plant was a full size fixed OWC pilot plant located on Pico Island in the Azores, Portugal, developed in 1999 (Brito-Melo et al., 2001). The plant used a concrete structure, mounted on the shoreline, and employed a Wells turbine as PTO. Pico plant was operational until April 2018.

Likewise, another OWC shoreline plant is LIMPET, deployed in the island of Islay, Scotland (Heath et al., 2000). LIMPET is a 500 kW OWC developed by the University of Belfast and Wavgen LTD in the UK. Although the majority of previous OWC systems have had vertical water columns, the LIMPET system is angled at 45° , which was proven to be more efficient during wave tank tests. LIMPET has been connected to the Scottish electricity grid since September 2000.

Similar principles can be applied on breakwaters. Such ideas are quite spread the recent years. An example is the Mutriku breakwater in the North coast of Spain (Torre-Enciso et al., 2009), but also the power plant in the harbour of Civitavecchia in Italy (Arena et al., 2013). The Mutriku wave power plant was equipped with a bi-radial turbine (Fig. 2.4), which recently was deployed on a floating OWC, at BiMEP in Basque country (Carrelhas et al., 2019). The aforementioned fixed structure devices are summarised in Table 2.1.

2.6 Floating structure WECs

With the evolution of various WEC technologies, there has been increasing interest in the development of floating devices. The floating OWC concept has been under development since the 1940s. It was first introduced by the Japanese naval commander Yoshio Masuda, operating as a small scale navigation buoy (Masuda, 1985).

2.6.1 Floating oscillating water column converters

The Mighty Whale floating OWC prototype has been under development at Japanese Marine Science and Technology Centre since 1987 (Hotta et al., 1996). It consists of three air turbine and generator units, one with a rated power output of 50 kW and two with a rated power output of 30 kW. The Mighty Whale operates on the OWC principal. This is to say, waves force a column of water to oscillate and act upon a column of air, which flows through an air turbine and drives an electrical generator.

The spar-buoy OWC operates according to the floating OWC principal. This is a floater connected to a spar-tube, open to the sea water at the bottom, and in contact with the atmosphere at the top through an air turbine (Falcão et al. (2012), Gomes et al. (2012)). A pneumatic chamber exists between the interior free surface and the air turbine. Waves force an oscillatory motion of the water column relative to the floater, and consequently, expansions and compressions of the air inside the chamber take place

Table 2.1: A summary of several representative fixed structure devices.

Fixed structure	Device name	Deployment location	PTO	References
Fixed structure oscillating bodies	WaveStar	Nearshore	Hydraulic circuit	Frigaard et al. (2016)
	Eco Wave Power	Nearshore	Hydraulic circuit	-
	Hyperbaric device	Nearshore	Hydraulic circuit	Estefen et al. (2008)
Overtopping	TAPCHAN	Nearshore	Hydroelectric power plant	Fredriksen (1986)
	SSG	Nearshore	Low-head hydroelectric turbine	Margheritini et al. (2009)
OWC	Pico plant	Onshore	Wells turbine	Brito-Melo et al. (2001)
	Mutriku	Breakwater	Bi-radial and Wells turbine	Torre-Enciso et al. (2009)



Figure 2.4: Bi-radial turbine for the Mutriku breakwater power plant by IST. Photo courtesy of Professor António Falcão.

(Fig. 2.5). The air flow passes through a turbine, driving an electrical generator. A similar device has been designed for the U-GEN project (Ribeiro e Silva et al., 2016).

The OE Buoy (Ocean Energy Ltd, Ireland) is a floating OWC system, based on a vertical water column with a bend, leading to a horizontal water intake. This is also known as the “Backward Bent Duct Buoy” (BBDB) (Masuda and McCormick, 1987). A large, quarter scale prototype was deployed near Galway, Ireland, but no data on its performance has been made publicly available. Following the successful testing of this prototype, the company has plans to build for a full scale, 1 MW device.

2.6.2 Floating oscillating body converters

A concept that has been the subject of several academic studies is the Inter Project Service (IPS) Buoy (Cândido (2010), Gomes (2013)). This device consists of a semi-submerged floater attached to a completely submerged hollow tube, open to the seawater at both ends. Part of this tube encloses a piston connected to a rod. Relative motion between the rod and the floater forms the basis of the PTO system. As the waves move the buoy up

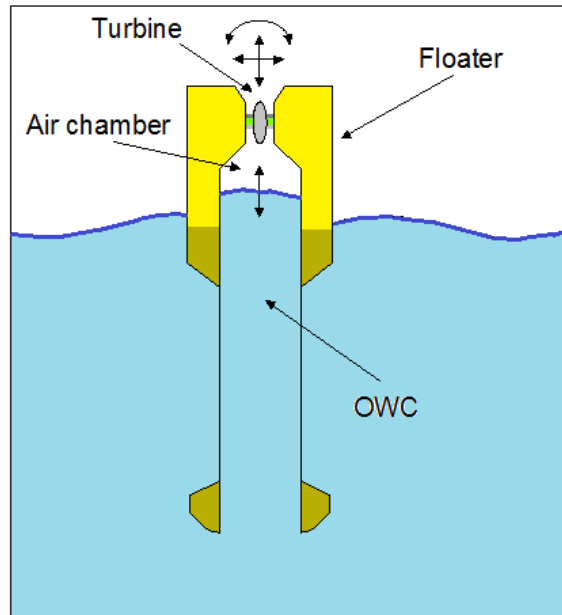


Figure 2.5: Illustration of the floating OWC, known as spar-buoy OWC, patented by IST (after Gomes (2013)).

and down, the acceleration tube – which is open in both ends – moves vertically relative to the water column inside it. The water column “traps” the piston, forcing it to move together with the water column relative to the acceleration tube. This pumping motion is hydraulically transformed into rotary motion, driving a generator. The Sloped IPS Buoy is a variation on the IPS Buoy that uses a sloped configuration to extract more energy from the waves. The floating buoy has a series of tubes reaching down into the water at a 45° angle, allowing it to extract energy from both the vertical and horizontal motions of the incoming waves. As in the original IPS Buoy, the movement of the buoy relative to a piston resting in the water column is used to power a hydraulic PTO system. Basic wave tank tests have been performed on this concept at the University of Edinburgh.

PowerBuoy was developed by Ocean Power Technologies. Its construction consists of two concentric bodies: a relatively immobile floating spar tube connected to a damping heave plate at the bottom, and a floater that surrounds the spar and oscillates in heave when driven by wave motion (Korde and Ertekin, 2014). The floater’s heaving oscillations drive a mechanical system, whose vertical translating motion is converted into rotary motion, which is used to drive an electrical generator.

PS Frog was developed by the Lancaster University Renewable Energy Group (LUREG) at the Engineering department of Lancaster University, and can be described as a floating oscillating body WEC (McCabe et al. (2006), Aggidis et al. (2005)). It consists of a large buoyant paddle and an internal ballasted handle lying below it. This device oscillates in the pitching mode in response to the waves’ action on the paddle (Fig. 2.6). The ballast provides the necessary restoring moment to bring the device back,

in anticipation of the next wave. Wave power absorption takes place by partially resisting the movement of a sliding PTO mass. The motion of the sliding mass is also used to tune the device to the incident wave frequency (Folley, 1993). The pressure exerted by the sliding mass is used to drive a hydraulic circuit, which in turn drives an electrical generator.

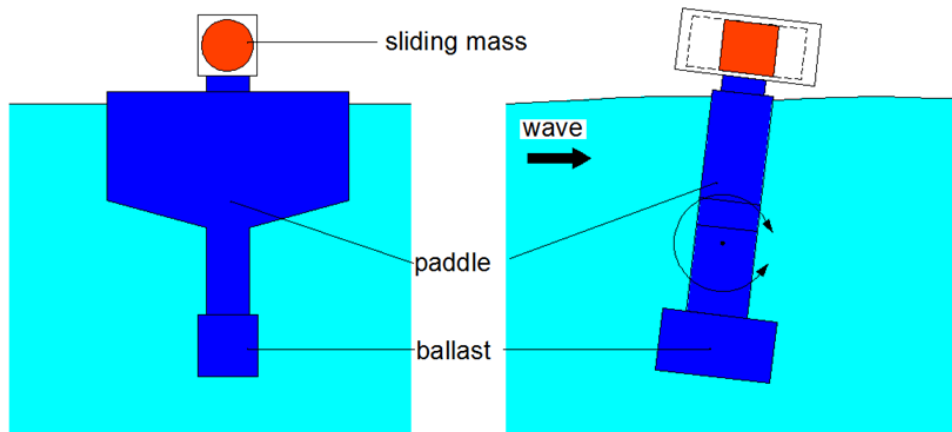


Figure 2.6: PS Frog (Mk5), illustration adapted from Falcão (2010).

SEAREV (Système Électrique Autonome de Récupération de l'énergie des Vagues) was developed at École Centrale de Nantes (Clément et al., 2005). It is a floating oscillating body type WEC, consisting of a sealed, watertight floater enclosing a heavy, rotating wheel whose centre of gravity is offset from its center of volume, making it act like an embedded pendulum. The upper half of the horizontal axis wheel is empty; weight is concentrated in the concrete filled lower half. The incoming waves make the SEAREV floater oscillate in pitch, causing the pendulum wheel to swing back and forth. Hydraulic pumps connected to the pendulum wheel charge the high and low pressure accumulators, which then discharge their energy into a hydraulic turbine that drives an electric generator. Unlike other floating devices (e.g. Wavebob, PowerBuoy, spar-buoy OWC), this device is not axisymmetric.

This method of wave energy capture is inherently highly non-linear, making these types of WECs more difficult to model.

2.6.3 Floating over-topping converters

In contrast to point absorbers, over-topping devices do not need to be in resonance with the incoming waves. This is due to the way in which energy is captured: by means of low-head hydropower turbines.

The Wave Dragon is a large floating structure whose main components are its reservoir and its two reflector arms (Kofoed et al., 2006). The reflectors are used to focus the waves towards the centre, where they are forced to flow up a ramp into the elevated

reservoir. Kaplan turbines are then used to convert the low head and high flow of the captured water into rotational energy. The turbines drive electrical generators, thereby generating electricity on the same principal as conventional land-based hydropower plants.

WaveCat was presented by Fernandez et al. (2012). It consists of two hulls, like a catamaran. But unlike a catamaran, however, the hulls are not parallel but converging. The bows of WaveCat are held open to the sea, so that incident waves propagate into the space between the hulls. Eventually, waves funnel into the inner hull sides, and overtopping water is collected in reservoirs at a level higher than the sea level. As water is drained back to the sea, it drives turbine-generator sets. The freeboard and draught, as well as the angle between the hulls, can be varied depending on the sea state. Examples of floating devices are summarised in Table 2.2.

2.7 Submerged structure WECs

This type of devices is in general better by means of survivability, and there is no visual impact. The operation and maintenance though might be more difficult than in the other types of devices presented in this chapter.

The Archimedes Wave Swing (AWS) consists of a submerged, mobile, air-filled cylinder that is fitted over top of another cylinder - one that is fixed to the seabed (Prado, 2008). When a wave crest approaches, the excess water pressure on top of the mobile cylinder increases, compressing the air trapped inside the device, and acting, as an upward restoring force. The reverse happens when a wave trough passes: the decrease in water pressure (relative to hydrostatic equilibrium) causes the trapped air to expand, making the weight of the mobile cylinder act as a downward restoring force. The relative motion between the mobile cylinder and the fixed lower part is converted directly to electricity through a linear generator. The system is suitable for deployment in water depths greater than 25 m, and can be configured for output power ratings between 25 kW and 250 kW, after selecting the appropriate scale to the corresponding wave climate. The technology was tested at an offshore location in Portugal, in 2004.

The CETO WEC⁶ consists of a large submerged buoy which is used to absorb the energy of the incoming waves above it and drive a hydraulic pump, which is tethered to the seabed. The pump converts the buoy's action into high pressure fluid energy, which is used to drive a hydraulic turbine that is coupled to an electrical generator, both of which are contained inside the buoy. An umbilical cable exports the generated electricity, either feeding the local grid or driving the direct desalination of seawater.

WaveRoller is a device that converts the surging action of ocean waves into electricity (Lucas et al., 2012). The WEC operates in the nearshore environment, submerged at depths where the surge is strongest. Its angular position oscillates about an axis that is

⁶<https://www.carnegiece.com/> (accessed in September 2017)

Table 2.2: A summary of several representative floating devices.

Floating WECs	Device name	Deployment location	PTO	References
Floating OWCs	Mighty Whale	Offshore	Air turbine	Hotta et al. (1996)
	spar-buoy OWC	Offshore	Air turbine	Falcão et al. (2012), Gomes et al. (2012)
	U-GEN	Offshore	Air turbine	Ribeiro e Silva et al. (2016)
	OE Buoy	Offshore	Air turbine	Masuda and McCormick (1987)
Floating oscillating body converters	IPS Buoy	Offshore	Hydraulic circuit	Cândido (2010)
	PowerBuoy	Offshore	Hydraulic circuit	Korde and Ertekin (2014)
	PS Frog	Offshore	Hydraulic circuit	McCabe et al. (2006), Aggidis et al. (2005)
	SEAREV	Offshore	Hydraulic circuit	Clément et al. (2005)
Floating overtopping	Wave Dragon	Nearshore	Hydroelectric turbine	Kofoed et al. (2006)
	WaveCat	Nearshore	Hydroelectric turbine	Fernandez et al. (2012)

perpendicular to the incoming surge - an axis that is secured by two pivot points that are anchored to the seabed. As the WaveRoller moves and absorbs energy from the surging ocean waves, the angular oscillation of its panel acts on a set of hydraulic pistons, which pump fluids around a closed hydraulic circuit. As is often used in hydraulic circuit PTO systems, some power smoothing is achieved using pressure accumulators, before driving a hydraulic turbine that is coupled to a rotary electrical generator.

WRASPA (Wave-driven, Resonant, Arcuate action, Surging Point-Absorber) (Chaplin and Aggidis (2007), Bhinder et al. (2009)) was developed at Lancaster University, designed for deployment in 20-50 m. The dynamics of this WEC are similar to other bottom-hinged WECs, such as Oyster (Whittaker and Folley, 2012) and WaveRoller (Lucas et al., 2012). In the WRASPA converter, wave forces act on the face of a collector body that is attached to an arm that rotates about a fixed horizontal axis below sea level. The body oscillates in pitch, at a frequency that is approximately equal to that of the ocean swell; its tuning may be achieved by changing the freeboard or pivot depth (Bhinder et al., 2009). For strong waves during storms, the arm is repositioned according to the converter's survival strategy, so that forces on the collector are minimised. A summary of submerged WECs can be found in Table 2.3.

2.8 Moorings for WECs

The mooring system is needed to keep the device in station, especially in the free surface plane where no hydrostatic restoring forces are present. It also plays a key role as long as survivability is concerned during extreme events. The energy absorption of the WEC or array of WECs can be influenced by the mooring system, as it may change its hydrodynamics, due to the coupling between the WEC and the mooring system responses (Johanning et al., 2007). Some practical mooring system design criteria have been proposed by the American Petroleum Institute (API) (2015), Det Norske Veritas (DNV) (2010), and British Standards Institution (BSI) (2014). These criteria should not necessarily be applied directly to WECs, since the consequences of mooring system failure in a WEC array are not expected to be as serious as those resulting from a mooring system failure of an offshore platform. In the case of offshore platforms, there are meticulous procedures in place to ensure the safety of the operating crew, and to minimise the risk of potentially severe environmental impacts. On the other hand, in the case of WECs, the potential consequence of mooring system failure would most likely involve vessel collision or drifting of the device. In terms of potential environmental impacts associated with WEC mooring system failure, these are still not very well understood, but they would most likely be less severe than in the case of offshore platforms. The influence of the mooring system on the WEC can be classified as follows (Harris et al. (2004), Karimirad et al. (2016), WETFEEET D6.2 (2016)):

1. Reactive mooring: the mooring system provides a means for PTO reaction, so that the PTO may benefit from the relative motion between the body and the

Table 2.3: A summary of several representative submerged devices.

Generic category	Device name	Deployment location	PTO	References
Submerged	AWS	Nearshore	Linear generator	Prado (2008)
	CETO WEC	Nearshore	Hydraulic circuit	-
	WaveRoller	Nearshore	Hydraulic circuit	Lucas et al. (2012)
	WRASPA	Nearshore	Hydraulic circuit	Chaplin and Aggidis (2007), Bhinder et al. (2009)

seabed. The resonance of the mooring system is designed to be close to the resonant frequency of the incoming waves. An example of such a system is the CETO WEC (Vicente et al., 2013).

2. **Passive mooring:** this type of mooring system provides only station keeping, where the WEC remains unaffected by the dynamics of the mooring system. The resonant frequencies of the mooring system are designed to be far from the typical ones of the incoming waves. Examples that operate with passive mooring systems include the OE Buoy, the Wave Dragon, and the Pelamis.
3. **Active mooring:** in this category, the stiffness of the mooring system plays a role in the dynamic response of the WEC, and might affect its resonance conditions. In this case, the mooring system is designed so that its resonant frequency is far from typical frequencies of the incoming waves. Examples of devices with active mooring systems are point absorbers.

2.8.1 Anchors

The anchoring system consists of mooring lines (which transmit the forces from the WEC to the anchor), the mooring line attachment to the WEC (also known as the fairlead), and the anchor itself, which is attached to the seabed and provides a stationary "touchdown point" to which the mooring lines may be connected. Existing anchoring systems may be classified as (Huang and Aggidis, 2008):

1. Drag embedment
2. Deadweight
3. Grappling
4. Direct embedment
5. Pile.

Anchor selection depends on a number of factors, such as the seabed (i.e. sediment type, topography, slope), the loads (direction and load range), and the economic viability (installation and maintenance costs) (Huang and Aggidis, 2008). A detailed description on the applicability of each anchor type to a given location can be found in the manual Direction of Commander (2000).

2.9 Mooring systems

Two principle mooring systems have been identified: the catenary system and the taut system (Karimirad et al. (2016), Vicente (2016)). Based on the WEC technology, one system might be preferred over the other. Mooring systems are necessary for station keeping of WECs, especially in the surge mode, where no hydrostatic restoring force naturally exists.

2.9.1 Catenary system

In this type of mooring system, the lines consist of free hanging catenaries. The lines' submerged weight produces a restoring force in the surge mode. This is the preferred system for devices and arrays where oscillations in all DoF take place (Johanning et al., 2018). The lower sections of the mooring lines are typically connected to heavier chains. Under calm sea conditions, the lower sections of the chains rest on the seabed. As soon as the mooring system begins to oscillate, the chains will undergo perturbations around their equilibrium positions. It is therefore important to leave enough chain on the seabed, so that it is not lifted up from the touchdown point, causing the anchor to experience an upward force. Depending on the type of seabed and the benthic life it supports, environmental impacts may be caused by the abrasive interaction between the moving chain and the seabed. Extra floaters and clump weight components may be included in the mooring system (e.g. Lazywave mooring geometry), similar to what is often done with umbilical cables (Weller et al., 2013). These slack mooring systems seem to be reliable during the action of high waves. In addition, this type of mooring system may be designed to minimise adverse effects on the converter's hydrodynamics, which still performing the critical function of preventing the device from drifting. Although the length and weight are higher compared to other mooring systems, the installation is easier, the costs are lower, and it appears to be less affected by corrosion than other systems.

2.9.2 Taut mooring system

In contrast to catenary system, where the restoring force is associated with geometric variations, in taut mooring systems the restoring force is associated with axial stretching. There is an angle between the mooring lines and the anchoring point, meaning that the anchors should be in a position to resist horizontal and vertical forces. For this reason, drag embedment anchors do not seem to be a good option for taut mooring systems.

In the case of the Tension Leg Platform (TLP), the mooring lines are positioned perpendicular to the seabed. Polyester ropes have been used for platforms in deep water locations. Compared to steel, polyester ropes are low cost and lightweight and they have load distribution properties that can be used to reduce peak loadings. However, unlike steel, synthetic materials have non-linear loading properties that are time-dependent (Weller et al., 2014). The aforementioned subcategories for catenary and taut moored systems are depicted in Fig. 2.7.

Compared to catenary systems, smaller lengths are needed in taut mooring systems, meaning that they have smaller footprint areas. On the other hand, environmental loads (i.e. lateral loading from currents and waves) present greater design challenges, since taut mooring systems have significantly higher stiffness. The integrity of the mooring system may be at risk, since no tangential contact with the seabed exists. The mooring line tension may become very large when the WEC undergoes a small lateral movement.

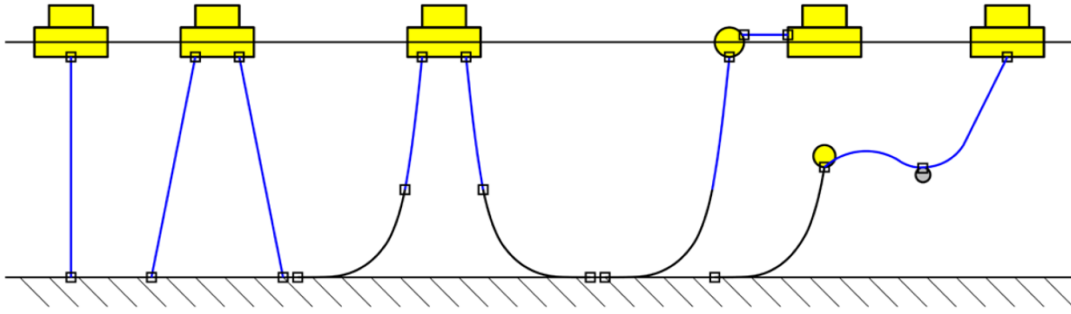


Figure 2.7: Possible mooring configurations for an axisymmetric device. From left to right, taut moored systems with single, taut moored with multiple lines, basic catenary system, catenary system with auxiliary surface buoy, and lazy wave system with subsea floater and sinker. Source: Karimirad et al. (2016).

Therefore, the probability of occurrence of large peak or snap loads should be examined in the design phase of the project, before the deployment. The selection of the mooring system should be based on; the costs, the footprint area, the environmental impacts, and the risk of failure or collision. This is particularly important for places with frequent storm occurrence. Paredes et al. (2016) performed an experiment where three different mooring configurations: one consisting of a synthetic cable and intermediate floater, one with floater and clump weight, and one with a catenary. By means of power extraction, the first configuration proved to be the best, and did not restrict the heaving motion of the body. However, this configuration did perform well with regards to maintaining tension in the cables under extreme conditions. The second case also performed quite well in terms of energy extraction, but its ability to keep the cables under tension while minimising dynamic tension was the best of the configurations studied.

2.10 Fundamentals of ocean waves

2.10.1 The momentum equation

Newton's Second Law is used to relate the change in momentum of a fluid mass due to an applied force. This change is expressed as

$$\frac{D(m\mathbf{u})}{Dt} = \mathbf{F}, \quad (2.1)$$

where \mathbf{F} is the applied force, m is the mass, and \mathbf{u} is the three-dimensional velocity field of water particles. The total derivative has been used, since the force on a particle is being calculated. This applied force consists of pressure gradients (∇p) and other forces (depending on the phenomenon studied). The above equation can also be written as follows

$$\frac{D\mathbf{u}}{Dt} = -\frac{1}{\rho}\nabla p + \text{other forces}, \quad (2.2)$$

where ρ is the fluid density.

2.10.2 The continuity equation

Another important mathematical relation in ocean dynamics is mass balance, also known as the continuity equation, which can be expressed as follows

$$\frac{1}{\rho} \frac{D\rho}{Dt} + \frac{\partial u}{\partial x} + \frac{\partial v}{\partial y} + \frac{\partial w}{\partial z} = 0. \quad (2.3)$$

Depending on the system studied and the scale of the phenomenon, Eqs. 2.2 and 2.3 will be modified accordingly. This is to say that their various terms may be expressed differently depending on whether a wave, a current, or a tsunami is being described. For example, in the case of a large scale phenomenon like a tsunami, the Coriolis force will also be taken into consideration. Another variation concerns the depths that are studied: when modelling the near-shore environment where radiation stresses are active due to wave-breaking, the modelling of currents is quite essential. This is also the case with tidal currents, where the shallow water equations are typically used, taking into consideration the fluid friction against the sea bed.

2.10.3 Wave theories in brief

There is a variety of wave propagation theories. Their applicability depends on the seabed depth, wave height, and wavelength, and it should be noted that all have their limitations. When studying regular waves, traditional approaches use Airy's theory (also known as linear wave theory), Dean, Stokes 5th, and Cnoidal. In the case of irregular waves, there are some semi-empirical wave spectra such as JONSWAP, Ochi-Hubble, Pierson Moskowitz, etc..

2.10.4 Modelling of ocean waves using linear wave theory

In this section, linear wave theory is reviewed, as it is the fundamental theory governing the content described in the next chapters. Standard text books on linear waves have been written by Newman (1977), Dean and Dalrymple (1984), Tucker and Pitt (2001), and Falnes (2002). Linear wave theory was developed a long time ago by Airy (1845). The main assumption in linear wave theory is that the wave amplitude A_w is small compared to the wavelength λ . The fluid is considered to be homogeneous, and ideal (i.e. zero friction). Viscous effects are neglected and the flow is assumed to be irrotational. Also, it is assumed that the flow is incompressible, meaning that the density remains constant. This leaves the continuity equation (Eq 2.3) to be expressed as the zero divergence condition

$$\nabla \cdot \mathbf{u} = 0, \quad (2.4)$$

for the fluid velocity vector $\mathbf{u}(x, y, z, t) = \langle u\hat{\mathbf{i}}, v\hat{\mathbf{j}}, w\hat{\mathbf{k}} \rangle$. Since irrotational flow is assumed, the curl of the velocity is 0,

$$\nabla \times \mathbf{u} = 0. \quad (2.5)$$

Since the curl of a gradient vanishes, the water velocity may be expressed as the gradient of velocity potential ϕ

$$\mathbf{u} = \nabla\phi. \quad (2.6)$$

The velocity potential has no direct physical meaning, and is expressed in units of m^2/s . Substituting Eq. 2.6 into Eq. 2.4, we obtain Laplace's equation

$$\nabla^2\phi = 0. \quad (2.7)$$

Boundary conditions

As with solving any differential equation problem, the boundary conditions need to be specified for Laplace's equation, in order to solve for the flow. The bottom boundary (i.e. seabed) is assumed to be rigid and impermeable. The water depth h (i.e. the distance between the undisturbed free surface and the seabed), is assumed to be constant in time and space. Based on the assumptions made, the kinematic boundary condition at the sea bottom is

$$\frac{\partial\phi}{\partial z} = 0, \text{ at } z = -h. \quad (2.8)$$

On the free surface, for a two-dimensional flow propagating along the x -axis positive direction, the vertical elevation of the free surface η must be followed by the motion of the fluid, $z = \eta(x, t)$, consequently the derivative of $z - \eta(x, t)$ disappears at the free surface

$$\frac{D}{Dt}(z - \eta) = \frac{\partial\phi}{\partial z} - \frac{\partial\eta}{\partial t} - \frac{\partial\phi}{\partial x} \frac{\partial\eta}{\partial x} = 0. \quad (2.9)$$

Assuming that the slope of the tangent line along the free surface is small in relation to the wavelength (which goes in line with the main assumption of waves of small amplitude), the term $\frac{\partial\eta}{\partial x}$ is neglected, and the kinematic free surface condition is written as

$$\frac{\partial\phi}{\partial z} = \frac{\partial\eta}{\partial t}, \text{ at } z = \eta(x, t). \quad (2.10)$$

From Bernoulli's equation for an unsteady irrotational flow (Landau and Lifshitz, 1987), the dynamic boundary condition to be satisfied on the free surface is

$$-\frac{p}{\rho} = \frac{\partial\phi}{\partial t} + \frac{1}{2}\nabla\phi \cdot \nabla\phi + gz = 0, \text{ at } z = \eta(x, t), \quad (2.11)$$

with g being the acceleration due to gravity. The variable p stands for the difference between the fluid hydrostatic pressure and atmospheric air pressure. The dynamic boundary conditions result from the inability of the free surface to withstand pressure differences. After substituting z for η in Eq. 2.11, and neglecting the small second order term $\nabla\phi \cdot \nabla\phi$, the linearised dynamic free surface condition is

$$\eta = -\frac{1}{g} \frac{\partial\phi}{\partial t}, \text{ at } z = 0. \quad (2.12)$$

This condition is applied on $z = 0$ (i.e. undisturbed free surface) instead of $\zeta = \eta$, so it goes in line with the previous linearisation. If Eq. 2.12 is differentiated with respect to t , and combined with the kinematic free surface condition (Eq. 2.10),

$$\frac{\partial \eta}{\partial t} + \frac{\partial \phi}{\partial z} = 0, \text{ at } z = 0, \quad (2.13)$$

a general form of the free surface boundary condition is obtained

$$\frac{\partial^2 \phi}{\partial t^2} + g \frac{\partial \phi}{\partial z} = 0, \text{ at } z = 0. \quad (2.14)$$

Regular waves in arbitrary water depth

The waves studied here are the simplest solution of the boundary condition presented in Eq. 2.14. Regular waves are sinusoidal in time with an angular frequency of ω , propagating along the positive x -axis, with a phase velocity v . The free surface elevation is written as

$$\eta(x, t) = A_w \cos(kx - \omega t - \varphi), \quad (2.15)$$

where A_w is the wave amplitude, k is the wave number, and φ is the phase angle (φ has been set to 0). The wave number is

$$k = \frac{\omega}{v}, \quad (2.16)$$

and it is related to the wavelength by

$$k = \frac{2\pi}{\lambda}. \quad (2.17)$$

The velocity potential ϕ is sinusoidal in time, and by itself it does not constitute a physical meaning. However, its spatial derivatives provide the flow velocity along the corresponding axes. The velocity potential is given by

$$\phi(x, z, t) = \Re \{ A_w \phi_0(x, z) \exp(i\omega t) \}, \quad (2.18)$$

where i is the imaginary unit, the $\Re \{ \}$ operator denotes taking the real part of a complex number. The parameter ϕ_0 stands for the complex amplitude of the velocity potential and it must satisfy the Laplace equation throughout the fluid domain. By applying the method of separation of variables on ϕ_0 , and taking into consideration the bottom boundary condition and the free surface dynamic boundary condition (and after applying some algebraic manipulation), the velocity potential may be expressed as

$$\phi(x, z, t) = \frac{g A_w}{\omega} \frac{\cosh k(z + h)}{\cosh kh} \sin(kx - \omega t). \quad (2.19)$$

Eq. 2.14 may be used to derive the relation between the wave number k and the wave frequency ω , which give the dispersion relation

$$\omega^2 = gk \tanh(kh). \quad (2.20)$$

The horizontal and vertical fluid velocity components are calculated by taking the partial derivatives of the velocity potential (Dean and Dalrymple, 1984),

$$u_x = \frac{gkA_w}{\omega} \frac{\cosh k(z+h)}{\cosh(kh)} \cos(kx - \omega t), \quad (2.21)$$

$$u_z = \frac{gkA_w}{\omega} \frac{\sinh k(z+h)}{\cosh(kh)} \sin(kx - \omega t). \quad (2.22)$$

The two components of the particles' motion are offset in phase by $\pi/2$. Therefore, they describe elliptical trajectories with a larger horizontal axis. At the surface, the amplitude of the vertical velocity component is closest to that of its larger horizontal counterpart. It then rapidly decreases with decreasing vertical position going to zero at the seabed. For $h > \lambda/2$, the effect of the bottom boundary vanishes, the orbitals of the particles become circular. From the free surface, the size of the orbitals decreases with depth until $z = -\lambda/2$, where the motion of the water particles has effectively ceased.

Similarly, from analysis of the dispersion relation (Eq. 2.20), as the water depth h tends to infinity, $\tanh(kh)$ tends to 1, and the dispersion relation becomes

$$\omega^2 = gk. \quad (2.23)$$

This relation has been validated experimentally for $h > \lambda/2$, with a discrepancy of less than 0.4% (Dean and Dalrymple, 1984). Consequently, the deep water limit is considered to be at $h = \lambda/2$. For such high values of h , the influence of the seabed on the waves is considered to be negligible. Analysis of deep water waves shows that the wave effects are concentrated near the free surface. With decreasing z , the velocities decrease exponentially. At the free surface, the particles move with the wave amplitude.

The other limiting case is obtained as the water depth h tends to 0, $\tanh(kh)$ tends to kh . Therefore the dispersion relation becomes

$$\omega^2 = gk^2h. \quad (2.24)$$

This condition is observed in the dispersion relation for $h < \lambda/20$, with a maximum experimentally validated discrepancy of 1.4% according to Dean and Dalrymple (1984). This implies that shallow waters are considered for depths $h < \lambda/20$. Recalling the wavenumber in Eq. 2.16, the influence of water depth on the phase velocity of a progressive wave is provided by the following expressions (Kamphuis, 2010):

- $v^2 \approx gh$, for $h/\lambda < 1/20$, for shallow water.
- $v^2 = \frac{g}{k} \tanh(kh)$, for $0 < h/\lambda < \infty$, for intermediate water depth.
- $v^2 \approx g/k$, for $h/\lambda > 1/2$, for deep water.

This velocity corresponds to the propagation velocity of the wave. In shallow water, v is independent of the wave frequency ω , it is just proportional to the water depth h .

Irregular waves

In nature, waves are not regular. The aforementioned theory is based on the assumption that plane progressive waves are a 2D regular cyclic process, and their free surface elevation is described via a sinusoidal variation in time, as described in Eq. 2.15. But in reality, ocean waves are random. They are waves with different frequencies, amplitudes, and directions. The multi-directionality of waves as well as their generation, can be described by the theory presented in Holthuijsen (2007). Irregular waves are approximated as a superposition of regular waves with frequencies, phases, and amplitudes. More explicitly, wave elevation η at a fixed position is assumed to be the sum of a large set of regular waves, each with different amplitude $A_{w,i}$, frequency ω_i , and phase φ_i ,

$$\eta(t) = \sum_{i=1}^N \eta_i = \sum_{i=1}^N A_{w,i} \cos(\omega_i t + \varphi_i), \quad (2.25)$$

where N is the number of harmonics considered and i is the index of each harmonic. A constant frequency interval $\Delta\omega$ is commonly used as the spacing between harmonics. The model assumes that the phases and amplitudes are random variables characterised by their respective probability density functions. The phase is uniformly distributed between 0 and 2π . The amplitude is assumed to have a Rayleigh distribution (Longuet-Higgins, 1952).

The superposition of regular waves is in agreement with linear wave theory. The differential equations that define the boundary-value problem are linear, so the velocity potentials of each harmonic can be superimposed. The free-surface elevation and particle velocity components can be derived using the same approach. The horizontal and vertical velocity components of a randomly generated wave at a point (x, z) are

$$u_x = \sum_{i=1}^N u_{x,i} = \sum_{i=1}^N \frac{gk_i A_{w,i}}{\omega_i} \frac{\cosh k_i(z+h)}{\cosh(k_i h)} \cos(k_i x - \omega_i t - \varphi_i), \quad (2.26)$$

$$u_z = \sum_{i=1}^N u_{z,i} = \sum_{i=1}^N \frac{gk_i A_{w,i}}{\omega_i} \frac{\sinh k_i(z+h)}{\cosh(k_i h)} \cos(k_i x - \omega_i t - \varphi_i), \quad (2.27)$$

where k_i is the wavenumber (from the dispersion relation) of the i -th regular wave. The amplitude distribution also gives information on the contribution of each regular wave component.

Wave spectra illustrate the sea surface as a stochastic process. A single observation constitutes a single realisation of a stochastic point. The spectrum basically describes all the possible observations that could take place for each observation within the wave record. Any finite signal of duration T (or infinite signal with a finite repeat period of

T) may be perfectly reproduced by a Fourier series when the number of harmonics n approaches infinity. In practice, there is always some number $n = N$ that is considered to be large enough to reproduce the signal to a high degree of accuracy. The wave record as a finite time-series can therefore be approximated as the sum of N wave components, based on a Fourier series. Through Fourier analysis of a wave record, the contribution of every harmonic can be determined. This gives the amplitudes $A_{w,i}$ and phases φ_i of Eq. 2.25. The computed values of $A_{w,i}$ and φ_i can be substituted in the aforementioned equation to approximately reproduce the wave record, under the criterion that the number of harmonics is large.

2.10.5 The wave climate

As stated in the previous section, it is possible to study irregular waves from the superposition of regular waves. Dealing with the sea surface elevation as a stationary Gaussian process, the statistics can be defined with the aid of an energy density spectrum $S(f)$ (where $f = 2\pi/\omega$). The moments of the spectrum are given by

$$m_n = \int_0^\infty f^n S(f) df. \quad (2.28)$$

The significant wave height H_s (i.e. highest one-third of wave heights in a wave record) is given by,

$$H_s = 4\sqrt{m_0}. \quad (2.29)$$

There is a variety of wave spectra that can be used: the Pierson-Moskowitz (P-M) spectrum (Pierson and Moskowitz, 1964), the JONSWAP (JOint North Sea WAve observation Project) spectrum (Hasselmann et al., 1973), and the Bretschneider spectrum (Kamphuis, 2010). The P-M spectrum can be a good representation of the Atlantic coast (e.g. Portugal and the west coast of France) (Correia da Fonseca, 2014), as it corresponds to waves that have been fully developed.

In general the energy period is given by

$$T_e = \frac{m_{-1}}{m_0} \quad (2.30)$$

which yields

$$T_e \simeq 0.857T_p, \quad (2.31)$$

for a P-M spectrum.

On the other hand, the JONSWAP spectrum applies well to the North Atlantic wave climate, as it considers that waves have not been fully developed, due to a fetch (distance where the wind has been acting on the waves) that is not long enough to fully develop the wave height. The two-parameter P-M spectrum is equivalent to the Bretschneider

spectrum (Goda, 2010), and can be applied to Portugal and to Ireland. In case where ocean waves are very quickly developed due to the effect of strong winds over a restricted body of water (e.g. the North Sea), the spectrum presents a much sharper peak, which is accounted for in the JONSWAP spectrum (Hasselmann et al. (1973) have proposed a factor for controlling the sharpness of the spectrum peak).

Information about the wave climate can be given by joint distribution tables of sea states (Oikonomou and Aggidis, 2015). Sea states are commonly presented as a combination of significant wave height H_s and energy period T_e , organised in bins, along with the probability of occurrence. The wave climate can be well described by wave spectra in the offshore zone. However, as waves approach the coast, they feel the bottom and they become parallel to the coast, as described by Snell's Law (Masselink et al., 2011). This phenomenon is known as refraction. Close to the coast, the energy periods become shorter and the waves grow significantly in height. Since they cannot handle the associated shear stresses, they break and they cause currents in the nearshore environment (longshore current). Along with tides, they are responsible for sediment transport patterns (rip currents). The nearshore environment is highly non-linear, and although linear wave theory can be applied in the nearshore zone under certain assumptions, it still reveals many problems in doing so. That being said, the offshore environment is also non-linear in different ways. Excess energy in the offshore also causes wave breaking (i.e. whitecapping) (Holthuijsen, 2007). However, for initial studies of the response of floating bodies, linear wave theory seems to be valid and a good starting point. Power matrices for a selection of WECs can be found in Babarit et al. (2012).

Prior to the development and deployment of a WEC design, extensive knowledge on the wave energy resource in a location is required. WEC designers give emphasis on making the machine tunable for the wave period T_e and adjustable over minutes as the sea state changes. The maximum wave height at any location of interest is quite essential in order to ensure survivability. Efficient operation of WECs requires device rating for the most common power levels, obtained from the most common sea states. However, the technology has to be designed to overcome the action of extreme events as well. It is well-known that in offshore locations, waves tend to be multi-directional. This means that when designing arrays for the offshore environment, special care should be given to their capability of extracting energy from various wave directions. This can be achieved through mooring configurations and symmetry of WECs.

2.11 Wave force theories

First order loads oscillate with the same frequency as the waves, and they are also proportional to the wave amplitude A_w . Second order loads, occur due to the presence of non-linearities in the pressure field generated by the waves' action, and they have been neglected throughout this thesis.

In the study of first order wave-induced forces, three methods are used: Morison's equation, the Froude-Krylov force, and the diffraction theory. All of them are applicable, but depending on the wave conditions and the size of the floating body, some are more relevant than others. If the characteristic dimension of the body is small compared to the wavelength, the body's presence will not significantly alter the wave field. However, if the body is large or of comparable size in relation to the wavelength, it will affect the wave field by means of scattered waves, as shown in the work of Chakrabarti (1987).

Fig. 2.8 shows the relationship between the Keulegan-Carpenter (KC) number (Keulegan and Carpenter, 1958) and the diffraction parameter. The latter provides information on whether or not diffraction is significant, and the former describes the ratio of drag to inertial forces. If the characteristic dimension of the structure is large or of comparable size in relation to the wavelength - which is to say $ka \geq O(1)$ - then the diffraction is significant. On the other hand, if the characteristic dimension of the body is small compared to the wavelength (i.e. $ka \ll 1$), then the wave field will not be significantly altered. In this latter case, it is the ratio of drag inertial forces that influence the dynamics of the body, and the loads depend on the flow regime around it. As the flow velocity increases, also the KC number increases, and drag effects become important. The Reynold's number is also important in this case, because the flow changes from laminar to turbulent, when the Reynold's number is sufficiently high. If the KC number is lower than 1.1, there is no flow separation.

2.11.1 Morison's equation

According to this theory, the force on a slender body from non-breaking waves consists of an inertial and a drag component. The former is a combination of the Froude-Krylov force and a force resulting from the change in fluid velocity due to the body's presence. That is to say, in addition to the force on a body from the accelerating fluid itself, moving fluid particles that meet an obstacle must pass around it, changing their momentum and hence exerting an additional force. Friction between the slender body and the fluid exerts a force on the fluid in a direction that is opposite to its flow, causing it to decelerate. But because for every action there is an equal and opposite reaction, it means that the drag component of the Morison's equation force acting on the slender body is actually oriented in the same direction as the flow velocity. The work of Sarpkaya (1976) provides a guide for drag and inertial coefficients, which have also been reported by Chakrabarti (1987).

2.11.2 Froude-Krylov theory

The Froude-Krylov force is the result of the hydrodynamic pressure on a body due to an incoming wave field that has not yet been disturbed by its presence. Together with the excess pressure caused by another wave field that is scattered from the body upon making contact, it describes the total excitation force acting on a body when hydrostatic

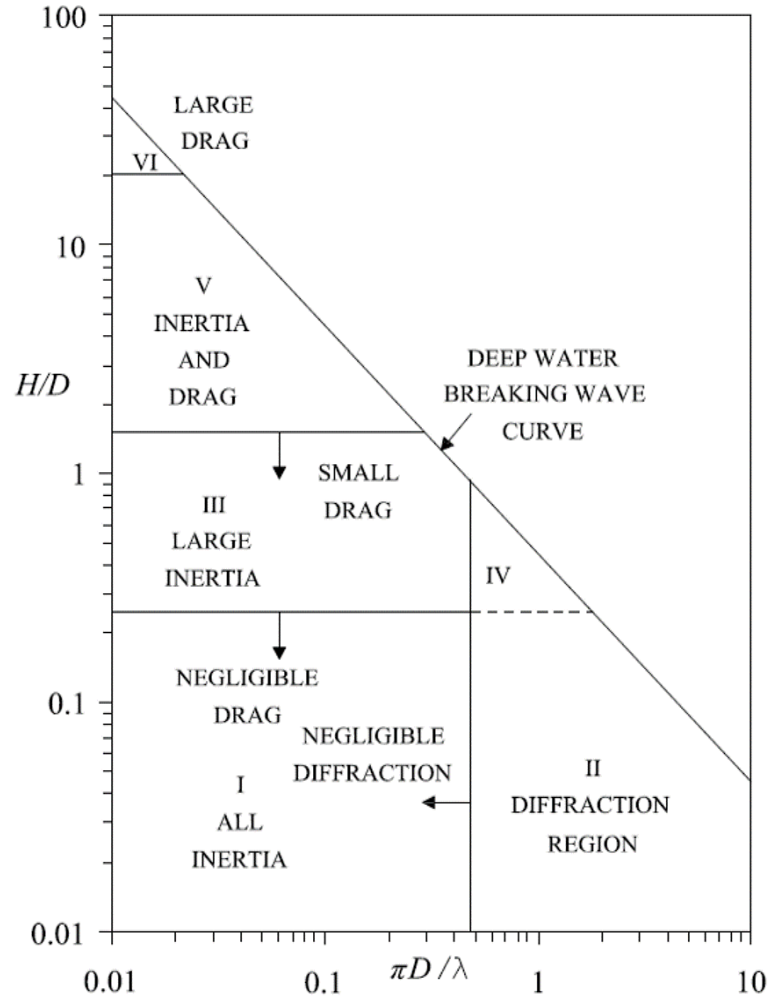


Figure 2.8: Load theories and their various regions of applicability, according to Chakrabarti (1987), where H is water depth, D is the characteristic dimension, and λ is the wavelength. Redrawn from Det Norske Veritas (DNV) (2014).

conditions are disturbed by an incoming wave.

2.11.3 Diffraction theory

As previously stated a marine structure whose characteristic dimension is small compared to the wavelength will not significantly alter the surrounding wave field, and hence Froude-Krylov theory may be used to approximate the diffraction field. However, when the characteristic dimension is of comparable size or large in relation to the wavelength, a significant scattered component will be introduced to the surrounding wave field - possibly enough to observe the incoming wavefronts being diffracted around the structure. Both the Froude-Krylov and the total diffraction field are computed using Boundary Integral Element Method (BIEM) codes, which are known to use either lower-order or higher-order discretisation schemes. For complex geometries, the lower-order discretisation method requires a large number of panels, which increases the computational time, making the higher-order discretisation method preferable in such cases, since it uses curved panels.

Chakrabarti (2005) believes that both methods give similar results. In the aforementioned work, all of these approaches describe first order loads on a floating body due to wave excitation.

The second order forces that have been neglected from Newton's Second Law throughout this thesis result from the following effects:

- The free surface term - When the water level around the structure changes position, the pressure distribution on the structure will also change, and the same will happen with the translational and the angular motion of the body.
- The velocity-squared term - Second order terms can become apparent in Bernoulli's equation, because of the velocity squared term in the energy balance equation, in addition to the linear pressure term.
- The body's motion term - The BIEM computation of a floating body's first order radiation force coefficients is performed assuming still water conditions, before combining the radiation force with the linear remaining linear forces. The principle of superposition may be applied as long as the system is linear. Second order forces are generated from the combination of first order pressure distribution and free body motion.

Another second-order term that is not included in Newton's Second Law, and omitted from this thesis is the drift term, which can be part of a time-domain model, since it is important in the analysis of mooring system dynamics. One example involves the drift forces from tidal currents, but this effect will only be noticeable at very low wave frequencies.

2.12 Oscillating body type wave energy converters

A floating body that oscillates in six (DoF), is characterised by three translational modes: surge, sway, and heave, and three rotational modes: roll, pitch, and yaw (Fig. 2.1). In a body that is axisymmetric about the xy -plane, translational modes surge and sway and rotational modes roll and pitch are redundant.

In response to an incoming wave, the motion amplitudes of floating bodies can be studied via (see Falcão (2016)):

1. Frequency-domain models
2. Stochastic models
3. Time-domain models.

Although all three of these approaches use linear wave theory (commonly), one will always be more appropriate than the others depending on whether or not the PTO is linear, and whether the waves considered are of a fixed frequency or are described by a spectrum. Table 2.4 presents a summary of the conditions which make a particular modelling approach most appropriate.

Table 2.4: A summary of techniques for modelling wave energy conversion systems.

Modelling approach	Waves	PTO
Frequency-domain	Regular	Linear
Stochastic	Irregular	Linear
Time-domain	Irregular	Non-linear

2.12.1 Single body system in the frequency-domain

In this section, the discussion is focused on an axisymmetric floating body whose motion is only described in heave. Calculating the position of the floating body is done by solving Newton's Second Law, where the sum of the forces may be obtained by considering isolated effects through the principle of superposition, since frequency-domain modelling is only concerned with linear systems and regular waves of constant frequency and phase. The system is linear and the incident wave is represented by a simple harmonic function of time. The body's displacements ($\xi(t)$) and forces ($f(t)$) are also simple harmonic functions of time

$$\xi(t) = x e^{i\omega t}, \quad (2.32)$$

$$f(t) = F e^{i\omega t}, \quad (2.33)$$

where x and F represent the complex amplitudes of the displacements of the body, and the amplitudes of the forces, respectively. In this section, the following forces will be considered: the excitation force, the radiation force, the hydrostatic restoring force, and the PTO reaction force.

In BIEM codes, the radiation-diffraction problem is solved numerically using Green's Theorem. Each problem may be solved separately, as permitted by the principle of linear superposition. The diffraction problem is set up to obtain the excitation forces on a body, and is solved in BIEM codes by considering the body to be fixed. For simple bodies, it may also be solved analytically. With the floating body held fixed in its position, an incoming wave of constant frequency generates an excess pressure field with respect to hydrostatic equilibrium. This wave-induced excess pressure field is known as the Froude-Krylov force. Then, due to the presence of the body, another excess pressure field is generated due to the waves that scatter upon making contact with the body. The sum of these two pressure fields is known as the diffracted wave field, and represents the total hydrodynamic pressure being applied on the body. Taking the integral of this total hydrodynamic pressure over the wetted surface area of the body solves the diffraction problem, gives the total excitation force on the body. For bodies like point absorber type of WECs (bodies whose characteristic dimension is small compared to the wavelength), the Froude-Krylov force represents the dominant component of the total excitation force, so their scattered field component may often be neglected.

The mooring/foundation system is needed to keep the device in station, but in this section it will not be included in the model. Due to their non-linearity, viscous effects will not be taken into consideration either. The system consists of a PTO that is responsible for converting mechanical energy into electricity. The body reacts against a fixed reference (i.e. the seabed) via the PTO (Fig. 2.9). The PTO consists of a linear spring and damper.

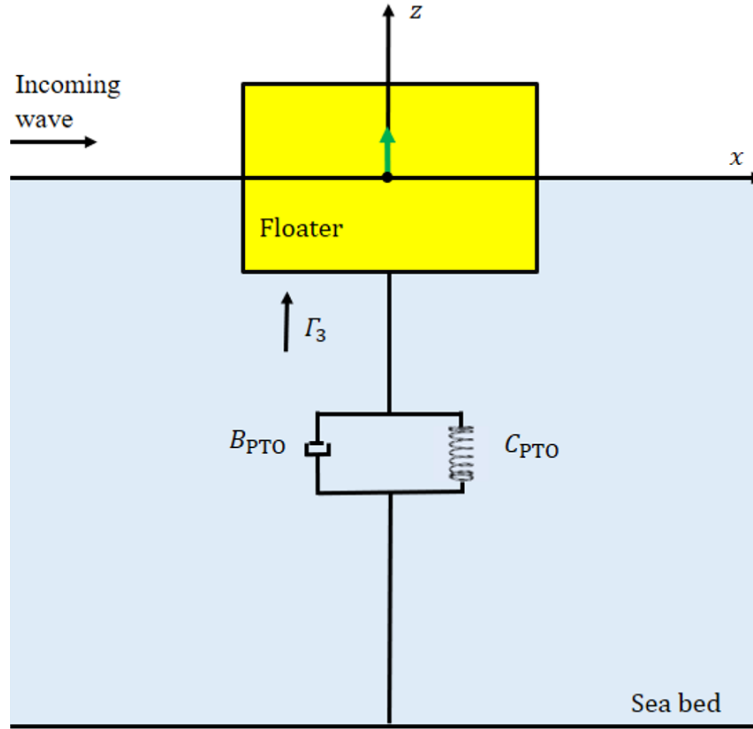


Figure 2.9: Single-body system oscillating in heave.

The PTO applies a reaction force on the WEC expressed as

$$f_{\text{PTO}}(t) = -B_{\text{PTO}}\dot{\xi}_3(t) - C_{\text{PTO}}\xi_3(t), \quad (2.34)$$

where $\dot{\xi}_3(t)$ is the body's velocity in heave, B_{PTO} is the PTO damping responsible for energy dissipation across an energy extraction medium (e.g. the compressed air inside an OWC air chamber), and C_{PTO} is the spring coefficient. The hydrostatic restoring force from Archimedes' principle is equal to $\rho g S_b$, where S_b is the floating body's waterplane area. The radiation problem is solved by considering a motionless free surface (i.e. no waves) and displacing the floating body along one of its six DoF, with oscillatory motion of a constant frequency. The waves radiated by the body itself that disturb the previously motionless free surface form a radiated excess pressure field. Integrating this radiated excess pressure along a particular DoF over the wetted surface area gives the radiation force acting on the body in that same DoF. It is important to note that there may be hydrodynamic coupling between various DoF. That is to say, waves may be radiated in all directions due to the body's motion along only one DoF, hence why the radiation

force is denoted as the force acting on DoF i due to waves radiated due to motion along DoF j .

In the **frequency domain**, the radiation force complex amplitude is written as

$$F_{\text{rad},3} = (\omega^2 A_{33} - i\omega B_{33})x_j, \quad (2.35)$$

where A_{33} is the added mass in heave due to waves radiated along heave and B_{33} is the radiation damping in heave also due to waves radiated along heave. In these two components of the radiation force, the added mass represents an energy storage term and the radiation damping represents a dissipation of energy to the surrounding fluid. The radiation force is

$$f_{\text{rad},3}(t) = \Re \{ F_{\text{rad},3} e^{i\omega t} \}. \quad (2.36)$$

The excitation force is given by

$$f_{\text{exc},3}(t) = \Re \{ F_{\text{exc},3} e^{i\omega t} \}. \quad (2.37)$$

The wave excitation force per unit wave amplitude is

$$\Gamma_3(\theta) = \frac{F_{\text{exc},3}(\theta)}{A_w}, \quad (2.38)$$

where θ is the angle wave of incidence. The Haskind Relation for deep water (Newman, 1977) relates B_{33} to $\Gamma_3(\theta)$ by:

$$B_{33} = \frac{\omega k}{4\pi\rho g^2} \int_{-\pi}^{\pi} [\Gamma_3(\theta)]^2 d\theta. \quad (2.39)$$

Combining all of these forces, Newton's Second Law may be written as

$$(-\omega^2(m_3 + A_{33}) + i\omega(B_{33} + B_{\text{PTO}}) + (\rho g S_b + C_{\text{PTO}})) x_3 = F_{\text{exc},3}. \quad (2.40)$$

The hydrodynamic coefficients can be calculated analytically for a simple geometry (e.g. sphere, cylinder), but to calculate the hydrodynamic coefficients for more complex geometries, codes based on BIEM should be employed (e.g. WAMIT (2006), AQUADYN, NEMOH (Babarit and Delhommeau, 2015), and ANSYS Aqwa).

For a single body WEC oscillating only in heave, the instantaneous power absorbed from the waves is equal to the force on its wetted surface times its vertical velocity. When the time-average of the instantaneous power is taken, it may be expressed in the frequency domain as

$$\bar{P} = \frac{1}{8B_{33}} |F_{\text{exc},3}|^2 - \frac{B_{33}}{2} \left| i\omega x_3 - \frac{F_{\text{exc},3}}{2B_{33}} \right|^2. \quad (2.41)$$

The absorbed power is thereby maximised when the second term on the right hand side

vanishes, which happens when

$$i\omega x_3 = \frac{F_{\text{exc},3}}{2B_{33}}. \quad (2.42)$$

This occurs when the system is resonant (i.e. when the velocity is in phase with the excitation force) and when the PTO damping is tuned to that of the absorbing medium. Putting the maximum transfer condition of Eq. 2.42 into Eq. 2.40 and separating the real and imaginary parts,

1.

$$B_{\text{PTO}} = B_{33}, \quad (2.43)$$

2.

$$\omega_{n,3} = \sqrt{\frac{\rho g S_b + C_{\text{PTO}}}{m_3 + A_{33}}}. \quad (2.44)$$

In order to more accurately depict the energy absorbing capability of a device, the capture width C_w is used to define a dimensional ratio between the amount of power absorbed by the converter in relation to the energy flux transported by every meter of incoming wavefront

$$C_w = \frac{\bar{P}}{\bar{P}_w}, \quad (2.45)$$

where \bar{P}_w is the time-averaged power per unit wave crest length. For an axisymmetric body oscillating in heave, Budal and Falnes (1975) and Evans (1976) have shown that

$$\bar{P}_{\text{max}} = \frac{\bar{P}_w \lambda}{2\pi}, \quad (2.46)$$

or

$$C_{w,\text{max}} = \frac{\lambda}{2\pi}, \quad (2.47)$$

implying that in the case of a point absorber - whose characteristic dimension is much smaller than the wavelength - the maximum absorbed power is equivalent to the energy flux transported by incoming regular waves whose wavefronts are longer than its own characteristic dimension. Chapter 3 of the thesis is elaborated on this generic frequency-domain approach.

2.12.2 Single body system in the time-domain

The time-domain modelling approach should be utilised when the PTO is non-linear. This is the case when the reaction force of the PTO in an oscillating body type WEC is not in its velocity and position. Similarly, an OWC type WEC should also be modelled in the time-domain when the pressure drop across its air turbine PTO is not a linear function of the flow rate. Even in the presence of regular waves, a non-linear PTO will prevent the absorbing body from oscillating at a fixed frequency, and hence expressing the radiation force as in Eq. 2.35 will not be possible. Therefore, the radiation force on the body must be computed at each time step, from waves radiated instantaneously as

well as waves radiated in the past. In other words, this force is dependent on the history of the body's motion through the radiated wave field - a memory effect. This dependence is expressed through the following relation (Cummins, 1962)

$$f_{\text{rad},3}(t) = - \int_{-\infty}^t g_r(t - \tau) \dot{\xi}_3(\tau) d\tau - A_{33}(\infty) \ddot{\xi}_3(t), \quad (2.48)$$

where $\ddot{\xi}_3(t)$ is the body's acceleration in heave, and $A_{33}(\infty)$ is the added mass in heave at infinite frequency. The impulse response function g_r physically represents ripples, and tends to zero as the argument tends towards infinity. The impulse response function is given by the following relation (Ricci et al., 2008),

$$g_r(t) = \frac{1}{2\pi} \int_0^\infty \frac{B_{33}(\omega)}{\omega} \sin \omega t d\omega. \quad (2.49)$$

The described time-domain approach has not been implemented throughout this thesis, as it is typically used in the more advanced stages of a technology's development. Furthermore, it may be used to model the non-linear behaviour of various system components, which is the case of the PTO and would involve knowledge on a specific air turbine pressure-flow characteristic or electrical generator control law algorithm. The time-domain modelling approach has been briefly described here for the sake of completeness, and may be used in future development of the model presented in this thesis.

2.12.3 Two-body system in the frequency-domain

Wave energy converters consisting of two bodies have been described in Falnes (1999). One body reacts against the other, and energy is extracted by the PTO through their relative motion. In this section, the two bodies are considered to oscillate only in heave, as depicted in Fig. 2.10. In addition to the work done by Falnes (1999), detailed analysis on modelling such systems can also be found in Gomes et al. (2016). Examples of two-body heaving WEC systems include Wavebob and Powerbuoy. The vertical displacements for Body 1 and 2 from their undisturbed positions are denoted by ξ_3 and ξ_9 , respectively. Using similar analysis as described in Section 2.12.1, Newton's Second Law may be written for each body as

$$m_3 \ddot{\xi}_3(t) = f_{\text{exc},3} + f_{\text{rad},33} + f_{\text{rad},39} - \rho g S_1 \xi_3(t) + f_{\text{PTO}} \quad (2.50)$$

$$m_9 \ddot{\xi}_9(t) = f_{\text{exc},9} + f_{\text{rad},99} + f_{\text{rad},93} - \rho g S_2 \xi_9(t) - f_{\text{PTO}}, \quad (2.51)$$

where m_3 and m_9 correspond to the masses of the two bodies, $f_{\text{exc},i}$ is the wave excitation force on DoF i , the terms S_1 , S_2 are the cross-sectional areas of the two bodies along heave, $f_{\text{rad},ii}$ is the radiation force on DoF i due to its own motion, and $f_{\text{rad},ij}$ is the radiation force of DoF i due to the motion along DoF j . As in the previous case, the PTO is considered to be linear, with a spring of stiffness C_{PTO} and a damper with damping

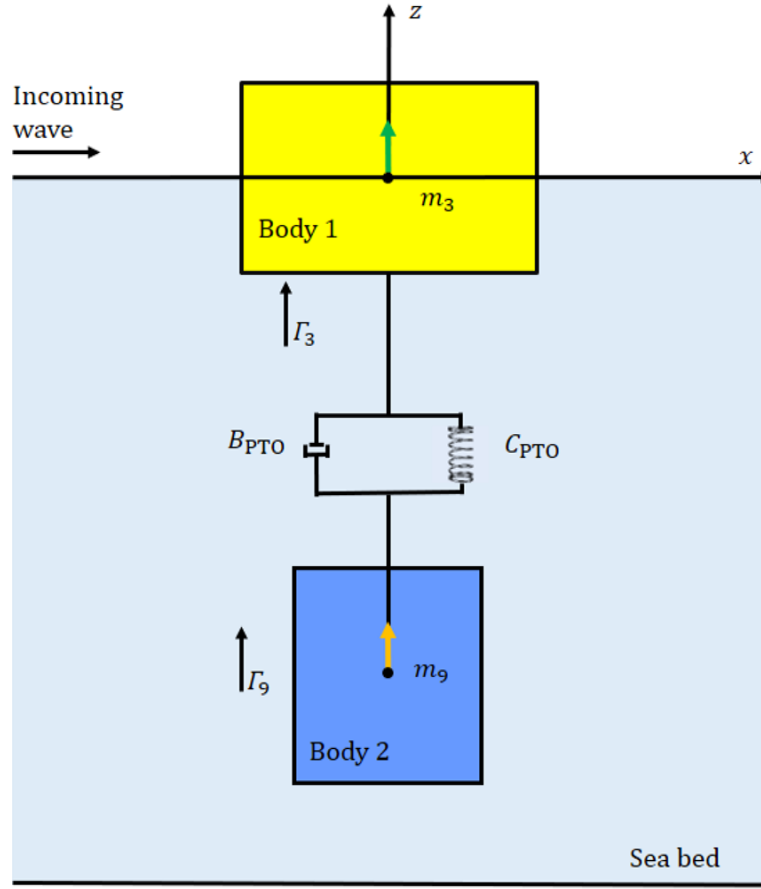


Figure 2.10: Two-body system oscillating in heave only.

coefficient B_{PTO} . The PTO force is given by

$$f_{\text{PTO}} = -B_{\text{PTO}}(\dot{\xi}_3(t) - \dot{\xi}_9(t)) - C_{\text{PTO}}(\xi_3(t) - \xi_9(t)). \quad (2.52)$$

The equations of motion for the two bodies (Eqs. 2.50 and 2.51) are expressed in the frequency-domain as follows

$$\begin{aligned} &(-\omega^2(m_3 + A_{33}) + \omega(B_{33} + B_{\text{PTO}}) + (\rho g S_1 + C_{\text{PTO}}))x_3 \\ &+ (-\omega^2 A_{39} + \omega(B_{39} - B_{\text{PTO}}) - C_{\text{PTO}})x_9 = F_{\text{exc},3}, \end{aligned} \quad (2.53)$$

$$\begin{aligned} &(-\omega^2(m_9 + A_{99}) + \omega(B_{99} - B_{\text{PTO}}) + (\rho g S_2 - C_{\text{PTO}}))x_9 \\ &+ (-\omega^2 A_{93} + \omega(B_{93} + B_{\text{PTO}}) + C_{\text{PTO}})x_3 = F_{\text{exc},9}. \end{aligned} \quad (2.54)$$

2.12.4 Two-body system in the time-domain

If the PTO is non-linear, the system should be analysed in the time-domain. For a two-body system oscillating only in heave, the radiation force on a body moving in DoF i due to waves radiated along DoF j may be expressed as

$$f_{\text{rad},j}(t) = - \int_{-\infty}^t g_{r,ij}(t-\tau) \dot{\xi}_j(\tau) d\tau - A_{ij}(\infty) \ddot{\xi}_j(t), \quad (2.55)$$

with

$$g_{r,ij}(s) = \frac{2}{\pi} \int_0^\infty B_{ij}(\omega) \cos(\omega s) d\omega, \quad (2.56)$$

with integration variable s instead of $t - \tau$, where $i = 3, 9$ and $j = 9, 3$. The equations of motion for Body 1 and Body 2 (Eqs. 2.50 and 2.51, respectively), are written in the time-domain as

$$\begin{aligned} (m_3 + A_{33}(\infty)) \ddot{\xi}_3(t) + \int_{-\infty}^t g_{r,33}(t-\tau) \dot{\xi}_3(\tau) d\tau + \rho g S_1 \xi_3(t) \\ + \int_{-\infty}^t g_{r,39}(t-\tau) \dot{\xi}_9(\tau) d\tau + A_{39}(\infty) \ddot{\xi}_9(t) - f_{\text{PTO}} = f_{\text{exc},3}, \end{aligned} \quad (2.57)$$

$$\begin{aligned} (m_9 + A_{99}(\infty)) \ddot{\xi}_9(t) + \int_{-\infty}^t g_{r,99}(t-\tau) \dot{\xi}_9(\tau) d\tau + \rho g S_2 \xi_9(t) \\ + \int_{-\infty}^t g_{r,93}(t-\tau) \dot{\xi}_3(\tau) d\tau + A_{93}(\infty) \ddot{\xi}_3(t) + f_{\text{PTO}} = f_{\text{exc},9}. \end{aligned} \quad (2.58)$$

It should be noted that Chapter 4 of the thesis elaborates on the generic approach in the frequency-domain, and it is also extended in the stochastic domain. No time-domain simulations were necessary at this stage of the project. Nevertheless, at a later stage, this approach would be necessary.

Modelling arrays of WECs

The same type of models used for the study of isolated devices, may be used for arrays of WECs, based on the focus of the research. Except for the historically important works on arrays described in Section 1.1.2, investigation on the array hydrodynamics has largely benefited from the advances in numerical modelling. A comprehensive review on the different types of modelling approaches for WEC arrays has been written by Folley et al. (2012). The authors identified approaches as follows: BIEM (e.g. WAMIT), semi-analytical methods, time-domain models, non-linear potential flow models, Bousinesq and mild-slope models, spectral models (SWAN), and CFD models. After comparing the different approaches, it was suggested that no single modelling technique would be appropriate for all scenarios, but that experimental validation would be necessary to select the best method for a given problem.

The work of Borgarino et al. (2012) studied arrays of cylinders oscillating in heave and barges oscillating in surge, organised in triangular and square configurations. The PTO damping was chosen to correspond with resonance conditions. The computations were undertaken for a realistic annual wave climate (Yeu Island, France). Very large PTO damping values were shown to limit the body's motion, and as a consequence of a poor match with its radiation damping, the power absorption was sub-optimal. They

used BIEM and contributed to the initial design stages of arrays, including the effect of separation distance. Arrays of triangular shape showed more promising results, due to their higher gain factor. Ning et al. (2018) presented a hybrid system of breakwater and oscillating bodies. The system was modelled using BIEM, and their results showed that the array would achieve higher gain factors when a pontoon system is considered.

Bossi et al. (2019) presented a model for investigating non-linear wave-body interaction, based on the depth-integrated Boussinesq equation. Results for a heaving WEC were validated using CFD and semi-analytical methods. Future work by the authors would aim to extend the current model to motion along more DoF.

Recently, optimisation algorithms have become popular for the design of WEC arrays. The optimum layout is found using a new algorithm, and accepted layouts are those which contribute to a gain factor slightly larger than 1 (Giassi and Götteman, 2018). However, a short-coming of this work is that the wave climate variability was not taken into consideration.

López-Ruiz et al. (2018) studied different array configurations for a wave climate in Spain, using a phase-averaged wave propagation model (SWAN). They also took the distance from the shore into account, which has a significant effect on operation and maintenance procedures.

2.13 Numerical modelling of mooring connections

The presence of the mooring system in a device may result in hydrodynamic interference between the moorings and the modes of operation of the WEC (Falcão, 2016). The scope of this thesis is to investigate the influence of the shared mooring configuration on the array hydrodynamics and the energetic performance. The mooring dynamics of WECs have been studied numerically through simplified models (quasi-static) (Gao and Moan, 2009, Vicente et al., 2009*a*) and non-linear models (Weller et al., 2017). Numerical modelling of the mooring system with different configurations should be undertaken at the initial stages of a project (Johanning et al. (2005, 2006), Vicente et al. (2009*a,b*)). Here, some methods for numerical modelling of mooring systems are described for completeness since the forthcoming chapters employ a simplified modelling method for the mooring configuration presented. For a comprehensive review on the numerical modelling of moorings the reader is directed to the paper of Davidson and Ringwood (2017).

Modelling the mooring connections can take place through different methods, depending on the stage of the WEC project, but also on the focus and direction of the research. A flowchart of the procedure undertaken when designing a mooring system has been suggested by Johanning et al. (2005), and is presented in Fig. 2.11. Johanning et al. (2005) suggested either the use of quasi-static or dynamic modelling, based on the

type of the configuration, for instance, for taut mooring configurations of a floating body, the tension characteristics of the mooring line will become non linear, due to the elastic properties of the material (Johanning and Smith, 2008a)

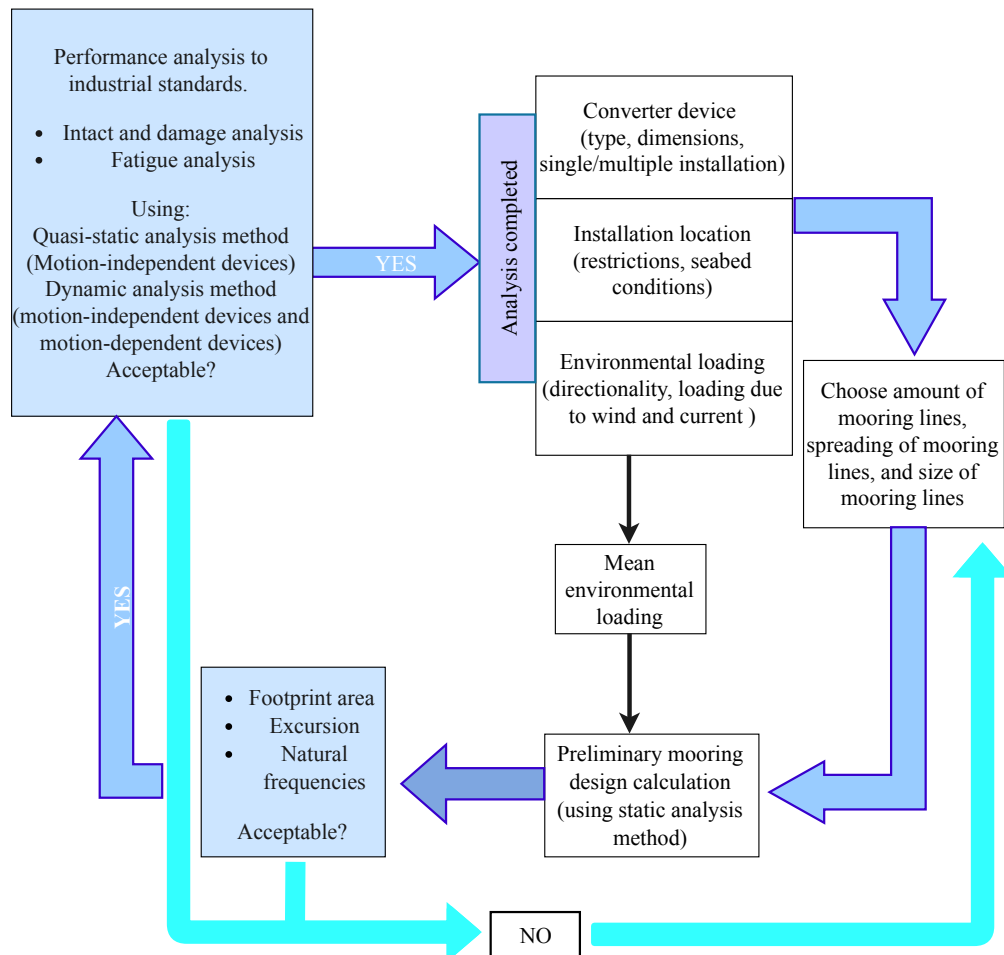


Figure 2.11: Flow chart for the procedure followed for mooring design. Redrawn from Johanning et al. (2005).

Especially during the initial design phase, it is important to understand the loads on a floating structure and its mooring system. In the case of current and wind loading, the loads will vary quite slowly, so for the purposes of dynamic analysis they may be considered constant, hence why they are neglected in the forthcoming chapters of this thesis.

2.13.1 Experimentally obtained mooring properties

Experimentally derived material properties are essential for modelling mooring line tension, since the mooring stiffness will affect the natural period, and will consequently alter the hydrodynamic response of the system. According to Johanning et al. (2007) and Bauduin and Naciri (1999), the relevant forces are: viscous damping, radiation damping, wave drift, and the damping from the mooring lines. In the initial studies

on mooring line dynamics, mooring line damping was not considered to be of great importance compared to the overall damping of a floating body. This changed after the contribution of Huse (1986) and Huse and Matsumoto (1988). More specifically, it was suggested that one point of the mooring line can have a much higher heave motion amplitude than the drift motion surge amplitude at the fairlead point. As a consequence, the mooring line can contribute to high damping in surge at lower frequencies, despite the small drag area of the mooring line. Free-decay tests can provide information on the mooring line damping (Faltinsen (1999), Vickers (2013), Harnois et al. (2014)).

Also the mooring line damping can be identified through the indicator diagram method Webster (1995) and Bauduin and Naciri (1999). Work by Johanning et al. (2007), presents experimental work on the determination of mooring line damping. The dynamics of a WEC model with a catenary mooring were investigated experimentally. The mooring line damping was determined using both approaches (free-decay tests and the indicator diagram). The results with the indicator diagram showed smaller spreading compared to the output from the free-decay tests. The damping changed with pre-tension, but nevertheless the results between the two approaches were not in close agreement. According to the indicator diagram method, with an increase in the pre-tension the damping should also increase, resulting in the line being fully lifted. This suggests that the system enters a taut mooring system state, since maximum displacement takes place. The elastic properties of the line are essential when the mooring line is lifted, because they will determine the mooring modelling approach used.

2.13.2 Quasi-static modelling

In quasi-static modelling, the solutions are solved in the frequency-domain, where the DoF of the WEC or array are accounted for. The restoring properties of the mooring system are introduced in the model as linear springs of a given stiffness (Fitzgerald and Bergdahl, 2008). Although this is a fast method, inertia of the mooring lines and the drag forces are not accounted for. This method should only be applied in the beginning of the project, and is not capable to account for extreme events. The mooring line damping may be neglected in this method. Brown and Mavrakos (1999) compared various numerical methods, and concluded that frequency-domain models are not appropriate for the cases where there is large motion of the cables.

Examples of this approach are presented in the work of Liu and Bergdahl (1998) and Bauduin and Naciri (1999). Bauduin and Naciri (1999) present a quasi-static model. For surge or sway the following relation applies if moorings were to be attached to a single body similar to the one presented in Section 2.12.1,

$$(-\omega^2(m_3 + A_{ii}) + i\omega(B_{ii} + B_{d,i}) + C_m)x_i = F_{exc,i}, \text{ for } i = 1, 2, \quad (2.59)$$

where A_{ii} is the added mass in surge or sway, B_{ii} is the radiation damping in mode i due to waves radiated along mode i . The term $B_{d,i}$ is the damping coefficient (which can

consist of the viscous damping and the mooring line damping), and C_m is the mooring line stiffness. According to Vickers (2013), the mooring line damping may be determined using Finite Element Analysis (FEA) or physical testing, by integrating the work done by top tension. The approach of Bauduin and Naciri (1999) may be applied, as long as it is reasonable to assume that friction of the seabed against the mooring line is negligible and the only significant drag forces are those that are perpendicular to the line. Morison's equation (Morison et al., 1950) may be used for calculating the drag force on a mooring line element dS

$$F_d = 0.5\rho_w A_{d,m} c_{d,m} |u - u_{dS}|(u - u_{dS}), \quad (2.60)$$

where ρ_w is the water density, $A_{d,m}$ is the mooring line drag diameter, $c_{d,m}$ is the drag coefficient, u is the fluid velocity in the plane that is perpendicular to the mooring line element under consideration, and u_{dS} is the velocity of the mooring line element. It should be noted that the drag coefficient from the above equation is usually not assessed based on Reynold's number or the KC number, but it is typically determined from experiments.

Quasi-static methods may also be utilised in the time-domain, where the mooring line forces and other forces on the WEC are modelled for each time instant (Vicente et al. (2011), Vicente (2016)), and the DoF of the WEC or array are accounted for. The mooring line damping may be taken into consideration, as well as its inertia.

A system with a reduced number of anchors was proposed by Ricci et al. (2012), where the authors adopted techniques from the aquaculture sector. Their system consists of a catenary mooring configuration with surface buoys and clump weights. Frequency-domain modelling was used during the initial design stages, whilst time-domain modelling was used to assess system survivability.

2.13.3 Dynamic analysis modelling

Dynamic models use a discretisation approach in order to describe the motion of the mooring lines and the forces on them (Thomsen et al. (2017), Palm and Eskilsson (2018)). Such models account for the inertial and damping effects of the mooring lines on the WEC, but they are computationally expensive.

A time-domain model with a focus on mooring lines was developed by Johanning and Smith (2008b) using OrcaFlex software. The results were validated against experimental output, and it was concluded that the mooring line tension of the experimental work was well-predicted by the time-domain model. The properties of the mooring system will contribute to a coupled response between the mooring line and the floating structure (WEC). The forces of the mooring system on the floating body are not only determined by the material properties of the mooring lines, but also by the type of environmental loading being applied on the structure. The sources of environmental loading are: the waves, the currents, and the wind (Det Norske Veritas (DNV), 2010). Also, the type of

seabed can be included in the analysis, since catenary mooring systems partly consist of chain, a portion of which constantly lies on the seabed. Based on the composition of seabed, the chain will behave differently. Wind and current loading can be treated as constant values (Bergdahl (2017) elaborates on this topic). For wave loading, the wave theories previously referred to in this thesis may be applied, depending on the stage of the project. Specifically regular waves may be used in the initial stages of system design, but ultimately irregular waves should be considered, as waves in nature are highly random.

The force of the mooring system on the floating body may be determined by dividing the lines into small segments and analysing them individually. Depending on the properties of the mooring lines, different adaptations to this approach will be made. For a simple mooring line, axial loading causes axial forces along the mooring line. In contrast, the axial tension in lines with complicated material properties or geometry (e.g. hollowed out moorings) could also be dependent on the strain rate of the pressure differential between the internal and external mooring structure. The axial stiffness (EA) describes the response of the mooring line to axial strain, and the Effective Tension (ET) is given by

$$ET = EA \underbrace{(L_{\text{ins}} - \lambda_{\text{ext}}L_0)/\lambda_{\text{ext}}L_0}_{\text{total mean axial strain}} + (1 - 2\nu)(p_{\text{ext}}A_{\text{ext}} - p_{\text{in}}A_{\text{in}}) + \frac{EA c_{d,m}}{L_0} \frac{dL_{\text{ins}}}{dt}, \quad (2.61)$$

where L_{ins} is the instantaneous length of the segment, λ_{ext} is the extension factor of the segment, L_0 is its unstretched length, ν is the Poisson ratio (which quantifies the lateral compression of a material when it is extended axially), p_{ext} is the external pressure, p_{in} is the internal pressure, $c_{d,m}$ is the damping coefficient of the mooring line, and $\frac{dL_{\text{ins}}}{dt}$ is the change in length per unit time. The terms A_{in} and A_{ext} are the internal and external cross sectional areas respectively.

In the case of modelling non-linear load extension, the relationship between load and strain may be defined by the user (e.g. in OrcaFlex). The axial stiffness may be determined from experiments, but when introducing it in a stochastic or frequency-domain model, it must be independent of time. Material properties such as bend stiffness for chains, may also be introduced in dynamic numerical models.

The mooring system hydrodynamics will depend on the weight, drag, added mass of the lines, as well as on the reaction forces from the floating bodies and clump weights, and possibly also on the wave excitation forces. Both lift and drag coefficients would ideally be taken into account, and may initially be estimated from the KC and Reynold's numbers, before being determined experimentally.

Palm et al. (2016) presented a method for analysing the non-linear aspects of WEC dynamics, which occur due to the interaction between the waves, the motion of the WEC, and the moorings. A cylindrical WEC was considered with three catenary moorings. The modelled hydrodynamics and mooring forces were validated against experimental results,

and were shown to be in close agreement. The modelling method was CFD, accounting for six DoF. The issue of snap loads was studied numerically by Palm et al. (2017). A shockwave was shown to build up in the mooring lines, possibly due to non-linear material properties. Another possibility is that these shockwaves resulted from their interaction with the seabed. But according to the authors, the main cause of snap load mooring failure is associated with the cable slack condition, where the load amplitude is dependent on the stiffness (Young's modulus) and local strain rate of the mooring line precisely as it becomes tensioned. Palm et al. (2017) suggested that with the Discontinuous Galerkin method, snap loads can actually be identified, which is also consistent with experimental results.

Chapter 3

Moored array of point absorbers

3.1 Introduction

This chapter follows the work presented in Vicente et al. (2009a). The deployment of arrays of Wave Energy Converters (WECs) requires knowledge on the hydrodynamic interference between individual devices, as it will influence the collective power absorption of all devices within the array. Interference between the devices is dependent on the separation between them, the size of the devices, and also the properties of the mooring system. It is suggested by Vicente et al. (2009a) that individual bodies should be connected to the bottom via slack moored connections, and that inter-body mooring lines should connect a group of devices to an additional weight that is submerged in the middle of the group. This array configuration has been previously suggested as a more economically viable option, compared to the standard mooring configuration modelled in the majority of studies (an individual device attached to the seabed by at least three mooring lines).

Depending on the array deployment location, the wave radiation characteristics of the devices, and the device separation distance, there may very well be other shared mooring configurations that could be better suited for a particular wave farm. Other potential array configurations are not explored in this thesis, because it was desired to build on an existing model with a well-established formulation. It has been suggested that the shared moored configuration proposed by Vicente et al. (2009a) would be more economical compared to conventional mooring systems, primarily due to the reduction in anchors needed to connect the mooring system to the seabed (WETFEEET D6.1, 2016). This type of shared mooring configuration has already been successfully adopted by the aquaculture industry in a fish farm deployment in the Gulf of Maine (Fredriksson et al., 2004). A potential limitation of this shared configuration involves the device separation distance: too great of a separation may decrease mooring line resilience to snap loads, whilst too small of a separation may cause too much unwanted interference between devices. As a first step in the mooring system design process, the hydrodynamic coupling between the devices in the array should be well understood.

The hydrodynamic model developed in this thesis is applied to a three body array in

a triangular configuration, connected to the seabed via slack moored lines and inter-body mooring connections, where a submerged weight pulls the three devices towards the centre of the array. Since the PTO system is assumed to be linear and only regular waves are examined, an analysis via frequency-domain modelling is permitted. Results of the oscillation amplitudes of the spherical bodies for intermediate water depths are presented. A sensitivity analysis is performed for the oscillation amplitudes of the bodies by changing various mooring characteristics (e.g. the stiffness of the bottom mooring line). In this way, the optimum configuration of mooring parameters is estimated, based on the response of the heave oscillation amplitude, which is essential for wave power absorption by the device.

Modelling of the dynamics of the triangular array of Spherical Point Absorbers (SPAs) closely follows the methodology of Vicente et al. (2009a), for a catenary mooring system. The same values are used for the radius of the spherical buoy, the spacing between the three bodies, and the mooring line parameters. The three devices are connected by means of inter-body mooring lines to a submerged Clump Weight (CW), as shown in Fig. 3.1.

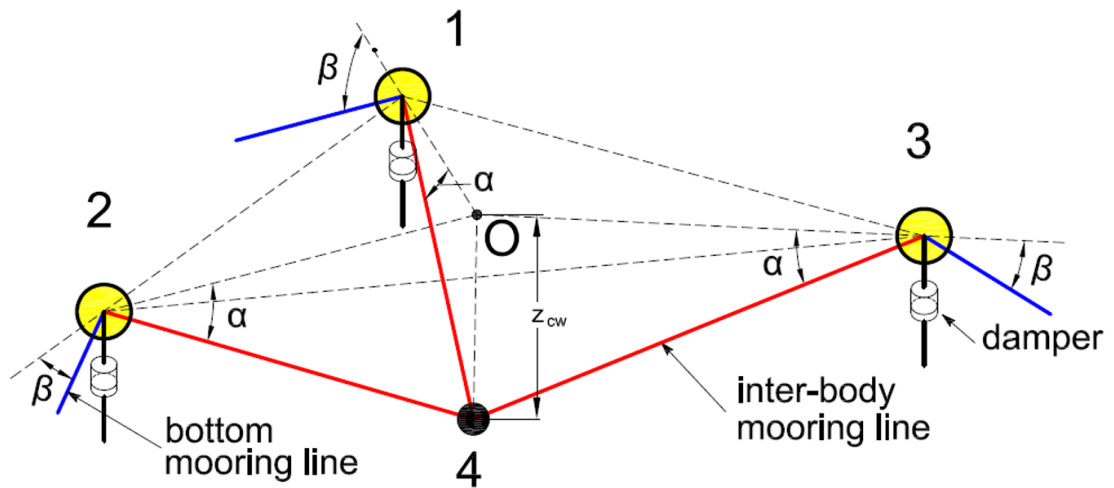


Figure 3.1: Three dimensional view of the array of SPAs, under calm sea conditions, along with inter-mooring connections and bottom mooring connections. The waves approach the three body array from left to right. Not to be scaled.

The hydrodynamic coefficients are calculated using the commercial BIEM tool WAMIT (2006), which is based on Green's function. By assuming linear wave theory and a linear system, the principle of linear superposition may be used. The radiation-diffraction problem is solved separately, providing the excitation force, the added inertia, and the radiation damping coefficient. The cross-terms resulting from the hydrodynamic coupling between an individual body's modes and from the coupling of modes between different bodies are taken into consideration.

3.2 Numerical model: spherical WECs

The numerical model presented in this chapter has been developed for frequency-domain analysis of a moored, triangular array of WECs. The model is linear, which permits the use of superposition to consider all relevant forces individually, before summing them together in Newton's Second Law. Linear water wave theory is considered, and any non-linearities in the system are either linearised or neglected altogether, when is reasonable to do so. The modelling approach makes the following assumptions:

- Incompressible and irrotational water flow.
- Wave amplitudes and body motions are much smaller than the typical wavelengths of incoming waves.
- All hydrodynamic forces, including coupling effects between the devices in the array, are linear.
- Linear approximations of quadratic drag forces when they are considered.

The inter-body mooring system studied here consists of mooring lines connected to a CW made of concrete. As in the original paper by Vicente et al. (2009a), the mooring lines are weightless and inelastic, and linear forces are applied by considering small perturbations around the rest position. The configuration of the array is illustrated in Fig. 3.1. Each of the devices is attached to the seabed via a bottom mooring line (highlighted in blue).

The horizontal distance from the centre each WEC to the centre of weight is denoted by L (if in a virtual triangle the length G of the inter-body mooring cable is the hypotenuse, the distance L would be the adjacent). Waves of various frequencies approach the array from left to right, in the positive x -direction (free surface plane view shown in Fig. 3.2). An angle α is generated between the inter-body mooring line and the free surface. The bottom mooring lines form an angle β with the free surface (as shown in Fig. 3.1). The clump weight is attached in the inter-body mooring lines, being in suspension. In this way the shared mooring lines are kept under constant tension. When no waves are acting on the structure, the clump weight is located at a depth z_{cw} . In the absence of waves, the centres of the buoys lie in the free surface plane, a distance L from the centre of the triangle and a distance $L\sqrt{3}$ apart from each other.

3.2.1 Equation of motion for the array

A top view of the array configuration, along with its mooring lines, is presented in Fig. 3.2, and a three-dimensional representation of the array can be seen in and in Fig. 3.1. The three buoys are labelled as Body 1 (SPA 1), Body 2 (SPA 2), and Body 3 (SPA 3), while the CW is labelled as Body 4. The origin of the fixed reference frame is located at the free surface, in the middle of the array. Regular waves propagate in the positive x -direction, with an amplitude A_w and a frequency ω . The motion of each device is

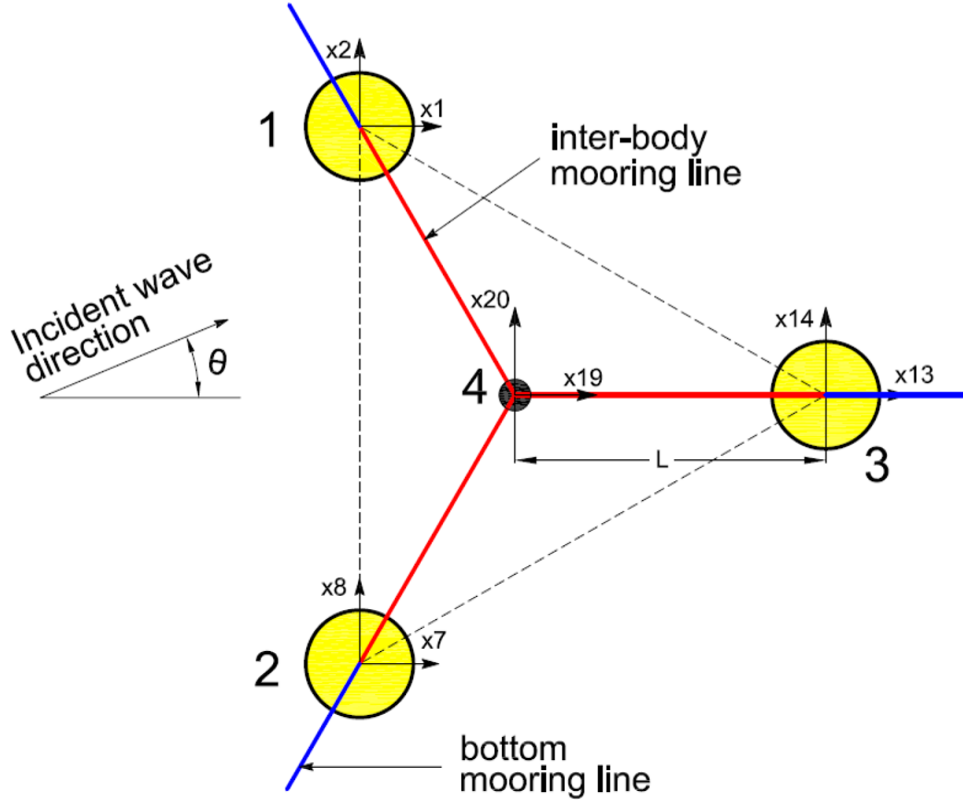


Figure 3.2: Top view of the array of spherical point absorbers, with bottom mooring and inter-body mooring connections.

defined by three translational DoF (surge, sway, and heave). The complex amplitudes of the DoF for SPA 1 are denoted by x_1 to x_3 , for SPA 2 by x_7 to x_9 , and for SPA 3 by x_{13} to x_{15} (as indicated in Fig. 3.2). Since the WECs are of spherical shape, rotational modes do not need to be considered.

The complex amplitudes of displacements x_{19} , x_{20} , and x_{21} refer to the translational oscillations of the clump weight. Table 3.1 summarises the symbols used for the displacements of the three spheres and the clump weight in three DoF. These motions are measured relative to a reference frame whose origin is located at the free surface in the centre of each device, with the same orientation as the fixed reference frame. A set of three equations is formulated for each SPA, corresponding to the three oscillating modes, expressed in the frequency-domain. The equations of motion may be written as:

$$m_b (-\omega^2 x_i) = F_{exc,i} + F_{rad,ij} + F_{hst,i} + F_{PTO,i} + F_{bm,i} + F_{im,i}, \quad (3.1)$$

where i and j refer to the mode being considered, and m_b represents the SPA mass. The term $-\omega^2 x_i$ corresponds to the acceleration complex amplitude of mode i . The terms in the right hand side of Eq. 3.1 represent the complex amplitudes of the forces acting on mode i , namely the wave excitation force $F_{exc,i}$, the radiation force $F_{rad,ij}$, the restoring hydrostatic force $F_{hst,i}$, the force due to the PTO damping $F_{PTO,i}$, the force

Table 3.1: Notation for the complex amplitudes of the displacements of the spherical point absorbers and the clump weight oscillating in three DoF. The rotational modes are not active.

Body	surge	sway	heave	roll	pitch	yaw
SPA 1	x_1	x_2	x_3	-	-	-
SPA 2	x_7	x_8	x_9	-	-	-
SPA 3	x_{13}	x_{14}	x_{15}	-	-	-
Clump weight	x_{19}	x_{20}	x_{21}	-	-	-

from the bottom mooring lines $F_{\text{bm},i}$, and the force from the inter-body mooring lines $F_{\text{im},i}$.

3.2.2 Hydrodynamic radiation and excitation coefficients

The radiation force complex amplitude $F_{\text{rad},ij}$ is given by:

$$F_{\text{rad},ij}(\omega) = - \left[-\omega^2 A_{ij}(\omega) + i\omega B_{ij}(\omega) \right] x_j, \quad (3.2)$$

where A_{ij} is the frequency-dependent added mass coefficient, due to the mass of fluid accelerated in mode i by the oscillatory motion of mode j , and B_{ij} is the frequency-dependent radiation damping coefficient, due to the damping affecting mode i caused by the generation of radiated waves from mode j . It should be noted that in the case where $i \neq j$, hydrodynamic coupling between modes i and j is being considered. This could represent interference between two different modes on the same body, the same mode on two different bodies, or even two different modes on two different bodies. The symbol i represents the imaginary unit ($i = \sqrt{-1}$).

The wave excitation force complex amplitude is:

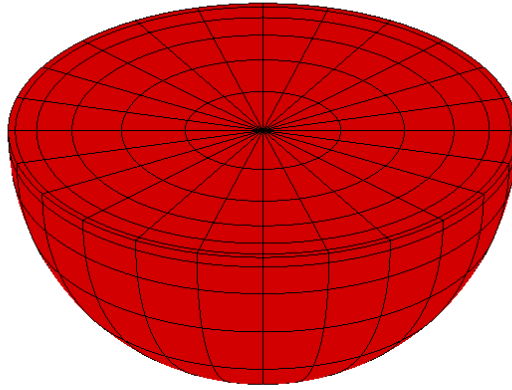
$$F_{\text{exc},i}(\omega) = A_w \Gamma_i(\omega). \quad (3.3)$$

where A_w is the incident wave amplitude and Γ_i represents the frequency-dependent wave excitation coefficient (force per unit wave amplitude). The hydrodynamics coefficients A_{ij} , B_{ij} and Γ_i (real and imaginary part) are computed using the BIEM (WAMIT, 2006) for a finite number of wave frequencies ω , making use of the higher order discretisation method, for a range of wave frequencies (Figs. 3.3a and 3.3b).

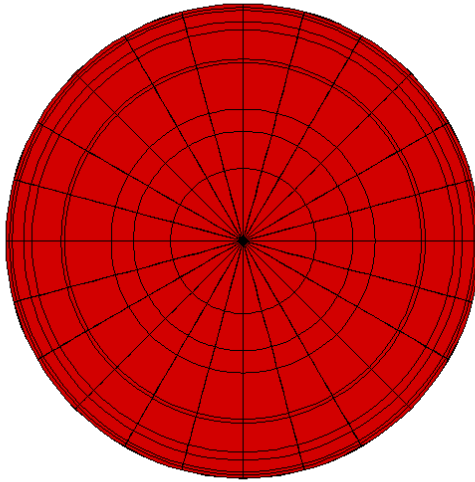
3.2.3 Hydrostatic coefficients

The hydrostatic force is considered in its linearised form:

$$F_{\text{hst},i} = -C_i x_j. \quad (3.4)$$



(a)



(b)

Figure 3.3: Mesh (3.3a) and top panel (3.3b) for the SPAs of the array used in the WAMIT calculations, higher-order discretisation method.

where C_i is the linear hydrostatic restoring coefficients from Archimedes' principle. For an axisymmetric device,

$$C_{ii} = \rho_w g S_b, \text{ for } i = 3, 9, 15, \quad (3.5)$$

where ρ_w is the water density, g is the acceleration of gravity, and S_b is the waterplane area of the buoy (SPA).

3.2.4 Linear PTO

A linear PTO is assumed in this case, constant for the range of wave frequencies. This is an idealised case, adapted from the work of Vicente et al. (2009a) and Vicente (2016). The PTO force is defined as:

$$F_{\text{PTO}} = -i\omega B_{\text{PTO}}x_i, \quad (3.6)$$

where the dimensionless damping coefficient B_{PTO}^* is given by

$$B_{\text{PTO}}^* = B_{\text{PTO}}\rho_w^{-1}\alpha^{-5/2}g^{-1/2}. \quad (3.7)$$

For these idealised cases, the value of the PTO damping can be determined via resonance conditions. This goes in line with Falnes words, "A good wave absorber must be a good wave maker" (Falnes, 1997).

3.2.5 Clump weight and inter-body mooring connections

The moorings consist of a three line system (1-4, 2-4, 3-4), connecting the three devices to the CW. All lines are considered to be attached to the centres of the buoys, and mooring line damping is neglected. Under calm sea conditions, the centre of clump weight (also defined as Body 4) is at a vertical position

$$z_{\text{cw}} = -\sqrt{G^2 - L^2}, \quad (3.8)$$

below the free surface, where G is the length of cables 1-4, 2-4, 3-4. The direction of propagation of incident waves forms an angle of θ with the x -axis, referred to as the angle of wave incidence. Variables x_{19} , x_{20} , and x_{21} correspond to the surge, sway, and heave oscillation amplitudes of Body 4 (see Table 3.1). The coordinates x_{19} , x_{20} , x_{21} of the clump weight depend on the instantaneous values of x_i for $i = \{1, 2, 3, 7, 8, 9, 13, 14, 15\}$ through linearised geometric relationships (Vicente et al., 2009a). Small wave amplitudes and small body motions are assumed throughout this study. The displacements of the three bodies in surge, sway, and heave are small compared to the distance L , and to the water depth h . The tension forces \bar{r}_1 , \bar{r}_2 , \bar{r}_3 correspond to the lines 1-4, 2-4, 3-4 and to the angles α_1 , α_2 , α_3 with the horizontal surface plane, and depend on the instantaneous positions of SPAs 1, 2, 3. In the absence of waves,

$$\alpha_1 = \alpha_2 = \alpha_3 = \alpha = \arctan(z_{\text{cw}}/L), \quad (3.9)$$

$$\bar{r}_1 = \bar{r}_2 = \bar{r}_3 = \bar{r}. \quad (3.10)$$

The tension force is

$$\bar{r} = (g/3)(m_{\text{cw}} - \rho_w v_{\text{cw}}) \csc \alpha, \quad (3.11)$$

where g is the acceleration due to gravity, m_{cw} is the mass of the clump weight, and v_{cw} is the volume of the clump weight. The virtual displacement is denoted by δx , and the real displacement is denoted by dx . The Virtual Work (VW) is given by

$$\text{VW} = \bar{r}_1 \cdot \delta x + \bar{r}_2 \cdot \delta x + \dots \stackrel{(\text{Eq. 3.11})}{\Rightarrow} \text{VW} = \bar{r} \cdot \delta x. \quad (3.12)$$

If a solid body is in balance then the sum of virtual work of the external forces acting on the solid body is 0 for every virtual displacement of the body:

$$\bar{r} \cdot \delta x = 0. \quad (3.13)$$

Therefore for every axis (x, y, z) , the inner product will be applied for SPA 3 and the CW

$$\bar{r} \cdot x_{\text{cw},x} + \bar{r} \cdot x_{\text{cw},z} - \bar{r} \cdot x_{\text{spa}_3,x} - \bar{r} x_{\text{spa}_3,z} = 0 \quad (3.14)$$

$$\Rightarrow \bar{r} x_{19} \cos \alpha + \bar{r} x_{21} \sin \alpha - \bar{r} x_{13} \sin \alpha - \bar{r} x_{15} \cos \alpha = 0 \quad (3.15)$$

$$\Rightarrow x_{19} - x_{13} + \frac{|z_{\text{cw}}|}{L} (x_{21} - x_{15}) = 0. \quad (3.16)$$

Similarly for SPAs 1 and 2, the following relations apply (Vicente et al. (2009a,b))

$$x_{19} - x_1 + \sqrt{3}(x_2 - x_{20}) + \frac{2|z_{\text{cw}}|}{L} (x_3 - x_{21}) = 0, \quad (3.17)$$

$$x_{19} - x_7 - \sqrt{3}(x_8 - x_{20}) + \frac{2|z_{\text{cw}}|}{L} (x_9 - x_{21}) = 0. \quad (3.18)$$

Based on the geometry of the array $z_{\text{cw}} = G \sin \alpha$. Taking the derivative with respect to α , and considering the parameters r_j, ε_j , as the perturbations to the calm sea values \bar{r}, α :

$$\varepsilon_j = \frac{x_j - x_{21}}{G} \sec \alpha, \quad (3.19)$$

where in this case $j = \{3, 9, 15\}$. The projections of the lines 1-4, 2-4, 3-4, relative to each body, onto the horizontal plane form the angles $\delta_1 - \pi/3$, $\delta_2 + \pi/3$, $\delta_3 + \pi$ (Vicente et al., 2009a). The length of an arc is equal to the angle times the radius ($\delta S = \delta \cdot L$). By considering the projections (in two axes: x, y , as z is out of the studied surface) of the displacements $(x_{19} - x_1)$, $(x_{20} - x_2)$, $(x_{19} - x_7)$, $(x_{20} - x_8)$, and $(x_{14} - x_{20})$ on δS yields

$$\delta_1 = \frac{\sqrt{3}}{2L} (x_{19} - x_1) + \frac{1}{2L} (x_{20} - x_2), \quad (3.20)$$

$$\delta_2 = -\frac{\sqrt{3}}{2L} (x_{19} - x_7) + \frac{1}{2L} (x_{20} - x_8), \quad (3.21)$$

$$\delta_3 = \frac{1}{L} (x_{14} - x_{20}). \quad (3.22)$$

The CW oscillates only in three DoF: surge, sway, and heave, and due to the geometry of its spherical shape, the rotations do not need to be considered. The equations of motion for the clump weight are included in the formulation to account for its dynamic behaviour. Therefore, it is subject to the inertia of the weight m_{cw} , the frequency-dependent hydrodynamic added masses $A_{\text{cw,hr}}$ and $A_{\text{cw,z}}$, the radiation damping coefficients $B_{\text{cw,hr}}$

and $B_{cw,z}$, the damping coefficient due to drag induced by the fluid on the weight, $B_{cw,d}$, but also to the excitation force $F_{cw,exc}$ and the inter-body mooring force $F_{im,i}$ for $i = \{19, 20, 21\}$. The parameters $A_{cw,hr}$ and $A_{cw,z}$ represent the horizontal and heave added mass coefficient of the clump weigh, and are denoted by subscripts h and z , respectively. The clump weight is assumed to have spherical geometry, therefore the added mass is the same for the horizontal and vertical modes, and was calculated as $A_{cw} = (2/3)\rho_w\pi a_{cw}^3$, where a_{cw} is the radius of the sphere. This corresponds to the added mass of an accelerating sphere in an unbounded fluid (Richardson, 1989). The equation of motion for the clump weight in the three modes, neglecting the terms that are zero is

$$[-\omega^2(m_{cw} + A_{cw}) + i\omega B_{cw}]x_j = F_{exc,cw,i} + F_{im,i}, \quad (3.23)$$

for $j = 19, 20, 21$, where the term $F_{exc,cw,i}$ corresponds to the excitation force due to the wave action in mode i . The forces $F_{im,j}$ are the forces the clump weight experiences due to the inter-body mooring connections with the three buoys, and are written as

$$F_{im,19} = \bar{r} \frac{\sqrt{3}}{2} (\delta_2 - \delta_1) \cos \alpha + \bar{r} \frac{\sin \alpha}{2} (\varepsilon_1 + \varepsilon_2) - \frac{\cos \alpha}{2} (r_1 + r_2) - \bar{r} \varepsilon_3 \sin \alpha + r_3 \cos \alpha, \quad (3.24)$$

$$F_{im,20} = -\bar{r} (\delta_1 + \delta_2) \frac{\cos \alpha}{2} + R \frac{\sqrt{3}}{2} (\varepsilon_2 - \varepsilon_1) \sin \alpha + \frac{\sqrt{3}}{2} (r_1 - r_2) \cos \alpha + \bar{r} \delta_3 \cos \alpha, \quad (3.25)$$

$$F_{im,21} = \bar{r} (\varepsilon_1 + \varepsilon_2 + \varepsilon_3) \cos \alpha + (r_1 + r_2 + r_3) \sin \alpha. \quad (3.26)$$

The individual terms representing the forces associated with the inter-body mooring connections for the three buoys are only associated with the three modes x_{19} , x_{20} , x_{21} , and are expressed as

$$F_{im,1} = r_1 \frac{\cos \alpha}{2} + \bar{r} \frac{\sqrt{3}}{2} \delta_1 \cos \alpha - \bar{r} \varepsilon_1 \frac{\sin \alpha}{2}, \quad (3.27)$$

$$F_{im,2} = -r_1 \frac{\sqrt{3}}{2} \cos \alpha + \bar{r} \delta_1 \frac{\cos \alpha}{2} + \bar{r} \frac{\sqrt{3}}{2} \varepsilon_1 \sin \alpha, \quad (3.28)$$

$$F_{im,3} = -\bar{r} \varepsilon_1 \cos \alpha - r_1 \sin \alpha, \quad (3.29)$$

$$F_{im,7} = r_2 \frac{\cos \alpha}{2} - \bar{r} \frac{\sqrt{3}}{2} \delta_2 \cos \alpha - \bar{r} \varepsilon_2 \frac{\sin \alpha}{2}, \quad (3.30)$$

$$F_{im,8} = r_2 \frac{\sqrt{3}}{2} \cos \alpha + \bar{r} \delta_2 \frac{\cos \alpha}{2} - \bar{r} \frac{\sqrt{3}}{2} \varepsilon_2 \sin \alpha, \quad (3.31)$$

$$F_{im,9} = -\bar{r} \varepsilon_2 \cos \alpha - r_2 \sin \alpha, \quad (3.32)$$

$$F_{im,13} = -r_3 \cos \alpha + \bar{r} \frac{\sqrt{3}}{2} \delta_3 \cos \alpha + \bar{r} \varepsilon_3 \sin \alpha, \quad (3.33)$$

$$F_{im,14} = -\bar{r} \delta_3 \cos \alpha, \quad (3.34)$$

$$F_{im,15} = -\bar{r} \varepsilon_3 \cos \alpha - r_3 \sin \alpha. \quad (3.35)$$

3.2.6 Bottom mooring line forces

Bottom mooring lines are attached to each device (Fig. 3.2). The tensions $\bar{f}_1, \bar{f}_2, \bar{f}_3$ from the bottom mooring lines at the fairlead form an angle denoted by β with the horizontal plane, which is assumed to be unaffected by the bodies' motions. In the absence of waves: $\bar{f}_1 = \bar{f}_2 = \bar{f}_3 = \bar{f}$. The bottom mooring tension \bar{f} is related to the inter-body line tension \bar{r} (applied on the lines 1-4, 2-4, 3-4) by

$$\bar{f} = \bar{r} \cos \alpha / \cos \beta. \quad (3.36)$$

The perturbation to the calm sea value \bar{f}_j is denoted by f_j , for $j = 1, 2, 3$ (for each bottom line). The forces applied on the three devices, due to the presence of the bottom mooring lines, are

$$F_{\text{bm},1} = -\frac{\cos \beta}{2} f_1, \quad (3.37)$$

$$F_{\text{bm},2} = \frac{\sqrt{3}}{2} \cos \beta f_1, \quad (3.38)$$

$$F_{\text{bm},3} = -\sin \beta f_1, \quad (3.39)$$

$$F_{\text{bm},7} = -\frac{\cos \beta}{2} f_2, \quad (3.40)$$

$$F_{\text{bm},8} = -\frac{\sqrt{3}}{2} \cos \beta f_2, \quad (3.41)$$

$$F_{\text{bm},9} = -\sin \beta f_2, \quad (3.42)$$

$$F_{\text{bm},13} = \cos \beta f_3, \quad (3.43)$$

$$F_{\text{bm},14} = 0, \quad (3.44)$$

$$F_{\text{bm},15} = -\sin \beta f_3. \quad (3.45)$$

The equations representing the bottom mooring forces are identical to those presented in Vicente et al. (2009a). These forces were originally introduced by Fitzgerald and Bergdahl (2008), where the authors explained the linear approximation of such forces, and their dependence on the static condition of the cable, as well as on the frequency and respective amplitude of the device motions. The attachment angle β - the angle formed between the horizontal surface plane and the bottom mooring cables on SPAs 1, 2, 3 - is based on the assumption that it remains constant, which is valid only for the case where the length of each bottom mooring line is much greater than the displacements of the bodies. The extensions ϕ_j of mooring line j ($j = 1, 2, 3$) due to displacements of each body j are

$$\phi_1 = (x_1 - \sqrt{3}x_2) \frac{\cos \beta}{2} + x_3 \sin \beta, \quad (3.46)$$

$$\phi_2 = (x_7 + \sqrt{3}x_8) \frac{\cos \beta}{2} + x_9 \sin \beta, \quad (3.47)$$

$$\phi_3 = -x_{13} \cos \beta + x_{15} \sin \beta. \quad (3.48)$$

For the perturbation f_j to the mooring force \bar{f}_j , the following dynamic formula in the frequency domain applies

$$[-\omega^2 A_{\text{bm}} + i\omega B_{\text{bm}} + C_{\text{bm}}] \phi_j = f_j, \quad (3.49)$$

where the terms $-\omega^2 A_{\text{bm}} \phi_j$, $i\omega B_{\text{bm}} \phi_j$, and $C_{\text{bm}} \phi_j$ are perturbation forces representing the inertia, linear damping and spring effect introduced by the bottom mooring cable j (for $j = 1, 2, 3$), respectively.

3.3 Numerical model: cylindrical WECs

The numerical model presented in Section 3.2 is modified accordingly to apply for arrays of Cylindrical Point Absorbers (CPAs), oscillating in six DoF. In Fig. 3.4, a three-dimensional representation of the array can be seen. For consistency with the previous section, the three CPAs are labelled as CPA 1, CPA 2 and CPA 3, while the CW is Body 4.

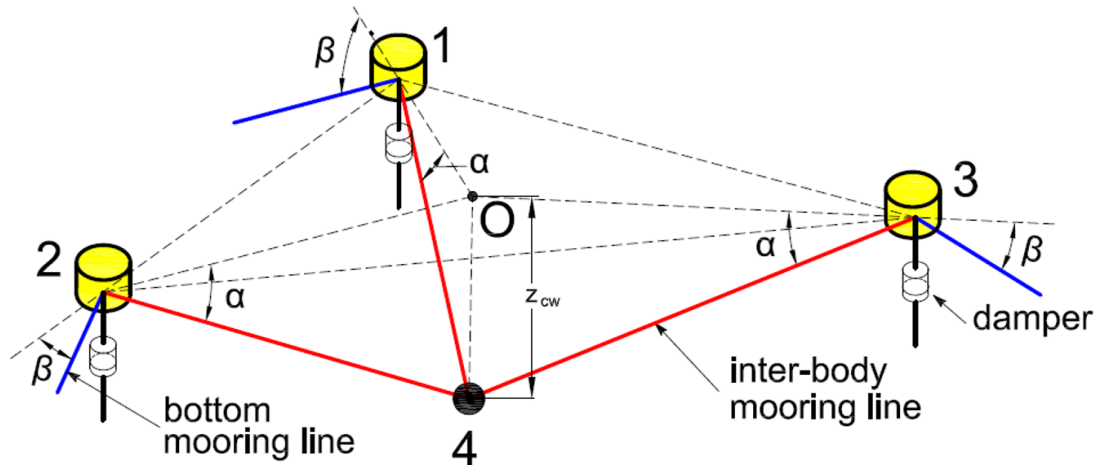


Figure 3.4: Three dimensional view of the array of cylindrical WECs, under calm sea conditions, along with inter-mooring connections and bottom mooring connections. The waves approach the three body array from left to right.

3.3.1 Equation of motion for the array

The origin of the fixed reference frame is located at the free surface, in the middle of the array. Regular waves propagate with the x -axis direction with an amplitude A_w and a frequency ω . The motion of each device is defined by six DoF, three translational (surge, sway, and heave) and three rotational (roll, pitch, and yaw). The complex amplitudes of the DoF for CPA 1 are denoted by x_1 to x_6 , for CPA 2 by x_7 to x_{12} , and for CPA 3 by x_{13} to x_{18} (as indicated in Fig. 3.2). The complex amplitude of displacements x_{19} , x_{20} , and x_{21} refer to the translational oscillations of the CW. The notations for the three CPAs and the CW are summarised in Table 3.2.

Table 3.2: Notation for the complex amplitudes of the displacements of the cylindrical point absorbers oscillating in six DoF, and the clump weight oscillating in three DoF.

Body	surge	sway	heave	roll	pitch	yaw
CPA 1	x_1	x_2	x_3	x_4	x_5	x_6
CPA 2	x_7	x_8	x_9	x_{10}	x_{11}	x_{12}
CPA 3	x_{13}	x_{14}	x_{15}	x_{16}	x_{17}	x_{18}
Clump weight	x_{19}	x_{20}	x_{21}	-	-	-

A set of equations is formulated for each WEC corresponding to the six oscillating modes. The equations of motion used for spheres (Eq. 3.1) will be modified as follows

$$M_{ij}(-\omega^2 x_j) = F_{\text{exc},i} + F_{\text{rad},ij} + F_{\text{hst},i} + F_{\text{pto},i} + F_{\text{d},i} + F_{\text{bm},i} + F_{\text{im},i}, \quad (3.50)$$

where M_{ij} represents the inertia matrix. The terms are the same as in the equation of motion for the array of SPAs, but in this case a drag force F_{d} will be introduced, and instead of the mass of the CPA, an inertia matrix will be considered, given by (Newman, 1977)

$$M_{ij} = \begin{bmatrix} m_{\text{b}} & 0 & 0 & 0 & m_{\text{b}}z_{\text{g}} & 0 \\ 0 & m_{\text{b}} & 0 & -m_{\text{b}}z_{\text{g}} & 0 & 0 \\ 0 & 0 & m_{\text{b}} & 0 & 0 & 0 \\ 0 & -m_{\text{b}}z_{\text{g}} & 0 & I_{44} & 0 & I_{46} \\ m_{\text{b}} & 0 & 0 & 0 & I_{55} & 0 \\ 0 & 0 & 0 & I_{46} & 0 & I_{66} \end{bmatrix}, \quad (3.51)$$

where m_{b} is the buoy mass (CPA mass) and z_{g} is the z -coordinate of the centre of gravity. The terms I_{44} , I_{55} , I_{66} correspond to the moments of inertia of the buoy about the x , y , and z axes of each buoy referential, aligned with the fixed reference frame. The same equations were considered for the forces as in the section of the SPA array (Eqs. 2.35, 3.3, and 3.6). Regarding the mooring system, the formulations presented in Sections 3.2.5 and 3.2.6 will apply. Therefore, the only modifications in the model are the updated hydrostatic restoring hydrostatic force and the drag force.

3.3.2 Hydrostatic coefficients

The hydrostatic force is considered in its linearised form in the same manner as Eq. 3.4, however, rotational modes are taken into consideration as well, for which, we assume small amplitude angles so that $\sin x_j \approx x_j$ for $j = 4, 5, 6$. For an axisymmetric device, C_{ii} has non-zero values for heave, roll and pitch,

$$C_{ii} = \rho_{\text{w}}gS_{\text{b}}, \text{ for } i = 3, 9, 15, \quad (3.52)$$

$$C_{ii} = \rho_{\text{w}}g\overline{VGM}, \text{ for } i = 4, 5, 10, 11, 16, 17, \quad (3.53)$$

where ρ_w is the water density, g is the acceleration of gravity, and S_b is the waterplane area of the buoy. The parameter V is the buoy's displaced water volume, and \overline{GM} is the buoy metacentric height given by

$$\overline{GM} = \frac{S_b}{V} + z_b - z_g, \quad (3.54)$$

where z_b is the z -coordinate of the centre of buoyancy. This is very important for the stability of a floating body and it is defined as the distance between the centre of gravity and the metacentre. Note that the metacentric theory is valid only for small angles of motion. By analysing the sign of the metacentric height, the stability of the body may be assessed (i.e. if $\overline{GM} > 0$, the body's equilibrium is stable, if $\overline{GM} < 0$, the body's equilibrium is unstable, and if $\overline{GM} = 0$, the body is neutral).

A great metacentric height would imply higher stability against overturning (Fig. 3.5). If the metacentric height is set to 0, the results for the RAOs will be identical to those as if only three DoF were considered (surge, sway, and heave). Nevertheless, this would be an unrealistic case for the cylindrical point absorbers. In addition, the influence of the pitch mode on the hydrodynamics of the WEC and the array of WECs is not negligible, as it is coupled with surge.

3.3.3 Cylindrical point absorbers: viscous damping

The viscous damping is included also in the equation of motion in surge and heave only, in its linearised form, based on Morison's equation (Morison et al., 1950). To maintain consistency with the linear model, the non-linear viscous drag force under regular waves (proportional to the square of the velocity) is approximated with a linear force by using only the first harmonic of the Fourier series (Gomes et al. (2016), Chakrabarti (1984), Terra et al. (2005)). The complex amplitudes of the linearised drag forces in surge ($i = 1, 7, 13$) are given by

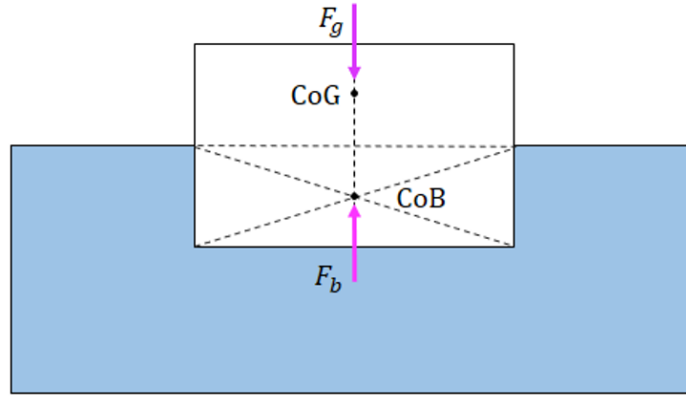
$$F_{d,i} = -i\omega B_{d,i} x_i, \quad (3.55)$$

where the linear damping coefficient is

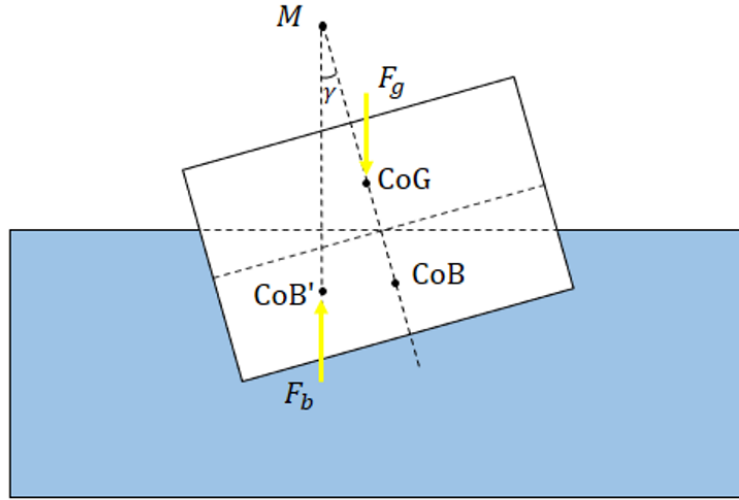
$$B_{d,i} = \frac{1}{2} \rho_w A_{d,i} c_{d,i} \left(\frac{3\pi}{8} \left| i\omega x_i^{(e)} \right| \right). \quad (3.56)$$

Here $A_{d,1}$ is the drag area (for $i = 1, 7, 13$) for the normal direction, and $c_{d,i}$ is the drag coefficient for the normal direction in surge. The term in parenthesis in Eq. 3.56 represents the linear approximation of the quadratic drag force. The term $x_i^{(e)}$ represents the estimated value of x_i . Since x_i is the solution of the system of equations presented in Eq. 3.50, these values require an iterative calculation.

For the computation of the drag forces in heave, viscous drag effects are taken into account, which apply to the buoy's drag inducing surface, and are proportional to the relative velocity between the buoy and the water flow. The complex amplitudes of the



(a)



(b)

Figure 3.5: The body in still water force equilibrium (3.5a) and righting moment (3.5b).

linearised drag forces in heave ($i = 3, 9, 15$) are given by

$$F_{d,i} = -B_{d,i}(\omega x_i - u_z), \quad (3.57)$$

where z is the z -coordinate of the drag surface, u_z is the complex amplitude of the velocity component aligned with the z -axis,

$$u_z = \frac{igkA_w \sinh[k(h+z)]}{\omega \cosh kh} e^{[-ik(x \cos \theta + y \sin \theta)]}, \quad (3.58)$$

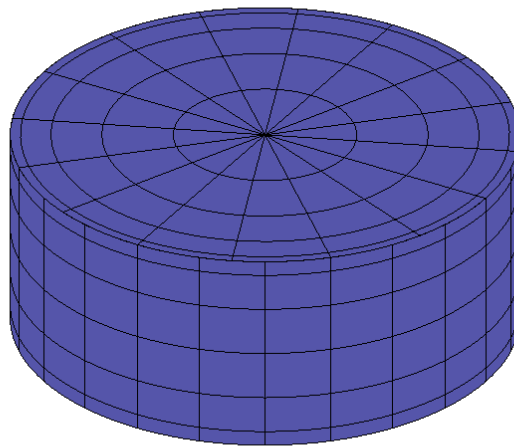
where k is the wavenumber and h is the water depth. The velocity u_z is taken at the position (x, y) of the axis of the corresponding device at rest. The heave drag damping term is given by

$$B_{d,i} = \frac{1}{2} \rho_w c_{d,3} A_{d,3,n} \left(\frac{3\pi}{8} \left| \omega x_i^{(e)} - u_z \right| \right), \quad (3.59)$$

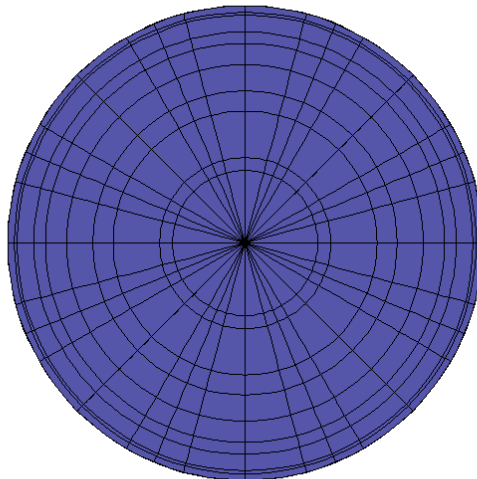
where $c_{d,i}$ is the heave drag coefficient of the buoy and $A_{d,3}$ is the area normal to the drag inducing surface, $i = 3, 9, 15$.

Cylindrical point absorber characteristics

Each CPA consisted of a steel structure enclosing a concrete ballast. The diameter and the draught for the CPAs were set to 12 m and 5 m respectively. The grid introduced in WAMIT for the cylinders can be seen in Figs. 3.6a and 3.6b. The CoG was set far from the CoB, to increase the metacentric height \overline{GM} . The moments of inertia were calculated with the aid of SW. The physical properties of the cylinders are presented in Table 3.3.



(a)



(b)

Figure 3.6: Mesh (3.6a) and top panel (3.6b) for the CPAs of the array used in the WAMIT calculations, with higher-order discretisation method.

Table 3.3: Cylindrical point absorber, physical properties.

Parameter	Value
Buoy diameter d (at $z = 0$) [m]	12.00
Draught l_t (unmoored) [m]	5.00
Mass m [kg]	573343.97
Moment of inertia I_{55} ($= I_{44}$) [kg m ²]	21.14×10^6
Moment of inertia I_{66} [kg m ²]	11.32×10^6
CoG z -coordinate z_g [m]	-4.7
CoB z -coordinate z_b [m]	-2.5
Metacentric height \overline{GM} [m]	4.0

3.4 Results: array of spherical point absorbers

The radius and the draught of the modelled SPA were 7.5 m and 7.5 m respectively. Waves were restricted to approach the array from left to right, with an incidence angle of 0. In other words, the three body array was positioned so that the horizontal plane projection of the mooring line connecting the submerged CW and SPA 3 was parallel to the direction of wave propagation. The calculations were performed for intermediate water depths (in terms of wave energy conversion), $h = 60$ m. The hydrodynamic coefficients of the three spheres in the array, as well as the excitation forces acting upon them, have been obtained using WAMIT. The output of the frequency-domain model (i.e. added mass, radiation damping coefficient, and excitation force) were obtained in dimensionless form, and converted to dimensional quantities for the purpose of this study. The amplitude of the incoming waves A_w was set 1 m. The displacement of the modelled devices was calculated taking into account the influence of the mooring lines. These displacement calculations have been performed in the Python environment, making use of the mathematical relations presented in this chapter. The non-dimensional damping coefficient of the PTO was of magnitude 10^{-1} , where this value was adopted from the original bibliographic references (Vicente et al., 2009*a,c*).

In the horizontal plane, the distance between the CW and each of the point absorbers was set to $L = 30$ m. The density of the weight was set to $\rho = 2500$ kg/m³, which is a good estimate for concrete material. The weight was also placed relatively far from the sea surface, thus the excitation force acting upon it was negligible (i.e. $f_{d3x} = f_{d3z} = 0$). The mass of the weight was set to 5% percent of the mass of the device. The viscous damping and radiation damping, as well as the inertia of the bottom-mooring cables were neglected.

3.4.1 Resonance frequency

The Response Amplitude Operators (RAOs) of the system are presented, these refer to the ratio between the amplitudes of the modes of interest (3 DoF for the spheres) and the incident wave amplitude A_w . The results are presented as a function of the incident wave frequency ω . The dashed vertical lines in Figs. 3.7 and 3.12 indicate the system's natural frequencies in heave. The natural frequency of heave mode i is

$$\omega_{n,i} = \left(\frac{\rho_w g S_b}{m_{ii} + A_{ii}(\omega)} \right)^{1/2}, \quad (3.60)$$

for $i = 3, 9, 15$. This is the frequency at which maximum power extraction may be achieved, provided that the PTO damping is set equal to that of the absorbing medium (Falnes, 1999). Furthermore, if an excitation is applied on a body in a wave tank whose free surface is initially at equilibrium, the body will undergo some free oscillations that decay in amplitude with time. The frequency of these decaying oscillations is known as the damped frequency, which, in water, is a close approximation to the body's natural frequency or resonance frequency. It is at this resonance frequency that the body's excitation in response to an incoming wave is greatest, and it is the best operating point when it comes to wave energy conversion. The resonance frequency for the sphere was estimated to be 1.174 rad/s.

Isolated spherical point absorber

First, the case of an isolated device is examined. This way, one can understand the hydrodynamics of a single device operating in isolation, without the added influence of other devices or mooring. The hydrodynamics of a single hemisphere have been discussed in Hulme (1982). Various values of the PTO damping coefficient were examined. The dimensionless heaving RAO for the sphere in its isolated and unmoored form is illustrated in Fig. 3.7. This is the oscillation displacement amplitude divided by the wave amplitude A_w . The RAO is also velocity, but phase shifted by 90° and scaled by ω . The damping coefficient B_{PTO} was selected after considering resonance conditions. The effect of viscous drag on the device was not taken into consideration.

Fig. 3.7 presents the heave RAO of the spherical buoy against the wave frequency ω , for different values of the PTO damping. For very low wave frequencies (high periods), the oscillation amplitude tends to be the same as the wave amplitude A_w . Ideally, the PTO damping should match the total damping of the system (Falnes, 1999). Doing so would maximise the PTO power which is equal to its reaction force times the velocity of the absorbing medium (as seen from the inertial reference frame of the PTO). According to the maximum power transfer theorem, resonance needs to occur and the total damping of the network (i.e. the absorbing medium) should be equal to that of the PTO. The higher the PTO damping is set from the optimal value, the more its reaction force will increase, at the price of a proportionally greater decrease in the absorbing body's velocity, decreasing the power extracted. And by decreasing the PTO damping, the velocity of the

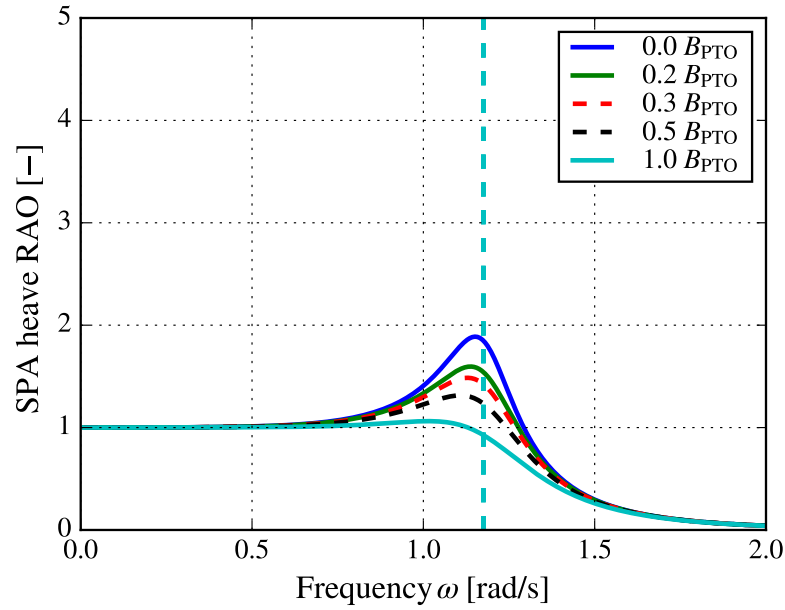


Figure 3.7: Heave RAO for an isolated SPA, against the wave frequency ω , for $A_w = 1$ m, and various PTO damping values. The value $1.0 * B_{PTO}$ corresponds to the optimum PTO value. The dotted vertical line corresponds to the body's resonance frequency.

absorbing body will increase but the PTO reaction force will decrease by a proportionally greater amount, also reducing the power extracted. For demonstration purposes in this chapter, only 20% of the optimal PTO damping is considered, so that the location of the resonance frequency can be made clearer to the reader.

Moored array of spherical point absorbers

SPAs 1 and 2, demonstrate the same hydrodynamic behaviour for an angle of wave incidence of 0, so from this point they will be referred to as SPA 1,2. In this section, first the influence of the array effect on the hydrodynamic coefficients and the excitation force amplitudes is examined (Fig. 3.8). The calculations for the isolated sphere are also presented to provide comparison perspective. Figs. 3.8a and 3.8b illustrate the added mass in surge and heave, respectively. By setting the devices in an array configuration, oscillations appear in their added masses. The oscillations are the same for all three bodies in the heave mode, but are slightly different in the surge mode. The exact same effect can be observed in the radiation damping in surge and heave (Figs. 3.8c and 3.8d), but also for the excitation force amplitude in these two modes (Figs. 3.8e and 3.8f). The effect of the oscillations appearing in the hydrodynamic coefficients and the excitation force amplitudes in wave frequencies higher than 1 rad/s, is due to the array interference, and it is subject to the size of the devices, and the array spacing. Such effects have been visible in previous works on arrays (e.g. Gomes et al. (2016), Borgarino et al. (2012)). If the SPAs were placed far apart, they would operate independently and it is likely this kind of harmonics would not appear. Nevertheless, it is important to understand the effect of mesh refinement on the presented results. Variation of the number of panels, for the SPAs of the array, suggested no effect on the hydrodynamic coefficients and the excitation force amplitudes. Appendix A presents the studied meshes for the SPAs.

The result shown in Fig. 3.9 is less intuitive. The individual bodies of the array experience intra-array coupling between the surge and heave modes. This effect is not present in the case of a single body, but it should be related to the array interference which is strongly influenced by the array spacing.

The next set of graphs presents the RAOs for the three SPAs, against the wave frequency ω for the unmoored and moored array cases. The results of the isolated case are also plotted, to provide comparison perspective. For the unmoored array, due to the array interference, minor surge oscillations were visible for SPA 1,2, but not for SPA 3, highlighted in light purple (Fig. 3.10). SPAs 1,2 also demonstrate some sway oscillations, which are not visible for SPA 3 (Fig. 3.11). As for the heave RAOs, for SPAs 1,2, the RAO appears to increase, but also the peak shifts towards lower frequencies, further from the isolated sphere's resonance frequency, after setting the SPAs in an array configuration (Fig. 3.12). Some mild oscillations can be seen in high frequencies, highlighted in light purple, due to the array interference. It seems from the resonances appearing in the heave RAO at high frequencies, that hydrodynamic coupling between surge and sway affects the heave oscillation amplitude. The heave RAO of SPA 3 is smaller compared to the other two buoys, and to the isolated case, due to its location.

It seems that the surge RAOs for SPAs 1,2 and SPA 3, are not affected after the inclusion of the mooring system, in the range of wave frequencies 1 – 2 rad/s (Fig. 3.10).

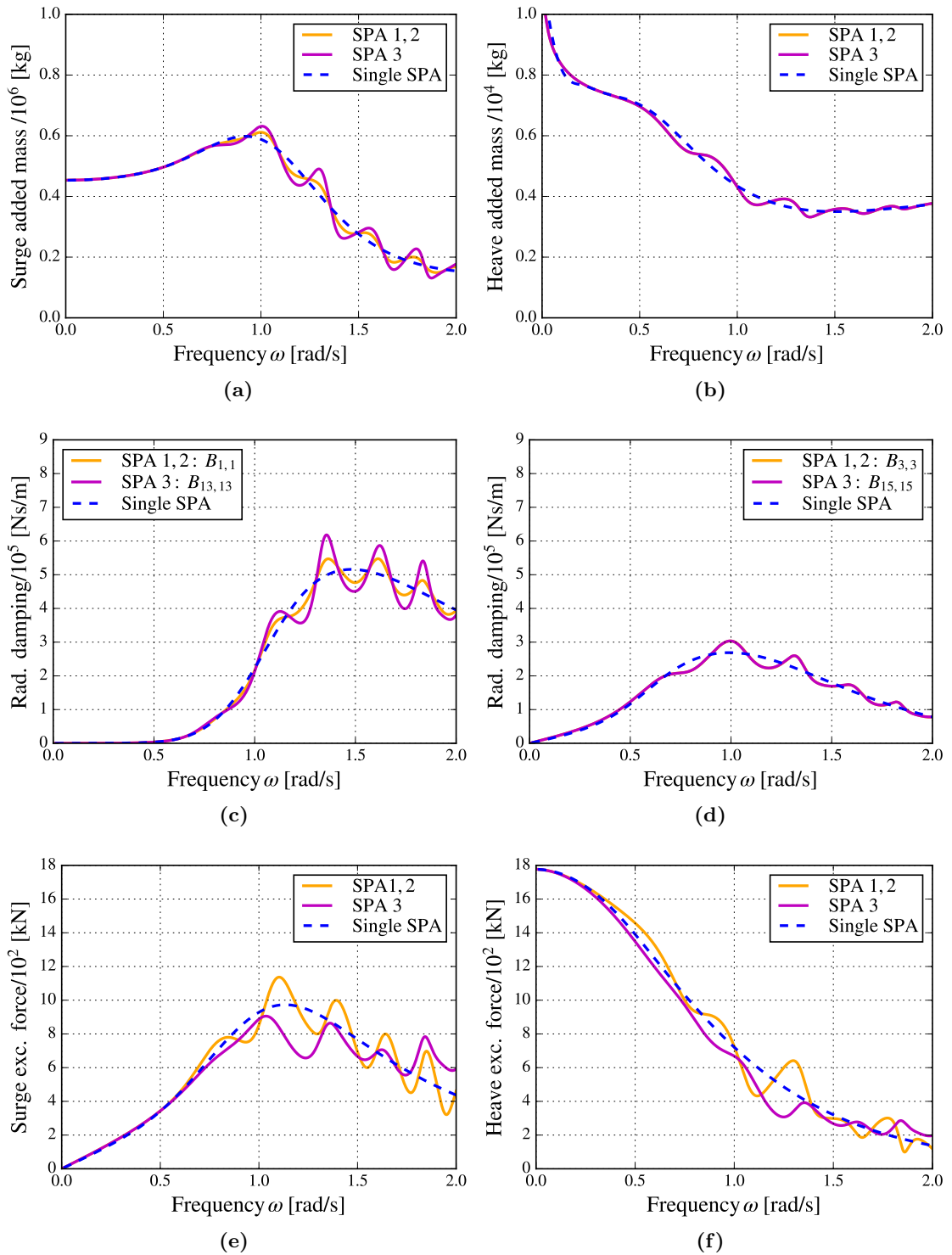


Figure 3.8: Hydrodynamic coefficients for the three spheres in surge (Figs 3.8a, 3.8c), and heave (3.8b, 3.8d), as a function of the wave frequency ω . Excitation force amplitudes for the three spheres in surge and heave (3.8e, 3.8f) as a function of the wave frequency ω , for $A_w = 1$ m, $\theta = 0$. These values were calculated by the BIEM.

Some unrealistic resonances can be seen at lower frequencies, where linear wave theory starts to break down (highlighted in light blue). A similar effect could be seen in the sway RAOs as well (Fig. 3.11). The inclusion of the mooring system, slightly decreased

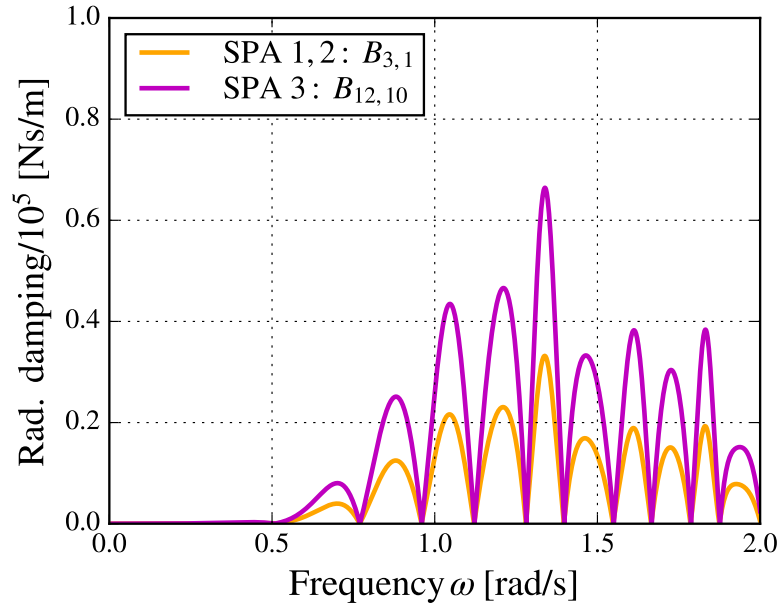


Figure 3.9: Cross terms of the radiation damping for the three spheres, as a function of the wave frequency ω , for $A_w = 1$ m and $\theta = 0$.

the heave RAOs of the three spheres at the peak frequency, whilst shifting the peak towards lower frequencies for SPA 3 (Fig. 3.12). The effect of the mooring system in the low wave frequencies is highlighted in light blue. It should be noted that no viscous damping was considered for the devices nor for the clump weight, following the original work of Vicente et al. (2009a).

In all the results in this section, referring to an array of spherical point absorbers with shared moorings, the RAOs obtained for the three bodies exhibited the same patterns: 1. oscillations in high frequencies, due to array interference, and 2. resonances in low frequencies, due to the influence of the inter-body mooring system. Although very low frequencies are shown in the responses throughout this work, special care should be taken by the reader to remember this linear model's region of validity when interpreting the results.

As in the work of Vicente et al. (2009a), the viscous damping introduced by the mooring lines was neglected, and the inelastic quasi-static approach was used. Although past studies have highlighted the importance of including the effects of mooring line damping in the surge mode, at low frequencies, it should be noted that for such low frequencies linear water wave theory already starts to break down, rendering a linearised model invalid in this region of operation. Furthermore, for the range of wave frequencies where a linearised model is valid, the magnitude of the damping introduced to the system from the waves radiated by the devices in the array is much larger than any viscous effects that could possibly be introduced by the presence of a mooring line.

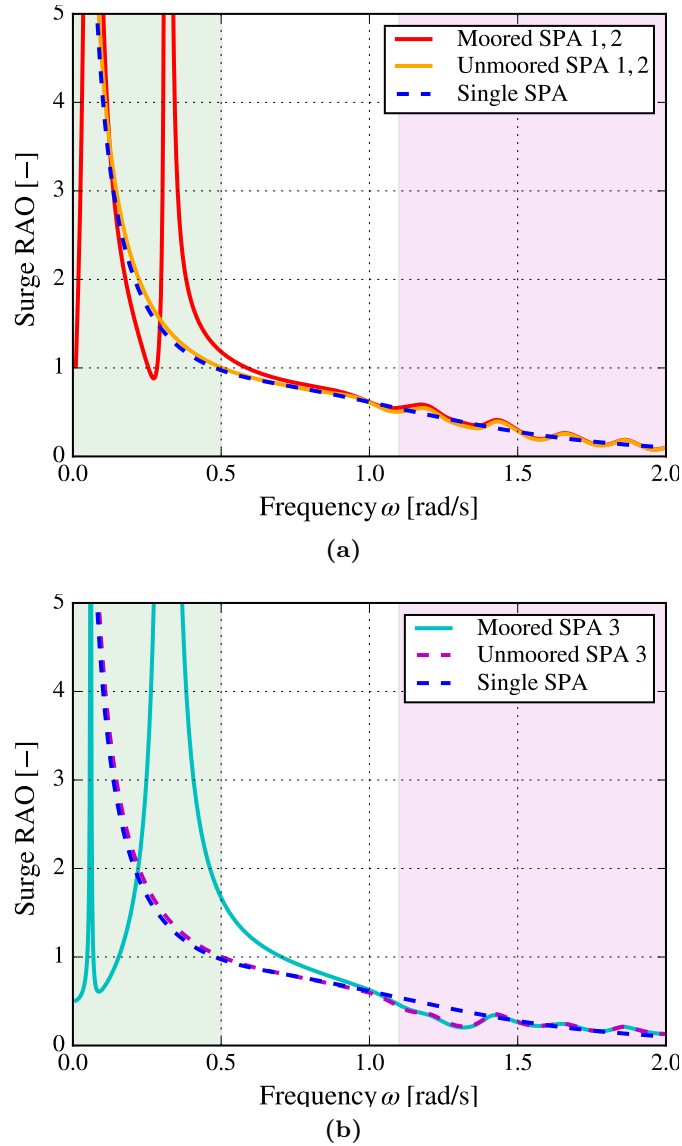


Figure 3.10: Surge RAOs for the three SPAs for the inter-body moored array, as a function of the wave frequency ω , for $A_w = 1$ m, $\theta = 0$, $C_{cw}^* = 0.1$, $\alpha = 30^\circ$, and $\beta = 30^\circ$. The surge RAOs for the unmoored array, and the single body are provided for comparison.

3.4.2 Sensitivity analysis

A sensitivity analysis was performed for the array of SPAs, varying several model parameters, and observing the effect on the RAOs. These model parameters are the bottom mooring line stiffness (C_{bm}^*), the angle between the bottom mooring line and the horizontal surface plane (β), the angle α between the inter-body mooring line and the horizontal surface plane, and the angle of wave incidence θ . This analysis can be found in Appendix B in its detailed form. For every variation of a particular parameter, the rest of the model parameters were kept constant (the default values were considered).

The variation of the angle formed between the free-surface plane and the inter-body mooring line (α), did not significantly affect the RAOs of the three SPAs and the CW in

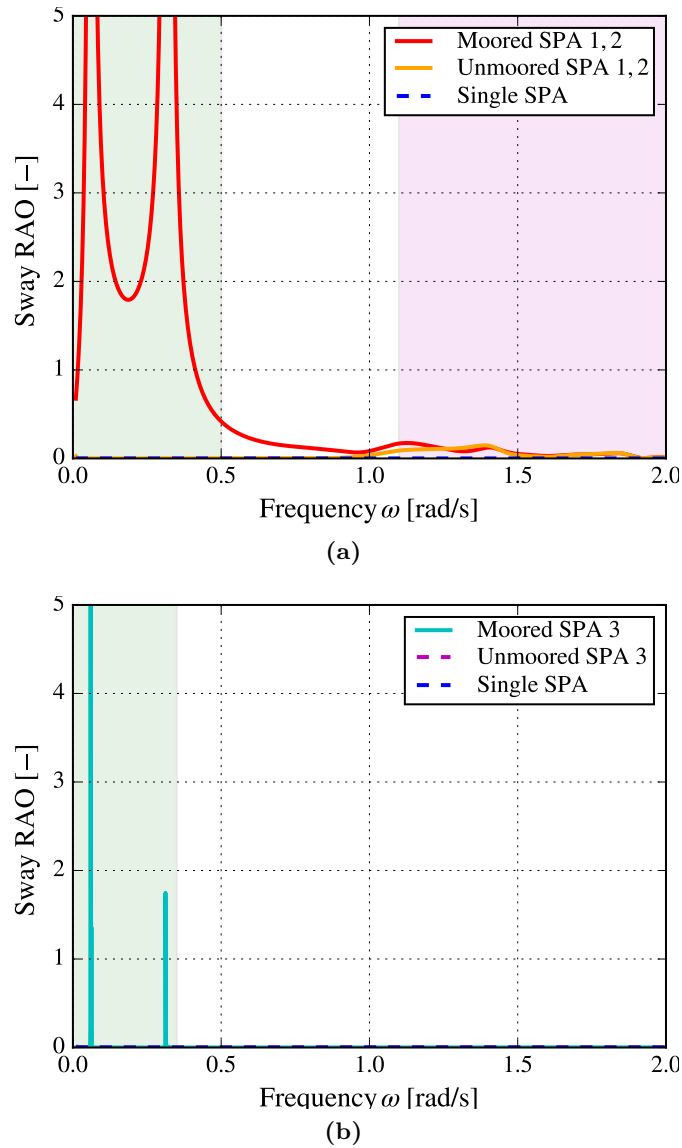


Figure 3.11: Sway RAOs for the three spheres for the inter-body moored array, as a function of the wave frequency ω , for $A_w = 1$ m, $\theta = 0$, $C_{cw}^* = 0.1$, $\alpha = 30^\circ$, and $\beta = 30^\circ$. The sway RAOs for the unmoored array, and the single SPA are provided for comparison.

surge, sway and heave. The responses in the translational modes were slightly shifted to the left in the low frequencies, but there was no effect in the operational range of wave frequencies. Similar responses were observed for the surge and heave RAOs of the SPAs, after varying the angle formed between the bottom mooring line and the free surface plane (β). However, this was not the case for the heave RAO of the SPAs, as a very low value of β results in a slight shift to lower frequencies of the response at the peak frequency. For low values of the bottom mooring line stiffness C_{bm}^* , the low frequency peaks of surge and sway RAOs were shifted towards lower wave frequencies. The same applies for the heave RAO, which was also profound at the heave peak frequency.

Although this initial study showed that the catenary mooring system has no effect on the operational states of the spherical buoys, the question still remains whether or not

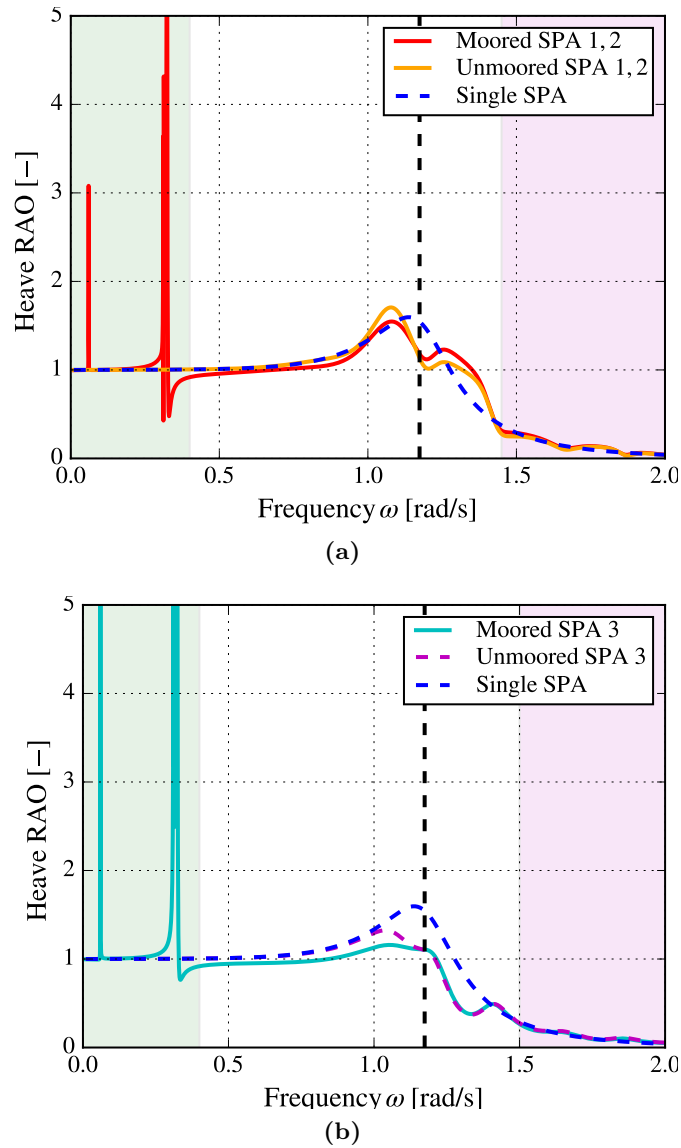


Figure 3.12: Heave RAOs for the three spheres for the inter-body moored array, as a function of the wave frequency ω , for $A_w = 1$ m, $\theta = 0$, $C_{cw}^* = 0.1$, $\alpha = 30^\circ$, and $\beta = 30^\circ$. The heave RAOs for the unmoored array, and the single body are provided for comparison.

the same conclusions could be made for a two-body WEC, where the damping of the PTO is frequency dependent. The majority of past studies is focused on the mooring lines, and little information has been provided on the dynamics of the WEC itself. This section therefore will serve as the foundation for the forthcoming study of cylindrical point absorbers.

3.4.3 Comparison with Vicente et al. (2009a)

The author provided his files with the hydrodynamic coefficients and the excitation forces, which turned out to be identical to those which were obtained in this study. There is a discrepancy in the RAOs for the three SPAs with the default parameters compared to those obtained in this thesis, but this could be attributed to the author choosing to

make the motion responses non-dimensional by dividing it by the wave height instead of the wave amplitude. Also, there is a suspicion that for SPA 3 the PTO damping was not applied. Nevertheless, with the exception of this discrepancy, there is close agreement between the results obtained in this thesis with those presented in Vicente et al. (2009a).

3.5 Results: array of cylindrical point absorbers

The heave resonance frequency of the CPA was estimated to be 1.103 rad/s, (based on Eq. 3.60) which was very close to the calculated pitch resonance frequency. It should be noted that this would not be desirable for an optimised WEC extracting energy in the heave mode, because excessive pitching could cause high bending moments in an oscillating body type WEC or unwanted inner free surface sloshing in an OWC. For the CPAs, the viscous effects were accounted for, in their linearised form. The drag coefficient for surge was set to $c_{d,1} = c_{d,7} = c_{d,13} = 0.8$, and for heave it was set to $c_{d,3} = c_{d,9} = c_{d,15} = 1.15$, based on the literature. Optimum PTO damping was applied at resonance conditions, and except for the viscous damping and the hydrostatic forces, the rest of the modelling approach followed the same approach as presented in the section referring to the array of SPAs.

Isolated cylindrical point absorber

Results are first presented for a single unmoored device oscillating in all six DoF, with and without the consideration of the drag forces $F_{d,i}$ in surge and heave (Fig. 3.13). The RAOs in surge (Fig. 3.13a), sway (Fig. 3.13b), and pitch (Fig. 3.13c) decrease at the peak frequencies, after including the viscous damping in surge and heave. Although no drag was introduced in pitch, the RAO also decreases, due to the coupling between surge and pitch. For all the modes, the viscous damping appears to be mostly effective at the resonance frequency.

Moored array of cylindrical point absorbers

As in the case of SPAs, since the angle of wave of incidence θ was set to 0° , CPAs 1 and 2 demonstrated the same hydrodynamic behaviour, so from herein after they will be referred to as CPA 1,2. As in the previous section, a mesh refinement sensitivity analysis was undertaken (Appendix A), but the results suggested that the hydrodynamic coefficients and the excitation force amplitudes were unaffected by the variation of the number of patches.

Fig. 3.14 presents the surge RAOs for the three CPAs, against the wave frequency ω . By setting the CPAs in an array configuration, small amplitude oscillations can be seen in the operational frequencies of CPA 1,2 and CPA 3. The same effect is also apparent for the pitch RAO (Fig. 3.17). For the sway RAO (Fig. 3.15), new oscillations are visible

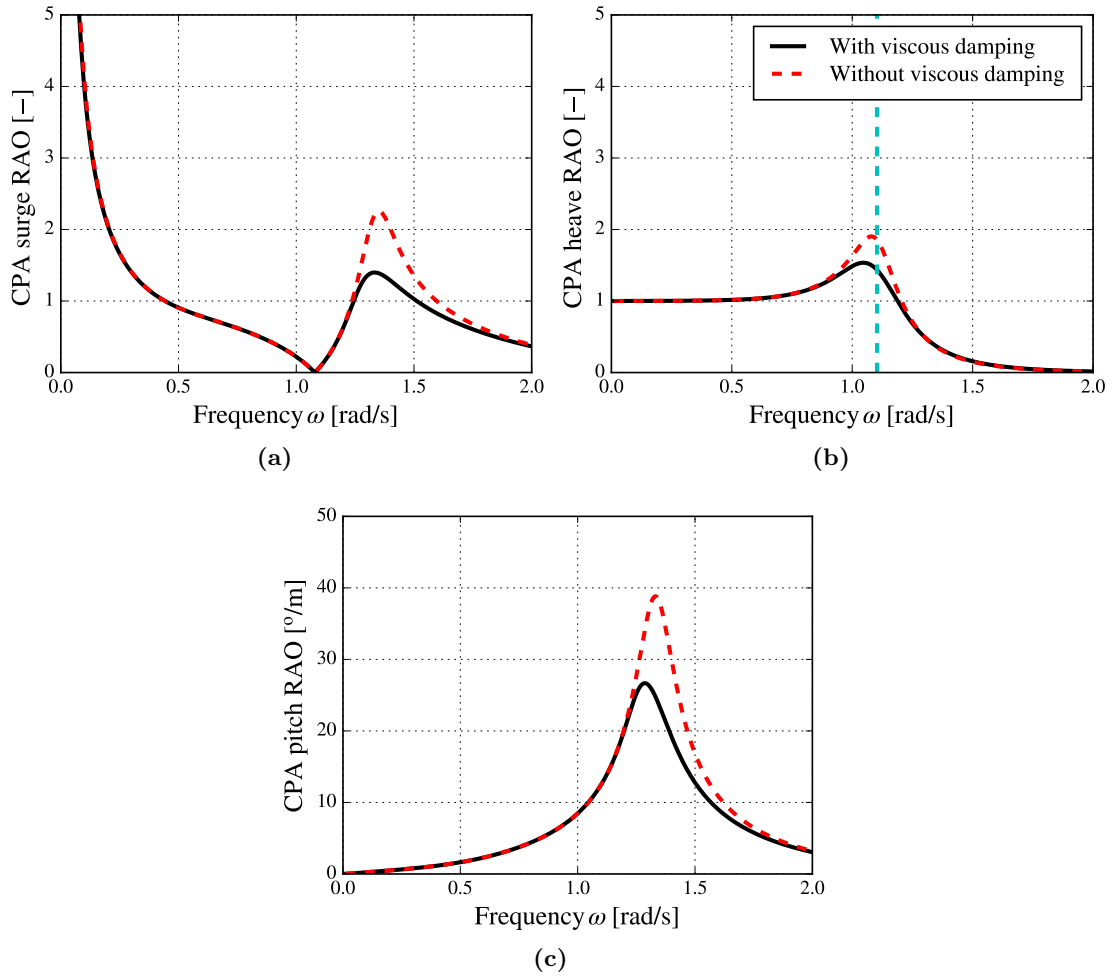
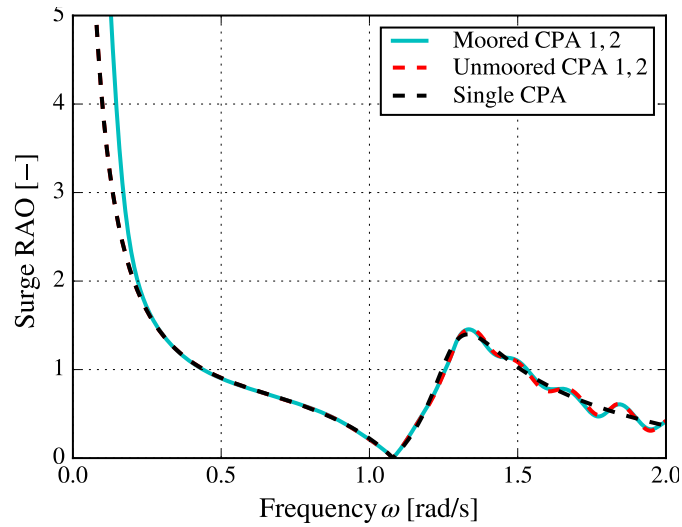


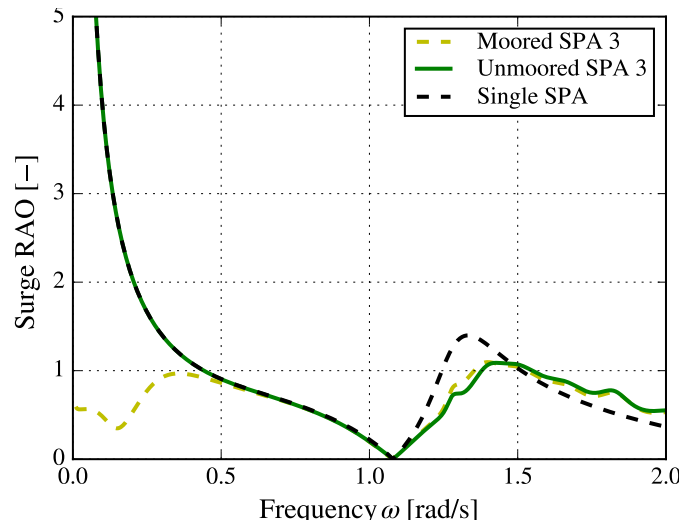
Figure 3.13: RAOs for a single cylinder as a function of the wave frequency ω , in surge (3.13a), heave (3.13b), and pitch (3.13c), with drag in surge and heave. The optimum PTO damping is applied, for $A_w = 1$ m as a function of the wave frequency ω .

for SPA 1,2 due to array interference. As for the heave RAO, there is a slight increase for SPA 1,2 and 3, and a shift of the peak towards lower frequencies, after setting the devices in an array configuration (Fig. 3.16).

By introducing mooring lines, none of the RAOs is affected at the operational frequency range. To make an allusion to the results for the triangular array of SPAs, the RAOs slightly decreased after the inclusion of the mooring system. However, in the former case, no viscous damping was introduced in the model. Since the model for the SPA array was an inviscid model, any excitation in the absence of damping could contribute to exaggerating influences of the mooring system presence. It is therefore concluded that the inclusion of viscous damping is necessary in this type of models, in order to obtain more realistic results.

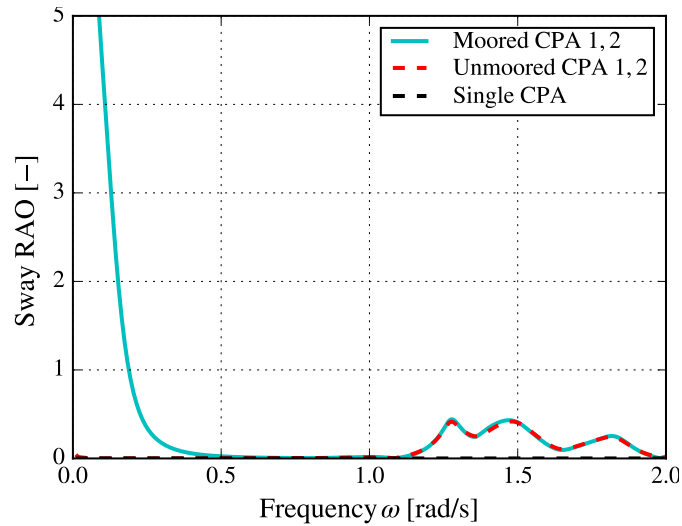


(a)

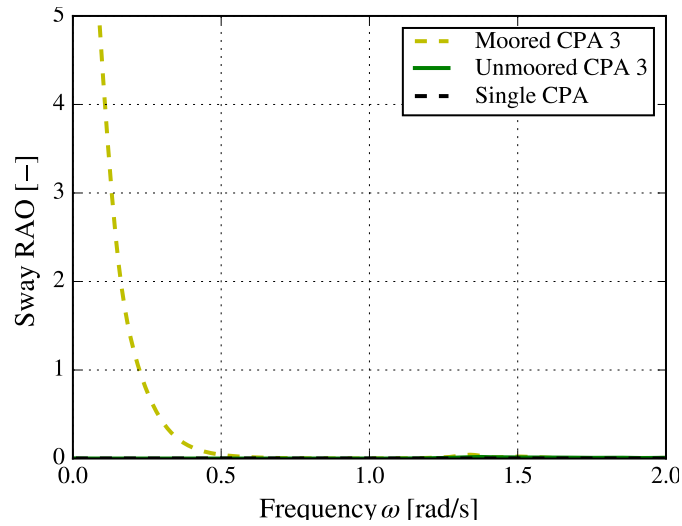


(b)

Figure 3.14: Surge RAOs for the three CPAs with inter-body mooring connections, as a function of the wave frequency ω , for $A_w = 1$ m, $\theta = 0$, $C_{bm}^* = 0.1$, $\alpha = 30^\circ$, and $\beta = 30^\circ$. The surge RAOs for the unmoored array, and the single CPA are provided for comparison.



(a)



(b)

Figure 3.15: Sway RAOs for the three CPAs with inter-body mooring connections, as a function of the wave frequency ω , for $A_w = 1$ m, $\theta = 0$, $C_{bm}^* = 0.1$, $\alpha = 30^\circ$, and $\beta = 30^\circ$. The surge RAOs for the unmoored array, and the single CPA are provided for comparison.

3.6 Limitations

Since the presented model is based on linear wave theory, only waves of small amplitude compared to the characteristic dimension of the body may be considered. Although linear wave theory is valid for all frequencies under such conditions, in practice ocean waves of very low frequencies correspond to extreme events and other phenomena where the small wave assumption would no longer hold. As such, the model presented is not considered valid for very low frequencies. Moreover, it was assumed that the mooring lines are attached at the centre of the floatation of each device. As an improvement, moments should be introduced, based on the exact fairlead position.

Another limitation is that snap and peak loads, as well as trapping modes are not

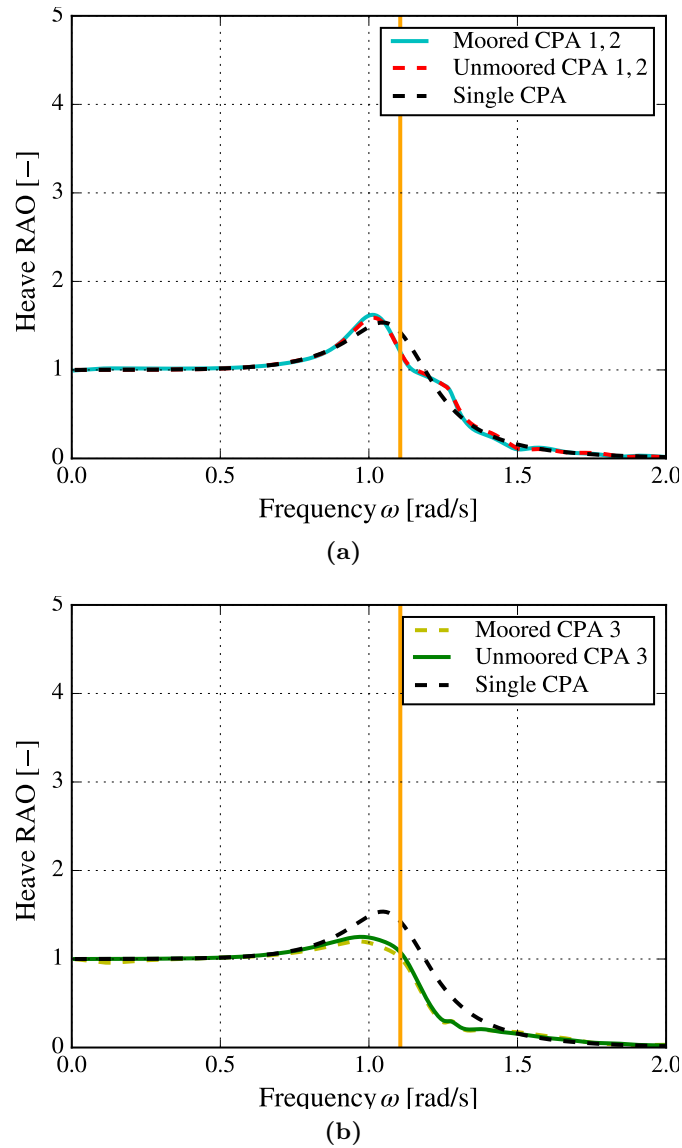


Figure 3.16: Heave RAOs for the three cylinders with inter-body mooring connections, as a function of the wave frequency ω , for $A_w = 1$ m, $\theta = 0$, $C_{bm}^* = 0.1$, $\alpha = 30^\circ$, and $\beta = 30^\circ$. The surge RAOs for the unmoored array, and the single buoy are provided for comparison.

discussed in this thesis. Also, despite the benefit of a reduction in anchors required, the proposed inter-body mooring system itself has a few shortcomings. One of them involves a potential increase in the risk of entanglement and collision with marine vessels in the event of mooring line failure. This thesis has not considered the economic impacts associated with potential increases to the risk of the project. For that matter, a techno-economic analysis of the mooring system analysed in this thesis has also not been carried out. In future work, a comparison of the mooring system's survivability should be carried out. If extreme loads were concerned, a CFD approach, or a time-domain model that is an extension of this thesis work, would need to be developed for this purpose, because frequency-domain and stochastic-domain modelling would not be able to model these effects.

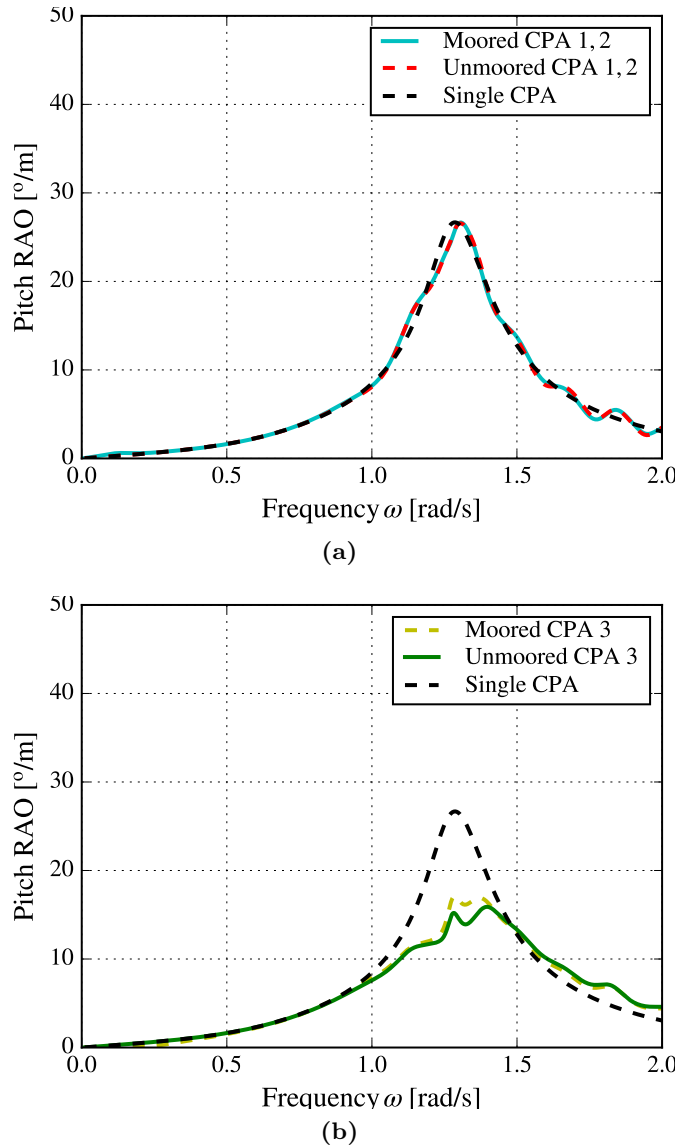


Figure 3.17: Pitch RAOs for the three cylinders with inter-body mooring connections, as a function of the wave frequency ω , for $A_w = 1$ m, $\theta = 0$, $C_{bm}^* = 0.1$, $\alpha = 30^\circ$, and $\beta = 30^\circ$. The pitch RAOs for the unmoored array, and the single buoy are provided for comparison.

Contribution to the initial work

With the addition of the formulation on cylindrical point absorber array dynamics, axially symmetric devices with active rotational DoF have now been included in the work on moored array modelling. This means that the hydrodynamic coupling influence between translational and rotational modes is now represented, which can have a significant effect on array dynamics, particularly coupling between surge and pitch modes. Linearised viscous damping of the point absorbers has also been included in the array dynamics.

3.7 Chapter discussion and concluding remarks

The results presented in this chapter were aimed at developing the foundation for a numerical model that describes the hydrodynamics of an array of three point absorbers, with shared moorings connected by a clump weight. Inter-body and bottom mooring connections were introduced in the array, and the system was studied in the frequency-domain. Initially, an array of spherical point absorbers was investigated. A value was chosen for the PTO damping that was sub-optimal in terms of energy extraction, but was convenient for demonstration purposes. For the array without moorings, some oscillations were introduced in the surge mode RAOs of the three bodies. Intra-array coupling was predicted to occur between heave and surge radiation damping for the individual bodies, due to the array configuration. This is an effect that does not take place in isolated floating bodies. After adding the mooring system to the numerical model, further resonances appeared at low frequencies in the surge RAOs of the three bodies. A similar effect could be seen in the sway RAOs as well. The heave mode responses were not significantly affected by the presence of the mooring system, which is a promising result for arrays of heaving WECs. The inclusion of the mooring system slightly decreased the heave RAOs, whilst shifting the peaks towards higher frequencies.

Furthermore, a sensitivity analysis was performed, investigating the effect of changing various parameters on the oscillation amplitudes, such as the stiffness of the bottom mooring lines, the inter-body mooring connection angle and the bottom mooring line angle, which helped determine the optimal default parameters for the system. By varying the angle of wave incidence from 0, the symmetry of the problem is broken.

In general, the model seemed to perform adequately in the range of typical ocean wave frequencies. For very low frequencies, the validity appears to be compromised. However, in practice, ocean waves of very low frequency will not have an amplitude that is small compared to the characteristic dimension of the WEC, which already violated a requirement for linear wave theory to hold true. The model has neglected the viscous damping of the spherical bodies, and it also has neglected the inertia and the viscous damping of the mooring cables. The latter involves vortex shedding and is non-linear, which may not be modelled in the frequency-domain, unless linearising assumptions are made. These simplifications may be refined at a later stage, using a more sophisticated model in the time-domain, although this is typically not needed in an initial examination of the hydrodynamics of a moored WEC array. It should be noted that in the initial stages, frequency-domain analysis serves as a means for discovering where the system resonance peaks are located, and less so as a method of predicting the exact magnitude of the floating bodies' motion responses.

On extending the model to cylindrical point absorbers

Previous work has focused on floating bodies where oscillation takes place in the three translational DoF, so it was of interest to investigate a moored array free to move in all

six DoF. This was studied by assigning a Centre of Gravity (CoG) to a floating body of cylindrical shape. Cylinders are axially symmetric, as are most point absorbers (e.g. W1 (Ocean Energy Systems (OES), 2016), spar-buoy OWC (Gomes et al., 2012), Wavebob (Beatty et al., 2015), Aquabuoy (Weinstein et al., 2004)). In this regard, the moored array of SPAs that was based on the work of Vicente et al. (2009a) served as a building block towards a more complete model that considers all six DoF. Three cylinders were introduced in the model, instead of spheres, and the same mooring configuration and modelling approach was employed with some improvements. It should be noted that in the case of spherical geometry of uniform mass distribution, there is no need to account for the three rotational DoF. Therefore, a mass matrix was introduced, which required knowledge of the centre of gravity and the moments of inertia. These were calculated with the aid of SolidWorks (SW).

On Degrees-of-Freedom

An important aspect of modelling devices which account for all six DoF is that coupling between the surge and pitch modes should be investigated. This is not possible for spherical floaters, considering that their oscillations are restricted to three DoF. Therefore, a "general recipe" has been developed for analysing a moored array of devices with axial symmetry, since most point absorbers fall into this category. Axial symmetry in WECs refers to bodies that are symmetric about an axis that is perpendicular to the plane of the free surface.

On the panel method

Because of the size of the device, the panel method was considered to be more appropriate, because with sufficient resolution - especially near the free surface - it can capture effects that are important for the array dynamics.

On irregular frequency removal

In this thesis, the higher order method of WAMIT was used to compute the velocity potential for the radiation and diffraction problems. The irregular frequency removal option was included in the modelling, even though most likely the frequencies analysed were not high enough to see the effect of high frequency numerical resonance causing spikes in the frequency response of the hydrodynamic coefficients. Nevertheless, an additional irregular frequency removal patch was modelled on top of the devices.

On neglecting the environmental loading of currents and wind

Throughout this thesis, only the environmental loading of waves has been considered, meaning that the effect of winds and currents has been neglected. The effect of wind loading could potentially affect the WEC hydrodynamics, but in the case of the spar-buoy OWC analysed in Chapter 4, the freeboard is probably small enough to comfortably make this assumption. The effect of current loading could potentially affect both the

mooring and the WEC dynamics, and such drift forces could be analysed with the help of Kochin functions, which are calculated by BIEM solvers such as NEMOH.

On neglecting the wave excitation force on the CW

The model presented in this work has assumed that the dominant force on the clump weight is gravity, which due to its high density, is dominant over the opposing buoyancy force. The force due to gravity on the clump weight was also assumed to be large compared to the wave excitation force, and considering that the clump weight is also deeply submerged (i.e. deep enough for the wave excitation force to have significantly decreased), it was reasonable to assume that there is no excitation force on the clump weight. Viscous effects on the clump weight have been ignored, but as a future improvement they should be included.

On mooring line damping

Mooring line viscous damping has been neglected from the analysis carried out in this thesis. This was assumed to be reasonable, since viscous drag forces depend on the cross-sectional area perpendicular to the direction of the motion. Nevertheless, previous work has suggested that mooring line damping can significantly impact floating body motions in the surge mode, particularly at low frequencies (Bauduin and Naciri, 1999). That being said, in time-domain models (based on more sophisticated, non-linear wave theories) and in survivability studies, mooring line viscous effects should certainly not be neglected, and should be modelled using accepted methods from previous studies (Liu and Bergdahl (1998), Bauduin and Naciri (1999)) or quantified empirically using free decay tests in a wave tank (Johanning et al., 2007). It should also be noted that the scope of the thesis is not to design the mooring system itself, but to examine the initial stage frequency-domain modelling of an array of WECs with mooring connections. However, this effect is outside the range of frequencies where the model presented would be valid in practice, since ocean waves of very low frequency do not have the low amplitude required to make linear wave theory valid.

Chapter 4

Moored array of spar-buoy OWCs

4.1 Introduction

The model developed in Chapter 3, provides an analysis on the hydrodynamics of point absorber arrays with arbitrary geometry, under regular wave conditions. A limitation in this analysis is that in the point absorbers examined, PTO impedance has been considered constant and purely resistive over the entire range of frequencies studied. It is now of interest to apply the foundation presented in the former chapter to an optimised technology, with PTO dissipation and restoring forces that are frequency-dependent. The present chapter investigates the effects of the mooring system on the hydrodynamics and performance of a triangular array of spar-buoy OWC devices under regular wave conditions. (Additional information on working principles of the spar-buoy OWC are described in Section 2.6.1 of this thesis). The calculations performed in this section will allow direct comparison between the shared mooring system, and a more conventional mooring approach, which uses only bottom mooring lines to keep each WEC in the array in station.

Theoretical studies on the dynamics of the OWC were first elaborated by McCormick in the 1970s (McCormick, 1974). Only more recently, with advances in Boundary Integral Equation Methods (BIEM) for wave-body interactions, more detailed simulations have been conducted to account for the hydrodynamic interference between the buoy and the OWC (Alves et al., 2010). Gomes et al. (2012) developed a geometry optimisation model for an axisymmetric floating OWC, with a non-uniform tail tube cross-section, which will be used as a case study for the model of this thesis.

In this thesis the work of Gomes et al. (2016) was extended as follows: an array was modelled in a triangular configuration, all six DoF were considered of the buoys, and mooring system dynamics were modelled. In addition to heave, viscous damping was also accounted in surge, sway, roll, and pitch. Two mooring systems were analysed and the array frequency-domain modelling was also extended to the stochastic-domain.

The turbine coefficient value was chosen to correspond with existing work by Gomes et al. (2016). The experimental array of Correia da Fonseca et al. (2016) has been scaled

up (the motions) for preliminary model verification, using Froude scaling, and this is a limitation of the work in this thesis because Reynold's number effects have been ignored in doing so. In the aforementioned paper, an orifice was used to model the turbine damping. A more sophisticated analysis of viscous effects may be carried out using CFD, but this is beyond the scope of this thesis. The numerical model presented in this thesis accounts for the compressibility effect inside the air chamber, which is important because otherwise the phase and amplitude of the system response will not be modelled correctly.

In terms of what is acting on the air chamber, the piston-like movement of the OWC is a reasonable assumption when its diameter is small compared to the wavelength, which is certainly the case here. Sarmiento and Falcão (1985) elaborate further on this concept. The frequency-domain model considered throughout this chapter uses linear hydrodynamic and hydrostatic forces; real fluid viscous effects are hence accounted for by using a linear approximation. The mooring connections are linearised using perturbation theory, following the method originally presented by Vicente et al. (2009a), and elaborated upon in Chapter 3. The analysis is also extended to be applicable for irregular wave conditions, via stochastic-domain modelling. The influence of the wave incidence angle on the array performance is also analysed.

4.2 Numerical model: regular wave analysis

The formulation considered here is applicable to axisymmetric floating OWC devices with an inner free surface that moves predominantly in heave. The formulation assumes incompressible and irrotational water flow. Wave amplitudes and body motions are assumed to be much smaller than the incident wavelength. Linear hydrodynamic forces, accounting for the array effects, are applied. Linear approximations of quadratic drag forces are considered. The inter-body connection studied here consists of mooring lines connected to a clump weight in the centre of the array (the same configuration and numerical approach was used for Ch. 3). The mooring lines are assumed weightless and inelastic, and linear forces are applied by considering small perturbations around the rest position. A frequency-domain formulation is presented to solve the equation of motion.

4.2.1 Equation of motion for the array

A top view of the array configuration and its mooring lines is shown in Fig. 4.1 and Fig. 4.2 displays a three-dimensional representation of the array. The devices are labelled as spar-buoy OWC 1, spar-buoy OWC 2, and spar-buoy OWC 3, while the clump weight is represented by index 4 in Figs. 4.1 and 4.2. The origin of the fixed reference frame is located at the free surface, in the middle of the array. The axis shows the positive x , y , and z direction. Regular waves propagate with the positive x -axis direction with amplitude A_w and frequency ω . The motion of each device is defined by six DoF: three translational (surge, sway, and heave) and three rotational (roll, pitch, and yaw). Both the OWC and the buoy are "bodies" because otherwise the water inside the OWC would move in the same way as the free surface outside. The fact that it moves differently

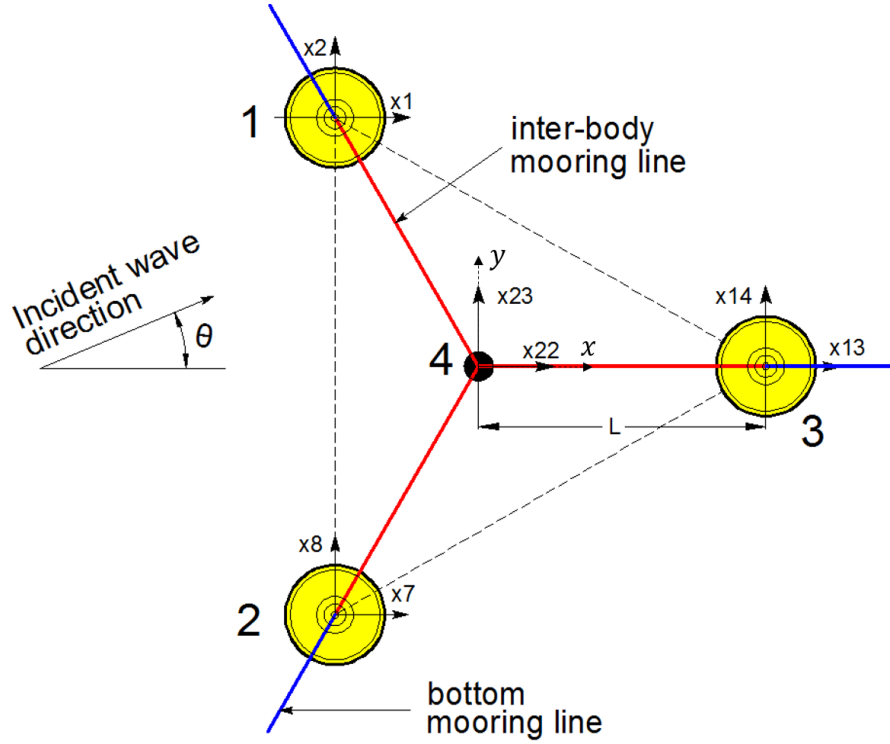


Figure 4.1: Top view of the triangular array with inter-body mooring connections. The spar-buoy OWC devices are represented by indices 1-3 and the clump weight is represented by index 4.

justifies modelling it as another body, and referring to it as such. From now on, each spar-buoy of the array will be defined as a buoy (Buoy 1, Buoy 2, and Buoy 3), and an OWC (OWC 1, OWC 2, and OWC 3). The complex amplitudes of the DoF for Buoy 1 are denoted by x_1 to x_6 , for Buoy 2 by x_7 to x_{12} , and for Buoy 3 by x_{13} to x_{18} (as indicated in Fig. 4.1). These motions are measured relative to a reference frame whose origin is located at the free surface in the centre of each device, with the same orientation of the fixed reference frame. The complex amplitude of displacements x_{19} , x_{20} , and x_{21} refer to the heave oscillation of the OWCs of each device. The notations for this chapter are summarised in Table 4.1.

The equation of motion for the three buoys and OWCs in the frequency-domain can be written as

$$M_{ij} (-\omega^2 x_j) = F_{\text{exc},i} + F_{\text{rad},i} + F_{\text{hst},i} + F_{t,i} + F_{d,i} + F_{\text{bm},i} + F_{\text{im},i}, \quad (4.1)$$

where M_{ij} represents the inertia matrix. The term $-\omega^2 x_j$ corresponds to the acceleration complex amplitude of mode j . The terms on the right hand side of Eq. 4.1 represent the complex amplitudes of the forces acting on mode i , namely the wave excitation force $F_{\text{exc},i}$, the radiation force $F_{\text{rad},i}$, the restoring hydrostatic force $F_{\text{hst},i}$, the force due to the air pressure variations inside the air chamber $F_{t,i}$, the drag force $F_{d,i}$, the force from the bottom mooring lines $F_{\text{bm},i}$, and the force from the inter-body mooring lines $F_{\text{im},i}$.

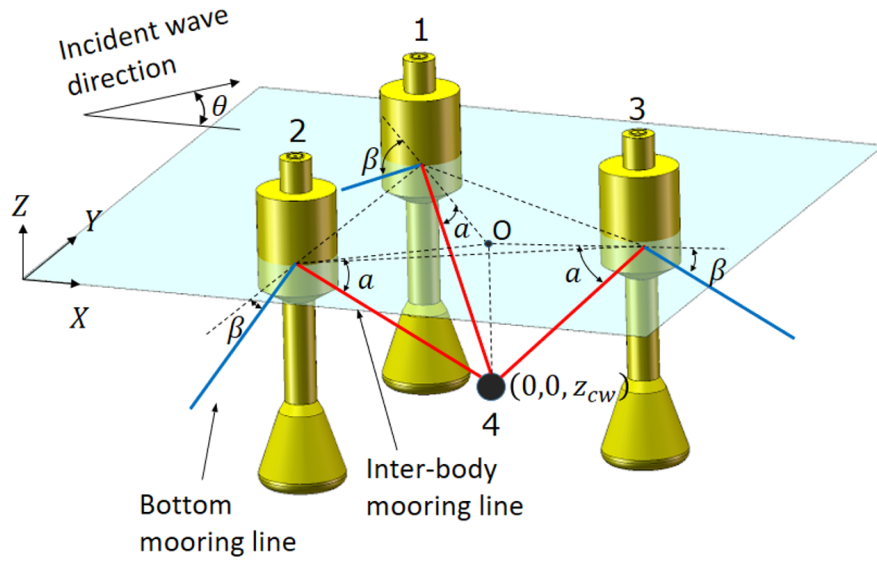


Figure 4.2: Three-dimensional view of the triangular array with inter-body mooring connections.

Table 4.1: Notation for the modes of the three buoys and their corresponding OWCs, as well as the weight mode notations.

DoF	surge	sway	heave	roll	pitch	yaw
Buoy 1	x_1	x_2	x_3	x_4	x_5	x_6
Buoy 2	x_7	x_8	x_9	x_{10}	x_{11}	x_{12}
Buoy 3	x_{13}	x_{14}	x_{15}	x_{16}	x_{17}	x_{18}
OWC 1	-	-	x_{19}	-	-	-
OWC 2	-	-	x_{20}	-	-	-
OWC 3	-	-	x_{21}	-	-	-
Clump weight	x_{22}	x_{23}	x_{24}	-	-	-

The inertia matrix M_{ij} contains the following non-zero terms,

$$M_{ii} = m_b, \text{ for } i = 1, 2, 3, 7, 8, 9, 13, 14, 15, \quad (4.2)$$

$$M_{ii} = I_{44} = I_{55}, \text{ for } i = 4, 5, 10, 11, 16, 17, \quad (4.3)$$

$$M_{ii} = I_{66}, \text{ for } i = 6, 12, 18, \quad (4.4)$$

$$M_{ij} = M_{ji} = m_b z_g, \text{ for } (i, j) = (1, 5), (7, 11), (13, 17), \quad (4.5)$$

$$M_{ij} = M_{ji} = -m_b z_g, \text{ for } (i, j) = (2, 4), (8, 10), (14, 16), \quad (4.6)$$

where m_b is the buoy mass and z_g is the z -coordinate of the centre of gravity. The terms I_{44} , I_{55} , I_{66} are the moments of inertia of the buoy about the x , y , and z axes of each buoy referential, aligned with the fixed reference frame.

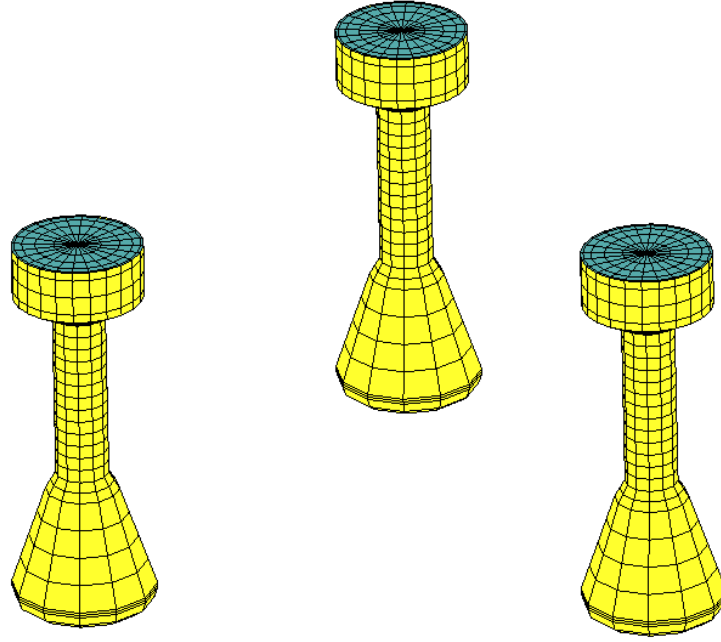


Figure 4.3: Grid of an array of three spar-buoy OWC devices, as modelled in WAMIT (higher order discretisation method).

4.2.2 Hydrodynamic radiation and excitation coefficients

The hydrodynamic radiation and excitation coefficients were calculated using WAMIT for radiation and diffraction wave-structure interaction problems (WAMIT, 2006), as in Chapter 3. The model considers six DoF (three translational and three rotational) for each floating structure's motion and one DoF (heave) for each OWC's motion. The computations make use of the higher order discretisation method used in (Gomes et al., 2012, 2016), for a triangular array configuration. The grid used in the computations is shown in Fig. 4.3. The top of the OWC device is modelled by a rigid piston of finite thickness, with a mass given by the product of the sea water density and its volume (as in Gomes et al. (2012, 2016)) (Fig. 4.4).

An alternative modelling approach is to use a weightless piston at the free surface. However, this approach is prone to numerical errors at high frequencies. The finite length piston approach solves this problem and provides equivalent results (Gomes, 2013). In Fig. 4.5, the bottom surface of the piston is presented in red, while the blue grid at the free surface is used for the removal of irregular frequencies (WAMIT, 2006). Since the simulation considers three devices, the total number of modes used in computations is 21. The radiation force complex amplitude $F_{\text{rad},i}$ is

$$F_{\text{rad},i}(\omega) = - \left[-\omega^2 A_{ij}(\omega) + i\omega B_{ij}(\omega) \right] x_j, \quad (4.7)$$

where A_{ij} is the frequency-dependent added mass coefficient due to the mass of fluid accelerated in mode i by the oscillatory motion of mode j , and B_{ij} is the frequency-dependent radiation damping coefficient due to the damping affecting mode i caused by the generation of radiated waves from mode j . The symbol i represents the imaginary

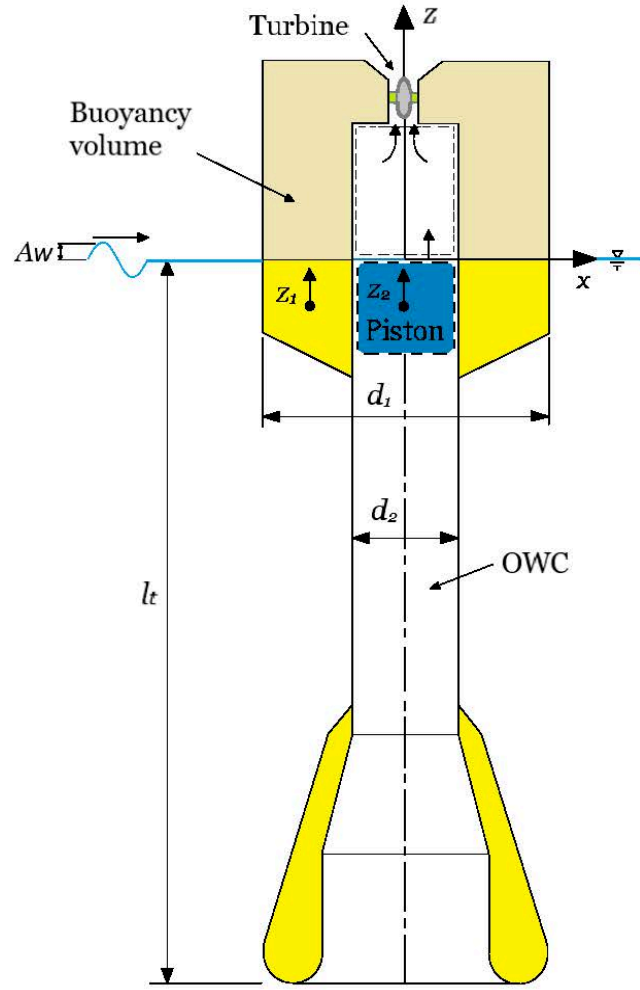


Figure 4.4: Illustration of the cross section of a spar-buoy OWC, redrawn from Gomes et al. (2016).

unit ($i = \sqrt{-1}$).

The wave excitation force complex amplitude is

$$F_{\text{exc},i}(\omega) = A_w \Gamma_i(\omega). \quad (4.8)$$

Here A_w is the incident wave amplitude and Γ_i represents the frequency-dependent wave excitation coefficient (force per unit wave amplitude). The hydrodynamic coefficients A_{ij} , B_{ij} , and Γ_i (real and imaginary part) are computed using WAMIT for a finite number of wave frequencies ω .

4.2.3 Hydrostatic coefficients

The linearised form of the hydrostatic force is considered,

$$F_{\text{hst},i} = -C_{ij} x_j, \quad (4.9)$$

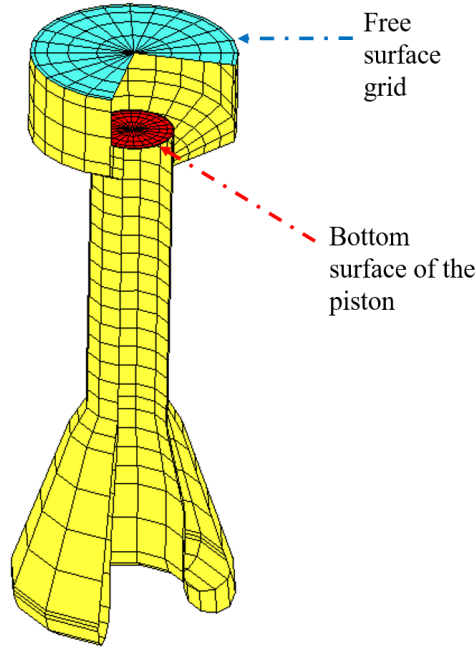


Figure 4.5: Cross-section of the spar-buoy OWC grid, the bottom surface of the piston is highlighted in red, while the free surface grid (in blue) was introduced for irregular frequency removal.

with C_{ij} denoting the linear hydrostatic restoring coefficients. As in the former chapter (Section 3.3.2), we also assume small amplitude angles for the rotational modes. For an axisymmetric device, C_{ij} has non-zero values for heave (buoy and OWC), roll, and pitch,

$$C_{ii} = \rho_w g S_b, \text{ for } i = 3, 9, 15, \quad (4.10)$$

$$C_{ii} = \rho_w g S_o, \text{ for } i = 19, 20, 21, \quad (4.11)$$

$$C_{ii} = \rho_w g V \overline{GM}, \text{ for } i = 4, 5, 10, 11, 16, 17, \quad (4.12)$$

where ρ_w is the water density, g is the acceleration due to gravity, S_b is the waterplane area of the buoy, S_o is the waterplane area of the OWC, V is the buoy's displaced water volume, and \overline{GM} is the buoy's metacentric height.

4.2.4 Power absorption and air compressibility effects

Considering air as an ideal gas and the air compression and expansion cycle inside the chamber as an isentropic process, as proposed in (Falcão and Justino (1999), Falcão and Henriques (2018)), the forces acting on the device due to the pressure variations can be linearised by assuming that variations in air chamber volume are small compared to the air chamber volume at rest (V_0). The force due to pressure variation in the air chamber can be represented by a damping and a restoring term

$$F_{t,i}(\omega) = -[\nu\omega B_{t,ij} + C_{t,ij}] x_j. \quad (4.13)$$

Here the damping terms $B_{t,ij}$ represent the damping introduced by the extraction of energy from the turbine-generator set, and the restoring terms $C_{t,ij}$ represent the air compressibility effect (Sarmiento and Falcão, 1985).

Both of these effects depend only on the relative heave motion between the buoy and OWC. The $B_{t,ij}$ matrix consists of the following non-zero terms,

$$B_{t,ii} = B_t, \text{ for } i = 3, 9, 15, 19, 20, 21, \quad (4.14)$$

$$B_{t,ij} = B_{t,ji} = -B_t, \text{ for } (i, j) = (3, 19), (9, 20), (15, 21), \quad (4.15)$$

where the turbine damping coefficient is

$$B_t = \frac{\rho_a S_o^2}{\omega^2 V_0^2 k_t} \frac{1}{1 + \frac{k_t^2 c_a^4}{\omega^2 V_0^2}}. \quad (4.16)$$

Here ρ_a is the average air density inside the chamber, V_0 is the air chamber volume at equilibrium, and c_a is the speed of sound at atmospheric conditions. The linear turbine coefficient k_t , representing the turbine mass flow rate to pressure drop ratio, depends on the turbine's geometry, size, and rotational speed.

Similarly, the non-zero terms of $C_{t,ij}$ are

$$C_{t,ii} = C_t, \text{ for } i = 3, 9, 15, 19, 20, 21, \quad (4.17)$$

$$C_{t,ij} = C_{t,ji} = -C_t, \text{ for } (i, j) = (3, 19), (9, 20), (15, 21), \quad (4.18)$$

where the linear restoring coefficient related to the compressibility of air trapped inside the air chamber is

$$C_t = \frac{\rho_a S_o^2}{\omega^2 V_0^2} \left(\frac{\omega^2 V_0}{k_t^2 c_a^2} \right) \frac{1}{1 + \frac{k_t^2 c_a^4}{\omega^2 V_0^2}}. \quad (4.19)$$

4.2.5 Drag force for regular waves

The calculation of the drag forces due to viscous fluid effects on the buoy is based on the Morison equation (Morison et al., 1950). The approach is similar to the one presented for the case of CPAs (Section 3.3.3). Nevertheless, it will be presented in detail in this section, since the equations are modified to apply to the spar-buoy OWC.

The complex amplitudes of the linearised drag forces in surge ($i = 1, 7, 13$) and sway ($i = 2, 8, 14$), and of the linearised drag moments in roll ($i = 4, 10, 16$) and pitch ($i = 5, 11, 17$) are given by

$$F_{d,i} = -i\omega B_{d,i} x_i, \quad (4.20)$$

where the linear damping coefficient is

$$B_{d,i} = \frac{1}{2} \rho_w A_{d,i} c_{d,i} \left(\frac{3\pi}{8} \left| \omega x_i^{(e)} \right| \right). \quad (4.21)$$

Here $A_{d,i}$ is the drag area (for $i = 1, 2, 7, 8, 13, 14$) or drag area moment (for $i = 4, 5, 10, 11, 16, 17$) for the normal direction, and $c_{d,i}$ is the drag coefficient for the normal direction in mode i . The term in parenthesis in Eq. 4.21 represents the linear approximation of the quadratic drag force. The term $x_i^{(e)}$ represents the estimated value of x_i . Since x_i is the solution of the system of equations presented in Eq. 4.1, these values require an iterative calculation.

For the computation of the drag forces in heave, two sources of viscous drag effects are taken into account, as presented in Gomes et al. (2016) (see Fig. 4.6). The first one applies to the buoy's drag inducing surfaces, and is proportional to the relative velocity between the buoy and the water flow. In this case, the Morison equation for a moving body in an oscillatory flow is considered. The second drag force, which accounts for the flow inside the OWC tube, is proportional to the relative heave velocity between the buoy and the OWC.

For the drag force induced by the buoy motion, the buoy is simplified into various drag sections, representing the dominant sources of drag effects. The heave drag force, due to the buoy's heave motion, is given by (Chakrabarti (1984), Gomes et al. (2016))

$$F_{d,z,i} = - \sum_{n=a,b,\dots} B_{d,z,n} (\omega x_i - u_z(z_n)) \quad , \text{ for } i = 3, 9, 15, \quad (4.22)$$

where n is the index of the drag surface, z_n is the z -coordinate of the drag surface, u_z is the complex amplitude of the velocity component aligned with the z -axis,

$$u_z = \frac{\nu g k A_w}{\omega} \frac{\sinh[k(h+z)]}{\cosh kh} e^{[-\nu k(x \cos \theta + y \sin \theta)]}, \quad (4.23)$$

where k is the wavenumber and h is the water depth. The velocity u_z is taken at the position (x, y) of the axis of the corresponding device at rest. The heave drag damping term is given by the sum of damping terms from each drag inducing surface

$$B_{d,z,n} = \frac{1}{2} \rho_w c_{d,3} A_{d,z,n} \left(\frac{3\pi}{8} \left| \omega x_i^{(e)} - u_z(z_n) \right| \right), \quad (4.24)$$

where $c_{d,3}$ is the heave drag coefficient of the buoy and $A_{d,z,n}$ is the area normal to the drag inducing surface.

With regards to the drag force accounting for the drag effect inside the tube, its magnitude depends on the relative heave motion between the buoy and the OWC,

$$F_{d,tb} = -\omega B_{d,tb} (x_i - x_j). \quad (4.25)$$

Here $(i, j) = (3, 19), (9, 20), (15, 21)$ and $B_{d,tb}$ is the linearised damping coefficient of the flow inside the tube,

$$B_{d,tb} = \frac{1}{2} \rho_w c_{d,tb} A_{d,tb} \left(\frac{3\pi}{8} \left| i\omega(x_i^{(e)} - x_j^{(e)}) \right| \right). \quad (4.26)$$

Here $c_{d,tb}$ is the drag coefficient of the flow inside the tube and $A_{d,tb}$ is the drag area, which we consider to be equal to S_o . The determination of the drag coefficients ($c_{d,3}, c_{d,tb}$) was based on experimental results Gomes et al. (2016). The total drag force in heave for the buoy is

$$F_{d,i} = (F_{d,z,i} + F_{d,tb}), \text{ for } i = 3, 9, 15, \quad (4.27)$$

and the drag force experienced by the OWC is

$$F_{d,i} = -F_{d,tb}, \text{ for } i = 19, 20, 21. \quad (4.28)$$

4.2.6 Clump weight and inter-body mooring connections

The moorings consist of a three line system (1-4, 2-4, 3-4), connecting the three devices to a centrally placed CW, following the logic established in Section 3.2.5. The same set of equations are used (Eqs. 3.8 - 3.35), as the same assumptions apply in this section, but the indexes of the equations are different, therefore when necessary they will be re-written to avoid confusion. The variables x_{22} , x_{23} , and x_{24} correspond to the surge, sway, and heave oscillation amplitudes of the CW. The coordinates x_{22}, x_{23}, x_{24} of Body 4 (CW) depend on the instantaneous values of x_i for $i = \{1, 2, 3, 7, 8, 9, 13, 14, 15\}$ through linearised geometric relationships Vicente et al. (2009a). Based on the principle of virtual works, and after neglecting products of small quantities, the following formulations are adopted:

$$x_{22} - x_1 + \sqrt{3}(x_2 - x_{23}) + \frac{2|z_{cw}|}{L}(x_3 - x_{24}) = 0, \quad (4.29)$$

$$x_{22} - x_7 - \sqrt{3}(x_8 - x_{23}) + \frac{2|z_{cw}|}{L}(x_9 - x_{24}) = 0, \quad (4.30)$$

$$x_{22} - x_{13} + \frac{|z_{cw}|}{L}(x_{24} - x_{15}) = 0. \quad (4.31)$$

The tension force vectors $\bar{r}_1, \bar{r}_2, \bar{r}_3$ corresponding to the lines 1-4, 2-4, 3-4 and to the angles $\alpha_1, \alpha_2, \alpha_3$ with the horizontal surface plane, are defined in the same manner as in Eq. 3.11.

The angles $\delta_1 - \pi/3, \delta_2 + \pi/3, \delta_3 + \pi$ are formed by the projections of the inter-body mooring line onto the horizontal plane:

$$\delta_1 = \frac{\sqrt{3}}{2L}(x_{22} - x_1) + \frac{1}{2L}(x_{23} - x_2), \quad (4.32)$$

$$\delta_2 = -\frac{\sqrt{3}}{2L}(x_{22} - x_7) + \frac{1}{2L}(x_{23} - x_8), \quad (4.33)$$

$$\delta_3 = \frac{1}{L}(x_{14} - x_{23}). \quad (4.34)$$

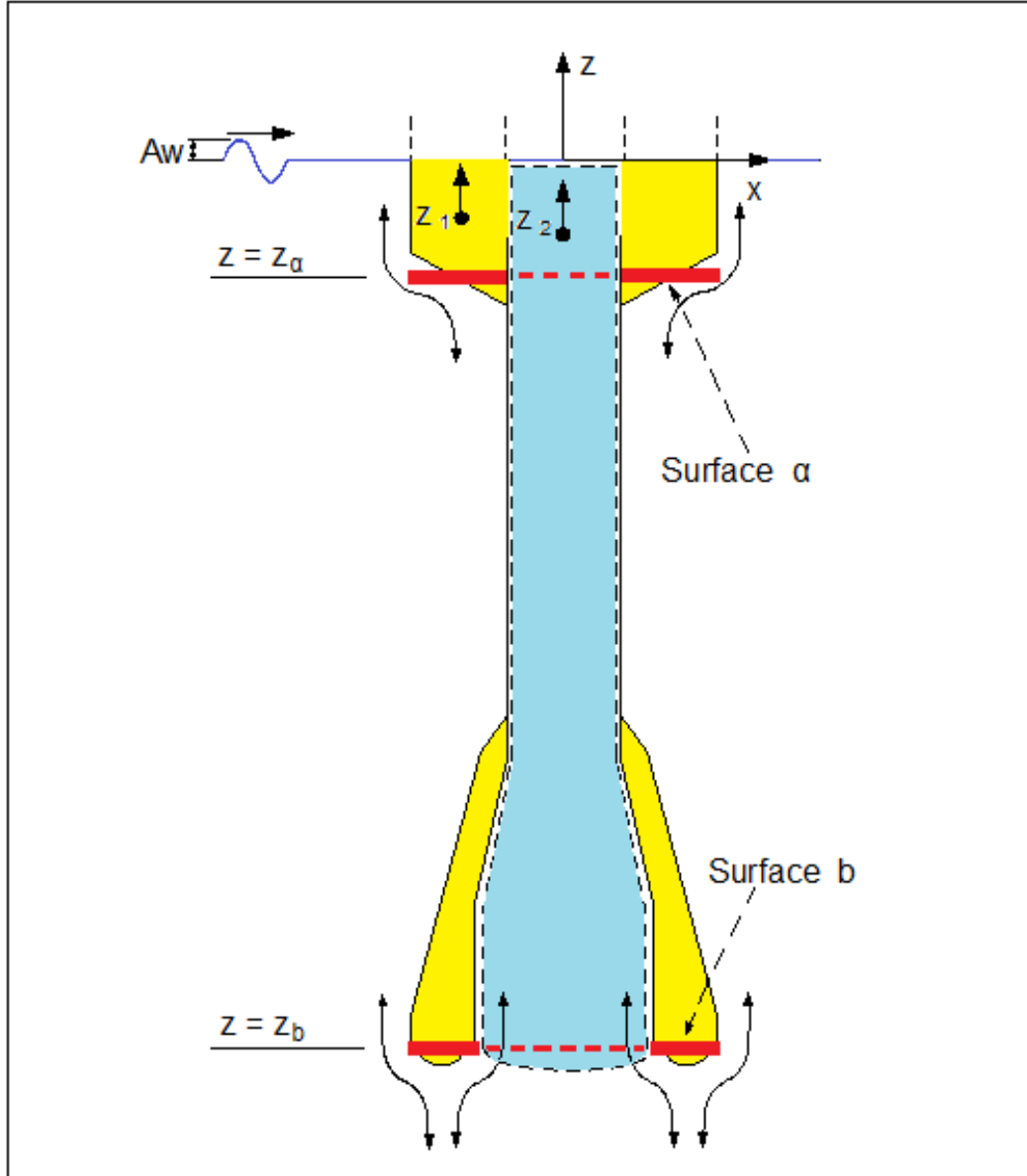


Figure 4.6: Surfaces experiencing drag. Originally from Gomes et al. (2016).

The equation of motion for the CW in the three modes, in the frequency-domain, is

$$\sum_{j=22}^{24} [-\omega^2(m_{cw} + A_{cw}) + i\omega B_{cw}]x_j = F_{exc,cw,i} + F_{im,i} + F_{d,cw,i}, \quad (4.35)$$

where $F_{d,cw,i}$ represents the amplitude of the drag force that the clump weight experiences from the motion in mode i . The forces $F_{im,j}$ the clump weight experiences due to the inter-body mooring connections with the three buoys are denoted by $F_{im,22}$, $F_{im,23}$, and $F_{im,24}$

The individual terms representing the forces associated with the inter-body mooring

connections for the three buoys are related with the three modes x_{22} , x_{23} , x_{24} , and are expressed in the same manner as in Eqs 3.27 - 3.35. The CW experiences drag which depends on the flow velocity in the x -, y - and z -axis direction. The clump weight drag force amplitude $F_{d,cw,i}$ in mode i is defined as in Eq. 4.20. The corresponding damping coefficients $B_{d,cw,j}$, associated with the drag of the flow on the clump weight is

$$B_{d,cw,i} = \frac{1}{2} \rho_w A_{cw} c_{d,cw} \left(\frac{3\pi}{8} \left| i\omega x_i^{(e)} - u_n(z_{cw}) \right| \right), \quad (4.36)$$

where A_{cw} is the projected surface area of the clump weight, $c_{d,cw}$ is the drag coefficient of a sphere, and the flow velocity in the x - and y -axis direction, in the absence of the weight and buoys, is

$$u_x = \frac{gkA_w}{\omega} \frac{\cosh[k(h+z)]}{\cosh kh} \cos \theta e^{-zk(x \cos \theta + y \sin \theta)}, \quad (4.37)$$

$$u_y = \frac{gkA_w}{\omega} \frac{\cosh[k(h+z)]}{\cosh kh} \sin \theta e^{-zk(x \cos \theta + y \sin \theta)}. \quad (4.38)$$

The flow velocity in the z -axis direction is given by Eq. 4.23.

4.2.7 Bottom mooring line forces

One bottom mooring line is attached to the centre of floatation of each device (Section 3.2.6). The forces applied on the three devices, due to the presence of the bottom mooring lines, are identical to Eqs. 3.36 - 3.49.

4.2.8 Independently moored array

The methodology presented previously was also applied for an array where the devices were only moored with bottom mooring lines (Fig. 4.7). Each device was attached to the sea bottom via three bottom mooring lines. In this case, the equation of motion (Eq. 4.1) still applies but the force amplitude of the inter-body line F_{im} is zero. Eqs. 4.1 - 4.27 remain the same, but a different set of equations is introduced for the three bottom mooring lines per device. The tensions on the bottom mooring lines are denoted as $\bar{f}_{j,s}$, where j is the index of the device ($j = 1, 2, 3$) and s refers to the line designation ($s = A, B, C$), with A referring to the bottom mooring line from the inter-body mooring configuration, and the others being distributed in a clockwise direction. Based on the works of Fitzgerald and Bergdahl (2008) and Vicente et al. (2009a), it can be easily shown that the forces applied to the three devices due to the presence of the bottom

mooring lines can be expressed as

$$f_{1,\text{bm}} = -\cos \beta \left(\frac{1}{2} f_{1,A} - f_{1,B} + \frac{1}{2} f_{1,C} \right), \quad (4.39)$$

$$f_{2,\text{bm}} = \frac{\sqrt{3}}{2} \cos \beta (f_{1,A} - f_{1,C}), \quad (4.40)$$

$$f_{3,\text{bm}} = -\sin \beta (f_{1,A} + f_{1,B} + f_{1,C}), \quad (4.41)$$

$$f_{7,\text{bm}} = -\cos \beta \left(\frac{1}{2} f_{2,A} + \frac{1}{2} f_{2,B} - f_{2,C} \right), \quad (4.42)$$

$$f_{8,\text{bm}} = -\frac{\sqrt{3}}{2} \cos \beta (f_{2,A} - f_{2,B}), \quad (4.43)$$

$$f_{9,\text{bm}} = -\sin \beta (f_{2,A} + f_{2,B} + f_{2,C}), \quad (4.44)$$

$$f_{13,\text{bm}} = \cos \beta \left(f_{3,A} - \frac{1}{2} f_{3,B} - \frac{1}{2} f_{3,C} \right), \quad (4.45)$$

$$f_{14,\text{bm}} = -\frac{\sqrt{3}}{2} \cos \beta (f_{3,B} + f_{3,C}), \quad (4.46)$$

$$f_{15,\text{bm}} = -\sin \beta (f_{3,A} + f_{3,B} + f_{3,C}). \quad (4.47)$$

As in the previous case, the extensions $\phi_{j,s}$ of mooring line s ($s = A, B, C$) from body j ($j = 1, 2, 3$) due to displacements of body j can be obtained by linear decomposition,

$$\phi_{1,A} = (x_1 - \sqrt{3}x_2) \frac{\cos \beta}{2} + x_3 \sin \beta, \quad (4.48)$$

$$\phi_{1,B} = -x_1 \cos \beta + x_2 \sin \beta, \quad (4.49)$$

$$\phi_{1,C} = (x_1 + \sqrt{3}x_2) \frac{\cos \beta}{2} + x_3 \sin \beta, \quad (4.50)$$

$$\phi_{2,A} = (x_7 + \sqrt{3}x_8) \frac{\cos \beta}{2} + x_9 \sin \beta, \quad (4.51)$$

$$\phi_{2,B} = (x_7 - \sqrt{3}x_8) \frac{\cos \beta}{2} + x_9 \sin \beta, \quad (4.52)$$

$$\phi_{2,C} = -x_7 \cos \beta + x_9 \sin \beta, \quad (4.53)$$

$$\phi_{3,A} = -x_{13} \cos \beta + x_{15} \sin \beta, \quad (4.54)$$

$$\phi_{3,B} = (x_{13} + \sqrt{3}x_{14}) \frac{\cos \beta}{2} + x_{15} \sin \beta, \quad (4.55)$$

$$\phi_{3,C} = (x_{13} - \sqrt{3}x_{14}) \frac{\cos \beta}{2} + x_{15} \sin \beta. \quad (4.56)$$

The dynamics of each mooring line are described by Eq. 3.49.

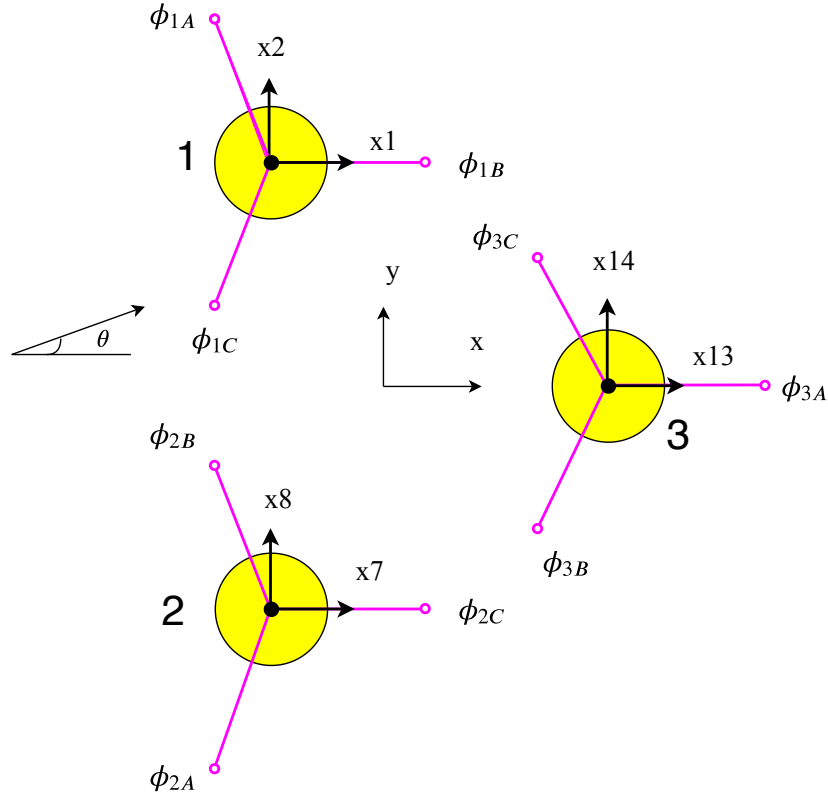


Figure 4.7: Three-dimensional view of the triangular array with inter-body mooring connections.

4.2.9 Capture width ratio

The power available to the turbine is calculated via the following formula

$$\bar{P}_t = \frac{1}{2} \omega^2 B_t |x_i - x_j|^2, \quad (4.57)$$

for $(i, j) = (3, 19), (9, 20), (15, 21)$. For a regular wave with wavenumber k propagating at a water depth h , the time-averaged power transported by a wave per unit wave crest length is

$$\bar{P}_w = \frac{\rho_w g \omega A_w^2}{4k} \left(1 + \frac{2kh}{\sinh(2kh)} \right). \quad (4.58)$$

The Capture Width Ratio (CWR) (Falnes (2002), Babarit (2015)) is a measure of the wave energy conversion efficiency, given by

$$\text{CWR} = \frac{\bar{P}_t}{\bar{P}_w d_1}, \quad (4.59)$$

where d_1 is the buoy's diameter.

4.3 Numerical model: irregular wave analysis

The model for the moored triangular array of spar-buoy OWCs is further extended in order to compute the performance of the array under irregular wave conditions. For the purposes of the study, a stochastic model was constructed following the methodology presented in Gomes et al. (2016), and originally presented in Falcão and Rodrigues (2002). The stochastic analysis is conducted for various sea states to assess the behaviour of the array with shared mooring connections. The park effect of the array is evaluated for a realistic wave climate.

The model assumes that a sea state is represented by the superposition of elementary regular wave components with frequency ω and amplitude A_w . The instantaneous free-surface elevation at a given position can be described as a stationary, ergodic, and Gaussian process. The linear relation between the free-surface elevation and system responses allows statistical estimations of these parameters to be made. Further details on this theory may be found in Sarpkaya and Isaacson (1981), Goda (2010).

4.3.1 Wave spectrum

To optimise a wave energy conversion technology for a particular wave climate, numerical modelling must be performed in either the stochastic or time-domain. Both these approaches consider irregular waves, for which a wave energy density spectrum needs to be introduced. As explained in Section 2.10.5, spectra such as P-M, JONSWAP, and two peak JONSWAP - the latter corresponding to separate sea and swell components (Luxmoore, 2014) - may be used to characterise a given wave climate. In this thesis, the wave resource on the west coast of Portugal is considered. It seems reasonable to classify this location as long fetch zone with fully developed swell, which is the result of remotely generated weather systems which allow waves to travel to hundreds of kilometers with little attenuation. This is contrary to locations like the North Sea, which are characterised by short fetch and newly developing wind seas. It should also be noted that the spar-buoy OWC was originally optimised to represent an offshore Portuguese location. For consistency, it is important to consider the same location, the same set of sea states, and the same spectrum. In future work, another location (e.g. in the North Sea using the JONSWAP spectrum, or in the Irish Sea using a two peak spectrum) could be considered in the modelling. However, it is expected that the performance will be lower compared to the case of Portugal with P-M, since this is the location for which the device geometry was tuned.

The semi-empirical P-M energy density spectrum for fully developed seas is given by Pierson and Moskowitz (1964)

$$S_\omega(\omega) = 262.99 \frac{H_s^2}{T_e^4 \omega^5} \exp\left(-\frac{1051.97}{T_e^4 \omega^4}\right), \quad (4.60)$$

where H_s is the significant wave height and T_e is the energy period, as shown in Eqs. 2.29

and 2.30. The variance in the system response is given by

$$\sigma_\chi^2 = \int_0^\infty S_\omega(\omega) \left| \frac{\chi(\omega)}{A_w} \right|^2 d\omega. \quad (4.61)$$

Here χ is a generic parameter that represents either motion (e.g. displacement, velocity, acceleration) or dynamic pressure head in the PTO air chamber.

4.3.2 Power available to the turbine

The time-averaged power available to the turbine for a given irregular wave sea state is

$$\bar{P}_t = \frac{k_t}{\rho_\alpha} \sigma_p^2, \quad (4.62)$$

where σ_p is the standard deviation of the pressure difference between the air chamber and the atmosphere. The CWR can now be calculated for the case of irregular waves, the same way as the case for regular waves presented in Eq. 4.59. In this case though, the time-averaged power transported by a wave per unit wave crest length $\bar{P}_{w,\text{irr}}$ can be computed via the sum of all discrete regular wave components, $\bar{P}_w(\omega, A_w(\omega))$ over the range of frequencies considered in the irregular-wave energy spectrum. This is to say,

$$\bar{P}_{w,\text{irr}} = \sum \bar{P}_w(\omega, A_w(\omega)), \quad (4.63)$$

where the regular wave components are a function of the frequency-dependent amplitude $A_w(\omega) = \sqrt{2S_\omega(\omega)\Delta\omega}$, and $\Delta\omega$ is the frequency interval being considered.

4.3.3 Viscous damping

For irregular waves, the linearised drag formulation presented in Sec. 4.2.5 is not applicable since the quadratic dependency with the wave amplitude A_w is not possible to verify. For this reason, the method described in Borgman (1967) is applied. The method linearises the drag forces using the standard deviation of the oscillatory velocity for a given sea state (Sarpkaya and Isaacson, 1981). This approach considers that a given oscillatory velocity u follows a Gaussian probability distribution with mean zero and standard deviation σ_u . A better linear approximation of the quadratic force (proportional to $|u|u$) is observed for $|u|u \approx \sqrt{8/\pi}\sigma_u u$. Therefore, for irregular waves, the linearised damping coefficients in surge ($i = 1, 7, 13$), sway ($i = 2, 8, 14$), roll ($i = 4, 10, 16$), and pitch ($i = 5, 11, 17$) are expressed as

$$B_{d,i} = \frac{1}{2}\rho_w A_{d,i} c_{d,i} \sqrt{\frac{8}{\pi}} \sigma_{\dot{x}_i}, \quad (4.64)$$

where the standard deviation of the velocity ωx_i of mode i can be obtained from Eq. 4.61.

The drag damping coefficient of the buoy in heave presented in Eq. 4.24 is replaced by

$$B_{d,z,n} = \frac{1}{2}\rho_w c_{d,3} A_{d,z,n} \sqrt{\frac{8}{\pi}} \sigma_{(\dot{x}_3 - u_z)}, \quad (4.65)$$

where $\sigma(\dot{x}_3 - u_z)$ is the standard deviation of the velocity $\omega x_3 - u_z(z_n)$, and $u_z(z_n)$ is the flow velocity at the z -coordinate z_n .

The drag damping coefficient of the flow inside the tube (replacing Eq. 4.25) is given by

$$B_{d,tb} = \frac{1}{2} \rho_w c_{d,tb} A_{d,tb} \sqrt{\frac{8}{\pi}} \sigma(\dot{x}_i - \dot{x}_j). \quad (4.66)$$

Here $\sigma(\dot{x}_i - \dot{x}_j)$ is the standard deviation of the heave velocity difference between the buoy and the OWC ($\omega x_i - \omega x_j$), for $(i, j) = (3, 19), (9, 20), (15, 21)$.

Similarly, the corresponding damping coefficients associated with drag effects on the CW are

$$B_{d,cw,i} = \frac{1}{2} \rho_w A_{cw} c_{d,cw} \sqrt{\frac{8}{\pi}} \sigma(\dot{x}_i - u_n), \quad (4.67)$$

where $\sigma(\dot{x}_i - u_n)$ is the standard deviation of relative velocity between the clump weight in mode i and the flow velocity in the same direction ($\omega x_i - u_n$).

4.3.4 Gain factor

The annual average gain factor is defined as

$$q = \frac{\sum_{i=1}^N \bar{P}_{ann,i}}{N \bar{P}_{ann,iso}}, \quad (4.68)$$

where $\bar{P}_{ann,i}$ is the annual average power available to the turbine of device i in the N -device array, and $\bar{P}_{ann,iso}$ is the annual average power available to the turbine of an unmoored isolated device with similar properties. The annual average power available to the turbine of device i is

$$\bar{P}_{ann,i} = \sum_{m=1}^M \phi_m \bar{P}_{irr,i}, \quad (4.69)$$

where ϕ_m represents the frequency of occurrence of a given sea state m over a long period of time, and M is the total number of sea states considered for defining the annual average wave climate. A total of 14 sea states were taken into consideration. The frequency of occurrence ϕ_m for these sea states was obtained from Gomes et al. (2012), which is a reduced version of a larger set of sea states representing the same wave climate, presented originally in Gomes et al. (2010) (Table 4.2).

4.4 Results and discussion

In this analysis, the geometry of the spar-buoy OWC device presented in Gomes et al. (2012) is considered, with a buoy diameter $d_1 = 12$ m, an OWC diameter $d_2 = 4.82$ m and a draught $l_t = 36$ m. The geometry was optimised for the wave climate presented in Table 4.2. The physical properties of the geometry are presented in Table 4.3, along with the default model parameters. The frequency-dependent hydrodynamic coefficients were calculated, considering a water depth $h = 80$ m.

Table 4.2: The 14 sea states and their characteristics, source: Gomes et al. (2010, 2012).

m	H_s [m]	T_e [s]	ϕ_m	P [kW/m]	$\phi_m P$ [kW/m]
1	1.10	5.49	7.04	3.26	0.23
2	1.18	6.50	12.35	4.41	0.55
3	1.23	7.75	8.17	5.78	0.47
4	1.88	6.33	11.57	11.02	1.27
5	1.96	7.97	20.66	15.02	3.10
6	2.07	9.75	8.61	20.49	1.76
7	2.14	11.58	0.59	26.11	0.15
8	3.06	8.03	9.41	36.74	3.46
9	3.18	9.93	10.07	49.34	4.97
10	3.29	11.80	2.57	62.62	1.61
11	4.75	9.84	4.72	109.01	5.14
12	4.91	12.03	2.81	142.06	3.99
13	6.99	11.69	1.01	280.12	2.83
14	8.17	13.91	0.39	454.85	1.77

4.4.1 Regular wave analysis

The current section presents an analysis of the Response Amplitude Operators (RAOs) of the system. The RAOs correspond to the ratio between the amplitudes of the modes of interest (that is, all 6 DoF for the buoy and one additional heaving mode for the OWC) and the incident wave amplitude A_w . For regular-wave analysis, the wave amplitude was set to $A_w = 1$ m.

For the formulation of the heave drag force (see Eq. 4.22), two drag surfaces are considered, as in Gomes et al. (2016). The first drag surface ($n = A$), located at $z_A = -5$ m has an area $A_{d,z,A} = 94.8658$ m². The second surface ($n = B$), located at the bottom part of the device, at $z_B = -36$ m has an area $A_{d,z,B} = 96.912$ m². Since the geometry is axisymmetric, surge and sway modes have the same frontal area. Therefore, $A_{d,i} = 282.989$ m², for $i = 1, 2, 7, 8, 13, 14$. The same rationale applies for roll and pitch, where $A_{d,i} = 4.1 \times 10^6$ m⁵, for $i = 4, 5, 10, 11, 16, 17$. The drag coefficients were determined using experimental data from small-scale wave flume tests (decay and regular wave tests). The damping forces associated with viscous effects are likely to be over-estimated, since the experimental coefficients also include scale effects. For all buoys, the same drag coefficients were considered. The drag coefficient of the buoy in heave was $c_{d,3} = 0.731$, for the tube was $c_{d,tb} = 1.965$, and for all other modes was $c_{d,i} = 2.0$. In the following set of graphs, the vertical lines in the heave RAOs, correspond to the system's natural frequencies. Since the spar-buoy OWC is a two-body heaving system, it has two natural frequencies, one for the buoy and one for the OWC. The natural frequency of

Table 4.3: Spar-buoy OWC physical properties. The moments of inertia are measured at the axes of the device reference frame. The table also includes the model default parameters.

Parameter	Value
Buoy diameter d_1 (at $z = 0$) [m]	12.00
OWC diameter d_2 (at $z = 0$) [m]	4.82
Draught l_t (unmoored) [m]	36.00
Mass m [kg]	1217.4×10^3
Moment of inertia I_{55} ($= I_{44}$) [kg m^2]	778.51×10^6
Moment of inertia I_{66} [kg m^2]	29.1×10^6
CoG z -coordinate z_g [m]	-19.29
CoB z -coordinate z_b [m]	-18.04
Metacentric height \overline{GM} [m]	2.08
First drag surface location z_A [m]	-5
Second drag surface location z_B [m]	-36
First drag surface area $A_{d,z,A}$ [m^2]	94.8658
Second drag surface area $A_{d,z,B}$ [m^2]	96.912
Drag area for surge and sway $A_{d,i}$ [m^2]	282.989
Drag area moment for roll and pitch $A_{d,i}$ [m^5]	4.1×10^6
Drag coef. in heave $c_{d,3}$ [-]	0.731
Drag coef. for the tube $c_{d,tb}$ [-]	1.965
Drag coef. for surge, sway, roll, and pitch $c_{d,i}$ [-]	2.0
Water depth h [m]	80
Wave amplitude A_w [-]	1.0
Wells turbine coef. k_t [ms]	0.00150
Bottom mooring line stiffness C_{bm}^* [-]	0.1
Angle of bottom mooring force β [$^\circ$]	30
Angle of inter-body mooring force α [$^\circ$]	30
Angle of wave incidence θ [$^\circ$]	30

each buoy was estimated to be 0.693 rad/s (period of 9.1 s), and for each corresponding OWCs it was estimated to be 0.555 rad/s (period of 11.3 s). The inclusion of the viscous damping in the numerical model was very important, since it appeared to affect the hydrodynamic responses of the devices, close to the natural frequency of each mode. The graphs indicating the importance of the inclusion of the viscous damping are presented in Appendix C.

Single device, variation of the turbine coefficient

The selection of the turbine coefficient k_t was made based on its effect on the buoy heaving RAO, $|Z_b|/A_w$ ($Z_b \equiv x_i$ for $i = 3, 9, 15$) (Fig. 4.8a), and on the relative heaving RAO between the buoy and the OWC, $|Z_r|/A_w$ ($Z_r \equiv x_i - x_j$ for $(i, j) = (3, 19), (6, 20), (15, 21)$) (Fig. 4.8b). Different values of the turbine coefficient k_t were tested: $k_t = 0.00023, 0.00150, 0.00500, 0.01, 0.02909$ m s. The selected value for the results presented in this study was $k_t = 0.00150$ m s, since it contributed to the optimum CWR. Air turbine coefficients of the same order of magnitude were used in Gomes et al. (2016), where a similar device with different dimensions was modelled. A very high turbine coefficient would correspond to nearly zero turbine damping - the case of a closed turbine chamber, meaning that there would be essentially no energy extracted by the PTO. This can be used as a survival strategy during stormy conditions, coupled with partial sinking of the device. On the other hand, a turbine coefficient that would provide a very high PTO damping would correspond to a low relative motion RAO, and may also not be ideal for energy extraction. In selecting the optimum turbine coefficient, a value should be chosen so that it contributes to the highest possible CWR (Fig. 4.9). This implies that a relative motion response which spans a wide range of frequencies is desired, where the two peaks - one for the buoy and one for the OWC - would merge into one wide response. This information provides preliminary insight into the design of the air turbine, since the turbine coefficient k_t is related to the turbine diameter.

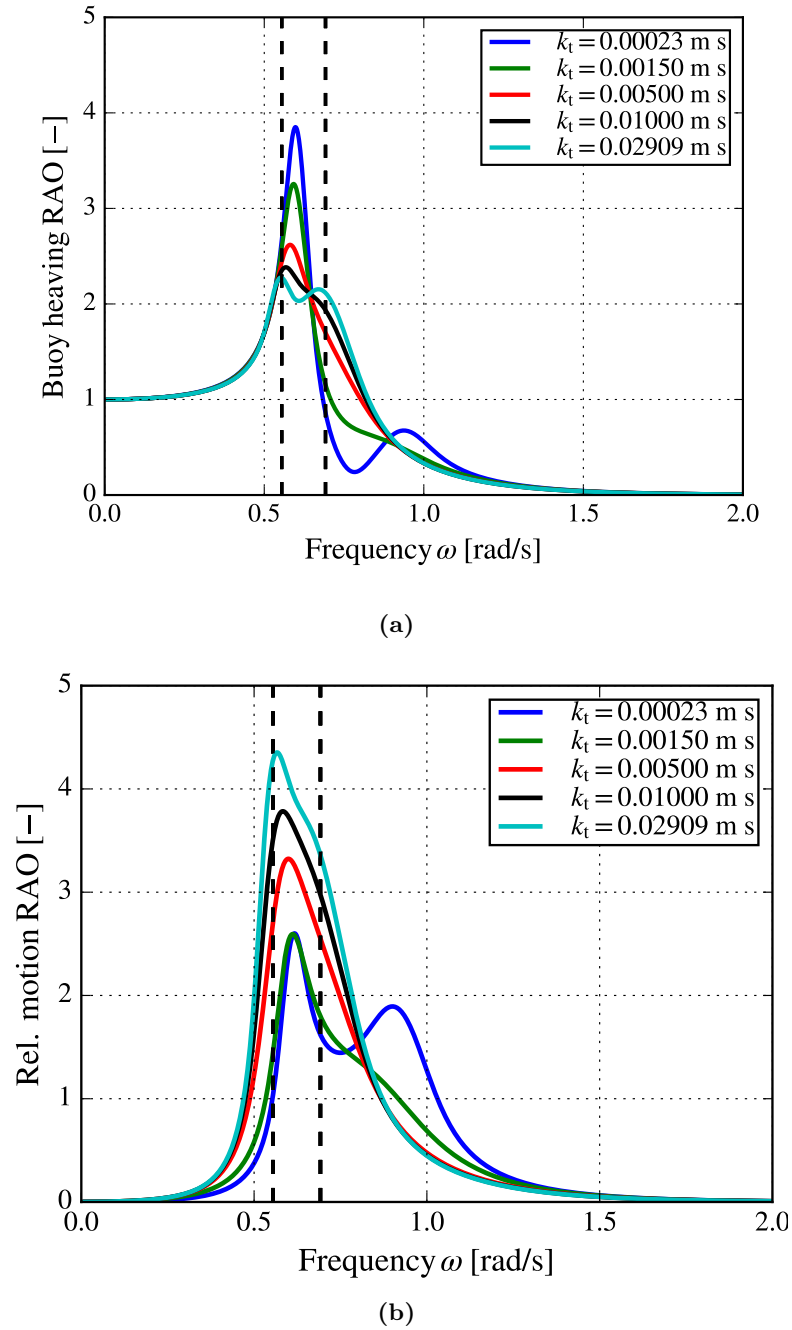


Figure 4.8: Heave RAO and relative motion RAO for a single spar-buoy OWC, as a function of the wave frequency ω , for a variation of turbine coefficients: $k_t = 0.00023, 0.00150, 0.005, 0.01, 0.02909$ ms.

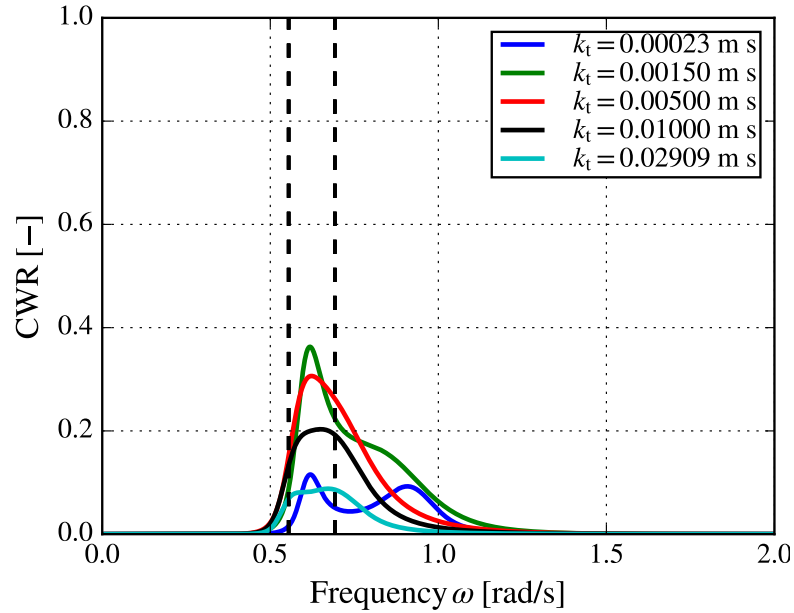


Figure 4.9: CWR as a function of the wave frequency ω for a single spar-buoy OWC, for a variation of turbine coefficients: $k_t = 0.00023, 0.00150, 0.005, 0.01, 0.02909$ ms.

4.4.2 Array of spar-buoy OWCs

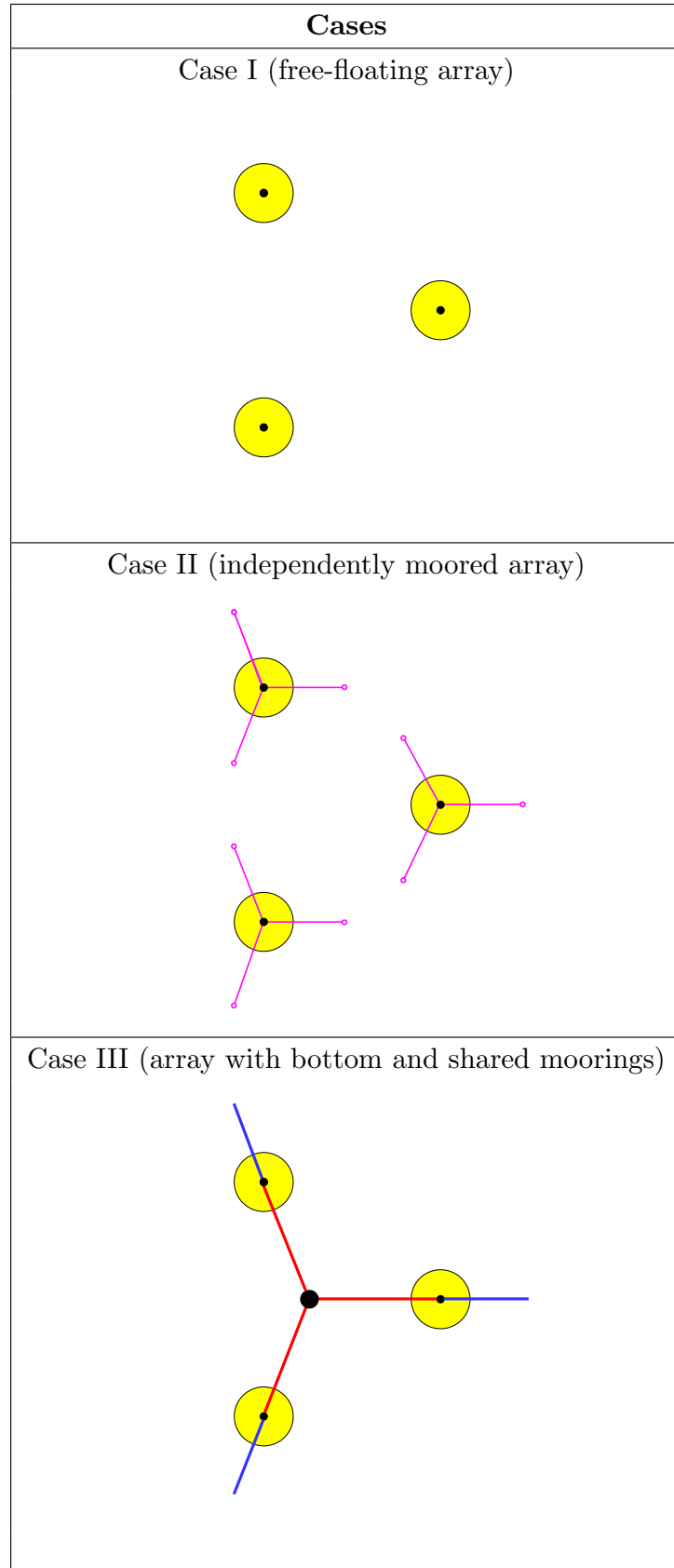
The following computations were undertaken (summarised in Table 4.4):

- Case I: Unmoored array of spar-buoy OWCs;
- Case II: Independently moored array of spar-buoy OWCs, with 3 bottom mooring lines each;
- Case III: Array of spar-buoy OWCs with bottom and inter-body mooring connections.

The three spar-buoy OWCs were set in a triangular configuration, separated by a distance of $\sqrt{3}L$, where L was set to 30 m. The added mass A_{ij} and the radiation damping coefficient B_{ij} for the individual buoys and the corresponding OWCs of the triangular array were calculated using WAMIT, considering a uniform water depth of $h = 80$ m.

For Case II, each device was bottom moored with three mooring connections. The dimensionless stiffness of the mooring line C_{bm}^* was set to 0.1 (where $C_{bm} = C_{bm}^* \rho g S_b$). The linear damping B_{bm} and inertia of the mooring cables A_{bm} were neglected in this analysis (as in Vicente et al. (2009a) and in the computations undertaken in Chapter 3). The angle formed between the bottom mooring line and the horizontal free surface plane, β , was set to 30° , and the angle of wave incidence θ was set to 0.

For Case III, the inter-body connections were modelled as in Fig. 4.1 and Fig. 4.2, where the clump weight is introduced in the centre of the array. The clump weight is of spherical shape, and has a density of $\rho_{cw} = 2500 \text{ kg/m}^3$. Its mass is equal to 5% of the mass of the device, to be consistent with Chapter 3.

Table 4.4: Schematic representation of the array cases studied.

Regarding the bottom mooring lines, the linear damping B_{bm} and inertia of the mooring cables A_{bm} were neglected, as for Case II and in Vicente et al. (2009a) and Chapter 3. The angle formed between the bottom mooring line and the horizontal free surface plane, β , was set to 30° . The angle α , formed between the inter-body mooring line and the horizontal free surface plane, was also set to 30° throughout these calculations. The angle of wave incidence θ was set to 0.

Since the clump weight is deeply submerged, and is located at a significant vertical distance from the free surface ($z = z_{\text{cw}}$), the frequency-dependent radiation damping coefficients ($B_{\text{cw,hr}}$ and $B_{\text{cw,z}}$) and excitation force coefficients ($F_{\text{cw,exc},i}$, for $i = 22, 23, 24$) were neglected in the equation of motion. Regarding the bottom mooring lines, the linear damping B_{bm} and inertia of the mooring cables A_{bm} were neglected, as for Case II and in Vicente et al. (2009a). The angle formed between the bottom mooring line and the horizontal free surface plane, β , was set to 30° . The angle α , formed between the inter-body mooring line and the horizontal free surface plane, was also set to 30° throughout these calculations. The angle of wave incidence θ was set to 0.

Due to the symmetry of the problem for $\theta = 0$, Buoy 1 and Buoy 2, and their respective OWCs experienced the same RAOs in all modes and the same CWR. Therefore, in the following results, Buoy 1 and Buoy 2 are referred as "Buoy 1,2". The following set of figures (Fig. 4.10 - 4.13) presents the surge, heave, and pitch RAOs, as well as the CWR, as a function of the wave frequency ω , for the unmoored array (Case I), the independently moored array (Case II), and the array with bottom and inter-body mooring connections (Case III). The results for a single unmoored device and a single device with three bottom mooring connections are presented for comparison.

For the triangular array with unmoored devices (Case I), an oscillatory behaviour is observed for the surge and pitch RAOs over frequency ω . This can be seen for wave frequencies higher than 0.6 rad/s , due to the hydrodynamic coupling between devices (array effect). When compared to the isolated unmoored device, the unmoored array shows a better capture width for Buoys 1 and 2 at the peak frequency, but a lower value for Buoy 3. This comes into agreement with the effect observed in the unmoored arrays of SPAs and CPAs in the previous chapter.

By introducing bottom mooring lines in a single device (i.e. a horizontal restoring effect) (Case II), the surge RAO peak appears at low frequencies, instead of tending to infinity at $\omega = 0$ in the unmoored case (Fig. 4.10). The pitch RAO significantly increases at frequencies lower than 0.5 rad/s due to the coupling effect between surge and pitch (Fig. 4.12). The CWR increases by 8.1% at the peak frequency, despite the decrease by approximately 12.2% in the heave RAO at the peak frequency (Fig. 4.11).

The CWR for the isolated moored device and independently moored array (Case II) shows the same trend (Fig. 4.13).

Regarding the array with inter-body connections (Case III), the heave RAO of Buoy 1,2 decreases by 9.0% at the peak frequency, compared to the heave RAO of Buoy 1,2 for the unmoored array, while the heave RAO of Buoy 3 decreases by 3.8%, compared to the heave RAO of Buoy 3 of the unmoored array (Fig. 4.11). Although this appears to have an adverse effect on the array's performance, the CWR must also be examined, as it is a function of the relative motion between the buoys and their respective OWCs.

When compared to the unmoored array configuration (Case I), the independently moored array (Case II) shows improvements in the CWR of 7.1% for Buoy 1,2 and 7.8% for Buoy 3, at the peak frequency (Fig. 4.13). Making the same comparison, Case III shows a similar value for Buoy 1,2 and an increase of 7.1% of Buoy 3, at the peak frequency. It is worth mentioning that these findings are strongly dependent on the value of the mooring stiffness C_{bm} . For example, in Case II, a higher mooring stiffness would contribute to a smaller increase in the capture width.

The peaks in the surge and pitch responses of the buoys at very low frequencies (Figs 4.10, 4.12) are likely due to a breakdown in the model's validity, which is based on linear theory. In this region of operation, the model is not able to account for the non-linearities introduced by the mooring lines. In the above responses, the peaks occur between 0.1 – 0.2 rad/s (wave periods of 31.4 – 62.8 s), which correspond to the long wavelengths seen in stormy seas. Although the model does not accurately predict the performance of the system during storms, it should also be noted that under these circumstances, a WEC would normally be entering its survivability mode of operation.

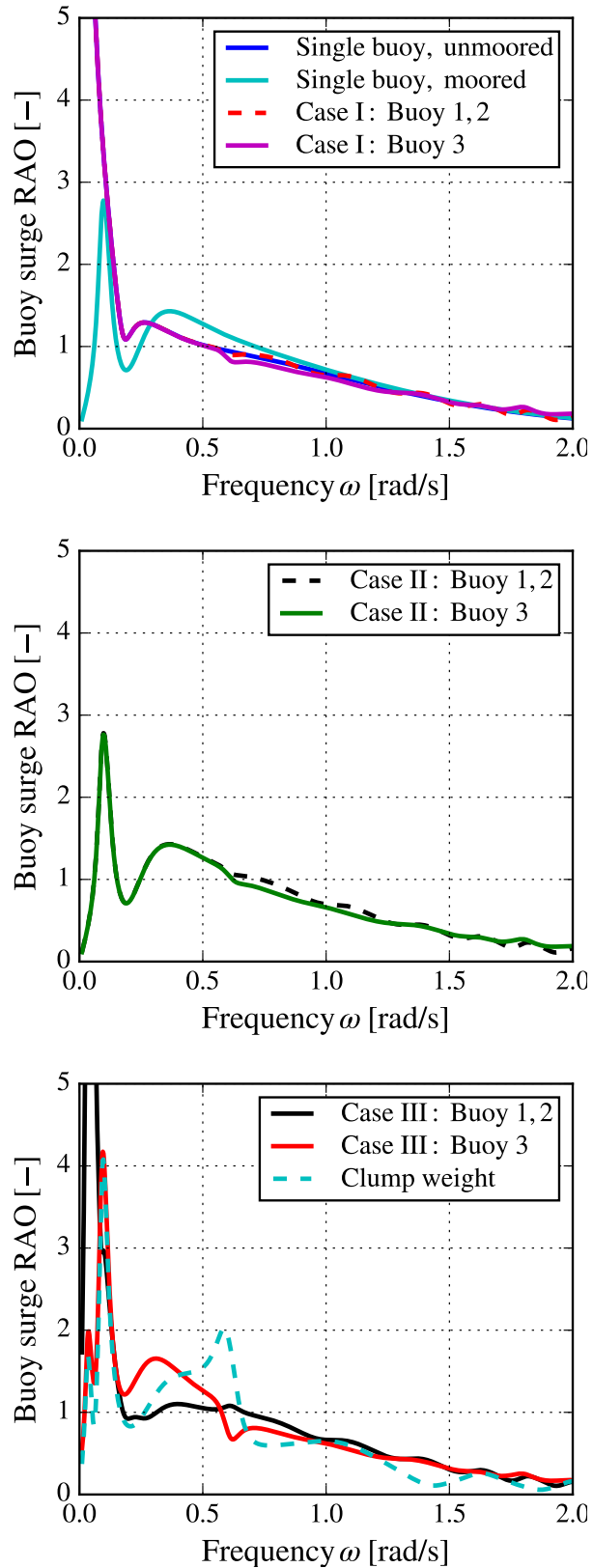


Figure 4.10: Surge RAOs against the wave frequency ω , for $k_t = 0.0015$ ms, $A_w = 1$ m, $C_{bm}^* = 0.1$, $\alpha = 30^\circ$, $\beta = 30^\circ$, and $\theta = 30^\circ$, for the unmoored array (Case I), the individually moored array (Case II), and the array with bottom and inter-body mooring connections (Case III), for the three buoys and the clump weight.

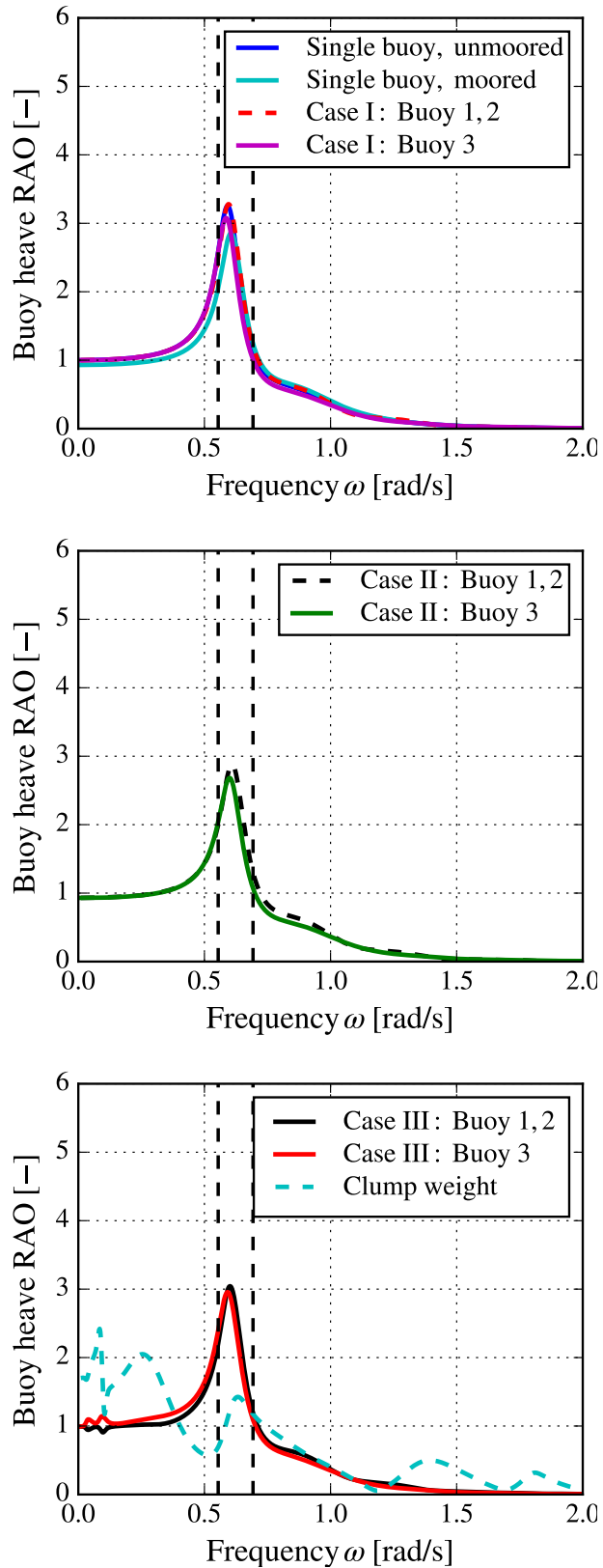


Figure 4.11: Heave RAOs against the wave frequency ω , for $k_t = 0.0015$ ms, $A_w = 1$ m, $C_{bm}^* = 0.1$, $\alpha = 30^\circ$, $\beta = 30^\circ$, and $\theta = 30^\circ$, for the unmoored array (Case I), the individually moored array (Case II), and the array with bottom and inter-body mooring connections (Case III), for the three buoys and the clump weight.

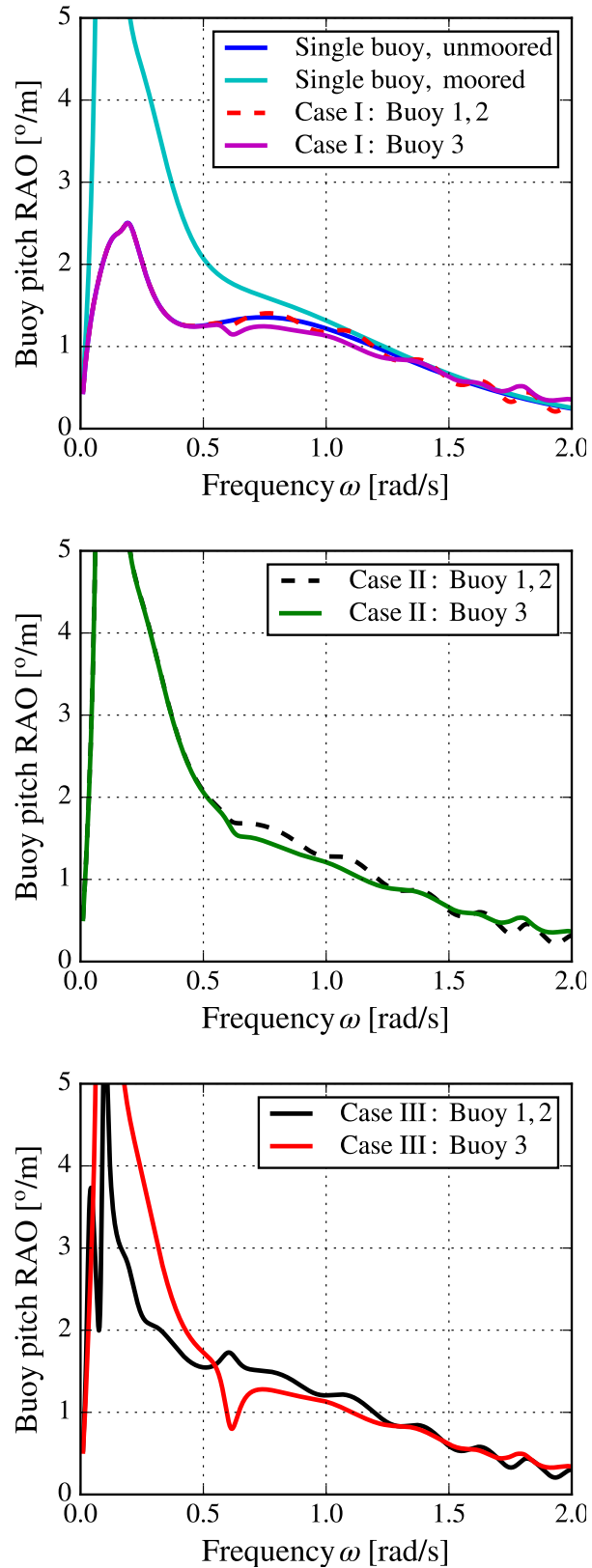


Figure 4.12: Pitch RAOs against the wave frequency ω , for $k_t = 0.0015$ ms, $A_w = 1$ m, $C_{bm}^* = 0.1$, $\alpha = 30^\circ$, $\beta = 30^\circ$, and $\theta = 30^\circ$, for the unmoored array (Case I), the individually moored array (Case II), and the array with bottom and inter-body mooring connections (Case III), for the three buoys and the clump weight.

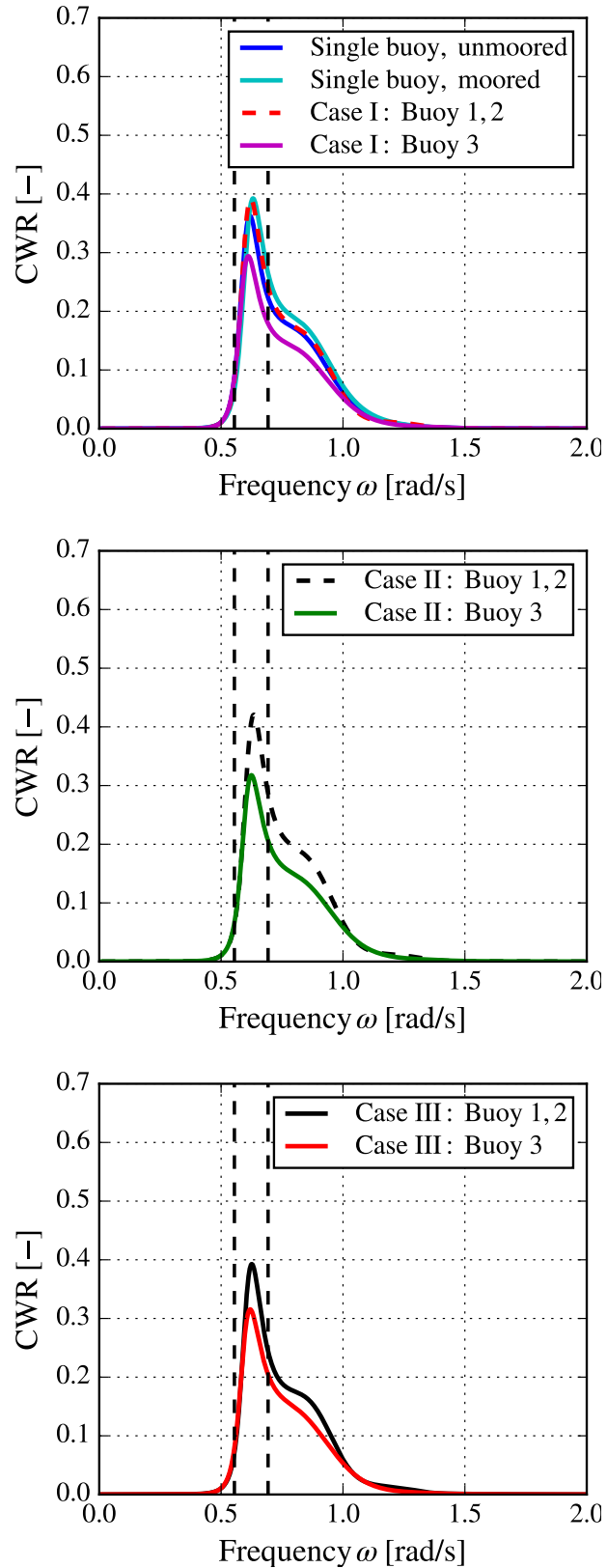


Figure 4.13: CWRs against the wave frequency ω , for $k_t = 0.0015$ ms, $A_w = 1$ m, $C_{bm}^* = 0.1$, $\alpha = 30^\circ$, $\beta = 30^\circ$, and $\theta = 30^\circ$, for the unmoored array (Case I), the individually moored array (Case II), and the array with bottom and inter-body mooring connections (Case III), for the three buoys and the clump weight.

4.4.3 Effect of wave incidence angle

Figs. 4.14, 4.15, 4.16, and Figs. 4.18, 4.19, 4.20, present the translational RAOs of the independently moored array (Case II) and the array with inter-body mooring connections (Case III), respectively, as a function of the wave frequency ω , with varying angle of wave incidence θ .

For higher values of the angle of wave incidence, the surge and sway RAOs of Buoys 1 and 2 for Case II and Case III are no longer identical, since there is no array symmetry about the direction of wave propagation. It should be noted that for the surge and sway RAOs, the presence of the high frequency oscillations are distance dependent, and are the result of array interference.

The heave RAO of the three devices for both cases (Figs. 4.16 and 4.20) appears to remain constant with variations in the angle of wave incidence, and small variations can be observed for the CWR. It should be noted that the device is axisymmetric, and also for a single device there would be not differences in the RAO, after varying the angle of wave incidence θ . Since heave is not significantly coupled with other modes, in the array configuration, it will be agnostic to the changes in θ . Likewise, some small differences can be observed in the CWRs, after varying the angle of wave incidence, at the peak frequency (Figs 4.17 and 4.21).

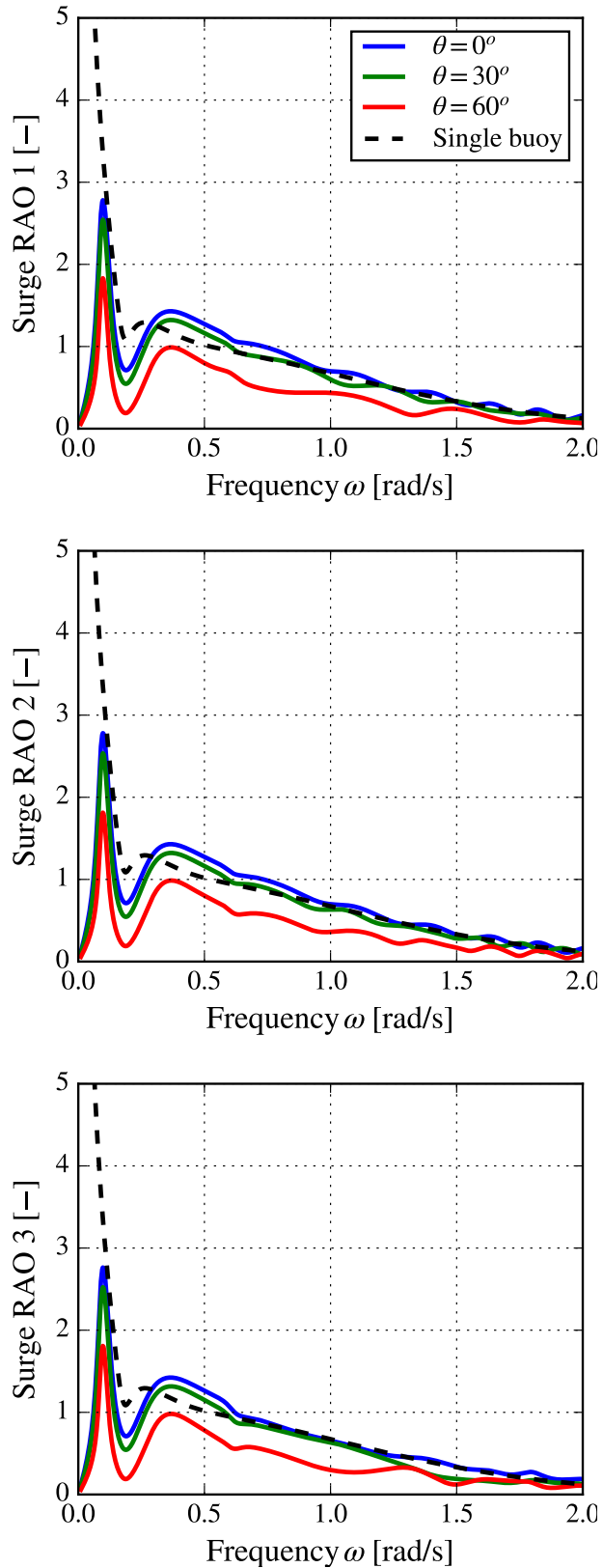


Figure 4.14: Surge RAOs against the wave frequency ω , for $k_t = 0.0015$ ms, $A_w = 1$ m, $C_{bm}^* = 0.1$, $\beta = 30^\circ$, for the individually moored array (Case II), for the three buoys, for three angles of wave incidence θ (0° , 30° , 60°). The results for the single buoy without moorings are provided for comparison.

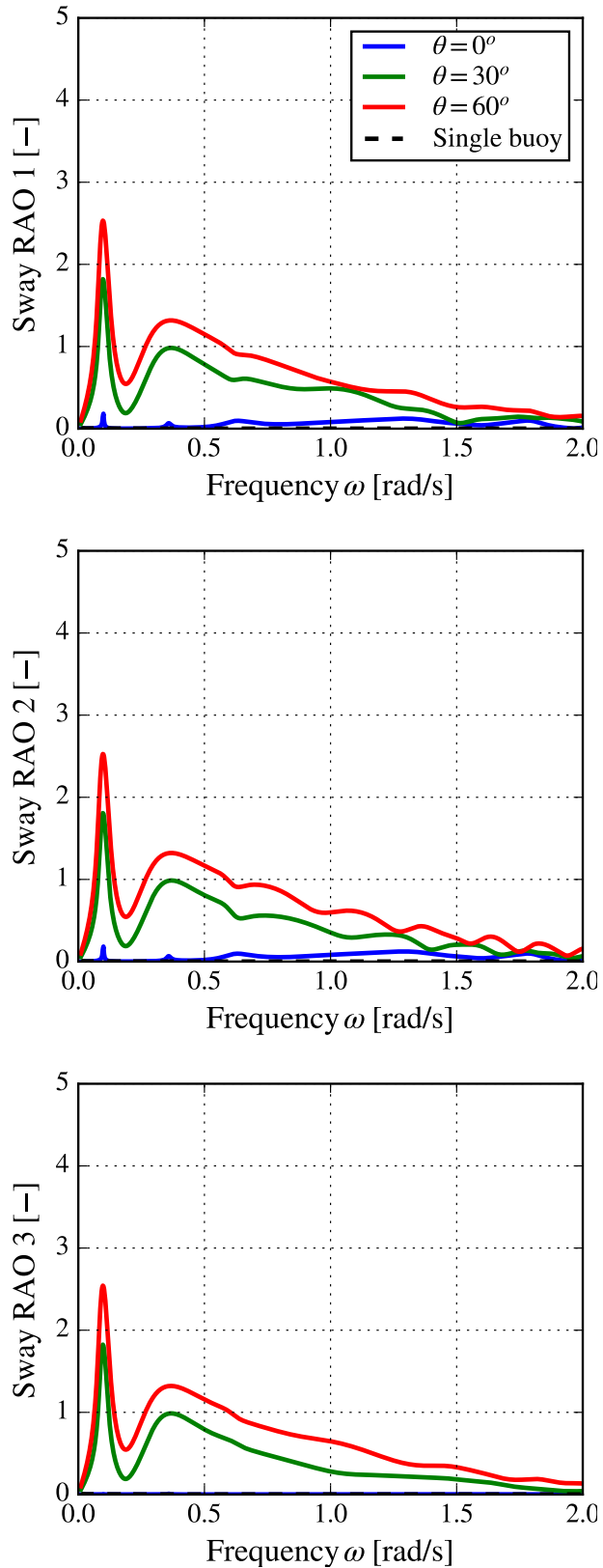


Figure 4.15: Sway RAOs against the wave frequency ω , for $k_t = 0.0015$ ms, $A_w = 1$ m, $C_{bm}^* = 0.1$, $\beta = 30^\circ$, for the individually moored array (Case II), for the three buoys, for three angles of wave incidence θ (0° , 30° , 60°). The results for the single buoy without moorings are provided for comparison.

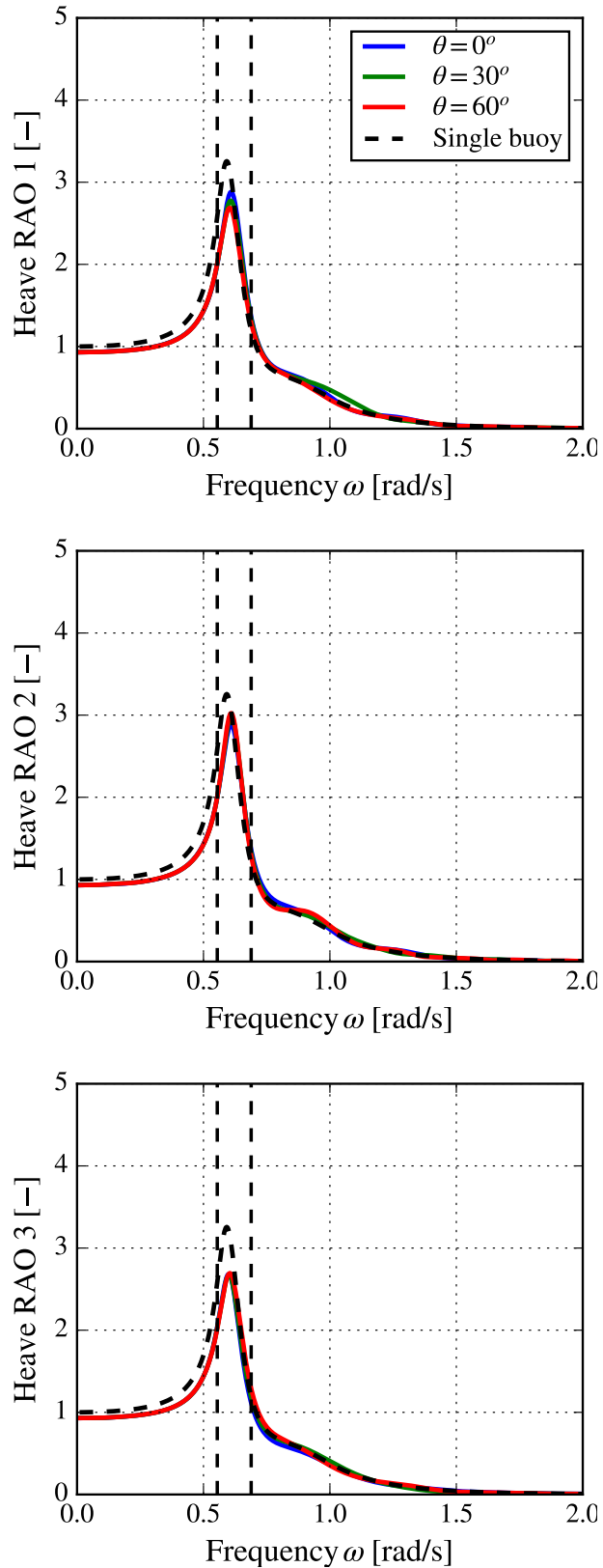


Figure 4.16: Heave RAOs against the wave frequency ω , for $k_t = 0.0015$ ms, $A_w = 1$ m, $C_{bm}^* = 0.1$, $\beta = 30^\circ$, for the individually moored array (Case II), for the three buoys, for three angles of wave incidence θ (0° , 30° , 60°). The results for the single buoy without moorings are provided for comparison.

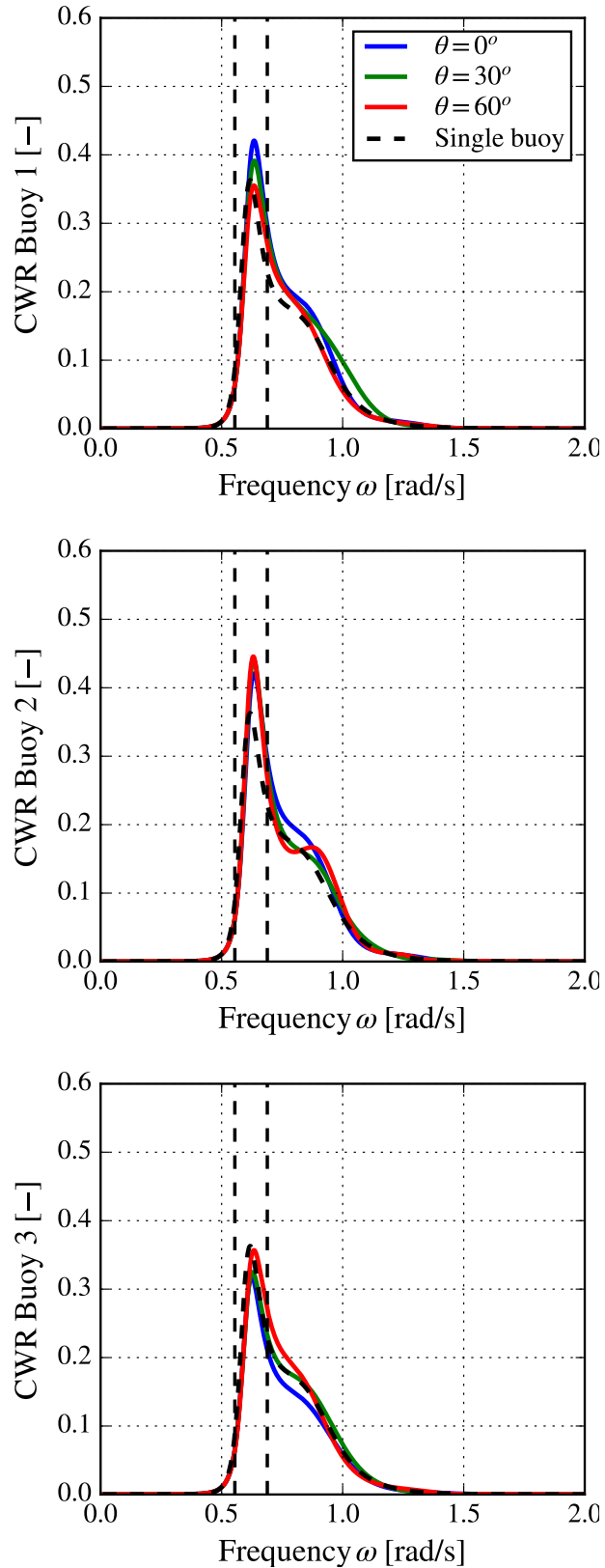


Figure 4.17: CWRs against the wave frequency ω , for $k_t = 0.0015$ ms, $A_w = 1$ m, $C_{bm}^* = 0.1$, $\beta = 30^\circ$, for the individually moored array (Case II), for the three buoys, for three angles of wave incidence θ (0° , 30° , 60°). The results for the single buoy without moorings are provided for comparison.

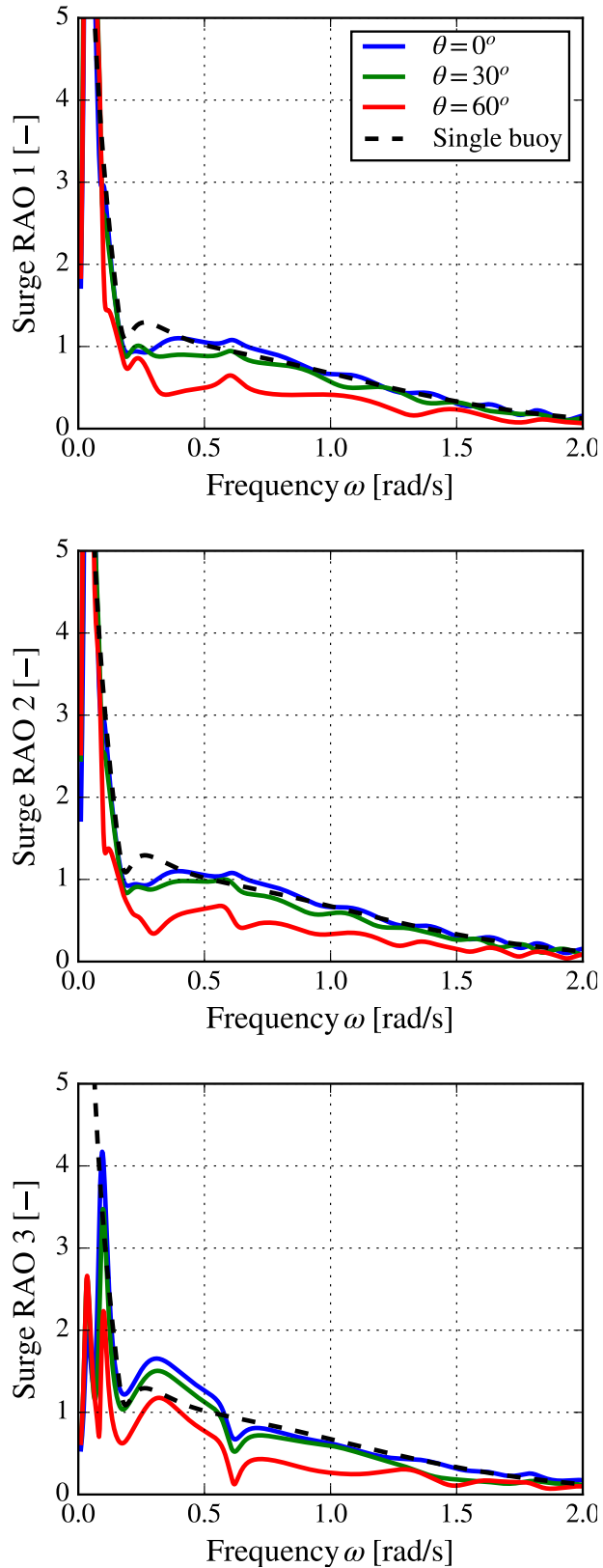


Figure 4.18: Surge RAOs against the wave frequency ω , for $k_t = 0.0015$ ms, $A_w = 1$ m, $C_{bm}^* = 0.1$, $\beta = 30^\circ$, $\alpha = 30^\circ$ for the array with shared moorings (Case III), for the three buoys and the clump weight, for three angles of wave incidence θ (0° , 30° , 60°). The results for the single buoy without moorings are provided for comparison.

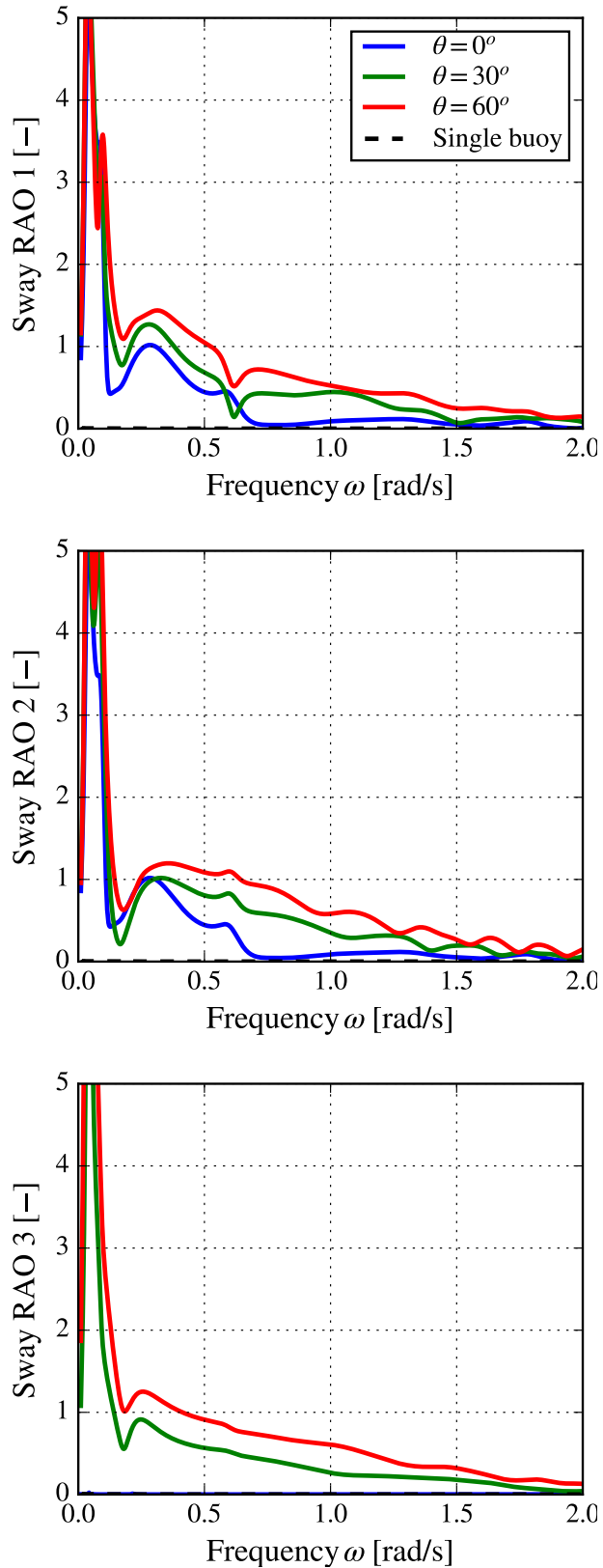


Figure 4.19: Sway RAOs against the wave frequency ω , for $k_t = 0.0015$ ms, $A_w = 1$ m, $C_{bm}^* = 0.1$, $\beta = 30^\circ$, $\alpha = 30^\circ$ for the array with shared moorings (Case III), for the three buoys and the clump weight, for three angles of wave incidence θ (0° , 30° , 60°). The results for the single buoy without moorings are provided for comparison.

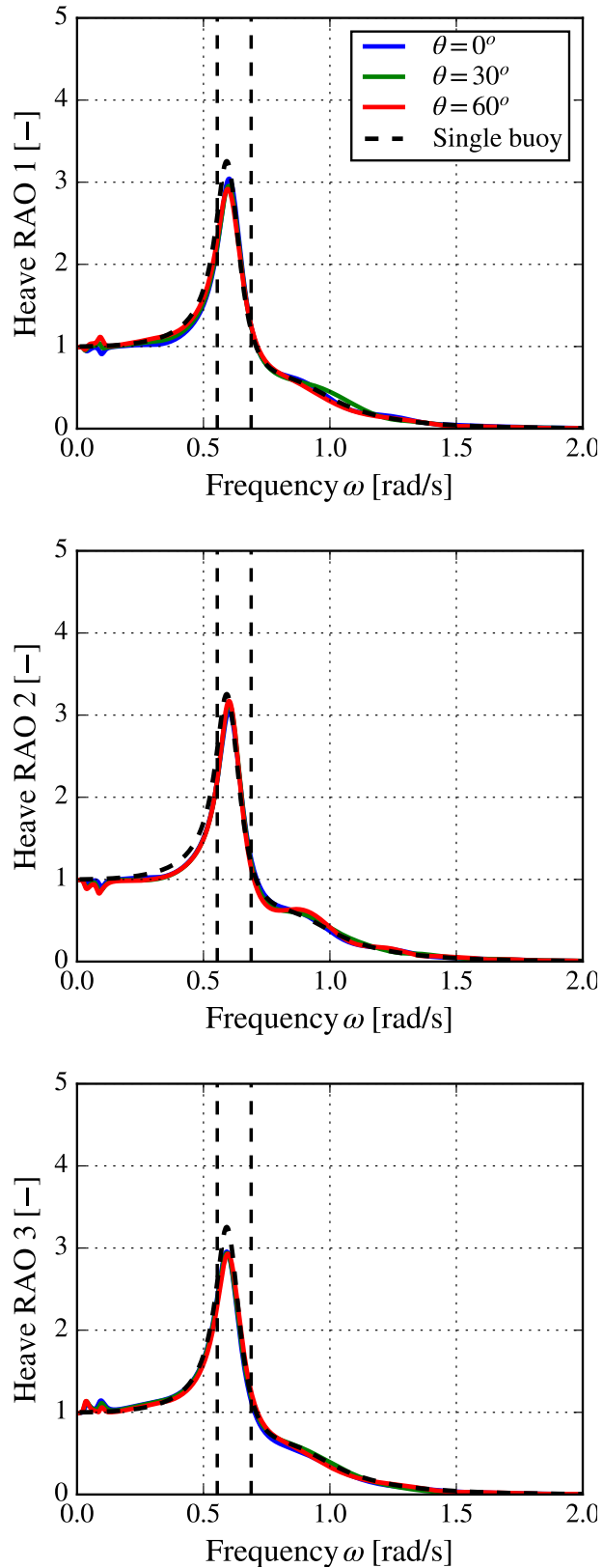


Figure 4.20: Heave RAOs against the wave frequency ω , for $k_t = 0.0015$ ms, $A_w = 1$ m, $C_{bm}^* = 0.1$, $\beta = 30^\circ$, $\alpha = 30^\circ$ for the array with inter-body and bottom mooring connections (Case III), for the three buoys and the clump weight, for three angles of wave incidence θ (0° , 30° , 60°). The results for the single buoy without moorings are provided for comparison.

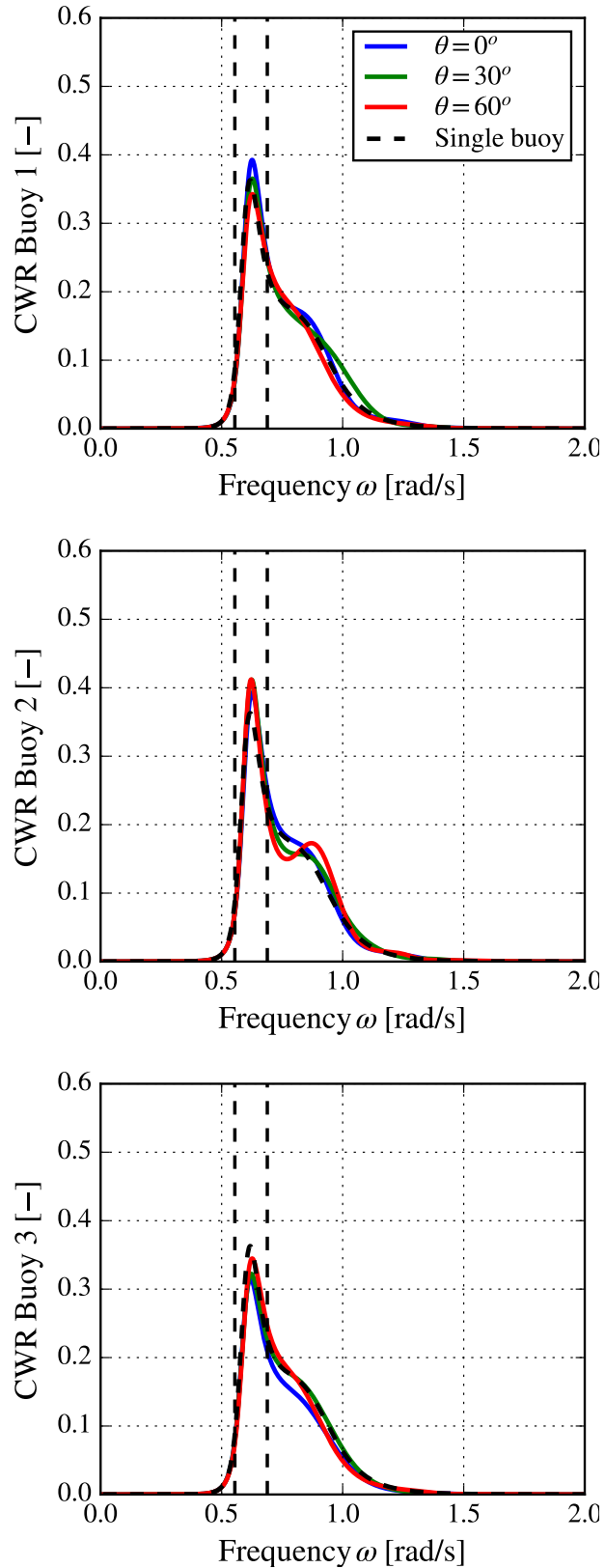


Figure 4.21: Heave RAOs against the wave frequency ω , for $k_t = 0.0015$ ms, $A_w = 1$ m, $C_{bm}^* = 0.1$, $\beta = 30^\circ$, $\alpha = 30^\circ$ for the array with inter-body and bottom mooring connections (Case III), for the three buoys, for three angles of wave incidence θ (0° , 30° , 60°). The results for the single buoy without moorings are provided for comparison.

4.4.4 Irregular wave analysis

Calculations were performed for irregular waves using the same default model parameters that were used throughout the regular waves analysis (i.e. the same turbine damping, angle of wave incidence, stiffness parameter, drag coefficients, wave amplitude, and mooring parameters). The output of these calculations is characterised by statistical values - standard deviations of the motion response amplitudes. The following results are given in dimensionless form; the standard deviations of the motion responses are divided by the standard deviation of the free surface elevation σ_η , for the wave spectrum presented in Eq. 4.60, $\sigma_\eta = H_s/4$.

Contrary to the case of regular waves, a different linearisation method was applied to model the drag force under irregular wave operation. For regular waves, the relative velocity standard deviation has the same value over all wave frequencies. For irregular waves, it varies with the sea state.

Single device

The next set of Figs. presents the dimensionless standard deviation for surge (Fig. 4.22), heave (Fig. 4.23), and pitch motions (Fig. 4.24), as well as the CWR for a single device (Fig. 4.25), over a range of energy periods T_e , and for a selection of significant wave heights $H_s = 0.5, 1.0, 2.0, 3.0, 4.0$ m, for an isolated device. Higher values of the significant wave height H_s contribute to lower values of the dimensionless standard deviation for surge, heave, and pitch. The CWR_{irr} also decreases with increasing H_s (Fig. 4.25). The linearisation of the quadratic viscous drag force is still dependent on the standard deviation of the velocity (Eqs. 4.64 - 4.66). Therefore, a higher relative flow velocity will lead to a more damped response, as observed in Figs. 4.22, 4.23, 4.24, 4.23, 4.25. Motions with a higher velocity will be subjected to a higher magnitude drag damping. This effect causes a reduction of CWR_{irr} with the increase of the H_s .

Array cases

The same cases that were studied in regular wave analysis, were examined in this section for irregular sea states with $H_s = 1.62$ m (Fig. 4.26), where the average values of the studied cases are presented for surge (Fig. 4.26), heave (Fig. 4.27), pitch (Fig. 4.28), and the CWR (Fig. 4.29). For high energy periods T_e , the average standard deviation of surge (Fig. 4.26) is slightly higher with mooring lines (Cases II and III), compared to Case I. This is in agreement with the regular waves results. Based on the CWR_{irr} (Fig. 4.29), the performance of the independently moored array appears to be similar to that of the array with inter-body mooring connections.

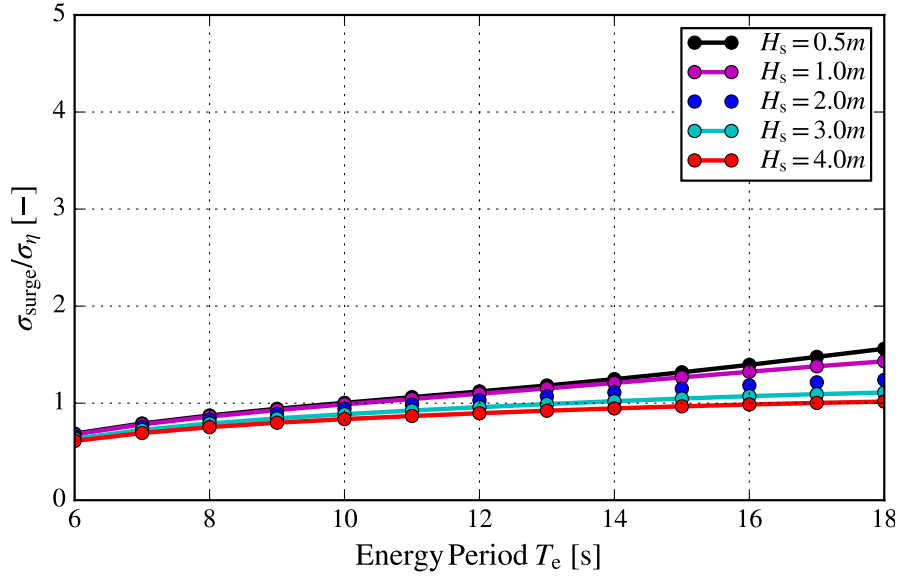


Figure 4.22: Standard deviation for surge against the energy period T_e , for an isolated device, for $k_t = 0.0015$ ms, $\theta = 0$, and various values of H_s .

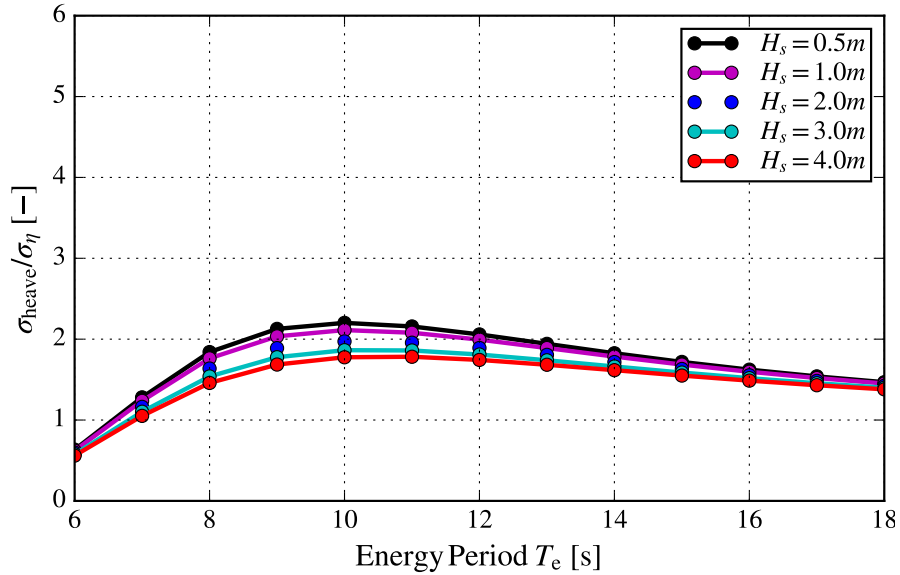


Figure 4.23: Standard deviation for heave against the energy period T_e , for an isolated device, for $k_t = 0.0015$ ms, $\theta = 0$, and various values of H_s .

Gain factor estimation

An annual wave climate off the western coast of Portugal was considered, which is characterised by a set of sea states described by a P-M wave spectrum (with inputs H_s and T_e). Table 4.5 presents the gain factors for the three cases, with varying model parameters. It is assumed that for all cases there is a dominant angle of wave incidence. Both mooring configurations (Case II and III), appear to be beneficial with the selection of the default turbine coefficient $k_t = 0.0015$ ms and varying mooring parameters α and β ($q > 1$). A higher turbine coefficient and a higher mooring stiffness parameter C_{bm}^* seem to adversely affect the system performance. For the default values ($k_t = 0.0015$ ms, $C_{bm}^* = 0.1$, $\beta = 30^\circ$, and $\alpha = 30^\circ$), Case II appears to perform slightly better than Case

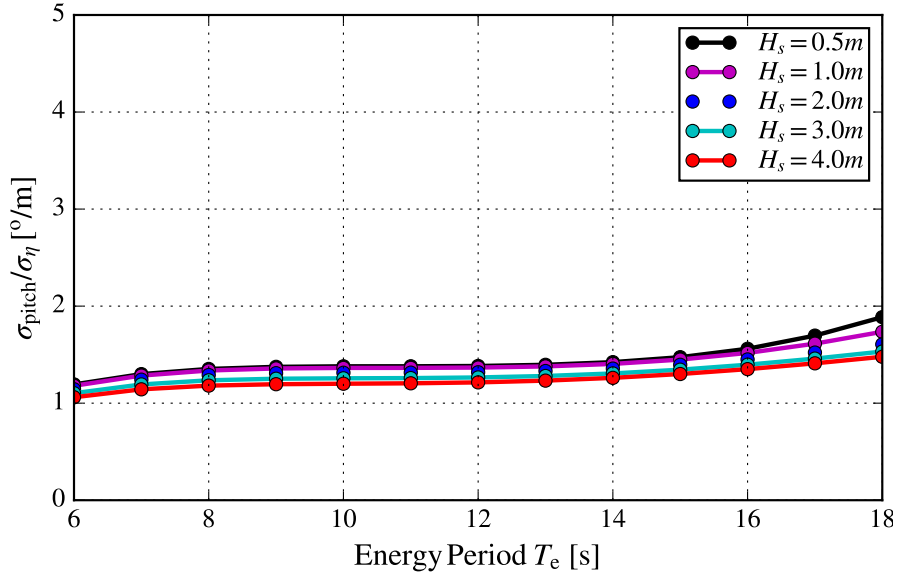


Figure 4.24: Standard deviation for pitch against the energy period T_e , for an isolated device, for $k_t = 0.0015$ ms, $\theta = 0$, and various values of H_s .

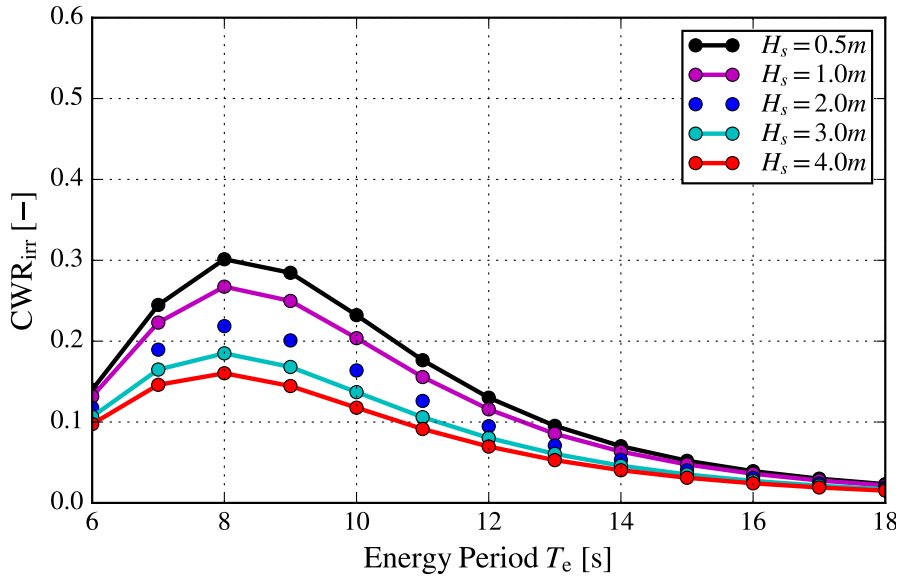


Figure 4.25: Standard deviations for the CWR_{irr} against the energy period T_e , for an isolated device, for $k_t = 0.0015$ ms, $\theta = 0$, and various values of H_s .

III for the studied wave climate. The gain factors values equal or higher than unity are highlighted in blue, yellow and red. The gain factor values below 1, are highlighted with green colour and they suggest a negative park effect as the result of certain model parameters (a more destructive interference between the devices).

For Case I (unmoored array), the most beneficial gain factor q appears for $\theta=30^\circ$, for the lowest turbine coefficient k_t , equal to 0.0015 ms. For the highest turbine coefficient $k_t=0.0050$ ms, the highest gain factor q appears for $\theta = 60^\circ$. In the latter case, the gain factor does not change for angles of wave incidence equal to 0 and 30° .

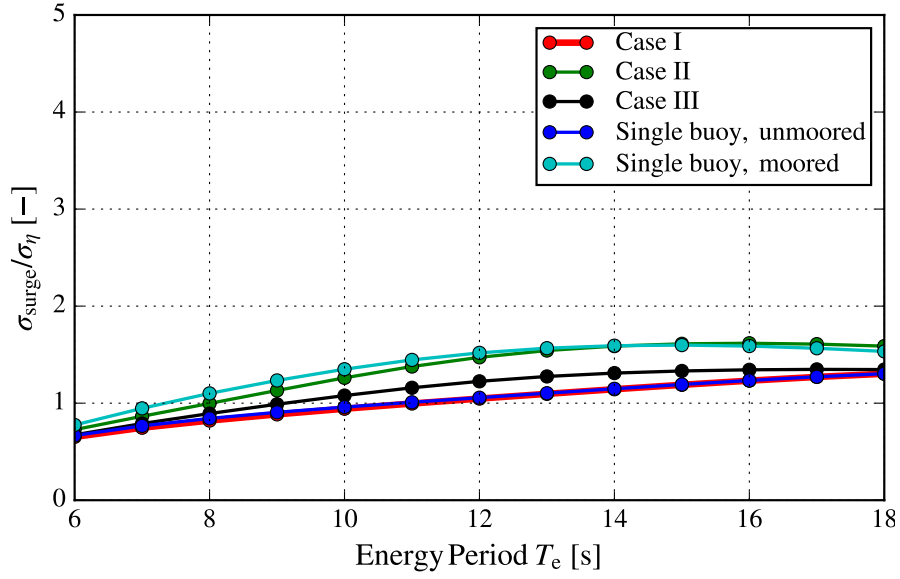


Figure 4.26: Standard deviations for surge, against the energy period T_e , for $k_t = 0.0015$ ms, $H_s = 1.62$ m, $C_{bm}^* = 0.1$, $\beta = 30^\circ$, $\alpha = 30^\circ$, and $\theta = 0$. For the array cases, the values presented refer to the array-averaged motions.

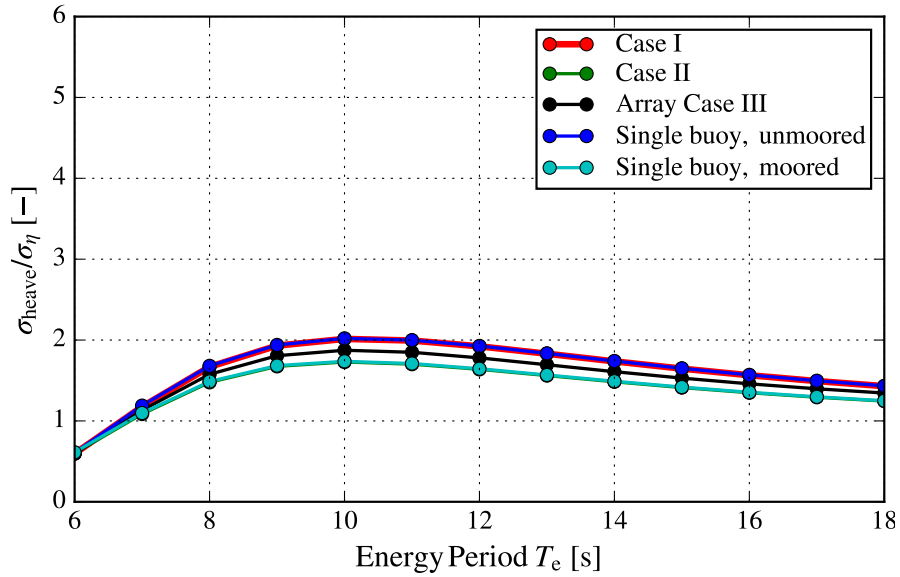


Figure 4.27: Standard deviations for heave, against the energy period T_e , for $k_t = 0.0015$ ms, $H_s = 1.62$ m, $C_{bm}^* = 0.1$, $\beta = 30^\circ$, $\alpha = 30^\circ$, and $\theta = 0$. For the array cases, the values presented refer to the array-averaged motions.

For Case II (individually moored array), a high bottom mooring line stiffness C_{bm}^* contributes to a higher gain factor, for the same studied angle of wave incidence, the same angle between the free surface plane and the mooring line β , and the same turbine coefficient k_t . This is different from the expected result of a single moored device, where higher stiffness shifts the response peak towards higher frequencies, often further away from the natural frequency of the buoy. Nevertheless, a very high stiffness ($C_{bm}^* = 0.2$) does seem to have this adverse effect on the array, as the gain factors decrease for the studied cases. In the case of increasing the angle between the free surface plane and the bottom mooring line, the results appear to be more favourable in terms of gain factors

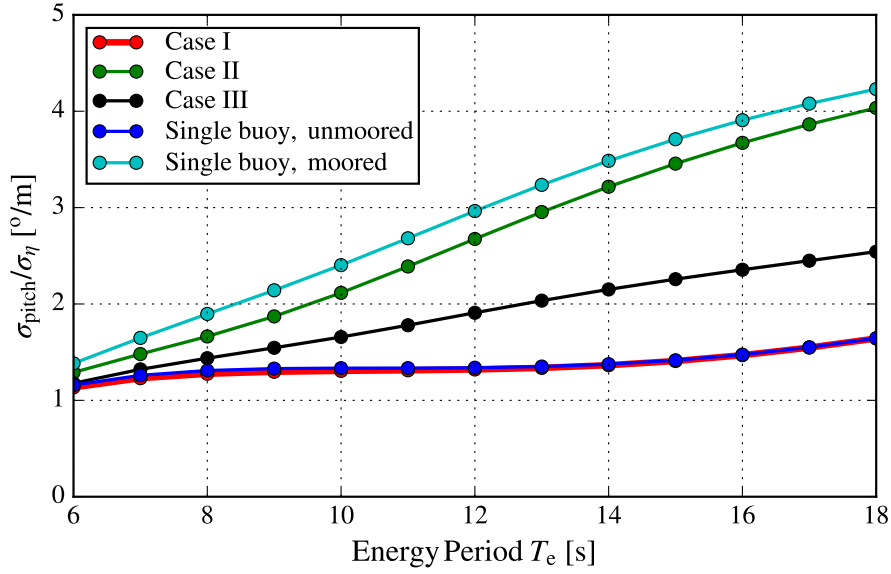


Figure 4.28: Standard deviation for pitch, against the energy period T_e , for $k_t = 0.0015$ ms, $H_s = 1.62$ m, $C_{bm}^* = 0.1$, $\beta = 30^\circ$, $\alpha = 30^\circ$, and $\theta = 0$. For the array cases, the values presented refer to the array-averaged motions.

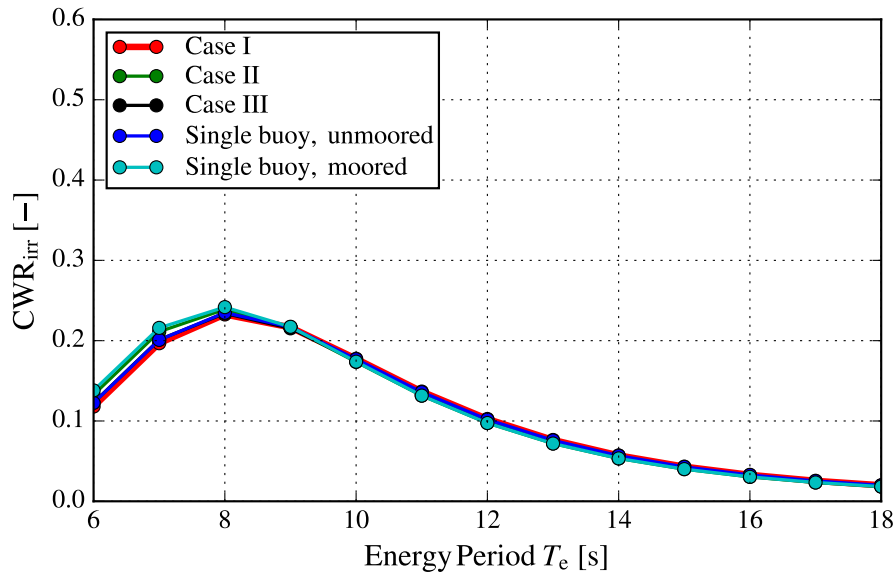


Figure 4.29: Standard deviation for CWR_{irr} , against the energy period T_e , for $k_t = 0.0015$ ms, $H_s = 1.62$ m, $C_{bm}^* = 0.1$, $\beta = 30^\circ$, $\alpha = 30^\circ$, and $\theta = 0$. For the array cases, the values presented refer to the array-averaged motions.

for a variety of angles of wave incidence, bottom mooring line stiffnesses, and turbine coefficients. For higher turbine coefficients with the default frequency-domain stiffness value for the bottom mooring line, and the default angle between the free surface plane and the bottom mooring lines, the gain factors for the three angles of wave incidence drop below unity, which suggests a slightly destructive park effect.

For Case III (array with inter-body and bottom mooring connections), the gain factor was studied for several combinations of model parameters. In the first line of Table 4.5, referring to Case III, the gain factor q for the default model turbine coefficient k_t , the

angle β , the angle α , with a lower value of bottom mooring line stiffness, was examined for three dominant angles of wave incidence θ . The most favourable result was obtained for $\theta = 30^\circ$. For the three dominant angles of wave incidence the gain factor was examined for $\beta = 30^\circ$, and the default stiffness of C_{bm}^* , varying the angle between the inter-body mooring line and the free-surface plane. The results showed that the optimum values would be obtained for $\theta = 30^\circ$ and the default value $\alpha = 30^\circ$. All of these nine gain factor values turned out to be higher than unity, suggesting a constructive park effect. The gain factor decreased for the three angles of wave incidence with a higher bottom mooring line stiffness and otherwise default values. The most favourable gain factor was obtained for the default parameters in this case. By increasing the turbine coefficient for a variety of model parameter combinations, the gain factors dropped below unity, meaning that the park effect was not favourable.

In general, the differences in simulated gain factor predicted were small. Nevertheless, other factors that have been identified as important when designing arrays of WECs (e.g. the spacing between devices, or even unequal spacing between them), have not been addressed in this section, as they are beyond the scope of this thesis. Also, throughout this study, a constant value for the mooring line stiffness has been considered, for all sea states. The same was done for the turbine coefficient. Ideally, the turbine coefficient should be optimised for each sea state. A turbine coefficient that is optimised for every sea state approximately models the situation where the device is equipped with an air turbine with movable guide vanes. Movable guide vanes provide the chance of changing the pressure-flow curve "on demand". It might be the case that the performance was underestimated in this work due to this generalisation. Another important aspect is that for the purpose of this analysis, a single angle of wave incidence has been assumed. In real sea conditions, there is a certain amount of directional spreading, even in offshore swell-dominated locations. Therefore, waves are irregular and multi-directional. By analysing a wave rose, an energy density distribution may be obtained for each dominant angle of wave of incidence, which is advised for the next steps of this research. Another equation can be introduced for the gain factor which takes into consideration the directional spreading.

Table 4.5: Annual-averaged gain factor q for the studied cases, for three angles of wave incidence θ , and varying model parameters.

Case I	Gain factor q			Input			
	$\theta = 0^\circ$	$\theta = 30^\circ$	$\theta = 60^\circ$	k_t [ms]			
	1.014	1.018	1.015	0.0015			
	1.016	1.016	1.018	0.0050			
Case II	Gain factor q			Input			
	$\theta = 0^\circ$	$\theta = 30^\circ$	$\theta = 60^\circ$	k_t [ms]	β [$^\circ$]	C_{bm}^* [-]	
	1.036	1.040	1.037	0.0015	30	0.05	
	1.046	1.090	1.046	0.0015	30	0.10	
	1.034	1.038	1.032	0.0015	30	0.20	
	1.053	1.057	1.054	0.0015	60	0.05	
	1.013	1.018	1.014	0.0015	60	0.10	
	0.832	0.842	0.832	0.0015	60	0.20	
	0.984	0.984	0.985	0.0050	30	0.10	
	Case III	Gain factor q			Input		
$\theta = 0^\circ$		$\theta = 30^\circ$	$\theta = 60^\circ$	k_t [ms]	β [$^\circ$]	C_{bm}^* [-]	α [$^\circ$]
1.012		1.017	1.013	0.0015	30	0.05	30
1.013		1.015	1.015	0.0015	30	0.10	20
1.017		1.022	1.019	0.0015	30	0.10	30
1.010		1.019	1.015	0.0015	30	0.10	40
0.995		1.013	1.012	0.0015	30	0.20	30
1.026		1.026	1.025	0.0150	60	0.05	20
1.027		1.032	1.030	0.0150	60	0.05	30
1.019		1.028	1.026	0.0150	60	0.05	40
1.033		1.034	1.036	0.0015	60	0.10	20
1.036		1.043	1.041	0.0015	60	0.10	30
1.031		1.041	1.039	0.0015	60	0.10	40
1.002		1.002	1.003	0.0050	30	0.05	30
0.991		0.992	0.993	0.0050	30	0.10	30
0.944		0.952	0.956	0.0050	30	0.20	30
0.971		0.972	0.975	0.0050	60	0.10	30

4.5 Preliminary model verification: critical reflection

The model could be adapted to correspond with the experimental work presented in Correia da Fonseca et al. (2016). Nevertheless, it should be noted that the wave tank walls could be responsible for a reflection effect. Despite the fact that wave tanks often introduce some kind of energy dissipation (e.g. a beach or absorbing paddles) in the direction of wave propagation, efforts should also be made to ensure that reflection from the side walls is minimised. If proper energy dissipation is not introduced in the wave tank, interference between the incident and the reflected wave could generate zones with higher and lower amplitudes. This is to say, zones with higher and lower energy available for WEC absorption could be formed. The required distance from the walls will hence be dependent on the wavelength of the incident wave. For irregular waves, which are the sum of many regular wave components with different frequencies, this effect will likely be smoothed out.

At present, there is no experimental work available to provide a direct validation of the numerical results presented. There are, however, existing pieces of work that could be used for preliminary model verification:

Gomes et al. (2016) (single device and five devices unmoored in a wave flume, where only the single device is used for model verification): here the spar-buoy OWC examined was of slightly different dimensions than the one considered in the presented computations. The relative motion between the single buoy and the OWC exhibits the same response characteristic - a two peak pattern, one corresponding to the buoy and the other to the OWC. Similar patterns were also observed for the CWR. For the regular wave dynamics studied, the same PTO was considered: a Wells turbine, and so the same formulation was adopted in this thesis. For very low k_t , two peaks were also visible in the heave RAO presented in the work of Gomes et al. (2016). For high k_t , only one peak was visible, which shifted towards higher frequencies in the graph of the heave RAO. The same effect was observed for the CWR. This goes in line with the results obtained in this thesis. Regarding the studied irregular wave dynamics, high values of significant wave height H_s also exhibited low values of heaving RAO standard deviation.

Gomes (2016) (single device): these laboratory instructions refer to the same device, with the exact same dimensions as the one presented here. The general patterns come into agreement. For turbine damping modelled by an orifice, the same two peak effect appears. Unfortunately, it is not possible to make any conclusions about the influence of the mooring system from these experiments.

Oikonomou et al. (2016) (single device): this experiment was an exercise, based on the laboratory instructions of Gomes (2016). It referred to a 1:100th scale model, with the same dimensions as in Gomes et al. (2012) and in the presented work. The model used an orifice, which resembles the damping characteristics of a Wells turbine. A low wave amplitude was used as in the calculations, making it ideal for comparison, since dimensionless values for the RAOs can be used within

the limitations of linear wave theory. The natural frequency of the buoy from the conducted experiments was 0.710 rad/s, which is very close to the calculated one in this work (0.689 rad/s). The RAO for low frequencies in the experiment was close to 1, as it was the case in the calculations, since the device moves with the incoming waves. For frequencies higher than the natural frequency of the buoy in heave, the heave RAO went to zero in the experiment. This was also the case in the calculations, and it makes sense since for very high frequencies (low periods), waves pass by a floating device without causing any excitation.

Correia da Fonseca et al. (2016) (single device and triangular array): experimental results cannot be compared directly to the numerical results of this thesis, primarily because the single spar-buoy OWC studied was of different dimensions, and the triangular array configuration with shared moorings was different. Also, the majority of the results were obtained for very high H_s or A_w , which is out of the validity range of the presented numerical model. However, from scaling up the results presented in the research publication of Correia da Fonseca et al. (2016), it is foreseen that the numerical model of this thesis will be able to predict the response of the system at operational frequencies, whilst certain frequencies will cause parametric resonance and cause some high motion amplitudes which will not be captured by the frequency and stochastic domain models. This type of effect is apparently quite common in spar-type structures, and has been investigated in Tarrant and Meskell (2016) and Gomes et al. (2017). The type of parametric resonance occurs for certain frequencies, and excites the roll mode, whilst affecting the heave mode and compromising the performance of the system. Nevertheless, this effect is non-linear and it is beyond the scope of this study. A numerical approach for studying this type of phenomenon can be found in Giorgi and Ringwood (2019).

4.6 Chapter summary and concluding remarks

This chapter presented a numerical analysis of a triangular array of spar-buoy OWCs, with bottom and inter-body mooring connections, for regular waves. The previously established numerical model was used to simulate the forces from the shared mooring system. The array performance was compared to an unmoored and an independently moored array. The latter refers to an array where each of the devices was attached to three bottom mooring lines.

The spar-buoy OWC was modelled as a two-body system, and six DoF were considered for each buoy, and one DoF (heave) was considered for their corresponding OWCs. The PTO damping (air turbine) was frequency-dependent and was represented by a damping and restoring term. The model considered a linearised approximation of the quadratic viscous drag force, with drag coefficient values based on experimental data. It should be noted though that the damping forces associated with viscous effects are likely to be over-estimated since the experimental coefficients also include scale effects.

The analysis showed that the unmoored array was influenced by the hydrodynamic coupling between the three bodies in surge; no significant difference was observed for the average heave amplitude of the array at the peak frequency. By including the inter-body connections, a coupling effect between surge/sway and heave was observed. The buoys' average heave amplitude at the peak frequency decreased by 7.2%. The average dimensionless capture width of all devices slightly increased after including the inter-body mooring lines, at the peak frequency.

The frequency-domain method was extended to be applicable for irregular wave conditions. A stochastic analysis was applied to provide motion and power absorption results under more realistic sea conditions. The simulations with a set of uni-directional irregular wave sea states, characterising a particular wave climate, showed that an angle of wave incidence of 30° provided better results for the different mooring configurations tested. The independently moored array configuration and the array with inter-body connections showed similar results for the different configurations tested, with variations around 2-3% of each other's values.

Since the individually moored array is more expensive than the one with inter-body mooring lines, the array with inter-body connections seems to be the more economically attractive solution, as it might contribute to a decrease in the overall costs of the project. However, further analysis is required on the economic aspects of the two arrays, in order to draw conclusions on their economic viability.

Chapter 5

Conclusions

This thesis has contributed to the field of wave energy conversion by building upon an existing frequency-domain numerical model of a moored array, using linear water wave theory. The resulting array dynamics due to device motion along the rotational degrees of freedom, and also due to the effects of viscous damping against the walls of the devices, have been added to the existing literature through several public presentations and published works.

First, the dynamics of a previously modelled array of moored spherical point absorbers moving only along the translational degrees of freedom were replicated and verified with good agreement. Then, after adding the effects of viscous damping into the model, the spherical point absorbers were replaced by cylindrical devices with a defined centre of gravity, so that motion along rotational degrees of freedom could also be analysed. The hydrodynamics of the spherical and cylindrical point absorber arrays were investigated with a mooring system where bottom mooring lines are only used along the perimeter of the array, inter-connecting the remaining device fairleads using shared mooring lines and a common clump weight. The predicted dynamics of converter arrays employing this type of mooring system were discussed.

The moored array of cylindrical point absorbers with viscous effects and all six degrees of freedom was then applied to model a case study of spar-buoy devices: an existing floating oscillating water column type wave energy converter, which has undergone significant research and development in recent years. The spar-buoy converter presents the additional modelling challenge of being a two-body system: the buoy and the oscillating water column inside it. The buoy was therefore considered free to move in all six degrees of freedom, whilst the oscillating water column was restricted to motion along heave. The hydrodynamics of the spar-buoy OWC array were investigated with two different mooring systems: one that uses the conventional technique of individually mooring every converter to the seabed, and the novel mooring configuration investigated in the case of spherical and cylindrical point absorber arrays of this thesis. The predicted dynamics of converter arrays employing each type of mooring system were compared, and the wave farm performance of both mooring systems was analysed alongside important

economic feasibility considerations of both options. Finally, after the moored spar-buoy array model was established and numerical results for both mooring configurations were obtained, the frequency-domain model was then brought into the spectral-domain, so that the irregular wave sea states of particular coastal locations could be analysed. Spectral-domain numerical results were obtained for an array of spar-buoy devices off the west coast of Portugal, with both types of mooring configurations taken into consideration.

It was found that it is important to account for the viscous effects against the walls of each single body cylindrical point absorber (and also against the walls of the inner tube, in the case of the two-body spar-buoy converter), especially near frequencies of heaving resonance. This type of linearised viscous damping is a function of the incoming wave amplitude, and so in the spectral-domain where irregular wave sea states were considered, those with higher significant wave heights actually predicted decreased standard deviations in device motion, due to their increased viscous drag. Even when modelling converters that extract wave energy in translational modes only, it was concluded that it is still important to model the rotational motions, due to their hydrodynamic coupling with translational motions. For the type of wave energy converter array modelled throughout this thesis, this was found to be particularly true in the case of surge and pitch coupling. Furthermore, hydrodynamic coupling not only exists between the modes within a particular device, but also between the modes of different devices.

The conventional and inter-body mooring configurations for arrays of wave energy converters were studied extensively throughout this thesis. For the converter separation distance considered, it was found that the difference in array performance between the two mooring systems would be minimal, both configurations achieving park effect coefficients near unity. This result is quite promising and desirable, as the shared mooring configuration is believed to have significant economic benefits over the conventional approach.

The aim of this thesis work was to start with a well-established numerical model of a moored array of point absorbers in the frequency-domain, and to build on it by including several important effects that can significantly influence the system dynamics, before moving the model into the spectral-domain. In this sense, the objectives of the thesis were achieved, even though it also marks the beginning of many new research questions that are yet to be answered in the field of wave energy conversion.

5.1 Limitations of the presented research

Linear wave theory: All calculations used in this thesis lie within the limitations of linear wave theory. The responses for periods higher than 30 s cannot be predicted accurately with this type of numerical model. They are therefore invalid for non-operational sea-states, since the device would be in survivability mode anyway. However, they may help identify wave periods for which mooring line breakage might occur. In addition to this, other real non-linear effects of waves are excluded from this theory, including

wave-wave interaction, wave breaking and so on.

Power available to the turbine VS Power output: In the present study, the power available to the turbine was used as a magnitude for calculating the capture width, instead of the power output.

Quasi-static model for mooring dynamics: This is a simplified approach used in the first stages of the present research, since it assumes small motion. This method does not account for the mooring line inertia and damping, both of which would have to be taken into account should the study be advanced.

Angle of wave incidence: In the calculations presented, a dominant angle of wave incidence was assumed. Although dominant angles exist, it would be more precise to account for the multi-directionality of irregular waves.

Turbine: In the stochastic model, a standard value for the turbine coefficient was considered for all sea states, which most likely underestimates the performance of the system.

Viscous damping: The values of the damping coefficients in Chapter 4 were obtained from small-scale experiments which might over-damp the system.

5.2 Recommendations for future work

The present research could be the basis of future work utilising more sophisticated mathematical techniques for mooring lines and a more detailed analysis of economic viability. An interesting possibility for the existing numerical model would be to use a dynamic model for the mooring lines. Examples of dynamic models for mooring lines are the commercial package Orcaflex by Orcina and MooDy developed by Chalmers University. The advantage of dynamic mooring models is that they account for the added inertia and the damping effects of the mooring lines on attached devices.

Another possibility would be to apply the proposed methodology to other devices that are currently under development. However, in the present study, the PTO was expressed in a linearised way (Wells turbine). Therefore, other devices may require a time-domain analysis for modelling the influence of the PTO on systems dynamics.

For the stochastic model analysis, turbine optimisation is possible for each sea state by making use of an optimisation algorithm. The model is able to model the damping from the Wells turbine, but could also be extended to account for the damping from a newly developed turbine known as the bi-radial turbine.

Another recommendation would be to apply the methodology to different wave spectra. To date, the numerical model has operated within the Pierson-Moskowitz spectrum which corresponds to fully developed seas (e.g. Portugal, west of France). Other locations would require the consideration of the JONSWAP spectrum (e.g. North Sea), or double-peak spectra, where the first peak in the density graph corresponds to swell (e.g. south of the UK). Note though, that this possibility might require the re-optimisation of a device for the selected wave climate, since the spar-buoy OWC used in the present study was optimised for the Portuguese wave climate.

As it stands, the numerical model presented in this thesis demonstrates great potential. Further investigation into strengths and weaknesses would, however, allow future improvements on the model, by experimentally validating the model's performance against experimental outputs. With proven validity, the model could be applied to various engineering applications. To facilitate this, numerical modelling conditions should be aligned with experimental conditions in a wave tank. Existing experimental work on shared moorings for WEC arrays has been undertaken as part of EU funded projects such as WETFEET and MaRINET. Validation is a critical step for the calibration of the presented model. It is expected, though, that the numerical model output will match the experimental model output but only to the best of its ability. For example, since the viscosity is taken into consideration in the numerical model in a linearised way, vortex shedding will not be accounted for in the numerical model output. In addition, non-linear effects such as parametric resonance will not be captured by this type of model.

An important future recommendation for the progress of this research is a detailed cost analysis for the shared mooring configuration as opposed to the individually moored system. However, shared moorings can be disadvantageous if a mooring line breakage occurs. In the proposed configuration, each device is attached to other devices and the array by one mooring line to the seabed. It is recommended that the security of this system is further investigated. So should the potential costs of mooring line breakage. Moreover, as the likelihood of extreme events is geographically dependent, the studied configuration might not be applicable to all locations and conditions. That is the reason it would be beneficial in the future to include a model that accounts for snap loads as well.

References

- Direction of Commander (2000), ‘Naval Sea Systems Command US Navy Salvage Engineer’s Handbook, Appendix G Anchoring Systems’.
- Aggidis, G. (2017), ‘Hydropower goes Marine’, IMechE Event, 15.02.2017.
- Aggidis, G. A., Bradshaw, A., McCabe, A. and Meadowcroft, J. (2005), ‘Developments in the design of the PS Frog MK5 Wave Energy Converter.’, *Ren. Energy* **31**(2), 141–151.
- Airy, G. B. (1845), ‘Tides and waves’, *Encyc. Metrop.* **192**, 241–396.
- Alves, M. A., Costa, I. R., Sarmiento, A. J. N. A. and Chozas, J. F. (2010), Performance evaluation of an axisymmetric floating OWC, *in* ‘Proc. 20th Int. Offshore and Polar Engineering Conference’, Beijing, China.
- American Petroleum Institute (API) (2015), *Design and Station Keeping Systems for Floating Structures*, American Petroleum Institute (API-RP-2SK): Washington, DC, USA.
- Arena, F., Romolo, A., Malara, G. and Ascanelli, A. (2013), On design and building of a U-OWC wave energy converter in the Mediterranean sea: a case study, *in* ‘Proc. ASME 2013 32nd International Conference on Ocean, Offshore, and Arctic Engineering, June 9-14 2013’, Nantes, France.
- Ashton, I. A. G., Johanning, L. and Linfoot, B. (2009), Measurement of the effect of power absorption in the lee of a wave energy converter, *in* ‘Proc. ASME 2009, 28th International Conference on Arctic Engineering, 31 May- 5 June’, Honolulu, Hawaii.
- Astariz, S. and Iglesias, G. (2015), ‘The economics of wave energy: a review’, *Ren. and Sustain. En. Rev.* **45**, 397–408.
- Babarit, A. (2013), ‘On the park effect in arrays of oscillating wave energy converters’, *Ren. Energy* **58**, 68–78.
- Babarit, A. (2015), ‘A database of capture width ratio of wave energy converters’, *Ren. Energy* **80**, 610–628.
- Babarit, A. and Delhommeau, G. (2015), Theoretical and numerical aspects of the open source BEM solver NEMOH, *in* ‘11th European Wave and Tidal Energy Conference (EWTEC2015)’, Proc. of the 11th European Wave and Tidal Energy Conference, Nantes, France.

- Babarit, A., Hals, J., Muliawan, M. J., Kurniawan, A., Moan, T. and Krokstad, J. (2012), 'Numerical benchmarking study of a selection of wave energy converters', *Ren. Energy* **41**, 44 – 63.
- Baker, N. J., Mueller, M. A. and Spooner, E. (2004), Permanent magnet air-cored tubular linear generator for marine energy converters, *in* 'Proc. of the 2nd IEE international conference on power electronics, machines and drives'.
- Bauduin, C. and Naciri, M. (1999), A contribution on quasi-static mooring line damping, *in* 'Proc. 18th International Conference on Offshore Mechanics and Arctic Engineering', St. Johns, Newfoundland, Canada.
- Beatty, S., Hall, M., Buckham, B., Wild, P. and Bocking, B. (2015), 'Experimental and numerical comparisons of self-reacting point absorber wave energy converters in regular waves', *Ocean Eng.* (104), 370–386.
- Bergdahl, L. (2017), Mooring design for WECs, *in* 'Pecher A., Kofoed J. (eds) Handbook of Ocean Wave Energy', Springer, pp. 159–202.
- Bhinder, M. A., Mingham, C. G., Causon, D. M., Rahmati, M. T., Aggidis, G. A. and Chaplin, R. V. (2009), A joint numerical and experimental study of a surging point absorbing wave energy converter (WRASPA), *in* 'ASME 28th International Conference on Ocean, Offshore and Arctic Engineering, OMAE2009', Honolulu, Hawaii, USA.
- Borgarino, B., Babarit, A. and Ferrant, P. (2012), 'Impact of wave interactions effects on energy absorption of large arrays of wave energy converters', *Ocean Eng.* **41**, 79–88.
- Borgman, L. S. (1967), 'Spectral analysis of ocean wave forces on piling', *J. Waterw. Harb. Div.* **93**, 129–156.
- Bossi, U., Engsig-Karup, A. P., Eskilsson, C. and Ricchiuto, M. (2019), 'A spectral/hp element depth-integrated model for nonlinear wave-body interaction', *Comput. Methods Appl. Mech. Eng.* **348**, 222–249.
- British Standards Institution (BSI) (2014), *BS 6349-4:2014 Maritime structures. Code of practice for design of fendering and mooring systems*, British Standards Institution, London, UK.
- Brito-Melo, A., Henriques, Hofman, T., Sarmiento, A. J. N. A., Clément, A. H. and Delhommeau, G. (2001), 'Numerical modelling of OWC shoreline devices including the effect of surrounding coastline and non-flat bottom', *Int. J. Offshore Polar Eng.* **11**(2), 147–154.
- Brown, D. T. and Mavrakos, S. (1999), 'Comparative study on mooring line dynamic loading', *Mar. Struc.* **12**(3), 131–151.
- Budal, K. (1977), 'Theory for absorption of wave power by a system of interacting bodies', *J. Ship Res.* **21**, 248–253.

- Budal, K. and Falnes, J. (1975), ‘A resonant point absorber of ocean waves’, *Nature* **256**, 478–479.
- Carrelhas, A. A. D., Gato, L. M. C., Henriques, J. C. C., Falcão, A. F. O. and Varandas, J. (2019), ‘Test results of a 30 kW self-rectifying biradial air turbine-generator prototype’, *Ren. and Sustain. En. Rev.* **109**, 187–198.
- Chakrabarti, S. K. (1984), *Offshore Structure Modeling*, World Scientific, Singapore.
- Chakrabarti, S. K. (1987), *Hydrodynamics of offshore structures*, Springer Verlag WIT Press.
- Chakrabarti, S. K. (2005), *Handbook of Offshore Engineering (2-volume set)*, Elsevier.
- Chaplin, R. V. and Aggidis, G. A. (2007), An Investigation into Power from Pitch-Surge Point-Absorber Wave Energy Converters, in ‘International Conference on Clean Electrical Power, 2007. ICCEP ’07’, Capri, Italy.
- Clément, A. P., McCullen, P., Falcão, A., Fiorentino, A., Gardner, F., Hammarlund, K. and Lemonis, G. (2002), ‘Optimal configurations of wave energy device arrays’, *Ren. and Sustain. En. Rev.* **6**(5), 405–431.
- Clément, A., Babarit, A., Gilloteaux, J. C., Josset, C. and Duclos, G. (2005), ‘The SEAREV wave energy converter’.
- Cândido, J. J. M. B. (2010), *Modelação Optimização e Controlo de Sistemas de Corpo Oscilante para Utilização da Energia das Ondas*, PhD thesis, Instituto Superior Técnico, Universidade Técnica de Lisboa.
- Correia da Fonseca, F. X. (2014), *Testing of a 1:32 scale model of a floating oscillating water column system for wave energy conversion*, Master’s thesis, Instituto Superior Técnico, Universidade Técnica de Lisboa.
- Correia da Fonseca, F. X., Gomes, R. P. F., Henriques, J. C. C., Gato, L. M. C. and Falcão, A. F. O. (2016), ‘Model testing of an oscillating water column spar-buoy wave energy converter isolated and in array: Motions and mooring forces’, *Energy* (112), 1207–1218.
- CRES (2002), ‘Wave energy utilization in Europe: current status and perspectives.’.
- Cruz, J. (2008), *Ocean Wave Energy: Current status and future perspectives*, Springer.
- Cummins, W. E. (1962), ‘The impulse response function and ship motions’, *Schiffstechnik* **9**, 101–109.
- Dalton, G. J., Alcorn, R. and Lewis, T. (2010), ‘Case study feasibility analysis of the pelamis wave energy convertor in ireland, portugal and north america’, *Ren. Energy* **35**(2), 443–455.
- Davidson, J. and Ringwood, J. (2017), ‘Mathematical modelling of mooring systems for wave energy converters - a review’, *Energies* **10**.

- Davis, R. A. and Fitzgerald, D. M. (2003), *Beaches and Coasts*, Willey Balckwell.
- de Swart, H. E. (2014), *Ocean waves, lecture notes*, Utrecht University, the Netherlands .
- Dean, R. G. and Dalrymple, R. A. (1984), *Water Wave Mechanics for Engineers and Scientists*, World Scientific, Singapore.
- Det Norske Veritas (DNV) (2010), *Offshore Standard DNV-OS-E301 Position Mooring*, Det Norske Veritas: Høvik, Norway.
- Det Norske Veritas (DNV) (2014), *Recommended Practice DNV-RP-H103*, Det Norske Veritas: Høvik, Norway.
- Drew, B., Plummer, A. R. and Sahinkaya, M. N. (2009), ‘A review of wave energy converter technology’, *Proc. ImechE Part A: J. Power and Energy* **222**, 887– 902.
- Estefen, S. F., Esperança, P. T. T., Ricarte, E., Costa, P. R., Pinheiro, M. M., Clemente, C. H. P., Franco, D., Melo, E. and de Souza, J. A. (2008), Experimental and Numerical Studies of the Wave Energy Hyberbaric Device for Electricity Production, *in* ‘Proc. ASME 2008 27th International Conference on Offshore Mechanics and Arctic Engineering’, Estoril, Portugal.
- Evans, D. V. (1976), ‘A theory for wave-power absorption by oscillating bodies’, *Journal of Fluid Mechanics* **77**, 1–25.
- Falcão, A. F. O. (2007), ‘Modelling and control of oscillating-body wave energy converters with hydraulic power take-off and gas accumulator’, *Ocean Eng.* **34**, 2021–2032.
- Falcão, A. F. O. (2010), ‘Wave energy utilization: A review of the technologies’, *Ren. and Sustain. En. Rev.* **14**(2), 899–918.
- Falcão, A. F. O. (2016), *Modelling of wave energy conversion*, Instituto Superior Técnico, Universidade Técnica de Lisboa.
- Falcão, A. F. O., Henriques, J. C. C. and Cândido, J. J. (2012), ‘Dynamics and optimization of the OWC spar buoy wave energy converter’, *Ren. Energy* **48**, 369–381.
- Falcão, A. F. O., Henriques, J. C. C. and Gato, L. M. C. (2016), ‘Air turbine optimization for a bottom-standing oscillating-water-column wave energy converter’, *J. Ocean Eng. Mar. Energy* **2**, 459–472.
- Falcão, A. F. O. and Justino, P. A. P. (1999), ‘OWC wave energy devices with air flow control’, *Ocean Eng.* **26**(12), 1275 –1295.
- Falcão, A. F. O. and Rodrigues, R. J. A. (2002), ‘Stochastic modelling of OWC wave power plant performance’, *Appl. Ocean Res.* **24**(2), 59–71.
- Falcão, A. F. O., Gato, L. C. and Nunes, E. P. A. S. (2013), ‘A novel radial self-rectifying air turbine for use in wave energy converters’, *Ren. Energy* **50**, 289–298.

- Falcão, A. F. O. and Henriques, J. (2018), The spring-like compressibility effect in owc wave energy converters: hydro-, thermo-, and aerodynamic analyses., in ‘Proc. 37th International Conference on Ocean, Offshore and Arctic Engineering, OMAE’, Madrid, Spain.
- Falcão, A. F. O., Henriques, J. C. C., Gato, L. M. C. and Gomes, R. P. F. (2014), ‘Air turbine choice and optimization for floating oscillating-water-column wave energy converter’, *Ocean Eng.* **75**, 148–156.
- Falnes, J. (1980), ‘Radiation impedance matrix and optimum power absorption for interacting oscillators in surface waves’, *Appl. Ocean Res.* **2**, 75–80.
- Falnes, J. (1997), ‘Principles for capture of energy from ocean. phase control and optimum oscillation’, http://folk.ntnu.no/falnes/web_arkiv/InstFysikk/phcontrl.pdf.
- Falnes, J. (1999), ‘Wave energy conversion through relative motion between two-single mode oscillating bodies’, *J. Offshore Mech. Arct. Eng.* **121**, 32–38.
- Falnes, J. (2002), *Ocean waves and oscillating systems: Linear interactions including wave-energy extraction*, Cambridge: Cambridge University Press.
- Falnes, J. (2007), ‘A review of wave-energy extraction’, *Mar. Structures* **20**, 185–201.
- Falnes, J. and Budal, K. (1978), ‘Wave-power conversion by power absorbers’, *Norwegian Mar. Res.* **6**, 2–11.
- Falnes, J. and Hals, J. (2012), ‘Heaving buoys, point absorbers and arrays’, *Phil. Trans. R. Soc. A.* **370**, 246–277.
- Falnes, J. and Kurniawan, A. (2015), ‘Fundamental formulae for wave-energy conversion’, *R. Soc. open sci.* **2**.
- Faltinsen, O. M. (1999), *Sea loads on ships and offshore structures*, Cambridge University Press.
- Fernandez, H., Iglesias, G., Carballo, R., Castro, A., Fraguera, J. A., Taveira-Pinto, F. and Sanchez, M. (2012), ‘The new wave energy converter WaveCat: Concept and laboratory tests’, *Marine Structures* **29**(1).
- Ferreira, J. A. and Guedes Soares, C. (1998), ‘An application of the Peaks Over Threshold method to predict extremes of significant wave height’, *Journal of Offshore Mechanics and Arctic Engineering* **120**, 165–176.
- Fitzgerald, J. and Bergdahl, L. (2008), ‘Including moorings in the assessment of a generic offshore energy converter: A frequency domain approach’, *Mar. Struct.* **21**(1), 23–46.
- Folley, M. (1993), The design of point absorbing wave energy converters, PhD thesis, Lancaster University, UK.

- Folley, M., Babarit, A., Child, B., Forehand, D., O'Boyle, L., Silverthorne, K., Spinneken, J., Stratigaki, V. and Troch, P. (2012), A review of numerical modelling of wave energy converter arrays, in 'Proc. ASME 2012 31st International Conference on Ocean, Offshore and Arctic Engineering OMAE2012, July 1-6, 2012', Rio de Janeiro, Brazil.
- Fredriksen, A. E. (1986), Tapered Channel Wave Power Plants, in 'Energy for Rural and Island Communities, 4th International Conference', Inverness, Scotland.
- Fredriksson, D. W., De Cew, J., Robinson Swift, M., Tsukrov, I., Chambers, M. D. and Celikkol, B. (2004), 'The design and analysis of a four-cage grid mooring for open ocean aquaculture', *Aquacultural Engineering* **33**, 77–94.
- Frigaard, P. B., Andersen, T. L., Kofoed, J. P., Kramer, M. M. and Ambühl, S. (2016), 'Wavestar Energy Production Outlook. Aalborg: Department of Civil Engineering, Aalborg University. DCE Technical reports, No. 201 '.
- Gao, Z. and Moan, T. (2009), Mooring system analysis of multiple wave energy converters in a farm configuration, in 'Proc. 8th European Wave and Tidal Energy Conference', Upsala, Sweden.
- Gaspar, F. J., Calvario, M., Kamarlouei, M. and Guedes Soares, C. (2018), 'Design tradeoffs of an oil-hydraulic power take-off for wave energy converters', *Ren. Energy* **129**, 245–259.
- Gaspar, F. J., Kamarlouei, M., Sinha, A., Xu, H., Calvario, M., Fay, F., Robles, E. and Guedes Soares, C. (2016), 'Speed control of oil-hydraulic power take-off system for oscillating body type wave energy converters', *Ren. Energy* **97**, 769–783.
- Gato, L. M. C. and Falcão, A. F. O. (1989), 'Aerodynamics of the wells turbine: Control by swinging rotor-blades.', *Int. J. Mech. Sc.* **31**(6), 425–434.
- Giassi, M. and Götteman, M. (2018), 'Layout design of wave energy parks by a genetic algorithm', *Ocean Eng.* **154**, 252–261.
- Giorgi, G. and Ringwood, J. V. (2019), 'A compact 6-DoF nonlinear wave energy device model for power assessment and control investigations', *IEEE Transactions on sustainable energy* **10**(1), 119–126.
- Goda, Y. (2010), *Random Seas and Design of Maritime Structures*, Vol. 33, 3 edn, World Scientific, Advanced, Series on Ocean Engineering.
- Gomes, R. P. F. (2013), Wave energy extraction from oscillating systems: numerical modelling and experimental testing, PhD thesis, Instituto Superior Técnico, Universidade Técnica de Lisboa.
- Gomes, R. P. F. (2016), *Guidelines for the report of the laboratory classes of Wave Energy and Modeling and Control of Ocean Energy Systems*, Instituto Superior Técnico, Universidade Técnica de Lisboa.

- Gomes, R. P. F., Henriques, J. C. C., Gato, L. M. C. and Falcão, A. F. O. (2010), 'IPS 2-body wave energy converter: acceleration tube optimisation', *J. of Offshore and Polar Eng.* **20**(4), 247–255.
- Gomes, R. P. F., Henriques, J. C. C., Gato, L. M. C. and Falcão, A. F. O. (2012), 'Hydrodynamic optimization of an axisymmetric floating oscillating water column for wave energy conversion', *Ren. Energy* **44**, 328–339.
- Gomes, R. P. F., Henriques, J. C. C., Gato, L. M. C. and Falcão, A. F. O. (2016), 'Wave power extraction of a heaving floating oscillating water column in a wave channel', *Ren. Energy* **99**, 1262–1275.
- Gomes, R. P. F., Malvar-Ferreira, J. D. C., Ribeiro e Silva, S., Henriques, J. C. C. and Gato, L. M. C. (2017), An experimental study on the reduction of the dynamic instability in the oscillating water column spar buoy, in 'Proc. of the 12th European Wave and Tidal Energy Conference', Cork, Ireland.
- Gunn, K. and Stock-Williams, C. (2012), 'Quantifying the global wave power resource', *Ren. Energy* **44**, 296–304.
- Harnois, V., Thies, P. R. and Johanning, L. (2016), 'On peak mooring loads and the influence of environmental conditions for marine energy converters', *J. Mar. Sci. Eng.* **4**(29), 24 pages.
- Harnois, V., Weller, S., Johanning, L., Thies, P. R., Le Boulluec, M., Le Roux, D., Soulé, V. and Ohana, J. (2014), 'Numerical model validation for mooring systems: method and application for wave energy converters', *Ren. Energy* **75**, 869–887.
- Harris, R., Johanning, L. and Wolfram, J. (2004), Mooring systems for wave energy converters: A review of design issues and choices., pp. 180–189. 3rd International Conference on Marine Renewable Energy ; Conference date: 01-07-2004.
- Hasselmann, K., Barnett, T., Bouws, E., Carlson, H., Cartwright, D., Enke, K., Ewing, J., Gienapp, H., Hasselmann, D., Kruseman, P., Meerburg, A., Muller, P., Olbers, D. J., Richter, K., Sell, W. and Walden, H. (1973), 'Measurements of wind-wave growth and swell decay during the Joint North Sea Wave Project (JONSWAP)', *Deut. Hydrogr. Z.* **8**(12), 93 pages.
- Heath, T., Whittaker, T. J. T. and Boake, C. B. (2000), The design construction and operation of the LIMPET wave energy converter (Islay, Scotland), in 'Proc. 4th European Wave Energy Conference', Aalborg, Denmark.
- Holthuijsen, L. H. (2007), *Waves in oceanic and coastal waters*, Cambridge University Press.
- Hotta, H., Washio, Y., Yokozaka, H. and Miyazaki, T. (1996), 'R & D on wave power device "Mighty Whale" ', *Ren. Energy* **9**, 1223–26.

-
- Huang, M. and Aggidis, G. A. (2008), ‘Developments, expectations of wave energy converters and mooring anchors in the uk’, *Journal of Ocean University of China* **7**(1), 10–16.
- Hulme, A. (1982), ‘The wave forces acting on a floating hemisphere undergoing forced periodic oscillations’, *J. Fl. Mech.* **121**, 443–463.
- Huse, E. (1986), Influence of mooring line damping upon rig motions, in ‘Proc. Offshore Technology Conference’, Houston, Texas.
- Huse, E. and Matsumoto, K. (1988), Practical estimation of mooring line damping, in ‘Proc. Offshore Technology Conference’, Houston, Texas.
- Ibrahim, R. A. and Grace, I. M. (2010), ‘Modeling of ship roll dynamics and its coupling with heave and pitch’, *Mathematical Problems in Engineering* **2010**, 32 pages.
- Jeffreys, H. (1924), ‘On the formation of water waves by wind’, *Proc. Royal Soc. of London* **107**, 189–206.
- Johanning, L. and Smith, G. H. (2008a), ‘Improved measurement technologies for floating wave energy converter (WEC) mooring arrangements’, *International Journal of the Society for Underwater Technology* **27**(4), 175–184.
- Johanning, L. and Smith, G. H. (2008b), Station keeping study for wec devices including compliant chain, compliant hybrid and taut arrangement, in ‘Proc. Offshore Mech. Arct. Eng.’.
- Johanning, L., Smith, G. H. and Wolfram, J. (2005), Towards design standards for wec moorings, in ‘Proc. 6th European Wave and Tidal Conference’, Glasgow, UK.
- Johanning, L., Smith, G. H. and Wolfram, J. (2006), Mooring design approach for wave energy converters, in ‘Proc. Inst. Mech. Eng. Part M-J Eng. Marit. Environ.’, Vol. 220, pp. 159–74.
- Johanning, L., Smith, G. H. and Wolfram, J. (2007), ‘Measurement of static and dynamic mooring line damping and their importance for floating wec devices’, *Ocean Eng.* **34**, 1918–1934.
- Johanning, L., Weller, S. D., Thies, P. R., Holmes, B. and Griffiths, J. (2018), Device design, in ‘Greaves D., Iglesias, G. (eds) Wave and Tidal Energy’, Wiley, pp. 151–190.
- Justino, P. A. P. and Clément, A. H. (2003), Hydrodynamic performance for small arrays of submerged spheres, in ‘Proc. 5th European Wave Energy Conference’, Cork, Ireland, pp. 266–273.
- Kalogeri, C., Galanis, G., Spyrou, C., Diamantis, D., Baladima, F., Koukoula, M. and Kallos, G. (2016), ‘Assessing the European offshore wind and wave energy resource for combined exploitation’, *Ren. Energy* **101**, 244–264.
-

-
- Kamphuis, J. W. (2010), *Introduction to Coastal Engineering and Management*, Vol. 30, 2 edn, World Scientific, Advanced, Series on Ocean Engineering.
- Karimirad, M., Koushan, K., Weller, S., Hardwick, J. and Johanning, L. (2016), Applicability of offshore mooring and foundation technologies for marine renewable energy (MRE) device arrays, in 'Proc. Renew 2016, 2nd International Conference on Renewable Energies Offshore', Lisbon, Portugal.
- Keulegan, G. H. and Carpenter, L. H. (1958), 'Forces on cylinders and plates in an oscillating fluid', *Journal of Research of the National Bureau of Standards* **50**(5), 423–440.
- Kofoed, J., Frigaard, P., E., F.-M. and Sørensen, H. (2006), 'Prototype testing of the wave energy converter wave dragon', *Ren. Energy* **31**.
- Korde, U. A. and Ertekin, R. C. (2014), 'On wave energy focusing and conversion in open water', *Ren. Energy* **62**, 84–99.
- Landau, L. D. and Lifshitz, E. M. (1987), *Fluid Mechanics: Volume 6 (Course of Theoretical Physics)*, Butterworth-Heinemann.
- Lee, C. H. and Newman, J. N. (2005), 'Computation of wave effects using the panel method', *WIT Transactions on State-of-the-art in Science and Engineering* **18**, 41 pages.
- Lighthill, M. J. (1962), 'Physical interpretation of the mathematical theory of wave generation by wind', *J. Fluid Mech.* **14**(3), 385–398.
- Liu, Y. and Bergdahl, L. (1998), 'Extreme mooring cable tensions due to wave-frequency excitations', *Appl. Ocean Res.* **20**(4), 237–249.
- Longuet-Higgins, M. S. (1952), 'On the Statistical Distribution of the Heights of Sea Waves', *Journal of Marine Research* **11**(3), 245–266.
- López-Ruiz, A., Begillos, R., Raffo-Caballero, J. M. and Ortega-Sánchez, M. (2018), 'Towards an optimum design of wave energy converter arrays through an integrated approach of life cycle performance and operational capacity', *Applied Energy* **209**, 20–32.
- Lucas, J., Livingstone, M., Vuorinen, M. and Cruz, J. (2012), Development of a wave energy converter (WEC) design tool – application to the WaveRoller WEC including validation of numerical estimates, in 'Proc. 4th International Conference on Ocean Energy', Dublin, Ireland.
- Luxmoore, J. F. (2014), Experimental studies on extreme waves and wave-induced loads on wind turbine support structures in intermediate depth water, PhD thesis, Lancaster University.

- Malvar Ferreira, J. D. C. (2016), Experimental study of the dynamic instability in the oscillating water column spar buoy, Master's thesis, Instituto Superior Técnico, Universidade Técnica de Lisboa.
- Margheritini, L., Vicinanza, D. and Frigaard, P. (2009), 'Ssg wave energy converter: Design, reliability and hydraulic performance of an innovative overtopping device', *Ren. Energy* **34**(5), 1371–1380.
- MARINET-TA1-SPAR-BUOY ARRAY (2016), 'Dynamics of oscillating water column spar-buoy wave energy converters deployed in array and its survivability in extreme conditions'.
- Masselink, G., Hughes, M. G. and Knight, J. (2011), *An Introduction to Coastal Processes and Geomorphology, Second edition*, Routledge.
- Masuda, Y. (1985), An experience of wave power generator through tests and improvement, in 'D. V. Evans, A. F. de O. Falcão (Eds), Hydrodynamics of Ocean Wave Energy Utilization Symposium', Lisbon, Portugal.
- Masuda, Y. and McCormick, M. E. (1987), Experiences in pneumatic wave energy conversion in Japan, in 'McCormick M. E., Kim Y. C., editors. Utilization of ocean waves-wave to energy conversion', New York: ASCE, pp. 1–33.
- Mavrakos, S. A. and McIver, P. (1997), 'Comparison of methods for computing hydrodynamic characteristics of arrays of wave power devices', *Appl. Ocean Res.* **19**, 283–291.
- McCabe, A. P., Bradshaw, A., Meadowcroft, J. A. C. and Aggidis, G. A. (2006), 'Developments in the design of the PS Frog Mk 5 wave energy converter', *Ren. Energy* **31**, 141–51.
- McCormick, M. E. (1974), 'Analysis of a wave energy conversion buoy', *Journal of Hydronautics* **8**(3), 77–82.
- McGuinness, J. P. L. and Thomas, G. (2016), 'Hydrodynamic optimisation of small arrays of heaving point absorbers', *J. Ocean Eng. Mar. Energy* **2**, 439–457.
- Miles, J. W. (1957), 'On the generation of surface waves by shear flows', *J. Fluid Mech.* **3**(2), 185–204.
- Morison, J. R., O'Brien, M. P., Johnson, J. W. and Schaaf, S. A. (1950), 'The force exerted by surface waves on piles', *Pet. Trans., Amer. Inst. Min. Eng.* **189**, 149–154.
- Mueler, M. and McDonald, A. S. (2008), C-GEN - a lightweight permanent magnet generator for direct drive power take off systems, in '2nd International Conference on Ocean Energy (ICOE)', Brest, France.
- Mulder, F. M. (2014), 'Implications of diurnal and seasonal variations in renewable energy generation for large scale energy storage', *Journal of Renewable and Sustainable Energy* **6**.

- Neill, S. P. and Hashemi, M. R. (2013), ‘Wave power variability over the northwest European shelf seas’, *Applied Energy* **106**, 31–46.
- Newman, J. N. (1977), *Marine hydrodynamics*, MIT Press.
- Ning, D. Z., Zhao, X. L., Chen, L. F. and Zhao, M. (2018), ‘Hydrodynamic performance of an array of wave energy converters integrated with a pontoon-type breakwater’, *Energies* **11**(3), 17 pages.
- Ocean Energy Systems (OES) (2016), ‘Annual report’.
- Oikonomou, C. and Aggidis, G. A. (2015), Wave energy resource assessment in the seas around Greece: estimation and prospects, in ‘Proc. 7th International Short Course/conference on Applied Coastal Research’, Florence, Italy.
- Oikonomou, C., Gomes, R. P. F., Gato, L. M. C. and Falcão, A. F. O. (2017), Analysis of a triangular array of floating oscillating water column devices with inter-body mooring connections in regular waves, in ‘Proc. 12th European Wave and Tidal Energy Conference’, Cork, Ireland.
- Oikonomou, C., Laitano-Segura, J., Guzzetti, M. and Gradowski, M. (2016), *Wave flume laboratory report, wave energy modelling and control of ocean energy systems*, Instituto Superior Técnico, Universidade Técnica de Lisboa.
- Palm, J. and Eskilsson, C. (2018), *MOODY USER MANUAL: VERSION 1.0.0.*, Chalmers University of Technology, Department of Mechanics and Maritime Sciences.
- Palm, J., Eskilsson, C. and Bergdahl, L. (2017), ‘An hp-adaptive discontinuous galerkin method for modelling snap loads in mooring cables’, *Ocean Eng.* **144**, 266–276.
- Palm, J., Eskilsson, C., Paredes, G. M. and Bergdahl, L. (2016), ‘Coupled mooring analysis for floating wave energy converters using CFD: Formulation and validation’, *International Journal of Marine Energy* **16**, 83–99.
- Paredes, G. M., Bergdahl, L., Palm, J., Eskilsson, C. and Pinto, F. T. (2013), Station keeping design for floating wave energy devices compared to floating offshore oil and gas platforms, in ‘Proc. 10th European Wave and Tidal Energy Conference’, Aalborg, Denmark.
- Paredes, G. M., Palm, J., Eskilsson, C., Bergdahl, L. and F., T.-P. (2016), ‘Experimental investigation of mooring configurations for wave energy converters’, *International Journal of Marine Energy* **15**, 56–67.
- Parmeggiani, S., Kofoed, J. P. and Friis-Madsen, E. (2013), ‘Experimental study related to the mooring design for the 1.5 MW Wave Dragon WEC demonstrator at DanWEC’, *Energies* **6**, 1863–1886.
- Phillips, O. M. (1957), ‘On the generation of waves by turbulent wind’, *J. Fluid Mech.* **2**(5), 417–445.

- Pierson, W. J. and Moskowitz, L. (1964), ‘Proposed spectral form for fully developed wind seas based on the similarity theory of s. a. kitaigorodskii’, *J. Geophys. Res.* **69**(24), 5181–5190.
- Plummer, A. R., Hillis, A. J. and Perez-Collazo, C. (2018), Power systems, in ‘Greaves D., Iglesias, G. (eds) Wave and Tidal Energy’, Wiley, pp. 191–232.
- Porter, A., Ruehl, K. and Chartrand, C. (2014), Further development of SNL SWAN, a validated wave energy converter array modeling tool, in ‘Proc. 2nd Marine Energy Technology Symposium METS2014, April 15-18, 2014’, Seattle, WA.
- Prado, M. (2008), Archimedes wave swing (AWS), in ‘Cruz J., editor. Ocean wave energy.’, Berlin: Springer, pp. 297–304.
- Pringle, A. W. (1995), ‘Erosion of a cyclic saltmarsh in Morecambe Bay, North-West England’, *Earth Surface Processes and Landforms* **5**, 387–405.
- Ribeiro e Silva, S., Gomes, R. P. F. and Falcão, A. F. O. (2016), ‘Hydrodynamic optimization of the UGEN: Wave energy converter with u-shaped interior oscillating water column’, *Int. J. of Mar. Energy* **15**, 112–26.
- Ricci, P., Rico, A., Ruiz-Minguela, P., Boscolo, F. and Villate, J. L. (2012), Design, modelling and analysis of an integrated mooring system for wave energy arrays, in ‘Proc. 4th International Conference on Ocean Energy, 17 October, Dublin’.
- Ricci, P., Saulnier, J. B., Falcão, A. F. O. and Pontes, M. T. (2008), Time-domain models and wave energy converters performance assessment, in ‘Proc. ASME 2008 27th International Conference on Offshore Mechanics and Arctic Engineering’, Estoril, Portugal.
- Richardson, S. M. (1989), *Fluid mechanics*, New York: Hemisphere Pub. Corp.
- Rinaldi, G., Portillo, J. C. C., Khalid, F., Henriques, J. C. C., Thies, P. R., Gato, L. M. C. and Johanning, L. (2018), ‘Journal of ocean engineering and marine energy’, *Multivariate analysis of the reliability, availability, and maintainability characterizations of a Spar–Buoy wave energy converter farm* pp. 1–17.
- Rémouit, F., Chatzigiannakou, M. A., Bender, A., Temiz, I., Sundberg, J. and Engström, J. (2018), ‘Deployment and maintenance of wave energy converters at the lysekil research site: A comparative study on the use of divers and remotely-operated vehicles’, *J. of Marine Science and Engineering* **6**(39), 21 pages.
- Rusu, E. and Guedes Soares, C. (2013), ‘Coastal impact induced by a Pelamis wave farm operating in the Portuguese nearshore’, *Ren. Energy* **58**, 34–49.
- Salter, S. (2016), ‘Wave energy: Nostalgic ramblings, future hopes and heretical suggestions’, *J. Ocean Eng. Mar. Energy* **2**, 399–428.
- Salter, S. H. (1974), ‘Nature’, *Wave power* **249**, 720–4.

- Sarmiento, A. J. N. A. and Falcão, A. F. O. (1985), ‘Wave generation by an oscillating surface-pressure and its application in wave energy extraction’, *J. of Fluid. Mech.* **150**, 467–85.
- Sarpkaya, T. (1976), ‘Forces on rough-walled vertical cylinders’, *Coastal Eng.* (15), 2301–2320.
- Sarpkaya, T. and Isaacson, M. (1981), *Mechanics of Wave Forces on Offshore Structures*, Van Nostrand Reinhold, New York, USA.
- Sartini, L., Mentaschi, L. and Besio, G. (2015), ‘Comparing different extreme wave analysis models for wave climate assessment along the italian coast’, *Coastal Eng.* **100**, 37–47.
- Saussay, A. (2018), ‘Can the US shale revolution be duplicated in continental Europe? an economic analysis of european shale gas resources’, *Energy economics* **69**, 295–306.
- Stratigaki, V., Troch, P., Stallard, T., Forehand, D., Kofoed, J. P., Folley, M., Benoit, M., Babarit, A. and Kirkegaard, J. (2014), ‘Wave basin experiments with large wave energy converter arrays to study interactions between the converters and effects on other users in the sea and the coastal area’, *Energies* **7**, 701–734.
- Svedsen, I. A., Madsen, P. A. and Buhr Hansen, J. (1978), ‘Wave characteristics in the surf zone’, *Coastal Engineering Proceedings* (16), 520–539.
- Tarrant, K. and Meskell, C. (2016), ‘Investigation on parametrically excited motions of point absorbers in regular waves’, *Ocean Engineering* **111**, 67–81.
- Terra, G., Jan van de Berg, W. and Maas, L. R. M. (2005), ‘Experimental verification of lorentz linearisation procedure of quadratic friction’, *Fluid Dyn. Res.* **35**, 175–188.
- Thomas, G. P. and Evans, D. V. (1981), ‘Arrays of three-dimensional wave energy absorbers’, *J. Fluid Mech.* **108**, 67–88.
- Thompson, A. and Aggidis, G. A. (2007), Review and state of the art of wave energy and wave energy converters, in ‘IMEchE, Fluid Machinery for Developing Engineers, Invited Paper IMechE, Event Publications’, Cranfield.
- Thomsen, J. B., Ferri, F. and Kofoed, J. P. (2017), ‘Screening of available tools for dynamic mooring analysis of wave energy converters’, *Energies* **10**, 18 pages.
- Thurman, H. V. and Trujillo, A. P. (2001), *Essentials of Oceanography, seventh ed.*, Prentice Hall.
- Torre-Enciso, Y., Ortubia, I., López de Aguilera, L. I. and Marquéz, J. (2009), Mutriku wave power plant: from the thinking out to the reality, in ‘Proc. 8th European Wave Energy Conf.’, Uppsala, Sweden, pp. 319–29.

- Troch, P., Stratigaki, V., Stallard, T., Forehand, D., Folley, M., Kofoed, J. P., Benoit, M., Babarit, A., Vantorre, M. and Kirkegaard, J. (2014), An overview of the WECwakes project: physical modeling of an array of 25 wave energy converters, *in* '3rd LAHR Europe Congress, Porto, Portugal'.
- Tucker, M. J. and Pitt, E. G. (2001), *Waves in Ocean Engineering*, Elsevier Science.
- Vicente, P. C. (2016), Moorings of Floating Point Absorber Wave Energy Converters in Arrays, PhD thesis, Instituto Superior Técnico, Universidade Técnica de Lisboa.
- Vicente, P. C., Falcão, A. F. d. O. and Justino, P. A. P. (2013), 'Nonlinear dynamics of a tightly moored point-absorber wave energy converter', *Ocean Eng.* **59**, 20–36.
- Vicente, P. C., Falcão, A. F. O., Gato, L. M. C. and Justino, P. A. P. (2009a), 'Dynamics of arrays of floating point-absorber wave energy converters with inter-body and bottom slack-mooring connections', *Appl. Ocean Res.* **31**(4), 267–281.
- Vicente, P. C., Falcão, A. F. O., Gato, L. M. C. and Justino, P. A. P. (2009b), Hydrodynamics of multiple floating point-absorber wave energy systems with inter-body and bottom slack-mooring connections, *in* 'Proc. 28th Int. conf. ocean offshore arctic eng.'.
- Vicente, P. C., Falcão, A. F. O. and Justino, P. A. P. (2011), Optimization of mooring configuration parameters of floating wave energy converters, *in* 'Proc. of the ASME 2011 30th Int. Conf. Ocean Offshore Arctic Eng.', Rotterdam, The Netherlands.
- Vicente, P., Falcão, A. F. O., Gato, L. and Justino, P. (2009c), Hydrodynamics of triangular grid arrays of floating point-absorber wave energy converters with inter-body and bottom slack-mooring connections., *in* 'Proc. 8th European Wave and Tidal Energy Conference', Uppsala, Sweden.
- Vickers, A. W. (2013), Improve the Understanding of Uncertainties in Numerical Analysis of Moored Floating Wave Energy Converters, PhD thesis, University of Exeter.
- Wadey, M. P., Robers, H. and Harris, J. (2013), 'Impacts of climate change on built structures (onshore and coastal)', *Marine Climate Change Impacts Partnership: Science Review* pp. 284–294.
- WAMIT (2006), *WAMIT, User's manual, Version 6.3*, WAMIT Inc., Available online at www.wamit.com.
- Webster, W. C. (1995), 'Mooring induced damping', *Ocean Eng.* **22**(6), 571–591.
- Weinstein, A., Fredrikson, G., Parks, M. J. and Nielsen, K. (2004), Aquabuoy, the offshore wave energy converter numerical modelling and optimization, *in* 'Proc. MTTS/IEEE Techno-Ocean '04 Conf.', Kobe, Japan.
- Weller, S. D., Parish, D., Gordelier, T., de Miguel Para, B., Garcia, E., A., Goodwin, P., Tornroos, D. and Johanning, L. (2017), Open sea OWC motions and mooring loads monitoring at BiMEP, *in* 'Proc. 12th European Wave and Tidal Energy Conference', Cork, Ireland.

- Weller, S., Davies, P., Vickers, A. W. and Johanning, L. (2014), ‘Synthetic rope responses in the context of load history: Operational performance’, *Ocean Eng.* **83**, 111–124.
- Weller, S., Johanning, L. and Davies, P. (2013), ‘Merific: Best practice report- mooring of floating marine renewable energy devices’.
- WETFEEET D6.1 (2016), ‘D6.1- Analysis of different potential mooring configurations of non-rigid inter-moored devices’.
- WETFEEET D6.2 (2016), ‘D6.2- Analysis of different potential configurations of rigidly inter-moored devices’.
- Whittaker, T. and Folley, M. (2012), ‘Nearshore oscillating wave surge converters and the development of Oyster’, *Phil. Tran. R. Soc. A* **370**, 345–364.
- Wolgamot, H. A., Taylor, P. H. and Eatock Taylor, R. (2013), ‘The interaction factor and directionality in wave energy arrays.’, *Ocean Eng.* **47**, 65–73.
- World Energy Council (2016), ‘World energy resources’.

Appendices

Appendix A

Mesh sensitivity analysis

This section shows the various meshes considered in the mesh refinement analysis for the arrays of spherical and cylindrical point absorbers presented in Chapter 3. The BIEM solver WAMIT was used, and discretisation was done via the higher order discretisation method. A sensitivity analysis on the hydrodynamic coefficients and excitation force amplitudes due to changes in the mesh discretisation was carried out. The mesh resolution was varied for both the single device and the array configurations on the SPAs and the CPAs. Since both of these geometries are axisymmetric, the BIEM solver only needed to consider one quarter of the wetted surface area when calculating the velocity potential; the same number N of azimuthal and radial/vertical panels was used to define this geometry quarter. The following discretisations of N azimuthal and N radial/vertical panels were simulated:

1. $N=2$: 4 panels per geometry quarter, 16 panels in total
2. $N=4$: 16 panels per geometry quarter, 64 panels in total
3. $N=6$: 36 panels per geometry quarter, 144 panels in total
4. $N=8$: 64 panels per geometry quarter, 256 panels in total
5. $N=10$: 100 panels per geometry quarter, 400 panels in total.

The range of studied mesh resolution for the two point absorbers is shown in Figs A.1 and A.2. An additional panel was introduced on top of each geometry (Figs. A.1f and A.2f) for irregular frequency removal. This is a special feature of WAMIT (Lee and Newman, 2005), because when solving for the velocity potential by integrating the Green functions over the wetted surface area, the numerical technique used can sometimes return singularities at very high frequencies. Despite the significant variation in the number of panels used, there was no noticeable effect on the resulting hydrodynamic coefficients of either the SPAs or the CPAs. Therefore, the hydrodynamic coefficients have not been plotted and presented in this section, because they are the same as those which have already been used throughout this thesis.

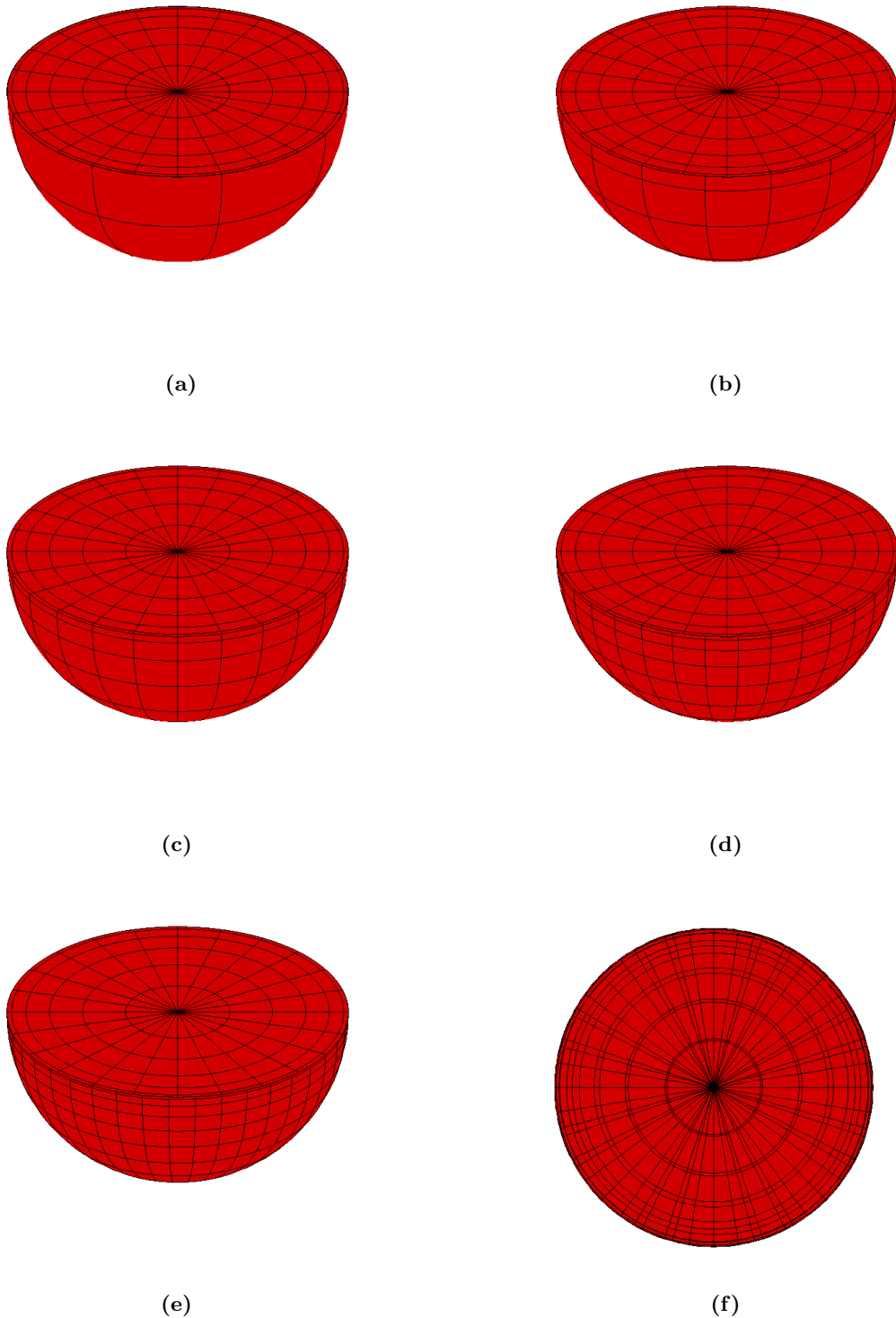


Figure A.1: Meshes for the SPAs used in the WAMIT calculations with the higher-order discretisation method, for a varying number of panels, $N=2$ (A.1a), $N=4$ (A.1b), $N=6$ (A.1c), $N=8$ (A.1d), $N=10$ (A.1e). The top panel for irregular frequency removal is depicted in A.1f.

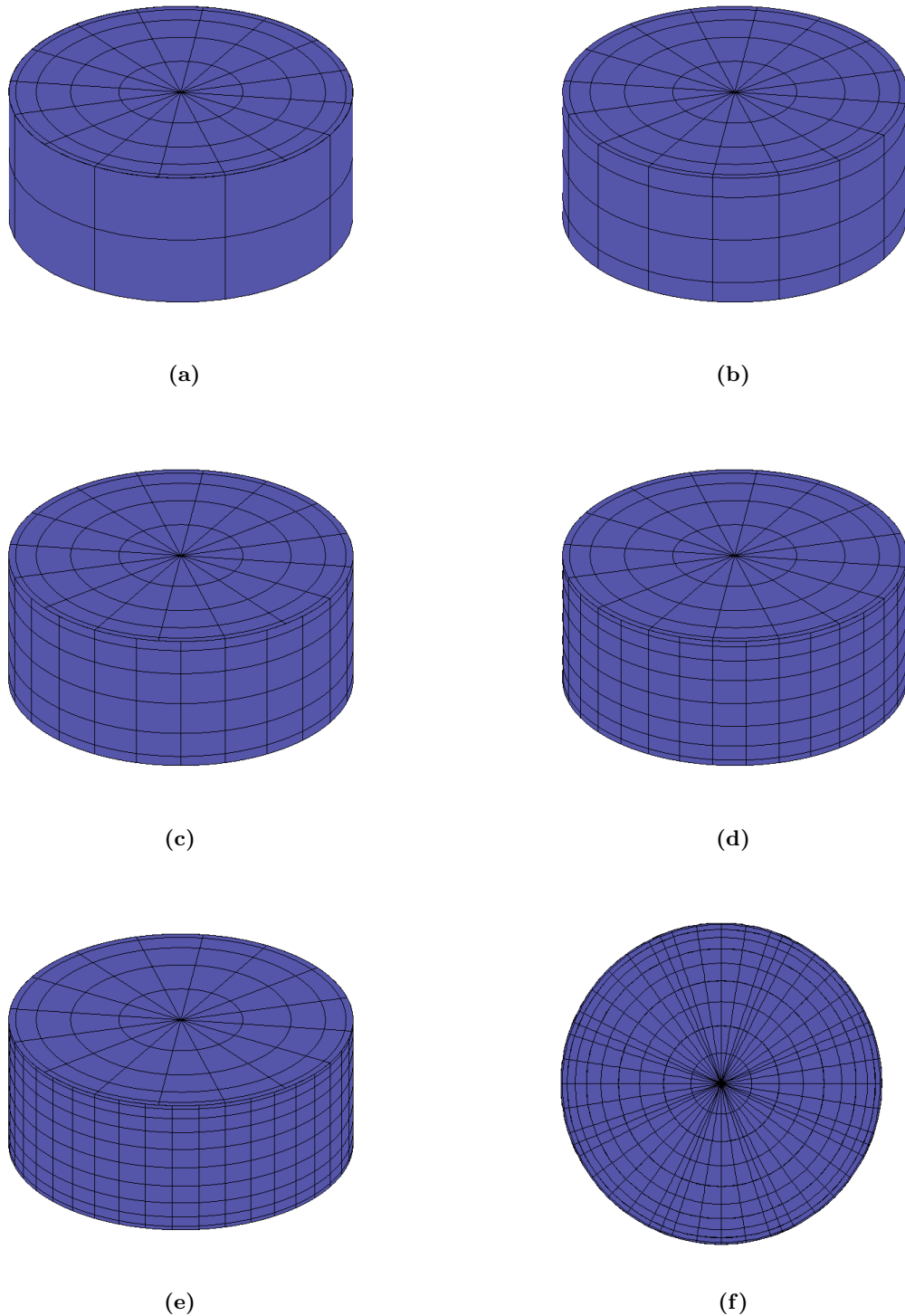


Figure A.2: Meshes for CPAs used in the WAMIT calculations with the higher order discretisation method, for a varying number of panels, $N=2$ (A.2a), $N=4$ (A.2b), $N=6$ (A.2c), $N=8$ (A.2d), $N=10$ (A.2e). The top panel for irregular frequency removal is depicted in A.2f.

Appendix B

Spherical point absorbers: sensitivity analysis

A sensitivity analysis was performed for the array of spherical point absorbers presented in Chapter 3, varying several mooring parameters, such as the mooring stiffness (C_{bm}^*), the angle between the bottom mooring line and the horizontal surface plane (β), and the angle between the inter-body mooring line and the horizontal surface plane (α). Since past studies have highlighted the significance of the directionality of wave heading, a sensitivity analysis on the angle of wave incidence (θ) was also performed to investigate the effect of breaking the symmetry of the problem (in the sense that for $\theta = 0$, SPAs 1 and 2 exhibited the same hydrodynamic behaviour). These results were particularly important for surge oscillations at operational wave frequencies.

Figs. B.1 depicts the RAOs of the three SPAs from the triangular moored array, as well as the RAO of the clump weight as a function of the wave frequency ω , for different values of the angle formed between the inter-body mooring line and the horizontal plane (α). The surging and swaying RAOs of SPAs 1, 2, and 3 remain almost constant to the variations of the angle α (Figs. B.1 and B.2). Higher values of α contribute to an increase in the weight surging RAO, for wave frequencies ω between 0.5 and 1.5 rad/s. The effect of varying α is not significant in heave either, for SPAs 1, 2, and 3, however lower values of α contribute to a decrease in the clump weight heaving RAO (Fig. B.3). It should be noted that no viscous damping has been introduced for the clump weight.

Figs. B.4, B.5, and B.6 illustrate the surge, sway, and heave RAOs respectively, of the three SPAs, and the corresponding RAO of the clump weight as a function of the wave frequency ω , for different values of the angle formed between the bottom mooring line and the horizontal surface plane (β). Higher values of β shift the low frequency peaks (that occurred due to the presence of the inter-body mooring system), to lower wave frequencies for all the modes, but the effect is not significant in the range of operational wave frequencies.

For the variation of the bottom mooring line stiffness C_{bm}^* , lower values of C_{bm}^* shift the peaks in the surge and sway RAOs, towards lower frequencies ω (Figs. B.7 and

B.8 respectively). For the heave RAO (Fig. B.9), higher values of C_{bm}^* contribute to a slight decrease at the peak frequency. The stiffness of each mooring line was considered to be 10% of the buoy's hydrostatic stiffness, and constant with wave frequency (not frequency-dependent). This approach assumes that the mooring line system never enters a semi-taut state, and hence there is always some amount of chain lying on the seabed. The clump weight was assumed to be made of concrete, and it was assumed that its mass was 5% of the mass of the converter.

Figs. B.10, B.11, and B.12 illustrate the RAOs of the three SPAs, the clump weight as a function of the wave frequency ω , for different values of the angle of wave incidence (θ). It is observed that by varying the angle of wave incidence, SPAs 1 and 2 do not experience the same surge and sway RAOs, due to the symmetry of the problem being broken. Regarding the heave RAO (Fig. B.12) there is a significant effect of the variation of the angle of wave incidence at the peak frequency, suggesting that $\theta = 30^\circ$ contributes to the highest response magnitude at the peak frequency. This suggests the bodies of the particular array experience high hydrodynamic interference which introduces coupling between the modes. This is subject to the spacing between the devices and their size, but also due to the fact that a reduced PTO damping was introduced, enriching this interference.

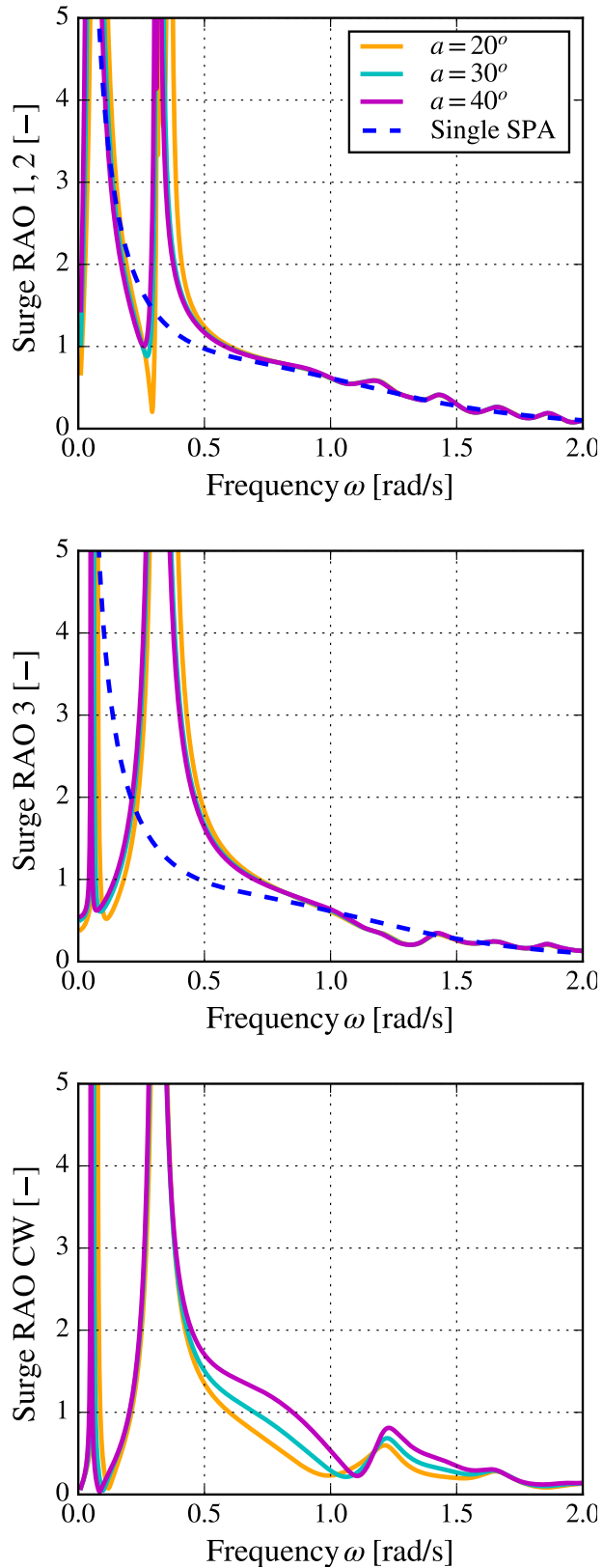


Figure B.1: Surge RAOs against the wave frequency ω for the three SPAs with bottom and inter-body mooring connections, and the clump weight for different values of the inter-body mooring force angle $\alpha=(20^\circ, 30^\circ, 40^\circ)$, with $A_w=1$ m, $C_{bm^*}=0.1$, $\theta = 30^\circ$, and $\beta = 30^\circ$.

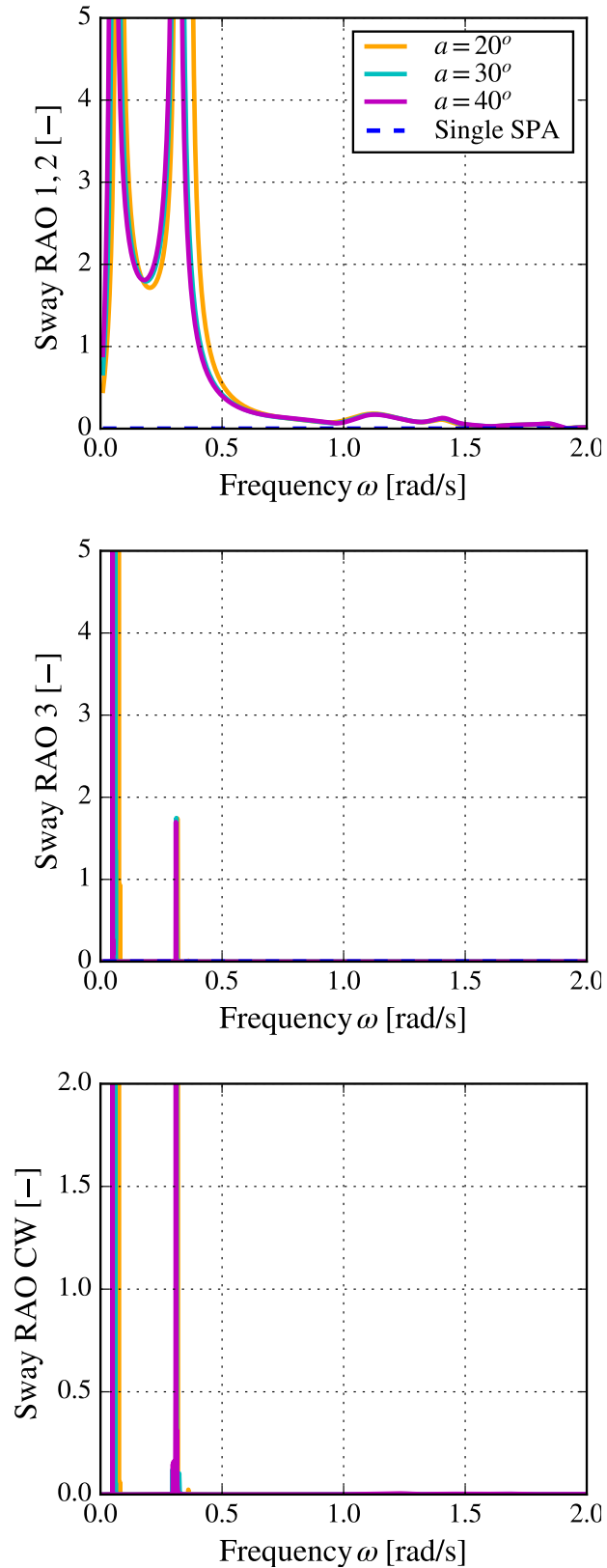


Figure B.2: Sway RAOs against the wave frequency ω for the three SPAs with bottom and inter-body mooring connections, and the clump weight for different values of the inter-body mooring force angle $\alpha=(20^\circ, 30^\circ, 40^\circ)$, with $A_w=1$ m, $C_{bm^*}=0.1$, $\theta = 30^\circ$, and $\beta = 30^\circ$.

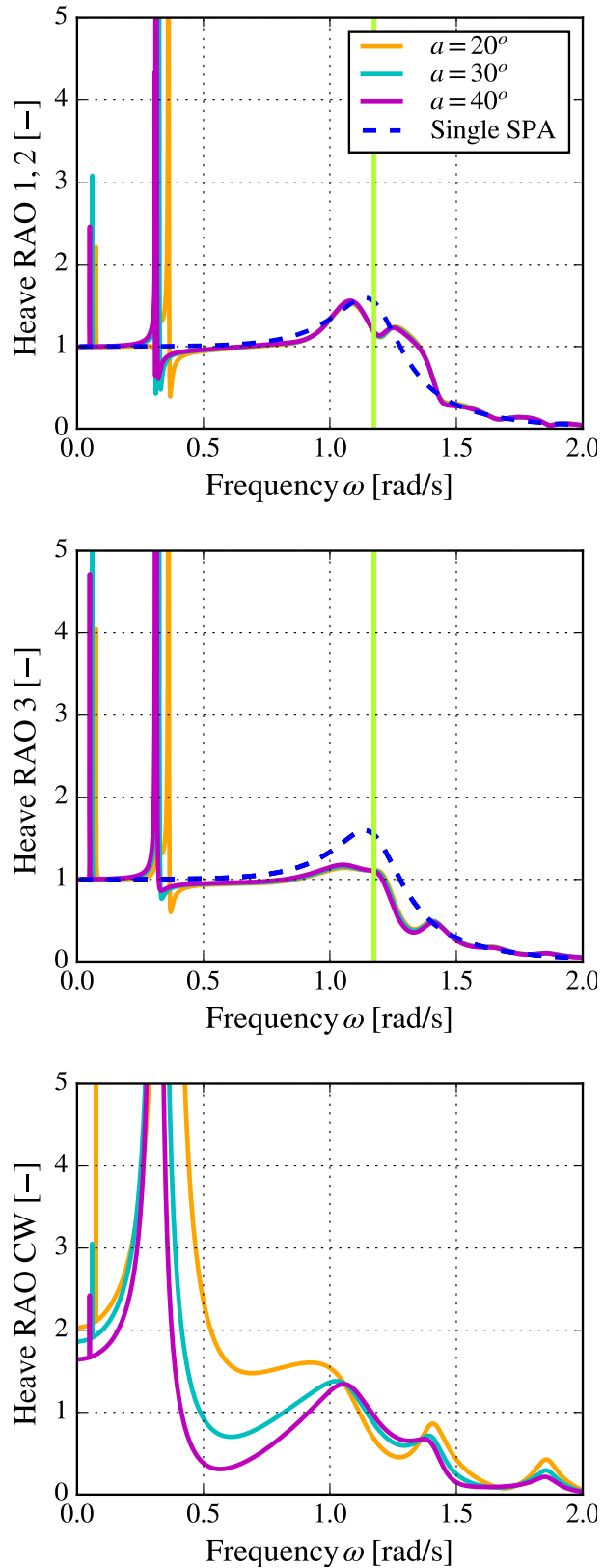


Figure B.3: Heave RAOs against the wave frequency ω for the three SPAs with bottom and inter-body mooring connections, and the clump weight for different values of the inter-body mooring force angle $\alpha = (20^\circ, 30^\circ, 40^\circ)$, with $A_w = 1$ m, $C_{bm}^* = 0.1$, $\theta = 30^\circ$, and $\beta = 30^\circ$. The vertical green lines represent the SPA's resonance frequency.

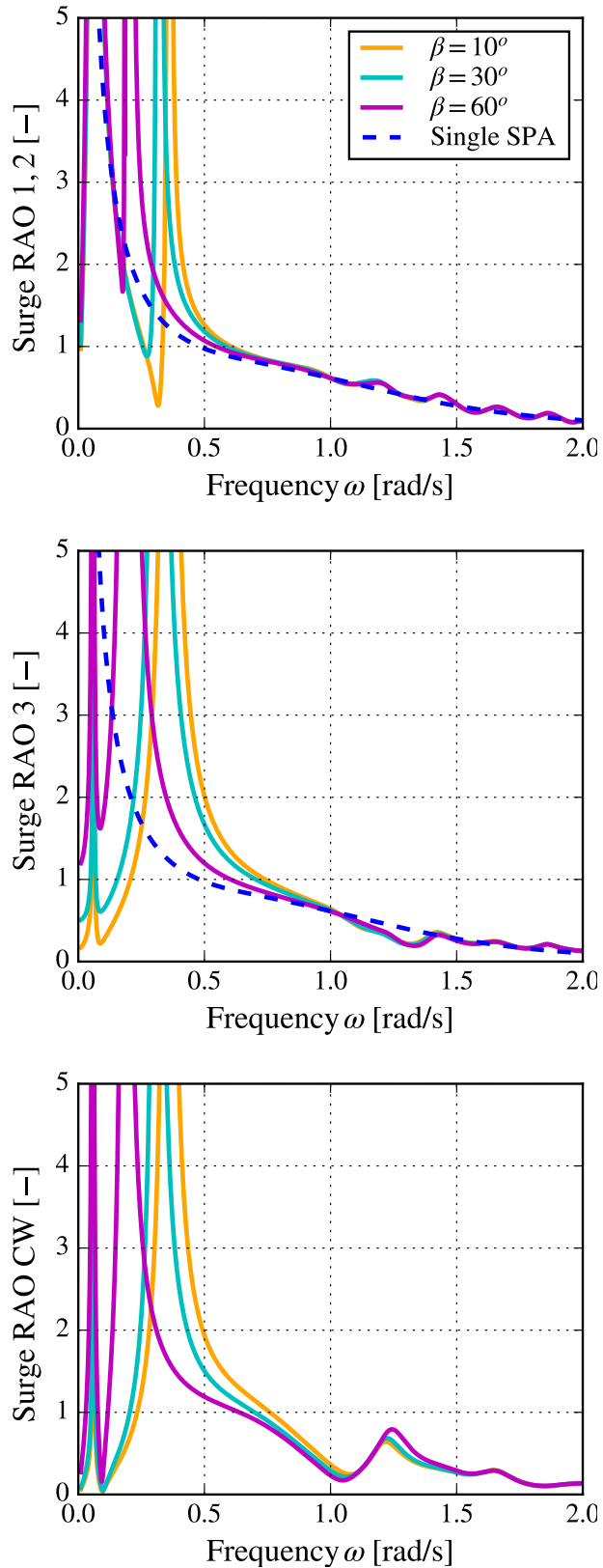


Figure B.4: Surge RAOs against the wave frequency ω for the three SPAs with bottom and inter-body mooring connections, and the clump weight for different values of the angle of the bottom mooring force $\beta=(0^\circ, 30^\circ, 60^\circ)$, with $A_w=1$ m, $\alpha = 30^\circ$, $\theta = 0^\circ$, and $C_{bm}^*=0.1$.

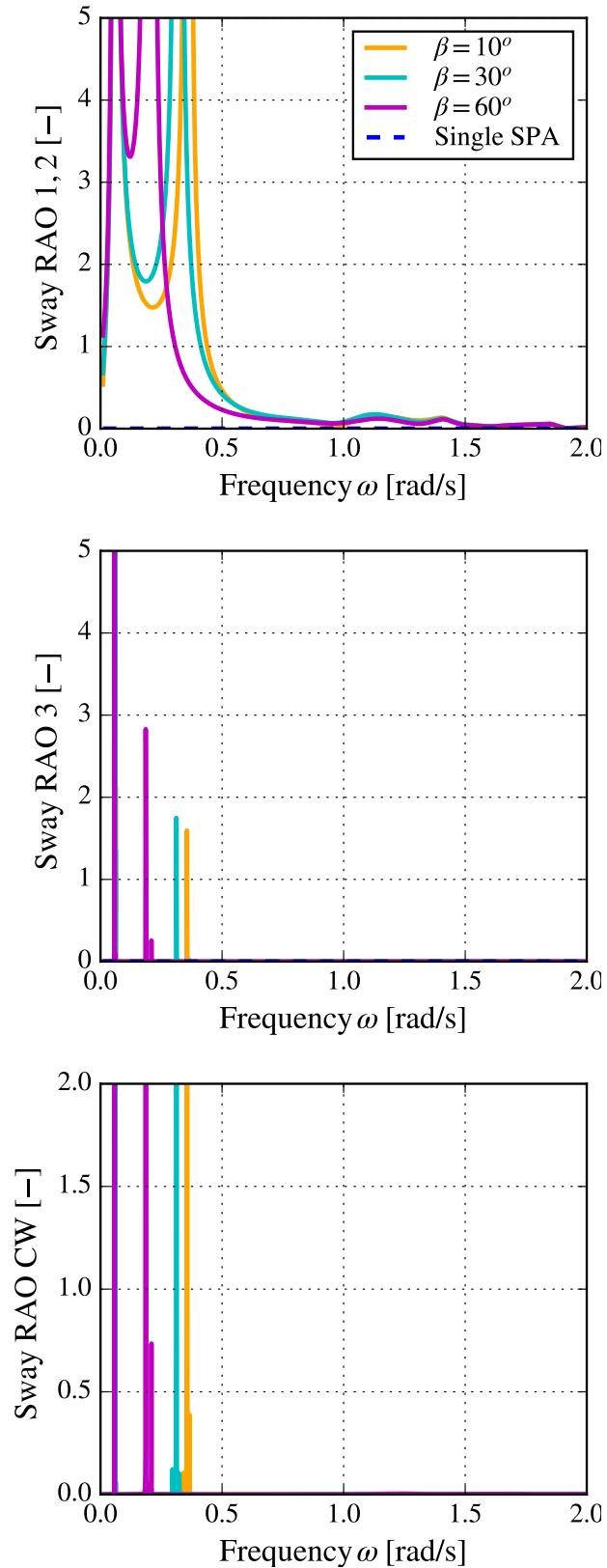


Figure B.5: Sway RAOs against the wave frequency ω for the three SPAs with bottom and inter-body mooring connections, and the clump weight for different values of the angle of the bottom mooring force $\beta=(0^\circ, 30^\circ, 60^\circ)$, with $A_w=1$ m, $\alpha = 30^\circ$, $\theta = 0^\circ$, and $C_{bm}^*=0.1$.

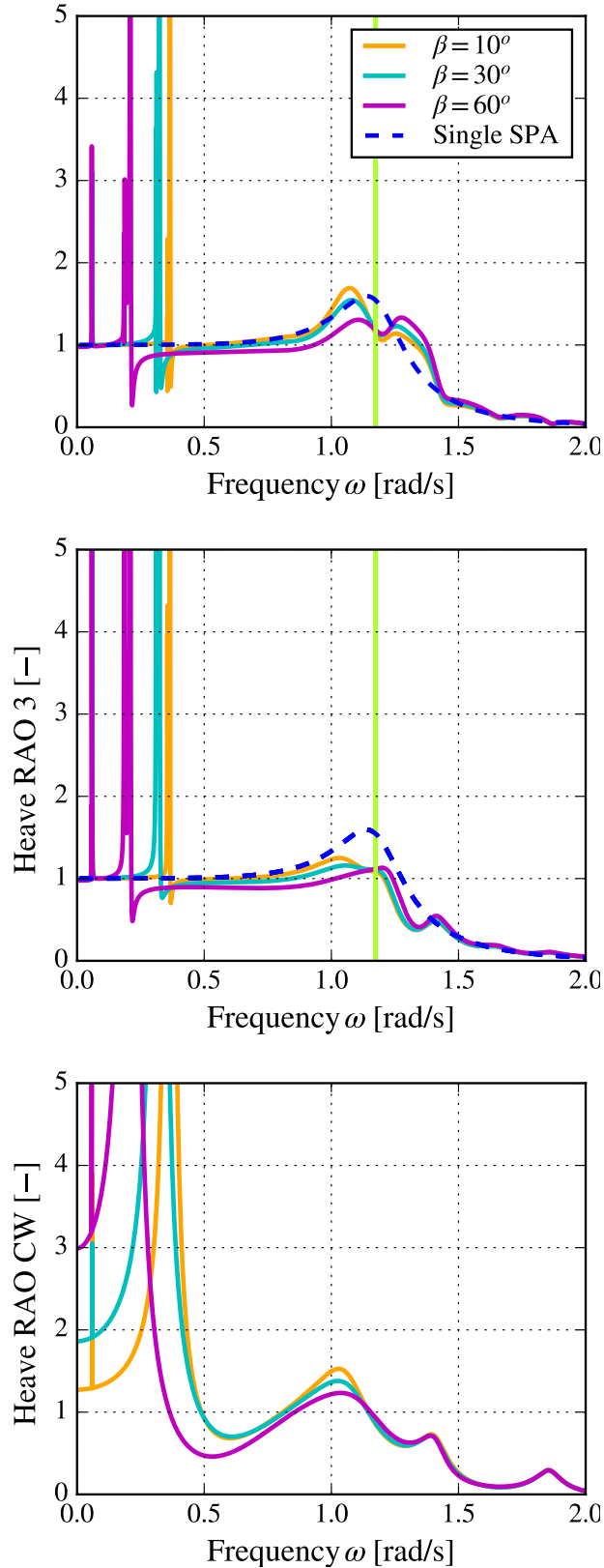


Figure B.6: Heave RAOs against the wave frequency ω for the three SPAs with bottom and inter-body mooring connections, and the clump weight for different values of the angle of the bottom mooring force $\beta=(0^\circ, 30^\circ, 60^\circ)$, with $A_w=1$ m, $\alpha = 30^\circ$, $\theta = 0^\circ$, and $C_{\text{bm}}^*=0.1$. The green vertical lines corresponds to the SPA resonance frequency.

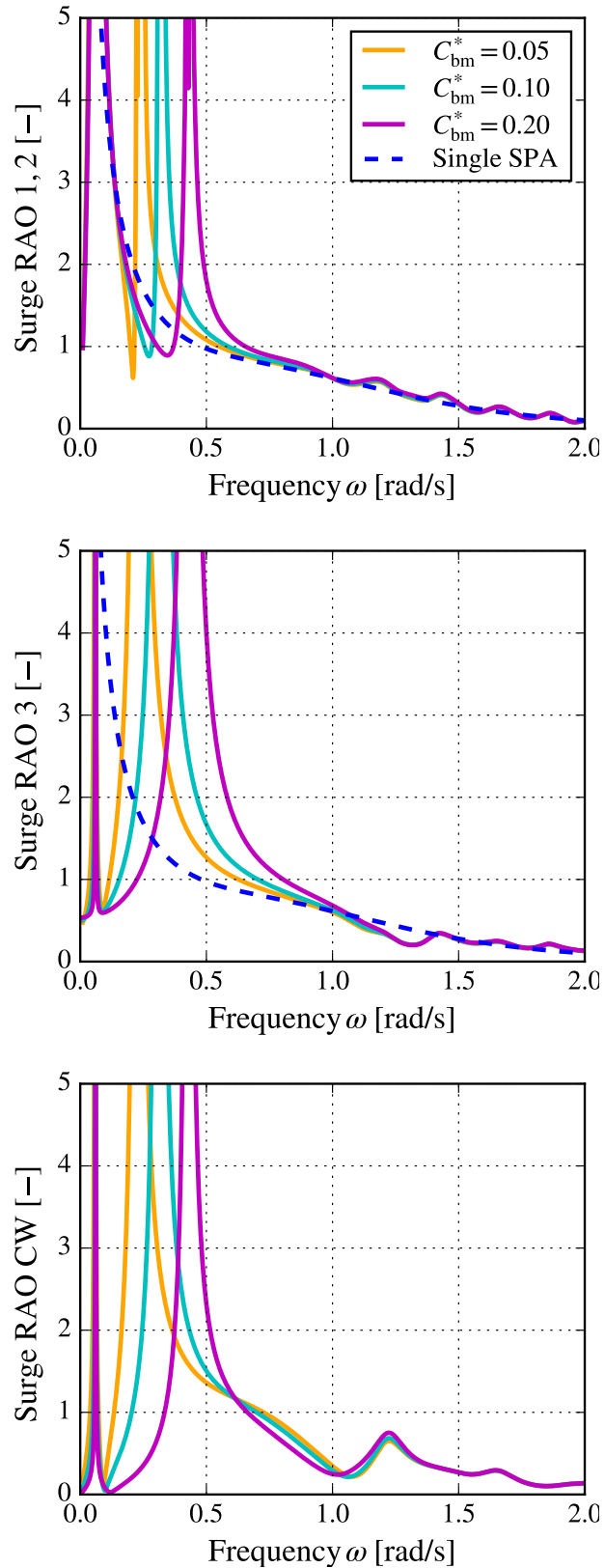


Figure B.7: Surge RAOs against the wave frequency ω for the three SPAs with bottom and inter-body mooring connections, and the clump weight, for different values the bottom mooring line stiffness $C_{bm}^*=(0.05, 0.1, 0.2)$, with $A_w=1$ m, $\alpha = 30^\circ$, $\theta = 0^\circ$, and $\beta = 30^\circ$.

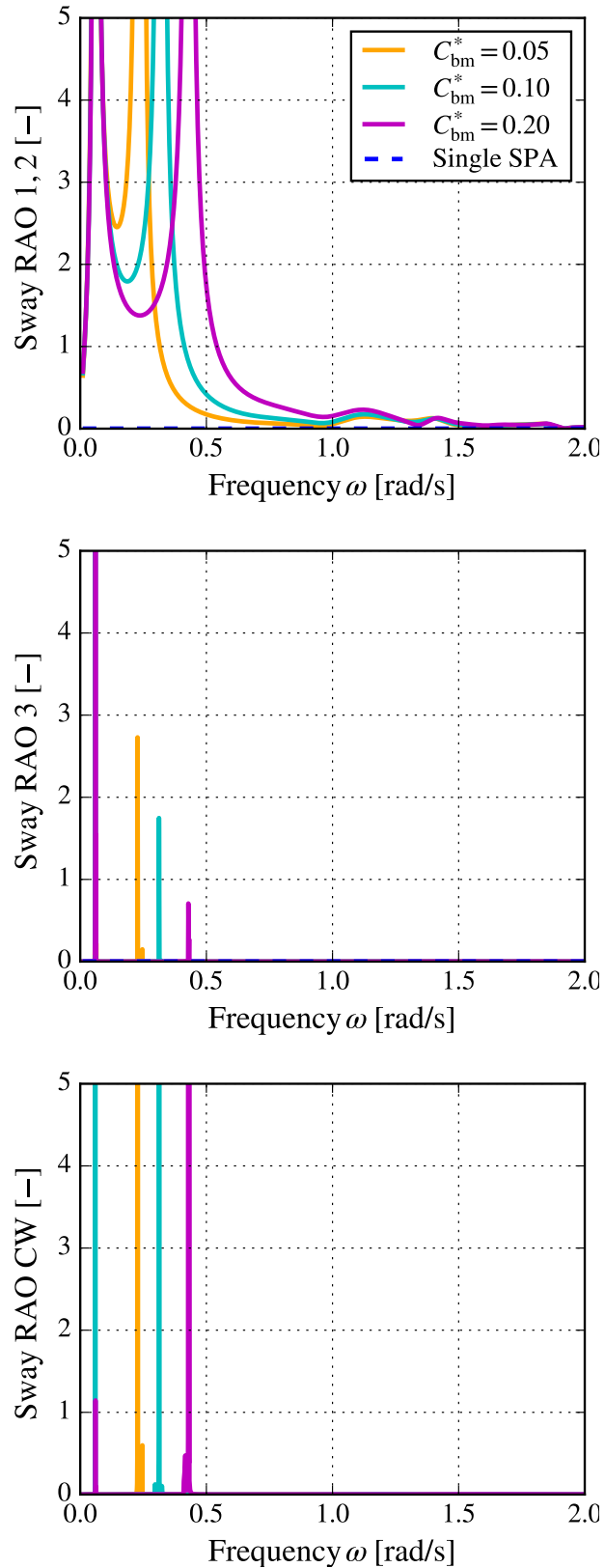


Figure B.8: Sway RAOs against the wave frequency ω for the three SPAs with bottom and inter-body mooring connections, and the clump weight, for different values the bottom mooring line stiffness $C_{bm}^* = (0.05, 0.1, 0.2)$, with $A_w = 1$ m, $\alpha = 30^\circ$, $\theta = 0^\circ$, and $\beta = 30^\circ$.

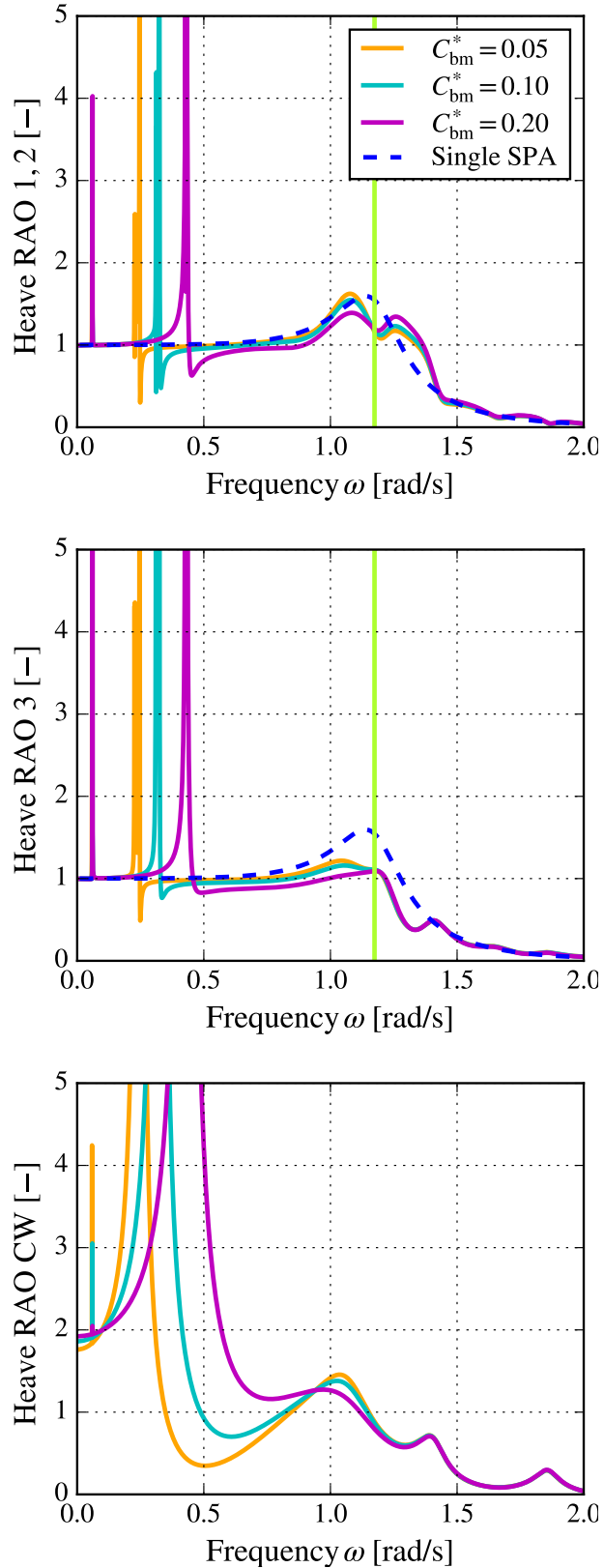


Figure B.9: Heave RAOs against the wave frequency ω for the three SPAs with bottom and inter-body mooring connections, and the clump weight, for different values the bottom mooring line stiffness $C_{bm}^*=(0.05, 0.1, 0.2)$, with $A_w=1$ m, $\alpha = 30^\circ$, $\theta = 0^\circ$, and $\beta = 30^\circ$. The green vertical lines correspond to the natural frequency of the SPA.

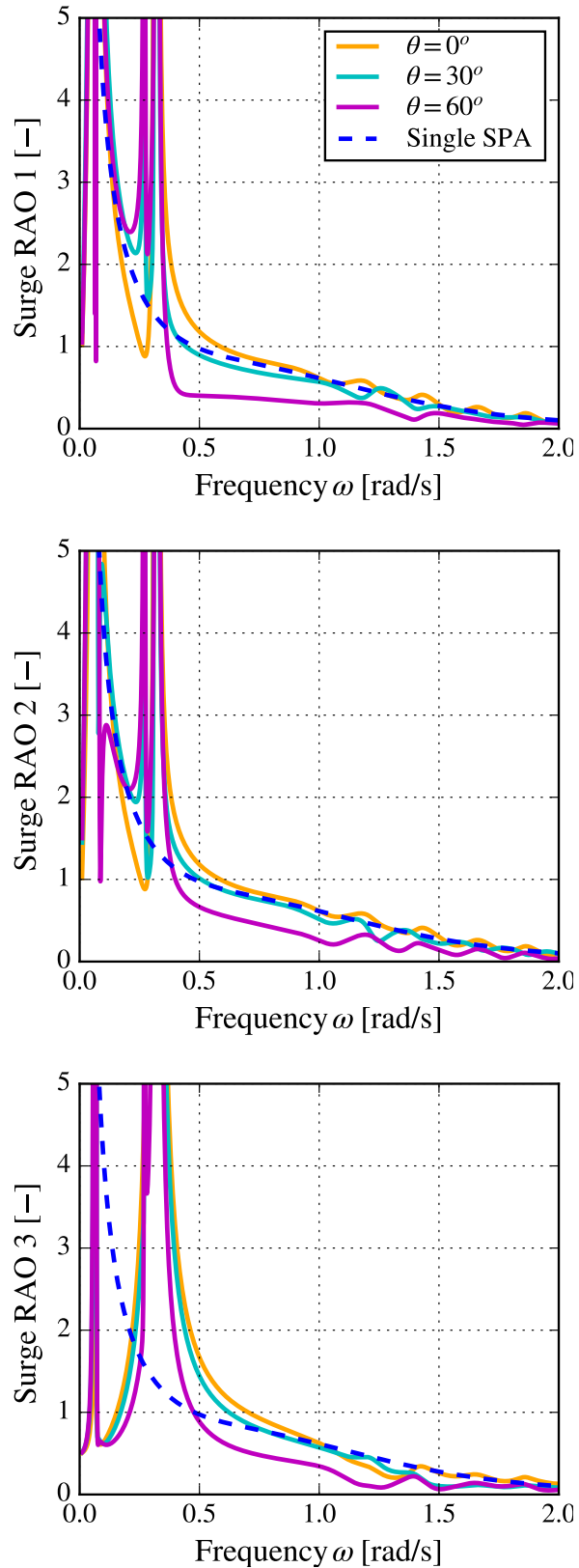


Figure B.10: Surge RAOs against the wave frequency ω for the three SPAs with bottom and inter-body mooring connections, for different values the angle of wave incidence $\theta=(0^\circ, 30^\circ, 60^\circ)$, with $A_w=1$ m, $\alpha = 30^\circ$, $\beta = 30^\circ$, and $C_{bm^*} = 0.1$.

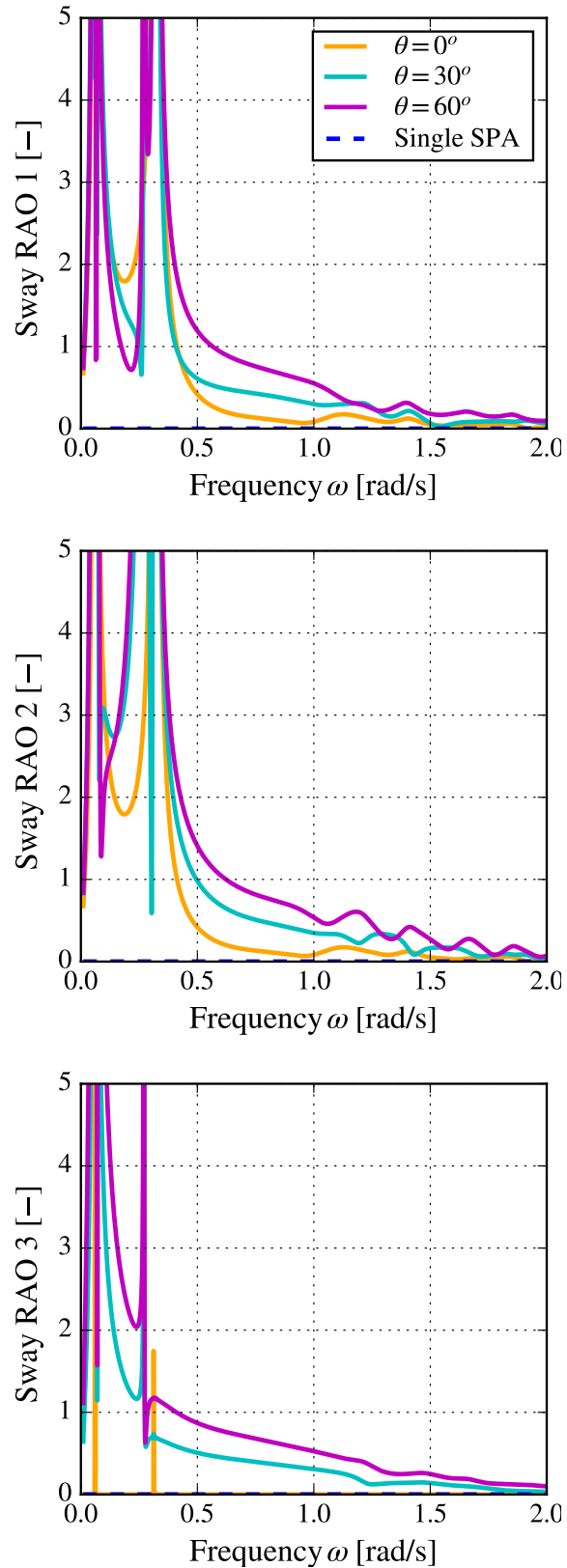


Figure B.11: Sway RAOs against the wave frequency ω for the three SPAs with bottom and inter-body mooring connections, for different values the angle of wave incidence $\theta=(0^\circ, 30^\circ, 60^\circ)$, with $A_w=1$ m, $\alpha = 30^\circ$, $\beta = 30^\circ$, and $C_{bm^*} = 0.1$.

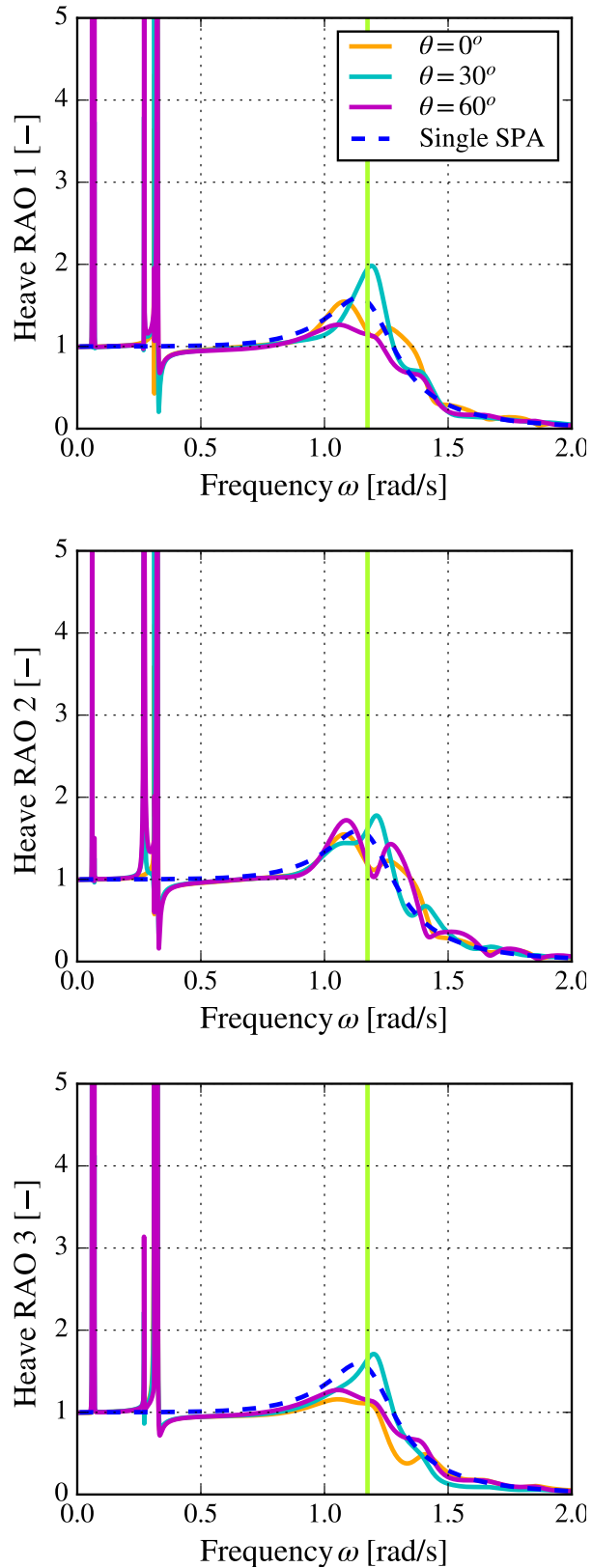


Figure B.12: Heave RAOs against the wave frequency ω for the three SPAs with bottom and inter-body mooring connections, for different values the angle of wave incidence $\theta=(0^\circ, 30^\circ, 60^\circ)$, with $A_w=1$ m, $\alpha = 30^\circ$, $\beta = 30^\circ$, and $C_{bm}^* = 0.1$. The green vertical lines correspond to the SPA resonance frequency.

Appendix C

Single spar-buoy OWC

Inclusion of viscous damping

The results for the RAOs of a single unmoored spar-buoy OWC discussed in Chapter 4 (Section 4.4.1) are presented, with and without viscous damping, with a turbine coefficient $k_t = 0.0015$ ms, and with default wave amplitude $A_w = 1$ m.

Fig. C.1 suggests that the inclusion of the viscous damping in surge, mainly affects the hydrodynamic response at the lower wave frequencies. The same effect can be observed for the case of the pitch RAO (Fig. C.3). The effect of the inclusion of the viscous damping in the hydrodynamics of a single device in heave (Fig. C.2) and in the relative motion between the buoy and the OWC (Fig. C.4) is quite profound, as these RAOs significantly decrease at the peak frequency. As a consequence, the CWR will also be affected, as it is dependent on the relative motion between the buoy and the OWC.

Although, the damping forces associated with the viscous effects may be overestimated, the present results suggest that their consideration in the numerical model is necessary, especially at the resonance frequency of each mode.

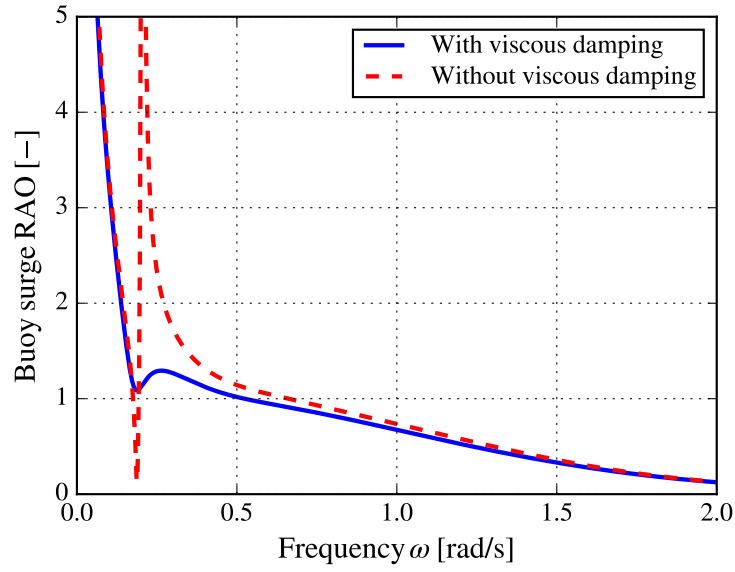


Figure C.1: Surge RAO for a single unmoored spar-buoy OWC, as a function of the wave frequency ω , with and without drag, for $A_w = 1$ m, $k_t = 0.0015$ ms.

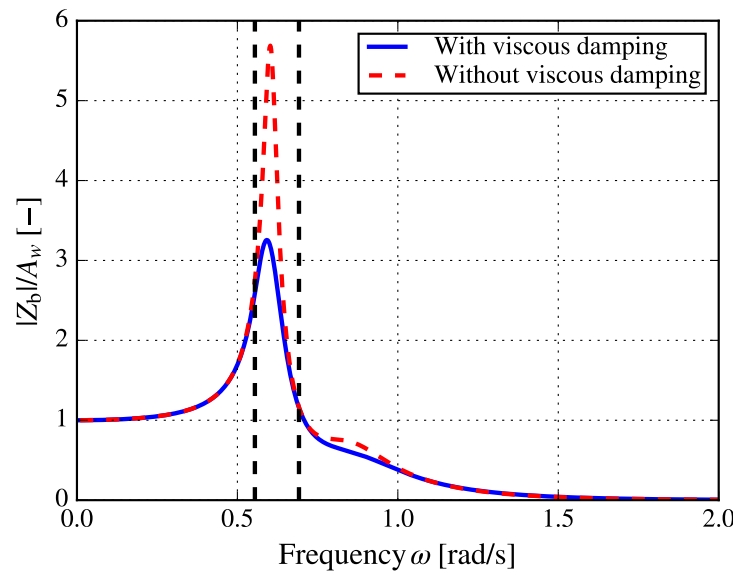


Figure C.2: Heave RAO for a single unmoored spar-buoy OWC, as a function of the wave frequency ω , with and without viscous damping, for $A_w = 1$ m, $k_t = 0.0015$ ms.

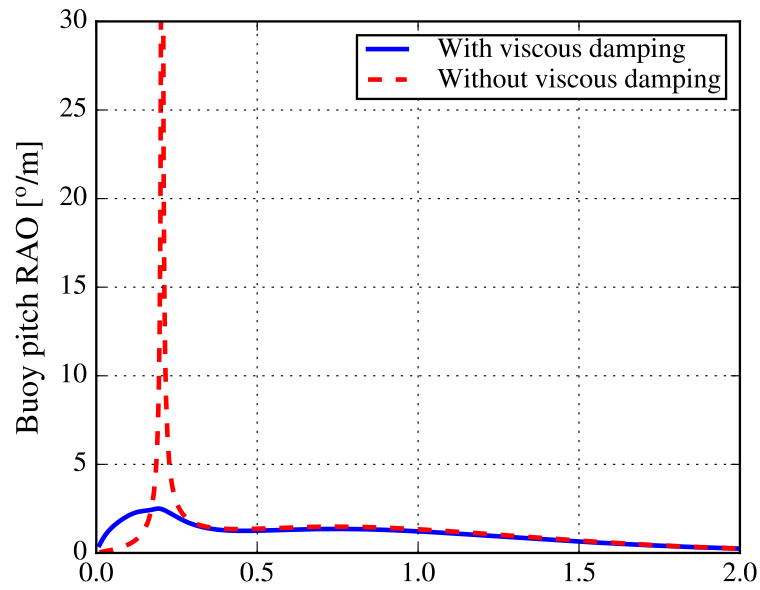


Figure C.3: Pitch RAO for a single unmoored spar-buoy OWC, as a function of the wave frequency ω , with and without viscous damping, for $A_w = 1$ m, $k_t = 0.0015$ ms.

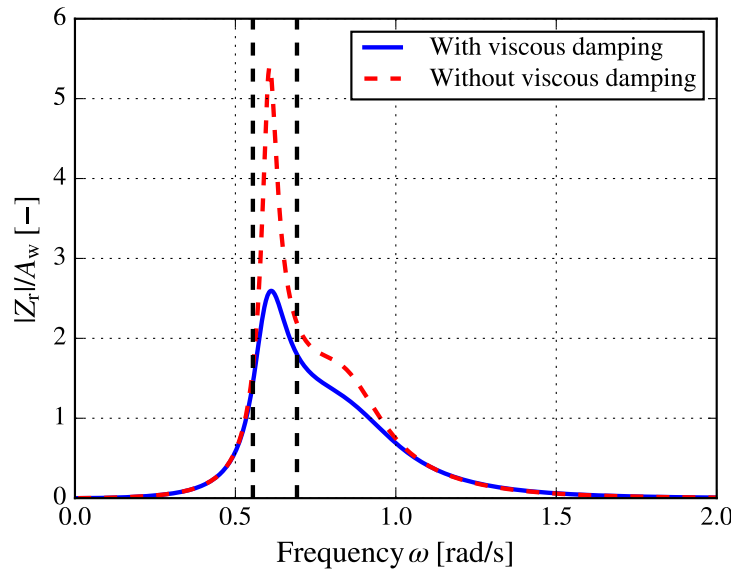


Figure C.4: Heave RAO of the relative motion between the buoy and the OWC, as a function of the wave frequency ω , for a single unmoored spar-buoy OWC, with and without viscous damping, for $A_w = 1$ m, $k_t = 0.0015$ ms.